Theoretische Physik

Squark Annihilation Contributions to Neutralino Dark Matter in NLO SUSY-QCD

Inaugural-Dissertation
zur Erlangung des Doktorgrades
der Naturwissenschaften im Fachbereich Physik
der Mathematisch-Naturwissenschaftlichen Fakultät
der Westfälischen Wilhelms-Universität Münster

vorgelegt von
Saskia Schmiemann
aus Lübbecke

- 2019 -

Dekan:	Prof. Dr. Gerhard Wilde
Erster Gutachter:	Prof. Dr. Michael Klasen
Zweiter Gutachter:	Prof. Dr. Alexander Kappes
Tag der mündlichen Prüfung:	.....
Tag der Promotion:	.....

Abstract

The Minimal Supersymmetric Standard Model (MSSM) is under intense scrutiny at the LHC and in dark matter searches. Interestingly, scenarios with light squarks of the third generation remain not only viable, but also well motivated by the observed Standard-Model-like Higgs boson mass and dark matter relic density. The latter often requires important contributions from squark pair and squark-anti-squark annihilation.

In this thesis, we consider the neutralino as the dark matter candidate. Constraints on the MSSM can be set by predictions on the relic density in comparison with the corresponding experimental value. Due to its high precision the uncertainties of the theoretical prediction have to be reduced. Main uncertainties arise in the investigation of the annihilation cross section. Our phenomenological study shows the importance of the squark annihilation into quark final states and the squark-anti-squark annihilation into quark pairs with respect to the relic density.

Following up on previous work, we present in this thesis a precision analysis of squark pair annihilation into quarks and squark-anti-squark annihilation into quark-anti-quark at next-to-leading order of QCD including Sommerfeld enhancement effects. We discuss all technical details of our one-loop, real emission and resummation calculations, their implementation in the precision tool DM@NLO, as well as the numerical impact on the annihilation cross section and in case of the squark pair annihilation into quarks the cosmological relic density in phenomenological MSSM scenarios respecting in particular current LHC constraints. We demonstrate that including these radiative corrections leads to substantial shifts in the preferred parameter regions by up to 20 GeV.

Zusammenfassung

Analysen am LHC und die Suche nach Dunkler Materie setzen immer höhere Limits auf den Parameterraum des Minimal Supersymmetrische Standard Models (MSSM). Interessanterweise bleiben Szenarien mit leichten Squarks der dritten Generation nicht nur realistisch, sondern sind auch gut motiviert durch die Beobachtung der standardmodellähnlichen Higgs-Bosonenmasse und der Reliktdichte der Dunklen Materie. Für die Bestimmung der Reliktdichte sind Beiträge von Squark-Paar- und Squark-Anti-Squark-Annihilation wichtig.

In der vorliegenden Dissertation wird das leichteste Neutralino als Dunkle Materie Kandidat betrachtet. Der Parameterraum des MSSM wird über die Vorhersagen der Reliktdichte im Vergleich zum entsprechenden experimentellen Wert eingeschränkt. Aufgrund der hohen Präzision des experimentellen Wertes müssen die Unsicherheiten der theoretischen Vorhersage reduziert werden. Die Hauptunsicherheiten in der Bestimmung der Reliktdichte stammen aus der Berechnung des Wirkungsquerschnitts. Unsere phänomenologische Studie zeigt den Einfluss der Squark- Annihilation in Quark-EndzustÃ¤nde und der Squark-Anti-Squark-Annihilation in Quark-Paare in Bezug auf die Reliktdichte.

Im Anschluss an frühere Arbeiten wird in dieser Arbeit eine Präzisionsanalyse der Annihilation von Squark-Paaren in Quarks und der Annihilation von Squark-Anti-Squarks in Quark-Anti-Quark unter Berücksichtigung der nächst höheren Ordnung von SUSY-QCD Korrekturen einschließlich des Sommerfeld-Effektes präsentiert. Alle technischen Details unserer Berechnungen zu den Schleifen, der Emissions zusätzlicher Teilchen und der Resummation, sowie deren Umsetzung im Präzisionstool `DM@NLO` werden in dieser Arbeit besprochen. Des Weiteren werden die numerischen Auswirkungen auf den Wirkungsquerschnitt und – im Falle der Squark-Paar-Annihilation in Quarks – auf die kosmologische Reliktdichte in phänomenologischen MSSM-Szenarien unter Berücksichtigung aktueller LHC-Limits gezeigt. Unter der Einbeziehung dieser Korrekturen kommt es zu erheblichen Verschiebungen der Parameterregionen um bis zu 20 GeV.

Publications

Main project:

- S. Schmiemann, J. Harz, B. Herrmann, M. Klasen, K. Kovařík, *Squark-pair annihilation into quarks at next-to-leading order*, arXiv:1903.1099 [hep-ph] (accepted for publication in Physical Review D)

Side projects:

- M. Klasen, K. Kovařík, S. Schmiemann, *Direct detection of neutralino dark matterwith DM@NLO* PoS EPS-HEP2017(2017)068, arXiv:1709.02681 [hep-ph]
- B. Fuks, M. Klasen, S. Schmiemann, M. Sunder, *Realistic simplified gaugino-higgsino models in the MSSM*, Eur. Phys.J C78 (2018) 209, arXiv:1710.09941 [hep-ph]
- M.A. Unland Elorrieta, L. Classen, J. Reubelt, S. Schmiemann, J. Schneider, A. Kappes, *Characterisation of the Hamamatsu R12199-01 HA MOD photomultiplier tube for low temperature applications*, JINST 14 (2019) P03015, arXiv:1902.01714 [physics.ins-det]

Contents

1. Introduction **1**

2. Supersymmetry **3**
2.1. Motivation . . . 3
2.1.1. The Hierarchy Problem . . . 4
2.1.2. Dark Matter . . . 4
2.1.3. The Grand Unified Theory . . . 5
2.2. The Theory Framework of SUSY . . . 5
2.2.1. SUSY Algebra . . . 5
2.2.2. Superfields . . . 7
2.2.3. Lagrangian . . . 9
2.3. The Minimal Supersymmetric Standard Model . . . 11
2.3.1. SUSY Breaking . . . 13
2.3.2. A Specific MSSM Model - the Phenomenological MSSM . . . 15
2.4. Particle Content of the MSSM . . . 15
2.4.1. Higgs Sector . . . 16
2.4.2. Sfermion Sector . . . 18
2.4.3. Chargino Sector . . . 19
2.4.4. Neutralino Sector . . . 19
2.5. SUSY Searches . . . 20
2.5.1. ATLAS . . . 20
2.5.2. Parameter Constraints on the pMSSM . . . 22
2.5.3. Impact of ATLAS Searches on Sparticle Masses . . . 22
2.5.4. CMS . . . 26

3. Dark Matter **31**
3.1. Evidence for Dark Matter . . . 31
3.1.1. Coma Cluster . . . 31
3.1.2. Rotation Curves . . . 32
3.1.3. Bullet Cluster . . . 32
3.1.4. Cosmic Microwave Background . . . 34
3.1.5. N-Body Simulations . . . 37
3.2. Properties of Dark Matter . . . 37
3.3. Dark Matter Candidates and Theories . . . 38

3.4. Dark Matter Searches . . . 39
3.4.1. Collider Searches . . . 40
3.4.2. Indirect Detection . . . 44
3.4.3. Direct Detection . . . 48
3.4.4. Conclusion . . . 50
3.5. Relic Density . . . 50
3.5.1. Boltzmann Equation . . . 50
3.5.2. Coannihilation within the Boltzmann Equation . . . 54
3.5.3. Thermal Averaging . . . 54
3.5.4. Computation of the Relic Density . . . 55

4. Influence of External Components in the Vicinity of a PMT on Its Electric Field 57
4.1. Photomultiplier Tubes . . . 58
4.2. Simulation . . . 59

5. DM@NLO 63
5.1. Status of DM@NLO . . . 63
5.2. Structure of the Tool . . . 66

6. Squark Annihilation into Quark Final States 69
6.1. Reference Scenarios . . . 73
6.2. Leading Order Cross Section . . . 80
6.3. Color Decomposition . . . 84

7. Virtual Corrections 89
7.1. Dimensional Regularization . . . 90
7.1.1. Generic Integral . . . 92
7.1.2. The Scalar Integral A_0 . . . 94
7.1.3. The Scalar Integral B_0 . . . 95
7.1.4. Tensor Reduction . . . 96
7.2. Calculation of Virtual Corrections . . . 97
7.2.1. Propagator Corrections . . . 99
7.2.2. Vertex Corrections . . . 102
7.2.3. Box Corrections . . . 107

8. Renormalization 109
8.1. Renormalization Principle . . . 109
8.2. Renormalization Scheme in DM@NLO . . . 113
8.2.1. Quark Sector . . . 113
8.2.2. Squark Sector . . . 115
8.2.3. Gluon Sector . . . 118

8.2.4. Gluino Sector . . . 118
8.2.5. α_S Renormalization . . . 120
8.3. Vertex Counterterms . . . 121

9. Real Emission **123**
9.1. The Phase Space Element for Three Particle Final States . . . 123
9.2. Parametrization of Final State Momenta . . . 127
9.3. Phase Space Slicing . . . 130
9.4. Soft Gluon Emission . . . 131

10. Sommerfeld Enhancement **137**

11. Numerical Results **143**
11.1. The NLO Cross Section Results . . . 143
11.1.1. Scenario I . . . 143
11.1.2. Scenario II . . . 145
11.1.3. Scenario III . . . 146
11.2. Impact on the neutralino relic density . . . 147
11.2.1. Scenario I . . . 147
11.2.2. Scenario II . . . 148

12. Conclusion **155**

A. Summary of Formulae **157**
A.1. Euler di-logarithm . . . 157
A.2. Dirac Algebra . . . 158
A.2.1. Dirac Matrices . . . 158
A.2.2. Spinors . . . 158
A.2.3. Traces . . . 159
A.3. Polarization . . . 159
A.4. Color . . . 160
A.4.1. SU(N) . . . 160
A.4.2. Useful Relations . . . 161

B. Couplings **163**
B.1. Gluons . . . 163
B.2. Gauginos . . . 165
B.3. 4 Squarks . . . 167
B.4. Vector Bosons . . . 167
B.5. Higgs Boson . . . 169

C. Tensor Reduction **171**
C.1. Loop Integrals . . . 171

C.2. Divergencies in Loop Integrals 172
C.3. Small Velocity Expansion of the Box Contribution 173

1 Introduction

One of the still unsolved questions in particle physics is the nature of *dark matter* (DM). There are several observations indicating the existence of an unknown mass in the Universe, the so-called dark matter. Even though no direct or indirect experiment could detect dark matter so far, cosmological observations have led to the assumption that there has to be some kind of dark matter. Dark matter is therefore a highly discussed topic. On the theoretical side various different theories try to explain the observation of the phenomena and the lack of detection of dark matter up to now. These theories go from minimal extensions of the Standard Model, where only a minimal amount of particles is added to the Standard Model, to complex theories like the Minimal Supersymmetric Standard Model (MSSM) based on the introduced Supersymmetry (SUSY). Supersymmetry is a new symmetry leading even in the MSSM to many new particles and a high number of undetermined free parameters. The MSSM provides a candidate for cold dark matter, due to R-parity conservation. This dark matter candidate fulfills several properties, which are known from astrophysical observations and experiments.

Via the measurement of the Planck satellite, the relic density of dark matter is known with high accuracy. The relic density represents the present amount of dark matter in the Universe. This parameter and also other observations and discoveries (like the Higgs particle) set constraints and exclude parts of the parameter space of the MSSM. In order to match the theoretical predictions with the experimental observations, the theoretical uncertainties have to be of the same order as the experimental errors. Due to the high precision of the Planck data, the theoretical uncertainties have to be reduced. In most public tools, the calculations of the cross-section are limited to tree-level calculations or include effective corrections at the most. In order to reduce the theoretical uncertainties, higher-order corrections have to be considered.

The relic density depends on the annihilation and co-annihilation cross sections of the dark matter particle and potential mass-degenerate particles. Within the MSSM, the stop and sbottom masses might be degenerate and close to the mass of the dark matter particle. Therefore, not only the dark matter annihilation and co-annihilation with squarks have to be taken into account, but also squark-squark and squark-anti-squark annihilation can provide large contributions to the relic density.

In this thesis, the focus lies on the squark annihilation to quark final states within

the MSSM, where a full next-to-leading order SUSY QCD calculation for QCD and Yukawa processes is performed. Additionally, the resummation is calculated for the initial particles at low velocities.

An introduction to SUSY is given in Chapter 2 including the motivation for SUSY and the theoretical framework. We then introduce the MSSM with its particle content and the dark matter candidate. Complementing this chapter, experiments for SUSY searches are presented with their current bounds and constraints.

In Chapter 3, we take a deeper look at dark matter in terms of astrophysical observations and possible particle candidates. Furthermore we review current experimental searches for dark matter. We additionally focus on the calculation of the relic density.

A short sidestep will be taken in Chapter 4 to an experimental side project within this thesis. In this experimental project, the electric field configuration of the Hamamatsu R12199-02 MOD three-inch photomultiplier tube (PMT) is investigated. This PMT is relevant for the newly developed optical module of the future extension of the IceCube neutrino telescope.

The project Dark Matter at Next-to-Leading Order `DM@NLO` will be introduced in Chapter 5, providing an overview on the project including the current status of implemented NLO calculations.

In Chapter 6, we discuss the phenomenology of the squark annihilation within the MSSM. We take a deeper look at the dominating channels within the tree level calculations and study the color structure.

The virtual corrections are discussed in Chapter 7. Starting with an introduction to dimensional regularization, we provide the most important tools for the calculation of the virtual corrections. The virtual corrections are described using selected examples.

Chapter 8 deals with the renormalization, first explained in the simple ϕ^4-theory and then applied to squark annihilation. Furthermore, different renormalization schemes are presented and the used scheme is described. Finally, the cancellation of the occuring ultraviolet divergent terms is demonstrated.

Within Chapter 9, the real emission is discussed. First, the phase space for three particles in the final state is shown and the parametrization is displayed. We discuss the method of phase-space slicing, with the factorization of the divergent part, shown for an example chosen from the processes in question.

The resummation is treated in Chapter 10. Due to the fact that the relevant processes are s-wave dominated, we concentrate on the s-wave resummation of identical and non-identical particles in the initial state.

In Chapter 11, we show the numerical results of the calculations and study the impact of the NLO calculation and the resummation on the relic density.

Finally we give a conclusion on the performed work and an outlook on further research in Chapter 12.

2 Supersymmetry

Up until now most experimental observations in astro-particle physics can be explained within the well-known Standard Model. However, there are still some open questions. Since the Standard Model describes many experiments with high precision, it is assumed that the Standard Model should be included in the extended theory. Such an extension can be formed by the consideration of a new symmetry, the so-called Supersymmetry. This symmetry is described by a set of generators that connect the bosons and fermions. If the Standard Model is extended only by a pair of these generators (one speaks also of a N=1 Supersymmetry), the so-called *Minimal Supersymmetric Standard Model* (MSSM) results. This model has more than a hundred free parameters, which makes the search for this model very difficult. There are experiments as ATLAS [1] and CMS [2], which have already produced large analyses of this model. So far there has been no sign from Supersymmetry. Due to the absence of signs, limits have been set on the existence of the MSSM and the corresponding parameter space. However, there is still a large parameter space open in the MSSM. In the following, the motivation, theoretical basics and algebra of Supersymmetry will be given with the focus on the resulting MSSM and its particle content. Furthermore, we will discuss the phenomenological MSSM (pMSSM), defined by a reduced number of free parameters. Finally, we give an overview of current experimental limits in the parameter space of the MSSM . The interested readers are referred to secondary literature on Supersymmetry, e.g. [3, 4, 5, 6].

2.1. Motivation

Even though there is no hint of supersymmetric particles in nature so far, SUSY and the resulting MSSM are theoretically appealing. Within the MSSM several unsolved problems can be explained at the same time. In the following, we very briefly discuss three motivations for Supersymmetry and the MSSM.

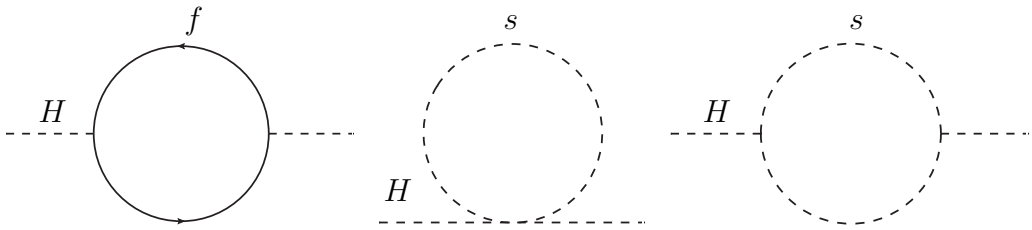

Figure 2.1.: Diagrams for SM contribution (left) and scalar contribution (middle, right) to the Higgs self energy.

2.1.1. The Hierarchy Problem

The discovery of the Higgs boson in 2012 by ATLAS [7] and CMS [8] and the experimental determination of the Higgs boson mass [9] highlights one of the problems in the SM, the so-called *Hierarchy Problem* [10, 11]. Assuming that the SM is part of a larger unified theory (GUT), one considers two scales, the electroweak symmetry breaking scale $\mathcal{O}(100\,\text{GeV})$ and the unification scale $\mathcal{O}(10^{16}\,\text{GeV})$. Quantum corrections (see Fig. 2.1), that contribute to the Higgs mass, depend on the unification scale (for example through the ultraviolet cutoff). To get rid of these much too large quadratic contributions, an unnatural fine-tuning would be needed. In the MSSM this problem is solved by the introduction of new particles which provide additional quantum corrections which cancel the quadratic dependence of the unification scale of the SM corrections.

2.1.2. Dark Matter

Another hint of physics beyond the Standard Model is given by some astrophysical observations. These observations cannot be described with the known baryonic mass of the Standard Model. They suggest that there is more matter in the Universe, the so-called dark matter. A popular assumption is that dark matter consists of *weakly interacting massive particles* (WIMPs) of about 100 GeV mass. Even though the neutrino can be a candidate for dark matter, it can not explain the amount of dark matter needed to explain the observations. In the supersymmetric extension of the SM where R-parity, an ad-hoc Z_2-symmetry, is conserved, the lightest supersymmetric particle is stable and if neutral it can be a candidate for dark matter. Typical candidates are ether the lightest neutralino $\tilde{\chi}_1^0$ or the sneutrino $\tilde{\nu}$. This topic will be discussed in more detail in Chapter 3.

2.1.3. The Grand Unified Theory

Based on the unification of forces in the electroweak model, the search for a theory with a unification of forces is appealing. Such a theory is called Grand Unified Theory (GUT). If the couplings in the Standard Model are evolved to high scales using the renormalization group equations (RGE), the gauge couplings do not lead to a unification at any arbitrary scale. However, for the dicussed minimal supersymmetric extension of the SM, adding the MSSM content to the RGE's, the couplings meet at an energy $\Lambda_{\mathrm{GUT}} \sim 10^{16}\,\mathrm{GeV}$ [12].

2.2. The Theory Framework of SUSY

In the following we give an introduction to the most important aspects of the theory framework of SUSY [5], [6], [13], [14]. First we focus on the SUSY algebra. We continue with the introduction of superfields and finally construct a supersymmetric Lagrangian.

2.2.1. SUSY Algebra

In 1967, the Coleman Mandula theorem [15] stated that the Poincaré supersymmetry group is the largest possible one. Therefore, the only way to add a new symmetry to it is by a direct product with another group. But in 1975, the Haag-Lopuszanski-Sohnius theorem [16] showed a non-trivial way to combine two algebras by considering anti-commuting generators. In parallel, Wess and Zumino [17, 18] used the same idea to build the first supersymmetric model. The extension of the Poincaré group with anti-commuting generators this led to a new kind of symmetry, the so-called Supersymmetry. Supersymmetry is therefore a non-trivial (in the sense that the new generators are related to the old ones) extension of the Poincaré symmetry.

In SUSY, the even (bosonic) generators of the Lie subalgebra obey the Coleman-Mandula theorem, it is a direct sum of the Poincaré algebra with an internal symmetry. The odd (fermionic) generators are represented by $(\frac{1}{2}, 0)$ and $(0, \frac{1}{2})$ of the homogeneous Lorentz group. The spinor generators exist in the fermionic subalgebra and lead to the supercharges Q_α. The generators are responsible for the transformations among the two subalgebras.

In the following we concentrate on the $N = 1$ Supersymmetry, where only one additional pair of fermionic generators $Q_\alpha^{N=1}$,$Q_\beta^{N=1}$ is added. The generators transform fermionic into bosonic degrees of freedom and vice versa, symbolically written:

$$Q|fermion\rangle = |boson\rangle \qquad Q|boson\rangle = |fermion\rangle. \tag{2.1}$$

The underlying algebra consists of the usual Poincaré algebra.

$$[P_\mu, P_\nu] = 0, \tag{2.2}$$
$$[M_{\mu\nu}, P_\rho] = i(\eta_{\nu\rho}P_\mu - \eta_{\mu\rho}P_\nu), \tag{2.3}$$
$$[M_{\mu\nu}, M_{\rho\sigma}] = -i(\eta_{\mu\rho}M_{\nu\sigma} - \eta_{\mu\sigma}M_{\nu\rho} - \eta_{\nu\rho}M_{\mu\sigma} - \eta_{\nu\sigma}M_{\mu\rho}), \tag{2.4}$$

P^μ is a four-momentum generator of space-time translations and $M_{\mu\nu}$ the generator of the Lorentz transformations. This leads to the Poincaré super-algebra

$$\{Q_\alpha, \bar{Q}_{\dot\beta}\} = 2\sigma^\mu_{\alpha\dot\beta}P_\mu, \tag{2.5}$$
$$\{\bar{Q}^{\dot\alpha}, Q^\beta\} = 2\sigma^\mu_{\dot\alpha\beta}P_\mu, \tag{2.6}$$
$$\{Q_\alpha, Q_\beta\} = \{\bar{Q}^{\dot\alpha}, \bar{Q}^{\dot\beta}\} = 0, \tag{2.7}$$
$$[Q_\alpha, P^\mu] = [\bar{Q}^{\dot\alpha}, P^\mu] = 0, \tag{2.8}$$
$$[M_{\rho\nu}, Q^\alpha] = -(\sigma_{\mu\nu})^\beta_\alpha Q_\beta \tag{2.9}$$
$$[M_{\rho\nu}, \bar{Q}^{\dot\alpha}] = -(\bar{\sigma}_{\mu\nu})^{\dot\beta}_{\dot\alpha}\bar{Q}_{\dot\beta}. \tag{2.10}$$

The index $\alpha = 1, 2$ indicates the representation $(\frac{1}{2}, 0)$, while $\dot\alpha = 1, 2$ indicates $(0, \frac{1}{2})$. The generalized Pauli matrices $\sigma^\mu_{\alpha\dot\beta} = (\mathbb{1}, \sigma_i)$ and $\bar{\sigma}^\mu_{\alpha\dot\beta} = (\mathbb{1}, -\sigma_i)$ were used, including the well known Pauli matrices σ_i.

Furthermore, the usual Minkowski space with its four "bosonic" commuting space-time coordinates has to be extended by four "fermionic" anticommuting Grassmann variables $\theta_{\alpha=1,2}$ and $\theta_{\dot\alpha=1,2}$, indicated as two-component Weyl spinors, which obey

$$\{\theta_\alpha, \theta_\beta\} = \{\bar\theta_{\dot\alpha}, \bar\theta_{\dot\beta}\} = \{\theta_\alpha, \bar\theta_{\dot\beta}\} = 0. \tag{2.11}$$

The superspace is built up out of these eight coordinates. Defining a unitary operator

$$U(x, \theta, \bar\theta) = e^{i(\theta^\alpha Q_\alpha + \bar\theta_{\dot\alpha}\bar{Q}^{\dot\alpha} - x_\mu P^\mu)} \tag{2.12}$$

in terms of the hermitian operators $P_\mu, Q_\alpha, \bar{Q}_{\dot\alpha}$, the product can be written as

$$U(a_\mu, \xi, \bar\xi)U(x_\mu, \theta, \bar\theta) = U(a_\mu + x_\mu + i(\xi\sigma\bar\theta - \theta\sigma\bar\xi), \theta + \xi, \bar\theta + \bar\xi). \tag{2.13}$$

The generators are linked via $\bar\theta_{\dot\alpha} = Q^+_\alpha$. Since Q and $\bar{Q}$ do not commute, an additional term appears in the Minkowski coordinates. This illustrates the non-trivial connection. Each function $\Phi(x, \theta, \bar\theta)$ is called a superfield, the superfield is defined using the unitary matrix

$$\begin{aligned} &U(a_\mu, \xi, \bar\xi)U(x_\mu, \theta, \bar\theta)\Phi(0)U^{-1}(x_\mu, \theta, \bar\theta)U^{-1}(a_\mu, \xi, \bar\xi) \\ &\quad = \Phi(a_\mu + x_\mu + i(\xi\sigma\bar\theta - \theta\sigma\bar\xi), \theta + \xi, \bar\theta + \bar\xi). \end{aligned} \tag{2.14}$$

$\phi(x), m(x), n(x)$	complex or pseudo-scalar fields
$\psi(x), \varphi(x)$	left-handed Weyl spinor fields
$\bar{\chi}(x), \bar{\lambda}(x)$	right-handed Weyl spinor fields
A_μ	Lorentz four-vector field
$d(x)$	real scalar field

Table 2.1.: List of the component fields arising in the general superfield.

The differential representation of group operators is obtained by the analysis of an infinitesimal variation of the superfield $\delta_S \Phi$

$$Q_\alpha = \frac{\partial}{\partial \theta_\alpha} - i\sigma^\mu_{\alpha\dot{\beta}} \bar{\theta}^{\dot{\beta}} \partial_\mu \qquad \bar{Q}_{\dot{\alpha}} = -\frac{\partial}{\partial \bar{\theta}^{\dot{\alpha}}} + i\sigma^\mu_{\beta\dot{\alpha}} \theta^\beta \partial_\mu. \tag{2.15}$$

The covariant derivatives are defined by

$$D_\alpha = \frac{\partial}{\partial \theta_\alpha} + i\sigma^\mu_{\alpha\dot{\beta}} \bar{\theta}^{\dot{\beta}} \partial_\mu \qquad \bar{D}_{\dot{\alpha}} = -\frac{\partial}{\partial \bar{\theta}^{\dot{\alpha}}} - i\sigma^\mu_{\beta\dot{\alpha}} \theta^\beta \partial_\mu, \tag{2.16}$$

which anticommute with the supersymmetric transformations

$$\{D_\alpha, Q_\beta\} = \{D_\alpha, \bar{Q}^{\dot{\beta}}\} = \{\bar{D}_{\dot{\alpha}}, Q_\beta\} = \{\bar{D}_{\dot{\alpha}}, \bar{Q}^{\dot{\beta}}\} = 0. \tag{2.17}$$

We refer to Refs. [19, 20] for further details.

2.2.2. Superfields

A superfield is understood as a function in superspace, depending on the coordinate set $z = \{x, \theta, \bar{\theta}\}$. Due to the commutation relations (2.11) higher orders of θ vanish within the expansion of the superfield in θ, making the expansion finite. A general superfield expanded in θ and $\bar{\theta}$ is given by

$$\begin{aligned} \Phi(x, \theta, \bar{\theta}) =& \phi(x) + \theta\psi(x) + \bar{\theta}\,\bar{\chi}(x) + \theta\theta m(x) + \bar{\theta}\,\bar{\theta} n(x) \\ &+ \theta\sigma^\mu\bar{\theta} A_\mu(x) + \theta\theta\bar{\theta}\,\bar{\lambda}(x) + \bar{\theta}\,\bar{\theta}\theta\varphi(x) + \theta\theta\bar{\theta}\,\bar{\theta} d(x). \end{aligned} \tag{2.18}$$

The superfield contains a finite multiplet of the component fields listed in Tab. 2.1.

The representation of the general superfield (2.18) can be reduced to an irreducible superfield by imposing covariant constraints

$$\bar{D}_{\dot{\alpha}} \Phi(x, \theta, \bar{\theta}) = 0, \tag{2.19}$$

$$D_\alpha \Phi^+(x, \theta, \bar{\theta}) = 0, \tag{2.20}$$

$$\Phi(x, \theta, \bar{\theta}) = \Phi^+(x, \theta, \bar{\theta}). \tag{2.21}$$

A superfield obeying (2.19) and (2.20) is called a *chiral superfield*, whereas a superfield obeying (2.21) is called a *vector superfield*. Both types of superfields are discussed below.

Chiral Superfields

The chiral superfield contains among its component fields the chiral SM fermion and its superpartner. There are two kinds of chiral fields, left-handed chiral superfields Φ_L, satisfying Eq. (2.19), and right-handed chiral superfields Φ_R, which satisfy Eq. (2.20). Using the condition (2.19) and performing a variable transformation $y^\mu = x^\mu + i\theta\sigma^\mu\bar{\theta}$, the left-handed superfield is simplified

$$\Phi_L(y,\theta) = \phi(y) + \sqrt{2}\theta\psi(y) + \theta\theta F(y). \tag{2.22}$$

Similarly the right-handed superfield can be determined using Eq. (2.20) and the variable transformation $z^\mu = x^\mu - i\theta\sigma^\mu\bar{\theta}$

$$\Phi_R(z,\theta) = \phi^*(z) + \sqrt{2}\bar{\theta}\bar{\psi}(z) + \bar{\theta}\bar{\theta}F^*(z). \tag{2.23}$$

Applying the general form of the supersymmetric transformation

$$\delta_\xi = \xi^a\left(\frac{\partial}{\partial\theta^a} + i(\sigma^\mu)_{a\dot{b}}\theta^{\dot{b}}\partial_\mu\right) + \xi_{\dot{a}}\left(\frac{\partial}{\partial\theta_{\dot{a}}} + i(\bar{\sigma}^\mu)^{\dot{a}b}\theta_b\partial_\mu\right) \tag{2.24}$$

gives the following infinitesimal transformations of the component fields

$$\delta_S\phi(y) = \sqrt{2}\alpha\psi(y)\,, \tag{2.25}$$

$$\delta_S\varphi(y) = \sqrt{2}\alpha F(y) + i\sqrt{2}\sigma^\mu\bar{\alpha}\partial_\mu\phi(y)\,, \tag{2.26}$$

$$\delta_S F(y) = -i\sqrt{2}\partial_\mu\psi(y)\sigma^\mu\bar{\alpha}\,. \tag{2.27}$$

The transformation from a bosonic to a fermionic degree of freedom takes place via the transformation (2.25), vice versa via (2.26). The auxiliary field $F(y)$ transforms into a total derivative. This transformation will later be usefull when we construct Lagrangians invariant under Supersymmetry.

Vector Superfields

A *vector superfield* V can be used to describe spin-1 bosons and is defined by the condition Eq. (2.21). The vector superfield can be written as

$$\begin{aligned} V(x,\theta,\bar{\theta}) =& C(x) + \theta\xi(x) + \bar{\theta}\,\bar{\xi}(x) + (\theta\theta)M(x) + (\bar{\theta}\,\bar{\theta})M^*(x) \\ &+ (\theta\sigma^\mu\bar{\theta})A_\mu(x) + (\theta\theta)\bar{\theta}\,\bar{\lambda}(x) + (\bar{\theta}\,\bar{\theta})\theta\lambda(x) + (\theta\theta)(\bar{\theta}\,\bar{\theta})D(x) \end{aligned} \tag{2.28}$$

with real scalar fields $C(x)$ and $D(x)$, a complex scalar field $M(x)$, complex spinor fields $\xi(x)$ and $\lambda(x)$ and a real vector field $A_\mu(x)$. As we will discuss in the next section, the Lagrangian containing vector superfields is invariant under a gauge transformation. The Wess-Zumino gauge [18]

$$V_{WZ}(x,\theta,\bar{\theta}) = V(x,\theta,\bar{\theta}) + \Lambda(x,\theta,\bar{\theta}) + \Lambda^+(x,\theta,\bar{\theta}) \tag{2.29}$$

is chosen as an appropriate gauge, where Λ is a general chiral superfield. In supersymmetric theories, the Wess-Zumino gauge is adopted where the Λ chiral superfield is used to make ζ, C and M vanish. By choosing $\xi(x) = C(x) = M(x) = 0$, the component fields vanish. Adopting the Wee-Zumino gauge still leaves the conventional freedom of gauge choice $A_\mu(x) \to A_\mu(x) + \partial_\mu \Psi(x)$. Finally, a general vector superfield in Wess-Zumino gauge can be written as

$$V_{\mathrm{WZ}}(x, \theta, \bar{\theta}) = (\theta\sigma^\mu\bar{\theta})A_\mu(x) + (\theta\theta)\bar{\theta}\bar{\lambda}(x) + (\theta\theta)(\bar{\theta}\bar{\theta})D(x). \tag{2.30}$$

The highest order component field $D(x)$ is an auxiliary field. Similar to $F(x)$, it transforms as a total derivative.

2.2.3. Lagrangian

In the following, we want to construct a supersymmetric Lagrangian. In order to be invariant under supersymmetric transformation, the Lagrangian has to vanish up to a total derivative. First, we investigate a product of left-handed chiral superfields

$$\begin{aligned}\Phi_{L,1}\Phi_{L,2} &= (\phi_1 + \sqrt{2}\theta\psi_1 + (\theta\theta)F_1)(\phi_2 + \sqrt{2}\theta\psi_2 + (\theta\theta)F_2) \\ &= \phi_1\phi_2 + \sqrt{2}\theta(\phi_1\psi_2 + \psi_1\phi_2) + \theta\theta(\phi_1 F_2 + \phi_2 F_1 - \psi_1\psi_2).\end{aligned} \tag{2.31}$$

The component field with the highest order in θ of the expanded chiral superfield transforms under supersymmetric transformation as a total space-time derivative. The terms linear in $(\theta\theta)$ are called *F-term* and contribute to the Lagrangian. The $-\psi_1\psi_2$ term gives rise to a fermion mass term. Now we consider the product of three left-handed chiral superfields

$$\begin{aligned}\Phi_{L,1}\Phi_{L,2}\Phi_{L,3} = \phi_1\phi_2\phi_3 &+ \sqrt{2}\theta(\phi_1\phi_2 + \psi_3 + \phi_1\psi_2\phi_3 + \psi_1\phi_2\phi_3) \\ &+ (\theta\theta)(\phi_1\phi_2 F_3 + \phi_1 F_2\phi_3 + F_1\phi_2\phi_3) \\ &- (\theta\theta)(\psi_1\psi_2\phi_3 + \psi_1\phi_2\psi_3 + \phi_1\psi_2\psi_3).\end{aligned} \tag{2.32}$$

The product of three chiral superfields would lead to a mass dimension greater than four and thus to a non-renormalizable interaction in the term $-(\theta\theta)(\psi_1\psi_2\phi_3 + \psi_1\phi_2\psi_3 + \phi_1\psi_2\psi_3)$.

Another possibility to combine chiral superfields is the product of a left-handed and a right-handed superfield. The resulting superfield product, is a vector superfield

$$\Phi_L\Phi_L^*|_D = FF^* - \phi\partial_\mu\partial^\mu\phi^* - i\bar{\psi}\sigma_\mu\partial^\mu\psi. \tag{2.33}$$

Only $\theta\ \theta\ \bar{\theta}\ \bar{\theta}$ is invariant under SUSY transformation. Therefore this part must be considered for the supersymmetric Lagrangian. The last two terms of the expression Eq. (2.33) are kinematic terms for the scalar ϕ and fermionic ψ component. The term FF^* is the scalar superpotential, by defintion greater than or equal to zero. The

kinematic term F for the component field does not appear, which means that the field does not propagate and is only a non-physical, auxiliary field.

The Lagrange constructed so far looks like

$$\mathcal{L} = \Phi_i \Phi_i^+|_D + (g_i \Phi_i + \frac{1}{2} m_{ij} \Phi_i \Phi_j + \frac{1}{3} \lambda_{ijk} \Phi_i \Phi_j \Phi_k + h.c)|_F, \tag{2.34}$$

where the first term is the canonical Kähler potential and the second term the *superpotential* $\mathcal{W}$

$$\mathcal{W} = (g_i \Psi_i + \frac{1}{2} m_{ij} \Psi_i \Psi_j + \frac{1}{3} \lambda_{ijk} \Psi_i \Psi_j \Psi_k + h.c)|_F. \tag{2.35}$$

The Lagrangian does not contain any derivatives of the auxiliarly field F. Hence the Euler-Lagrange equations read

$$\begin{aligned} \frac{\partial \mathcal{L}}{\partial F_i(x)} &= F_i^*(x) + g_i + m_{ij} \phi_j(x) + \lambda_{ijk} \phi_j(x) \phi_k(x) = 0 \\ \frac{\partial \mathcal{L}}{\partial F_i^*(x)} &= F_i(x) + g_i^* + m_{ij}^* \phi_j^*(x) + \lambda_{ijk}^* \phi_j^*(x) \phi_k^*(x) = 0 \Rightarrow \; F_i = -\frac{\partial \mathcal{W}^+}{\partial \Psi_i^+}. \end{aligned} \tag{2.36}$$

Terms containing the auxiliarly filed F can be expressed in terms of the scalar field $\phi(x)$. Therefore, the chiral superfield has only two bosonic degrees of freedom from the complex scalar field ϕ. With the two fermionic degrees of freedom of the Weyl-spinor field ψ, they form a supermultiplet.

By looking at the spin-1-particle interaction, we construct the Lagrangian of the supersymmetric Abelian theory. The supersymmetric field strength

$$W_\alpha = -\frac{1}{4} (\bar{D}\bar{D}) D_\alpha V(x, \theta, \bar{\theta}), \tag{2.37}$$

$$\bar{W}_{\dot{\alpha}} = -\frac{1}{4} (DD) \bar{D}_{\dot{\alpha}} V(x, \theta, \bar{\theta}) \tag{2.38}$$

is similar to the electromagnetic field strength tensor $F_{\mu\nu} = \partial_\mu A_\nu - \partial_\nu A_\mu$. W_α and $\bar{W}_{\dot{\alpha}}$ are chiral superfields, $D_\alpha, \bar{D}_{\dot{\alpha}}$ covariant derivatives and V a general vector superfield. The supersymmetric field strengths expanded in terms of component fields read in Wess-Zumino gauge

$$W_\alpha = \lambda_\alpha(y) + D(y)\theta_\alpha - (\sigma^{\mu\nu}\theta)_\alpha F_{\mu\nu}(y) + i(\theta\theta)\sigma^\mu_{\alpha\dot{\beta}} \partial_\mu \bar{\lambda}^{\dot{\beta}}(y), \tag{2.39}$$

$$\bar{W}_{\dot{\alpha}} = \bar{\lambda}_{\dot{\alpha}}(z) + D(z)\bar{\theta}_{\dot{\alpha}} - \epsilon_{\dot{\alpha}\dot{\beta}} (\bar{\sigma}^{\mu\nu}\theta)^{\dot{\beta}} F_{\mu\nu}(z) + i(\bar{\theta}\,\bar{\theta})(\partial_\mu \lambda(z) \sigma^\mu)_{\dot{\alpha}}. \tag{2.40}$$

The supersymmetric field strength is a chiral superfield, so $W_\alpha W^\alpha$ are chiral superfield as well. Again, terms linear in $\theta\theta$ are the relevant expressions for the Lagrangian. Thus the corresponding Lagrangian for Abelian case is

$$\begin{aligned} \mathcal{L} &= \frac{1}{4} (W^\alpha W_\alpha + \bar{W}_{a\dot{\alpha}} \bar{W}^{\dot{\alpha}}|_F \\ &= \frac{1}{2} D^2(x) . \frac{1}{4} F_{\mu\nu}(x) F^{\mu\nu}(x) + \frac{i}{2} \lambda(x) \sigma^\mu \partial_\mu \bar{\lambda}(x) - \frac{i}{2} (\partial_\mu \lambda(x)) \sigma^\mu \bar{\lambda}(x), \end{aligned} \tag{2.41}$$

where $z^\mu = x^\mu - i\theta\sigma\bar{\theta}$ and $y^\mu = x^\mu + i\theta\sigma\bar{\theta}$ are used. The auxiliary field $D(x)$ is substituted by the use of the equations of motion (2.36). The fermion λ entering the gauge interaction is called gaugino.

Now, regarding the non-abelian gauge interactions, the vector field transforms under a general non-abelian supersymmetric gauge transformation like

$$e^{V'} \to e^{-i\Lambda^+} e^V e^{i\Lambda}. \tag{2.42}$$

Λ is a chiral superfield, specifying the gauge transformation. This can be performed similarly for the field strength

$$W_\alpha \to e^{-i\Lambda} W_\alpha e^{i\Lambda}, \tag{2.43}$$

$$\bar{W}_{\dot{\alpha}} \to e^{i\Lambda} \bar{W}_{\dot{\alpha}} e^{-i\Lambda}. \tag{2.44}$$

Combining Eq.(2.34) with Eq.(2.41) and taking into account the modified expressions Eq.(2.42)-(2.44), the final supersymmetric Lagrangian becomes

$$\mathcal{L} = \Phi_i^+ (e^V)_{ij} \Phi_j \Big|_D + \frac{1}{4} \left(W^{\alpha a} W^a_\alpha + \bar{W}^a_{\dot{\alpha}} \bar{W}^{\dot{\alpha} a} \right) \Big|_F + \left(\mathcal{W}(\Phi_i) + h.c. \right) \Big|_F, \tag{2.45}$$

where a indicates the gauge indices. The Lagrangian, again rewritten in terms of component fields, reads

$$\begin{aligned} \mathcal{L} = {} & i\psi_j \sigma_\mu D^{+\mu}_{ij} \bar{\psi}_i + (D^\mu_{ij}\phi_j)^+ (D_{\mu ik}\phi_k) \bar{\lambda}^a - \sqrt{2} g (\bar{\lambda}^a \bar{\psi}_i T^a_{ij} \phi_j + h.c.) \\ & - \frac{1}{4} F^a_{\mu\nu} F^{\mu\nu a} + i\lambda^a \sigma^\mu D_\mu - V(\phi_i, \phi_j^*) - \left[\frac{1}{2} \psi_i \psi_j \mathcal{W}_{ij}(\phi) + h.c. \right]. \end{aligned} \tag{2.46}$$

The covariant derivatives $D^\mu_{ij} = \delta_{ij}\partial^\mu + igA^{\mu a} T^a_{ij}$ are defined with the gauge field $A^{\mu a}$, the gauge coupling g and T^a_{ij} as a generator of the group. The scalar superpotential is given by

$$V(\phi_i, \phi_j^*) = F_i F_i^* + \frac{1}{2} D^a D^a, \tag{2.47}$$

with $F_i = -\frac{\partial \mathcal{W}^+}{\partial \Psi_i^+}$ and $D^a = -g\phi_i^+ T^a_{ij} \phi_j$. Starting with this most general supersymmetric Lagrangian we can now construct an extension of Standard Model. In the following, we focus on the smallest possible extension, the *Minimal Supersymmetric Standard Model* (MSSM).

2.3. The Minimal Supersymmetric Standard Model

The minimal extension of the Standard Model with $N = 1$ supersymmetry is called the *Minimal Supersymmetric Standard Model* (MSSM). In this extension, each fermionic

Chiral superfields		spin 0	spin 1/2	$SU(3)_C, SU(2)_L, U(1)_Y$
squarks, quarks (3 families)	Q	$(\tilde{u}_L, \tilde{d}_L)$	(u_L, d_L)	$(\mathbf{3}, \mathbf{2}, \frac{1}{6})$
	$\bar{u}$	$\tilde{u}_R^*$	u_R^+	$(\bar{\mathbf{3}}, 1, -\frac{2}{3})$
	$\bar{d}$	$\tilde{d}_R^*$	d_R^+	$(\bar{\mathbf{3}}, 1, \frac{1}{3})$
sleptons, leptons (3 families)	L	$(\tilde{\nu}, \tilde{e}_L)$	(ν, e_L)	$(1, \mathbf{2}, -\frac{1}{2})$
	$\bar{e}$	$\tilde{e}_R^*$	e_R^+	$(1, 1, 1)$
Higgs, higgsinos	H_u	(H_u^+, H_u^0)	$(\tilde{H}_u^+, \tilde{H}_u^0)$	$(1, \mathbf{2}, +\frac{1}{2})$
	H_d	(H_d^0, H_d^-)	$(\tilde{H}_d^0, \tilde{H}_d^-)$	$(1, \mathbf{2}, -\frac{1}{2})$

Table 2.2.: Chiral superfields in the MSSM [3].

Gauge superfields	spin 1/2	spin 1	$SU(3)_C, SU(2)_L, U(1)_Y$
gluino, gluon	$\tilde{g}$	g	$(\mathbf{8}, 1, 0)$
winos, W bosons	$\tilde{W}^\pm\ \tilde{W}^0$	$W^\pm\ W^0$	$(1, \mathbf{3}, 0)$
bino, B boson	$\tilde{B}^0$	B^0	(1,1,0)

Table 2.3.: Gauge superfields in the MSSM [3].

chirality state from the SM has a corresponding spin-0 superpartner, the so-called sfermion[1]. Each pair is embedded in a chiral superfield. All superfields are listed with the corresponding SM fermion in Tab. 2.2 and with the corresponding SM boson in Tab. 2.3. For every generation of quarks, a $SU(2)_L$-doublet Q of left-handed chiral superfields exists as well as two $SU(2)_L$-singlets of right-handed superfields $\bar{u}$ and $\bar{d}$. For leptons each family has a $SU(2)_L$-doublet L of left-handed superfields and a singlet of right-handed chiral superfield $\bar{e}$. To obtain up and down quark masses, two Higgs doublets are necessary. Furthermore, these doublets cancel anomalies introduced by the higgsinos. There exist two chiral superfields containing a Higgs boson and its superpartner, the higgsino, forming two Higgs doublets H_u and H_d. Each gauge boson gets a fermionic spin-1/2 superpartner, the so-called gaugino.

In order to construct a renormalizable MSSM superpotential, the following contribu-

[1]The nomenclature refers to a supersymmetric particle as a sparticle, also a supersymmetric fermion as sfermion, the same goes for quarks and leptons and their superpartners. It is different with bosons, where the gluon becomes the gluino, the W-boson becomes the wino and so on.

tions of the aforementioned chiral superfields are possible:

$$\mathcal{W}_{MSSM} = (y_u)_{ij} H_u Q_i \bar{u}_j + (y_d)_{ij} H_d Q_i \bar{d}_j + (y_e)_{ij} H_d L_i \bar{e}_j - \mu H_d H_u, \tag{2.48}$$

$$\mathcal{W}_{\Delta L=1} = \frac{1}{2}\lambda^{ijk} L_i L_j \bar{e}_k + \lambda'^{ijk} L_i Q_j \bar{d}_k + \mu'^i L_i H_u, \tag{2.49}$$

$$\mathcal{W}_{\Delta B=1} = \frac{1}{2}\lambda''^{ijk} \bar{u}_i \bar{d}_j \bar{d}_k \,. \tag{2.50}$$

Here i, j are generation indices, y_u, y_d and y_e are the 3×3 Standard Model Yukawa coupling matrices, μ is the supersymmetric mass term of the Higgs doublets and λ, λ' and λ'' are 3×3 matrices similar to the Yukawa couplings. The terms in Eqs. (2.49) and (2.50) violate baryon number B (2.50) or lepton number L (2.49) conservation. There are stringent constraints on the couplings λ', λ'' due to the non-observation of proton decay and due to the fact that no $B-$ or $L-$ violating processes have been observed. To forbid the decay of the proton, a new multiplicative quantum number called R-parity is introduced

$$P_R = (-1)^{3(B-L)+2s}, \tag{2.51}$$

where s stands for the spin of the particle. This discrete Z_2 symmetry causes all Standard Model particles to have an even R-parity ($P_R = +1$) and all supersymmetric particles an odd R-parity ($P_R = -1$). The conservation of R-parity forbids $B-$ and $L-$ violating terms. Furthermore, the conservation of R-parity forbids the *lightest supersymmetric particle* (LSP) to decay. If this LSP is stable and interacts only weakly, it provides a suitable candidate for dark matter (for more detail see Section 3.3).

Since Q_α commutes with P^2 (2.8), all sparticles in the supermultiplets[2] must have the same mass. But if a seletron had the same mass as the electron, it would have had to be discovered in the experiments. Therefore, the masses cannot be the same, which means that SUSY must be broken, see Section 2.3.1.

2.3.1. SUSY Breaking

Due to the symmetry between the new superparticles and the Standard Model particles, the superpartners would have the same mass as their Standard Model partners. Therefore, one would have expected signatures of particles in several experiments. But this is not the case. This leads to the assumption that the supersymmetric particles must be heavier than their Standard Model partners, which means that SUSY has to be broken. Furthermore, taking a look at the parameter μ from Eq.(2.48), μ yields masses for the higgsinos and leads to a non-negative scalar potential

$$|\mu|^2 \Big(|H_u^0|^2 + |H_u^+|^2 + |H_d^0|^2 + |H_d^-|^2 \Big) \tag{2.52}$$

with a minimum at $H_u^0 = H_d^0 = 0$.

[2] The irreducible representation of the Poincaré super-algebra.

This non-negative scalar potential implies that the general MSSM Lagrangian is not able to generate the electroweak symmetry breaking. One way in which SUSY can be broken is the spontaneous SUSY breaking. This means that the vacuum state is not invariant under SUSY transformations

$$Q_\alpha|0\rangle \neq 0 \qquad \bar{Q}_{\dot{\alpha}}|0\rangle \neq 0, \tag{2.53}$$

with the SUSY generators Q_α and $\bar{Q}_{\dot{\alpha}}$. If supersymmetry is a global symmetry, the Hamilton operator H is expressed by the SUSY generators as

$$H = P^0 = \frac{1}{4}\Big(Q_1\bar{Q}_{\dot{1}} + \bar{Q}_{\dot{1}}Q_1 + Q_2\bar{Q}_{\dot{2}} + \bar{Q}_{\dot{2}}Q_2\Big)\,. \tag{2.54}$$

A spontaneously broken SUSY would lead to a positive vacuum expectation value (VEV)

$$\langle 0|H|0\rangle = \frac{1}{4}(||Q_1|0\rangle||^2 + ||\bar{Q}_{\dot{1}}|0\rangle||^2 + ||Q_2|0\rangle||^2 + ||\bar{Q}_{\dot{2}}|0\rangle||^2) > 0. \tag{2.55}$$

Furthermore, a positive expectation value is implied in $\langle 0|H|0\rangle = \langle 0|\mathcal{L}|0\rangle = \langle 0|V|0\rangle$. Taking Eq. (2.47), this can be obtained by

$$\langle 0|F|0\rangle \equiv \Lambda^2 \neq 0 \quad \text{or} \quad \langle 0|D|0\rangle \equiv \Lambda^2 \neq 0 \tag{2.56}$$

with the mass scale Λ^2 and F as well as D as the introduced auxiliary fields. By now, we have no clear hint how SUSY should be broken. Therefore we assume the most general form for SUSY breaking, which breaks SUSY explicitly. These so-called *soft SUSY breaking terms* have a positive mass dimension, maintaining the mass hierarchy and avoiding new divergences. The most general soft SUSY breaking Lagrangian is given by

$$\begin{aligned}
\mathcal{L}_{soft}^{MSSM} = &-\frac{1}{2}(M_1\tilde{B}\tilde{B} + M_2\tilde{W}\tilde{W} + M_3\tilde{g}\tilde{g} + h.c.) \\
&- (M_{\tilde{Q}}^2)_{ij}\tilde{Q}_i^+\tilde{Q}_j - (M_{\tilde{u}}^2)_{ij}\tilde{\bar{u}}_i^+\tilde{\bar{u}}_j - (M_{\tilde{d}}^2)_{ij}\tilde{\bar{d}}_i^+\tilde{\bar{d}}_j \\
&- (M_{\tilde{L}}^2)_{ij}\tilde{\bar{L}}_i^+\tilde{\bar{L}}_j - (M_{\tilde{e}}^2)_{ij}\tilde{\bar{e}}_i^+\tilde{\bar{e}}_j \\
&- m_{H_u}^2 H_u^+ H_u - m_{H_d}^2 H_d^+ H_d - (b_\mu H_d H_u + h.c.) \\
&+ (A_u)_{ij}H_u\tilde{Q}_i\tilde{\bar{u}}_j + (A_d)_{ij}H_d\tilde{Q}_i\tilde{\bar{d}}_j + (A_e)_{ij}H_d\tilde{L}_i\tilde{\bar{e}}_j + h.c.,
\end{aligned} \tag{2.57}$$

where M_1, M_2 and M_3 are the complex bino, wino and gluino mass parameters and $M_{\tilde{Q}}^2$, $M_{\tilde{L}}^2$, $M_{\tilde{e}}^2$, $M_{\tilde{u}}^2$ and $M_{\tilde{d}}^2$ are the 3×3 hermitian matrices of the soft SUSY breaking mass terms of the squarks and sleptons. Additionally, we introduce the real soft SUSY breaking Higgs mass terms $M_{H_u}^2$ and $M_{H_d}^2$, the trilinear couplings A_u, A_d and A_e as well as the complex parameter b_μ, depending on the off-diagonal Higgs squared mass term $m_{12}^2 \equiv b_\mu$. In the unbroken MSSM, only one additional parameter μ was introduced, whereas with soft SUSY breaking we now have 124 free parameters in the MSSM. 18 parameters are still Standard Model parameters, one new parameter is introduced in the Higgs sector, and 105 parameters result from the soft SUSY breaking.

2.3.2. A Specific MSSM Model - the Phenomenological MSSM

Not all 105 parameters can be completely free. The fact that the SM already predicts most of the experimental data with high accuracy, implies that those predictions should not be influenced by the extension of the SM. Therefore, parameters entering those predictions should be highly restricted. There are several constraints to be considered to reduce the amount of parameters [21].

1. No new sources of CP-violation
   Due to experimental constraints on the electric moment of the electron and neutron, new sources of CP-violation must be avoided, even if the fine tuning of the parameters can allow the contributions to cancel each other. It is simpler to assume that all phases in the soft SUSY-breaking potential vanish. This leads to the elimination of new CP-violating sources and has the advantage of reducing the number of free parameters.

2. No flavor changing neutral currents
   Today's experimental data constrain the existence of flavor changing neutral currents (FCNC), which can be induced by the off-diagonal terms in the sfermion mass and the trilinear coupling matrices. These restrictions lead to two possibilities for the sfermion mass matrices: either they are close to the unit matrix in flavor space, or they are almost proportional to the corresponding fermion mass. Assuming that the sfermion mass matrices and the trilinear coupling matrices are diagonal, the number of free parameters is reduced and large effects on the FCNC are avoided.

3. First and second generation universality
   It is a valid assumption that the soft-SUSY breaking scalar masses are equal for the first and second generation, while there are few experimental constraints on the third generation. The trilinear couplings are only important for the third generation, because they multiply the fermion masses. This leads to the assumption that A_u, A_d and A_l are equal for the first and second generation. In addition, they can be set to zero without phenomenological consequences.

Some parameters in the Higgs sector can also be associated with SM parameters. All in all, this leads to the 19 parameters for the pMSSM, see Table 2.4.

2.4. Particle Content of the MSSM

For the further discussion of the next-to-leading order calculation within the MSSM, especially the renormalization, the essential formulae of the sparticle masses and mixing

$\tan\beta$	ratio of the vev of the two Higgs doublet fields
M_A	mass of the pseudoscalar Higgs boson
μ	Higgs-higgsino mass parameter
M_1, M_2, M_3	bino, wino and gluino mass parameters
$m_{\tilde{q}_{1,2}}$, $m_{\tilde{u}_R}$	first and second generation sfermion masses
$m_{\tilde{q}_L}$, $m_{\tilde{t}_R}$, $m_{\tilde{b}_R}$,	third generation sfermion masses
A_t, A_b, A_τ	third generation trilinear couplings

Table 2.4.: The 19 parameters of the pMSSM.

matrices are summarized in the following, and the sparticle spectrum of the MSSM is discussed.

2.4.1. Higgs Sector

In the MSSM, an additional Higgs doublet must be added to the theory for consistency reasons. The new doublet is assigned the opposite hypercharge to the original Higgs doublet and is used to give masses to the up-type fermions. The Higgs potential in the MSSM is given by

$$V = m_1^2|H_1|^2 + m_2^2|H_2|^2 - m_{12}^2(H_1H_2 + H_1^\dagger H_2^\dagger) \tag{2.58}$$

$$+\frac{1}{8}(g^2+g'^2)(|H_1|^2-|H_2|^2)^2 + \frac{1}{2}g^2|H_1^\dagger H_2|^2\,, \tag{2.59}$$

with $m_{1,2}^2 = m_{H_{1,2}}^2 + |\mu|^2$. The gauge couplings g and g' determine the self-interaction of the Higgs fields in the MSSM.
The neutral Higgs boson fields have non-zero vacuum expectation values (VEVs)

$$\langle H_1\rangle = \begin{pmatrix} \frac{v_1}{\sqrt{2}} \\ 0 \end{pmatrix}, \qquad \langle H_2\rangle = \begin{pmatrix} 0 \\ \frac{v_2}{\sqrt{2}} \end{pmatrix}. \tag{2.60}$$

The doublets are parametrized as

$$H_1 \equiv \begin{pmatrix} H_1^0 \\ H_1^- \end{pmatrix} = \begin{pmatrix} (v_1+\phi_1^0+i\chi_1^0)/\sqrt{2} \\ \phi_1^- \end{pmatrix}, \tag{2.61}$$

$$H_2 \equiv \begin{pmatrix} H_1^0 \\ H_1^- \end{pmatrix} = \begin{pmatrix} \phi_2^+ \\ (v_2+\phi_2^0+i\chi_2^0)/\sqrt{2} \end{pmatrix}. \tag{2.62}$$

The free parameter $\tan\beta$ is defined as the ratio of the VEV's

$$\tan\beta \equiv \frac{v_2}{v_1} \geq 0\,, \qquad 0 \leq \beta \leq \frac{\pi}{2}\,. \tag{2.63}$$

The electro-weak symmetry breaking gives masses to the gauge bosons. The VEVs are fully determined by the relation of the masses of the gauge bosons and the gauge couplings as

$$m_Z^2 = \frac{g^2+g'^2}{4}(v_1^2+v_2^2)\,, \qquad m_W^2 = \frac{g^2}{4}(v_1^2+v_2^2)\,, \tag{2.64}$$

$$v^2 \equiv (v_1^2+v_2^2) = \frac{4m_Z^2}{g^2+g'^2} \approx (246\text{GeV})^2\,. \tag{2.65}$$

The Higgs mass matrix is defined as

$$M_{ij}^{2,Higgs} = \frac{1}{2}\left.\frac{\partial^2 V}{\partial H_i \partial H_j}\right|_{\langle H_n^0\rangle = v_n}\,. \tag{2.66}$$

The mixing is given by

$$\begin{pmatrix} H^0 \\ h^0 \end{pmatrix} = \begin{pmatrix} \cos\alpha & \sin\alpha \\ -\sin\alpha & \cos\alpha \end{pmatrix} \begin{pmatrix} \phi_1^0 \\ \phi_2^0 \end{pmatrix}\,, \tag{2.67}$$

$$\begin{pmatrix} G^0 \\ A^0 \end{pmatrix} = \begin{pmatrix} -\cos\beta & \sin\beta \\ \sin\beta & \cos\beta \end{pmatrix} \begin{pmatrix} \chi_1^0 \\ \chi_2^0 \end{pmatrix}\,, \tag{2.68}$$

$$\begin{pmatrix} G^\pm \\ H^\pm \end{pmatrix} = \begin{pmatrix} -\cos\beta & \sin\beta \\ \sin\beta & \cos\beta \end{pmatrix} \begin{pmatrix} \phi_1^\pm \\ \phi_2^\pm \end{pmatrix}\,. \tag{2.69}$$

After the vector bosons have absorbed the Goldstone bosons G^0 and $G^\pm$ as their longitudinal components, three neutral Higgs bosons – two CP even states (h^0, H^0), one CP odd state (A^0) and two charged Higgs bosons $(H^\pm)$ remain. This leads to three free parameters in the Higgs sector, which are conventionally chosen to be

$$m_{A^0}\,, \qquad \tan\beta\,, \quad \text{and} \quad \mu\,. \tag{2.70}$$

The masses of the Higgs bosons can be expressed using these free parameters at leading order as

$$m_{h^0,H^0}^2 = \frac{1}{2}\left[m_{A^0}^2 + m_Z^2 \mp \sqrt{(m_{A^0}^2+m_Z^2)^2 - 4m_{A^0}^2 m_Z^2\cos^2\beta}\right]\,, \tag{2.71}$$

$$m_{H^\pm}^2 = m_{A^0}^2 + m_W^2\,. \tag{2.72}$$

2.4.2. Sfermion Sector

The sfermions are scalar superpartners of the fermions. Every chiral part of a fermion gets a scalar superpartner, i.e. for each fermion there are two scalar fermions $\tilde{f}_{L,R}$. However, these scalar fermions are not the mass eigenstates. The sfermion mass matrix is off-diagonal in the basis $(\tilde{f}_L, \tilde{f}_R)$ and has the form

$$\mathcal{M}^2_{\tilde{f}} = \begin{pmatrix} m^2_{\tilde{f}_L} & a_f\, m_f \\ a_f\, m_f & m^2_{\tilde{f}_R} \end{pmatrix}, \tag{2.73}$$

with

$$m^2_{\tilde{f}_L} = M^2_{\{\tilde{Q},\,\tilde{L}\}} + (I^{3L}_f - e_f\, s^2_W)\cos 2\beta\, m^2_Z + m^2_f\,, \tag{2.74}$$

$$m^2_{\tilde{f}_R} = M^2_{\{\tilde{U},\,\tilde{D},\,\tilde{E}\}} + e_f\, s^2_W \cos 2\beta\, m^2_Z + m^2_f\,, \tag{2.75}$$

$$a_f = A_f - \mu\,(\tan\beta)^{-2I^{3L}_f}\,. \tag{2.76}$$

$M_{\tilde{q}}$, $M_{\tilde{L}}$, $M_{\tilde{u}}$, $M_{\tilde{d}}$ and $M_{\tilde{e}}$ are the soft SUSY-breaking masses, A_f is the trilinear scalar coupling parameter, μ the higgsino mass parameter, $\tan\beta = \frac{v_2}{v_1}$ is the ratio of the vacuum expectation values of the two neutral Higgs doublet states , I^{3L}_f denotes the third component of the weak isospin of the fermion f, e_f is the electric charge in terms of the elementary charge e, and s_W is the sine of the weak mixing angle θ_W.

The mass eigenstates are determined by diagonalization of the mass matrix with the introduced mixing angle $\theta_{\tilde{f}}$ in the mixing matrix $R^{\tilde{f}}$,

$$\mathcal{M}^2_{\tilde{f}} = \begin{pmatrix} m^2_{\tilde{f}_L} & a_f\, m_f \\ a_f\, m_f & m^2_{\tilde{f}_R} \end{pmatrix} = \left(R^{\tilde{f}}\right)^\dagger \begin{pmatrix} m^2_{\tilde{f}_1} & 0 \\ 0 & m^2_{\tilde{f}_2} \end{pmatrix} R^{\tilde{f}}\,, \tag{2.77}$$

where

$$R^{\tilde{f}} = \begin{pmatrix} \cos\theta_{\tilde{f}} & \sin\theta_{\tilde{f}} \\ -\sin\theta_{\tilde{f}} & \cos\theta_{\tilde{f}} \end{pmatrix}. \tag{2.78}$$

The masses of the sfermions and the mixing angle are

$$m^2_{\tilde{f}_{1,2}} = \frac{1}{2}\left(m^2_{\tilde{f}_L} + m^2_{\tilde{f}_R} \mp \sqrt{(m^2_{\tilde{f}_L} - m^2_{\tilde{f}_R})^2 + 4a^2_f m^2_f}\right), \tag{2.79}$$

$$\cos\theta_{\tilde{f}} = \frac{-a_f\, m_f}{\sqrt{(m^2_{\tilde{f}_L} - m^2_{\tilde{f}_1})^2 + a^2_f m^2_f}} \qquad (0 \le \theta_{\tilde{f}} < \pi)\,. \tag{2.80}$$

2.4.3. Chargino Sector

The charged gauginos and higgsinos mix to two mass eigenstates, the so-called charginos $\chi^{\pm}_{i=1,2}$. The Weyl-spinor chargino fields are

$$\psi^+ = (-i\tilde{W}^+, \tilde{H}_2^+)\,, \qquad \psi^- = (-i\tilde{W}^-, \tilde{H}_1^-)\,. \tag{2.81}$$

The chargino mass term in the Lagrangian in this basis is

$$\mathcal{L} = -\frac{1}{2}\left(\psi^+, \psi^-\right)\begin{pmatrix} 0 & X^T \\ X & 0 \end{pmatrix}\begin{pmatrix} \psi^+ \\ \psi^- \end{pmatrix} + h.c.\,, \tag{2.82}$$

with the chargino mass matrix

$$X = \begin{pmatrix} M & \sqrt{2}m_W \sin\beta \\ \sqrt{2}m_W \cos\beta & \mu \end{pmatrix}. \tag{2.83}$$

This mass matrix is diagonalized by using two unitary matrices U and V

$$UXV^{-1} = \mathrm{diag}(m_{\chi_1^\pm}, m_{\chi_2^\pm}), \qquad |m_{\chi_1^\pm}| \leq |m_{\chi_2^\pm}|\,. \tag{2.84}$$

The Dirac spinors of the mass eigenstates are constructed by

$$\tilde{\chi}_i^\pm \equiv \begin{pmatrix} V_{ij}\,\psi_j^+ \\ U_{ij}\,\bar{\psi}_j^- \end{pmatrix}. \tag{2.85}$$

The chargino masses are given by

$$m^2_{\chi^\pm_{1,2}} = \frac{1}{2}\left[M^2 + \mu^2 + 2m_W^2 \mp \sqrt{(M^2+\mu^2+2m_W^2)^2 - 4(m_W^2 \sin 2\beta - \mu M)^2}\right]. \tag{2.86}$$

2.4.4. Neutralino Sector

The neutralinos $\chi^0_{i=1,4}$ result from the mixing of the neutral gauginos and higgsinos. The mass Lagrangian of the four Weyl states

$$\varphi_j^0 = (-\mathrm{i}\tilde{B}, -\mathrm{i}\tilde{W}_3^0, \tilde{H}_1^0, \tilde{H}_2^0) \tag{2.87}$$

is given by

$$\mathcal{L} = -\frac{1}{2}(\varphi^0)^T Y \varphi^0 + h.c., \tag{2.88}$$

where Y is the neutralino mass matrix

$$Y = \begin{pmatrix} M' & 0 & -m_Z s_W \cos\beta & m_Z s_W \sin\beta \\ 0 & M & m_Z c_W \cos\beta & -m_Z c_W \sin\beta \\ -m_Z s_W \cos\beta & m_Z c_W \cos\beta & 0 & -\mu \\ m_Z s_W \sin\beta & -m_Z c_W \sin\beta & -\mu & 0 \end{pmatrix}. \tag{2.89}$$

s_W and c_W are abbreviations for $\sin\theta_W$ and $\cos\theta_W$. The neutralinos are Majorana particles. Therefore, the matrix can be diagonalized using only one unitary rotation matrix Z as

$$ZYZ^{-1} = \mathrm{diag}(m_{\tilde{\chi}_1^0}, m_{\tilde{\chi}_2^0}, m_{\tilde{\chi}_3^0}, m_{\tilde{\chi}_4^0}), \quad \left|m_{\tilde{\chi}_1^0}\right| \leq \left|m_{\tilde{\chi}_2^0}\right| \leq \left|m_{\tilde{\chi}_3^0}\right| \leq \left|m_{\tilde{\chi}_4^0}\right|. \tag{2.90}$$

Finally, the 4-component Majorana spinors for the neutralino fields can be constructed as

$$\tilde{\chi}_i^0 = \begin{pmatrix} Z_{ij}\varphi_j^0 \\ Z_{ij}\bar{\varphi}_j^0 \end{pmatrix}. \tag{2.91}$$

2.5. SUSY Searches

The Large Hadron Collider (LHC) at CERN houses two of the leading experiments for SUSY searches, ATLAS and CMS. In the following, we review SUSY searches in the phenomenological MSSM recently performed by these experiments.

2.5.1. ATLAS

The ATLAS detector detects head-on collisions of high-energy protons. The recorded data are analyzed for evidence of beyond the SM physics. In addition, theoretical models such as the pMSSM can be constrained by the lack of observations of new physics typically by placing lower limits on their mass parameters.

ATLAS conducted a large study [1] in the 19 parameter pMSSM with the LHC Run 1 data, including 22 separate ATLAS searches in this analysis. These searches are based on data recorded by an integrated luminosity of up to 20.3 fb^{-1} of proton-proton collisions at the center of mass energies of $\sqrt{S} = 7$ and 8 TeV.

Experimental Constraints on the pMSSM

In order to determine the constraints on pMSSM, the analysis has taken into account electroweak precision measurements and some measurements of flavor observables. In addition, measurements of dark matter observables were also considered. LHC searches which provide crucial constraints on the pMSSM parameter space can be summarized as

- Decay products of sparticles
- Missing Energies E_T^{miss}
- Disappearing tracks
- Long-lived charged particles

Inclusive	Third generation
0-lepton + 2-6 jets + E_T^{miss}	0-lepton stop
0-lepton + 7-10 jets+ E_T^{miss}	1-lepton stop
1-lepton + jets + E_T^{miss}	2-leptons stop
$\tau(\tau/l)$ + jets + E_T^{miss}	Monojet stop
same-sign/3-leptons + jets + E_T^{miss}	Stop with Z boson
0/1-lepton + 3b -jets + E_T^{miss}	2b-jets + E_T^{miss}
Monojet	tb + E_T^{miss}, stop
Electroweak	**Others**
lh	Long-lived sparticle
2-leptons	$H/A \to \tau^+\tau^-$
2-τ	
3-leptons	
4- leptons	
Disappearing Track	

Table 2.5.: Different ATLAS searches for supersymmetry [1]

- Monojet signatures
- Dedicated searches for heavier neutral Higgs bosons.

Within this study, only pMSSM parameters were considered where the neutralino is the LSP. The various search strategies are listed in Tab. 2.5.

The searches considered in the analysis are divided into four different categories, with sensitivity to other categories overlapping. The categories are briefly explained below. A detailed description of the searches can be found in [1] or in several separate publications on the respective analyses.

Inclusive Searches

These data are primarily based on decays initiated by the production of first and second generation squarks or gluinos with direct decays to the LSP $\tilde{q} \to q + \tilde{\chi}_1^0$, $\tilde{g} \to q + \bar{q} + \tilde{\chi}_1^0$ or cascade decays that have additional jets, large missing energy E_T^{miss} or possible leptons (including τ). For example, in the case of 0-lepton+2-6 jets $+E_T^{miss}$ [22], the proton-proton collisions produce a pair of squarks or gluinos ($\tilde{q}\tilde{q}^*, \tilde{g}\tilde{g}, \tilde{q}\tilde{q}^*$). These can decay into

weakly interacting neutralinos $\tilde{\chi}_1^0$ by $\tilde{q} \to q\tilde{\chi}_1^0$ and $\tilde{g} \to q\bar{q}\tilde{\chi}_1^0$. There may also be a decay of squarks into charged charginos $\tilde{q} \to q\tilde{\chi}^{\pm}$. The chargino can decay into neutralinos in further steps $\tilde{\chi}^{\pm} \to W^{\pm}\tilde{\chi}_1^0$.

Third-Generation Searches

These searches take into account the direct production of squarks of the third generation with masses expected in the TeV range or below. This is due to the reduction of unnatural corrections to the Higgs mass. The decay of $\tilde{t}$ and $\tilde{b}$ leads to unmistakable experimental signatures, optionally including the production of top or bottom quarks with additional large E_T^{miss}.

Electroweak Searches

Sparticles generated by electroweak interactions are considered here, leading to the production of sleptons and electroweakinos. These in turn typically decay into states containing high p_t leptons and a significant E_T^{miss}.

Other Searches

Other searches include searches for long-lived particles such as stop or sbottom, gluinos, staus or charginos.

2.5.2. Parameter Constraints on the pMSSM

The assumptions about the parameter space are motivated by experimental observations and the desire for theoretical simplicity. The model must have the same constraints as mentioned in Sec. 2.3.2 to feature the pMSSM model. The 19 parameters of the model are shown in the Tab. 2.6 with the corresponding limits.

4 TeV is set as the upper limit so that all parameters are accessible at the LHC. Limitations due to particle decays and experiments with dark matter are listed in Tab. 2.7.

2.5.3. Impact of ATLAS Searches on Sparticle Masses

With increasing sparticle mass, the corresponding cross section decreases. In addition, the masses of other particles influence the visible decay products and their kinematics. If a heavy LSP is produced at the end of the decay chain, less energy is available for the observable decay products.

Stops are particularly are interesting for SUSY searches, since they provide the leading contribution to the solution of the hierarchy problem of the Higgs boson mass. In Fig.

Parameter	Min value	Max value	Note
$m_{\tilde{L}_1}(= m_{\tilde{L}_2})$	90 GeV	4 TeV	Left-handed slepton (first two gens.) mass
$m_{\tilde{e}_1}(= m_{\tilde{e}_2})$	90 GeV	4 TeV	Right-handed slepton (first two gens.) mass
$m_{\tilde{L}_3}$	90 GeV	4 TeV	Left-handed stau doublet mass
$m_{\tilde{e}_3}$	90 GeV	4 TeV	Left-handed stau mass
$m_{\tilde{Q}_1}(= m_{\tilde{Q}_2})$	200 GeV	4 TeV	Left-handed squark (first two gens.) mass
$m_{\tilde{u}_1}(= m_{\tilde{u}_2})$	200 GeV	4 TeV	Right-handed up-type squark (first two gens.) mass
$m_{\tilde{d}_1}(= m_{\tilde{d}_2})$	200 GeV	4 TeV	Right-handed down-type squark (first two gens.) mass
$m_{\tilde{Q}_3}$	100 GeV	4 TeV	Left-handed squark (third gen.) mass
$m_{\tilde{u}_3}$	100 GeV	4 TeV	Right-handed stop mass
$m_{\tilde{d}_3}$	100 GeV	4 TeV	Right-handed sbottom mass
$\lvert M_1 \rvert$	0 GeV	4 TeV	Bino mass parameter
$\lvert M_2 \rvert$	70 GeV	4 TeV	Wino mass parameter
$\lvert \mu \rvert$	80 GeV	4 TeV	Bilinear Higgs mass parameter
M_3	200 GeV	4 TeV	Gluino mass parameter
$\lvert A_t \rvert$	0 GeV	8 TeV	Trilinear top coupling
$\lvert A_b \rvert$	0 GeV	4 TeV	Trilinear bottom coupling
$\lvert A_\tau \rvert$	0 GeV	4 TeV	Trilinear τ lepton coupling
M_A	100 GeV	4 TeV	Pseudo scalar Higgs boson mass
$\tan\beta$	1	60	Ratio of the Higgs VeV

Table 2.6.: Ranges for the 19 pMSSM parameters[1]. ("gen(s)" is short for generation(s))

Parameter	Minimum value	Maximum value
$\Delta\rho$	-0.0005	0.0017
$\Delta(g-2)_\mu$	-17.7×10^{-10}	43.8×10^{-10}
$\mathrm{BR}(b \to s\gamma)$	2.69×10^{-4}	3.87×10^{-4}
$\mathrm{BR}(B_s \to \mu^+\mu^-)$	1.6×10^{-9}	4.2×10^{-9}
$\mathrm{BR}(B^+ \to \tau^+\nu_\tau)$	66×10^{-6}	161×10^{-6}
$\Omega_{\chi_1^0} h^2$	—	0.1208
$\Gamma_{\mathrm{invisible(SUSY)}}(Z)$	—	2 MeV
Masses of charged sparticles	100 GeV	—
$m(\tilde{\chi}_1^\pm)$	103 GeV	—
$m(\tilde{u}_{1,2}, \tilde{d}_{1,2}, \tilde{c}_{1,2}, \tilde{s}_{1,2})$	200 GeV	—
$m(h)$	124 GeV	128 GeV

Table 2.7.: Acceptance of pMSSM due to electroweak and flavor results, relic density and other collider measurements. The dash means that no requirements are made [1].

2.2 the left image shows the fraction of excluded models in the pMSSM by ATLAS in the $\tilde{t}_1 - \tilde{\chi}_1^0$ mass plane. For small masses of the lightest top squark there are not many models: Either a large mass or mixing in the stop sector is required to obtain the large quantum corrections required to explain the low SM Higgs boson mass. In addition, most models below a mass of 600 GeV are already excluded by the ATLAS analysis.

The white lines indicate analyses with different decay channels. The decay channel $\tilde{t}_1 \to t\tilde{\chi}_1^0$ (solid white line) is constrained through $m_{\tilde{t}_1} > m_t + m_{\tilde{\chi}_1^0}$. Due to the heavy top quark in the final state within this decay channel the region close to the boarder, of equal stop and neutralino mass, cannot be analyzed. To close this gap in the analysis, two other decay channels are considered, $\tilde{t}_1 \to Wb\tilde{\chi}_1^0$ (dotted white line) and $\tilde{t}_1 \to bff'\tilde{\chi}_1^0$ (dashed white line), featuring only weak constraints on the masses.

The right figure is similar to the left figure, but shows the $\tilde{b}_1 - \tilde{\chi}_1^0$ mass plane. The sensitivity is already well captured by a simplified model that contains only one additional sbottom and the lightest neutralino. The decay $\tilde{b}_1 \to b\tilde{\chi}_1^0$ captures also the range for small mass differences between sbottom and neutralino, due to the small bottom mass. Considering the entire phenomenology of the pMSSM, there is a larger parameter space to explore where SUSY can be realized in nature.

Fig. 2.3 shows the fraction of model points excluded by ATLAS analysis depending on the gluino and neutralino mass. The shaded area shows the fraction of excluded models. In the black area more or less all scenario points are excluded. This corresponds to the light gluino range. For higher gluino masses fewer and fewer scenario points are

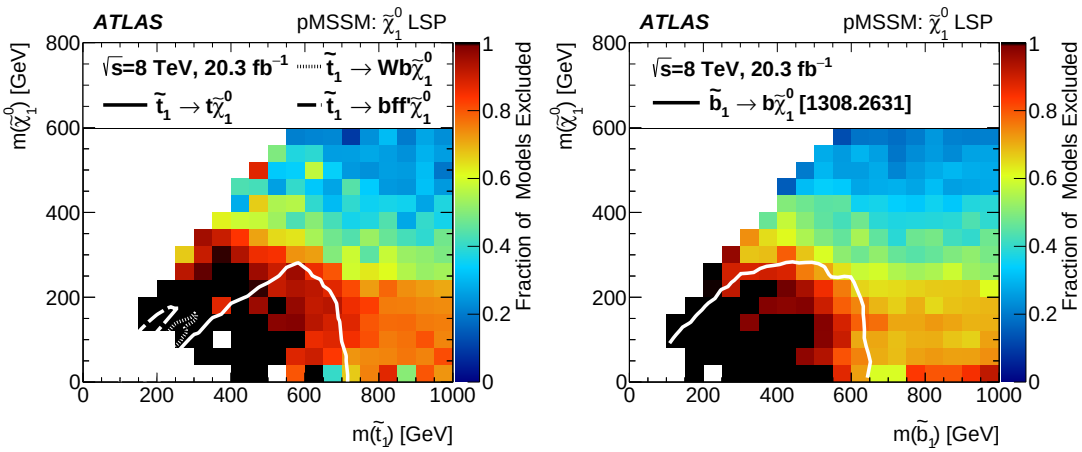

Figure 2.2.: Exclusion from ATLAS analysis of 22 searches. Left: Stop-lightest neutralino mass plane. Right: Sbottom-lightest neutralino maa plane [1].

excluded. The white line in the illustration shows a previous analysis performed on the 0 leptons + 2-6 jets $+E_T^{miss}$ searches [22]. In this analysis, the model was only accessible for gluino decays to 2 jets and the LSP. This model successfully captures the most important pMSSM phenomenology. The new analysis not only includes several further experimental constraints, but also takes into account the influence of other sparticle masses. For the nearly degenerate region ($m(\tilde{g}) \sim m(\tilde{\chi}^0)$), the sensitivity of ATLAS is underestimated by the process of $\tilde{g} \to q\bar{q}\tilde{\chi}_1^0$, where low-energy quarks are produced that do not meet the kinematic requirements of jets. But based on the monojet analysis, the sensitivity in this area is adequate.

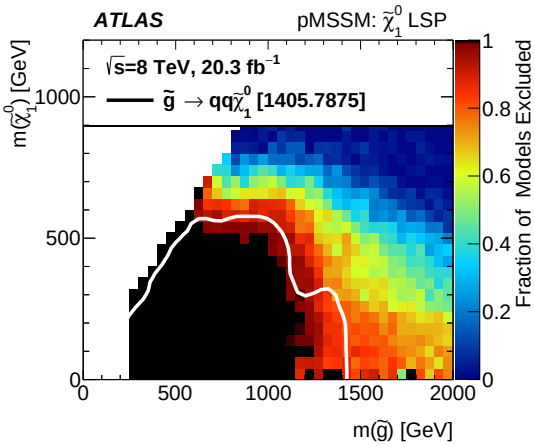

Figure 2.3.: Exclusion from ATLAS analysis of 22 searches in the gluino-lightest neutralino mass plane [1].

Overall, the model points with the lowest fine tuning remain possible even after the

LHC run 1. However, due to the fact that the lowest fine tuning models have relatively light stop masses, this indicates the possibility that these models are accessible for the ATLAS search within the LHC run 2.

2.5.4. CMS

A similar study was conducted by CMS [2]. CMS took their data with similar center-of-mass energies $\sqrt{S} = 7$ and 8 TeV. CMS used integrated luminosities of 5.0 fb^{-1} and 19.5 fb^{-1}.

The analysis is based on the weak-scale R-parity conserving MSSM, where the gravitino is considered to be heavy. With restricted CP violation, all parameters are considered real. Further FCNC restrictions require that all sfermion mass matrices and trilinear couplings are flavor-diagonal. Moreover, first and second generation squarks are not experimentally relevant due to the very small Yukawa couplings. The upper and lower bounds of the 19 pMSSM parameters are given in Table 2.8. The lower limit of 2 for $\tan\beta$ avoids non-pertubative effects in the upper Yukawa coupling.

In the analysis, not only the parameter space limits were considered, but also several theoretical conditions, the lifetime of the charginos and constraints by non-direct CMS SUSY searches (non-DCS) data, as well as high-precision measurements and pre-LHC searches for beyond the SM physics, see Tab. 2.9.

A range for the SM Higgs boson masses from 120 GeV to 130 GeV takes the theoretical uncertainties into account when calculating the mass within the MSSM. The uncertainties about the anomalous magnetic moment also consider the theoretical uncertainties in the SUSY calculations. Dark matter searches are not considered in the analysis of the points.

While in the analysis by the ATLAS, Figures 2.2 and 2.3, the fraction of excluded model points was represented, CMS shows the surviving points in their analysis, see Figure 2.4. At a low gluino mass less points survive, at a gluino mass of 500 GeV all points are excluded. In addition, the lightest colored particle must be above 300 GeV. CMS has a sensitivity of up to $m_{\tilde{t}} \approx 700$ GeV, but the total effect on the stop mass is low. The highest sensitivity is below 500 GeV, which is already suppressed by results of earlier experiments ($b \to s\gamma$). In total, neutralino and chargino masses below 300 GeV are strongly suppressed, but are not excluded by the CMS data.

Parameter	Min value	Max value	Note
$\lvert M_1 \rvert$	0 TeV	3 TeV	Bino mass parameter
$\lvert M_2 \rvert$	0 TeV	3 TeV	Wino mass parameter
$\lvert \mu \rvert$	0 TeV	3 TeV	Bilinear Higgs mass parameter
M_3	0 TeV	3 TeV	Gluino mass parameter
M_A	0 TeV	3 TeV	Pseudo scalar Higgs boson mass
$\tan\beta$	2	60	Ratio of the Higgs VeV
$m_{\tilde{L}_{1,2}}$	0 TeV	3 TeV	Left-handed slepton (first two gens.) mass
$m_{\tilde{e}_{1,2}}$	0 TeV	3 TeV	Right-handed slepton (first two gens.) mass
$m_{\tilde{L}_3}$	0 TeV	3 TeV	Left-handed stau doublet mass
$m_{\tilde{e}_3}$	0 TeV	3 TeV	Left-handed stau mass
$m_{\tilde{Q}_{1,2}}$	0 TeV	3 TeV	Left-handed squark (first two gens.) mass
$m_{\tilde{u}_{1,2}}$	0 TeV	3 TeV	Right-handed up-type squark (first two gens.) mass
$m_{\tilde{d}_{1,2}}$	0 TeV	3 TeV	Right-handed down-type squark (first two gens.) mass
$m_{\tilde{Q}_3}$	0 TeV	3 TeV	Left-handed squark (third gen.) mass
$m_{\tilde{u}_3}$	0 TeV	3 TeV	Right-handed stop mass
$m_{\tilde{d}_3}$	0 TeV	3 TeV	Right-handed sbottom mass
$\lvert A_t \rvert$	0 GeV	7 TeV	Trilinear top coupling
$\lvert A_b \rvert$	0 GeV	7 TeV	Trilinear bottom coupling
$\lvert A_\tau \rvert$	0 GeV	7 TeV	Trilinear τ lepton coupling

Table 2.8.: Constraints for the 19 pMSSM parameters in the CMS analysis [2] ("gen(s)" is short form for generation(s)).

Observables	Constraints
$BR(b \to s\gamma)$	$(3.43 \pm 0.21^{\text{stat}} \pm 0.24^{th} \pm 0.07^{\text{sys}}) \times 10^{-4}$
$BR(B_s \to \mu^+\mu^-)$	$(2.9 \pm 0.7 \pm 0.29^{th}) \times 10^{-9}$
$BR(B^+ \to \tau^+\nu_\tau)$	1.04 ± 0.34
Δa_μ	$(26.1 \pm 6.3^{\text{exp}} \pm 4.9^{SM} \pm 10.0^{SUSY}) \times 10^{-10}$
$\alpha_s(m_Z)$	0.1184 ± 0.0007
m_t	$173.20 \pm 0.87^{\text{stat}} \pm 1.3^{\text{sys}}$ GeV
$m_b(m_b)$	$4.19\ ^{+0.18}_{-0.06}$ GeV
m_h	LHC: $m_h^{\text{low}} = 120$ GeV, $m_h^{\text{high}} = 130$ GeV
μ_h	CMS and ATLAS in LHC Run 1, Tevatron
sparticle masses	LEP (by MicrOMEGAs)

Table 2.9.: Non-DCS measurements to set a prior on random points in SUSY space [2].

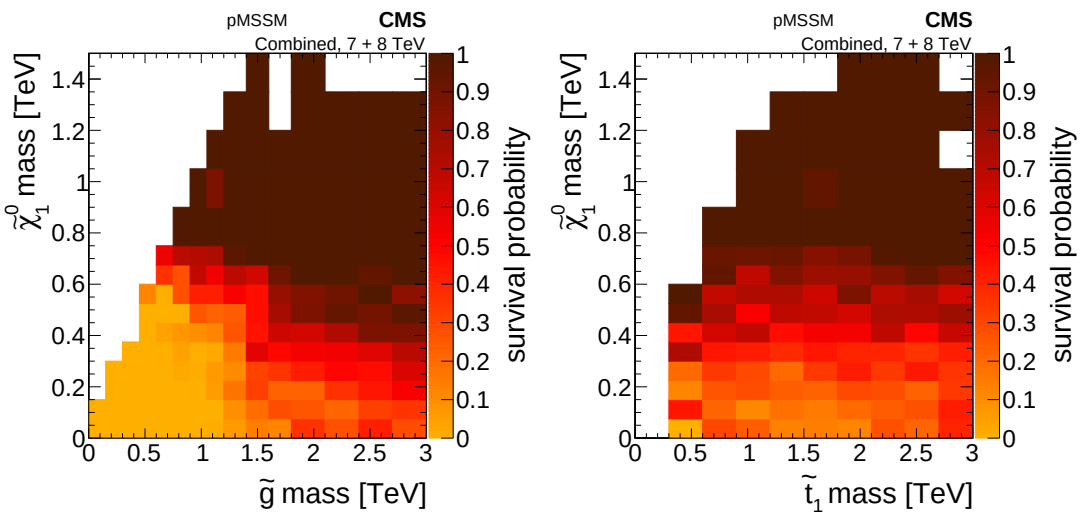

Figure 2.4.: Survival probabilities after inclusion of the considered CMS searches left: gluino lightest neutralino plane, right: stop lightest neutralino plane [2].

Analysis	$\sqrt{S}$ [TeV]	$\mathcal{L}$ [fb^{-1}]
Hadronic $H_T + H_T^{miss}$ search	7	4.98
Hadronic $H_T + E_T^{miss}$+ b-jets search	7	4.98
Leptonic search for EW prod. of $\tilde{\chi}^0, \tilde{\chi}^{\pm}, \tilde{l}$	7	4.98
Hadronic $H_T + H_T^{miss}$ search	8	19.5
Hadronic M_{T2} search	8	19.5
Hadronic $H_T + E_T^{miss}$+ b-jets search	8	19.4
Monojet searches	8	19.7
Hadronic third generation squark search	8	19.4
OS dilepton (OS II) search (counting experiment only)	8	19.4
LS dileptonic (LS II) search (only channels w/o third lepton veto)	8	19.5
Leptonic search for EW prod$\tilde{\chi}^0, \tilde{\chi}^{\pm}, \tilde{l}$ (only LS, 3 lepton and 4 lepton channels)	8	19.5
Combination of 7 TeV searches	7	—
Combination of 7 TeV and 8 TeV searches	7,8	—

Table 2.10.: Considered data for the CMS study on non-excluded pMSSM scenarios [2]. (H_T: scalar sum of transverse momenta of jets, E_T^{miss}, H_T^{miss}: magnitude of the vector sum of the transverse momenta of final state particles, M_{T2}: transverse mass in events with two semi-invisibly decaying particles, OS: lepton multiplicities including opposite-sign, LS: lepton multiplicities including like-sign)

3 Dark Matter

Only around 5 % of the energy content of the Universe consists of known baryonic matter [23]. The rest is unknown but it can be divided into two distinct parts. 25 % of the energy content is made of dark matter. There is plenty of evidence for the existence of dark matter, but its nature is still an open question today. The remaining 70% of the energy content of the Universe is called Dark Energy, about which even less is known. The following is a brief summary of the evidence pointing to the existence of dark matter. We discuss the properties of dark matter and possible candidates and review the current state of various experiments looking for dark matter. Finally, we take a detailed look at one of the most precisely determined dark matter observables, the relic density. There are several reviews [24], [25], [26], lectures [27] and doctoral theses [5], [28], [29], [30] with further information on dark matter.

3.1. Evidence for Dark Matter

At the beginning of the twentieth century, astrophysicists assumed for the first time that there is invisible matter in the Universe. In 1922 Kapteyn [31] and Jeans [32] called this invisible matter dark matter. In 1932 Jan Oort [33] studied the movements of nearby stars, from which he deduced, there must be more mass than just the mass of the visible stars to explain the movement of the stars. Only one year later Fritz Zwicky published his studies about the Coma cluster [34]. Since then many further pieces of evidence have been published, which additionally can be used to point out to the properties of dark matter. In the following, we show different kinds of observations of dark matter. This following list is not complete and should serve only as a short overview.

3.1.1. Coma Cluster

As already mentioned above, one of the first hints of dark matter came from Fritz Zwicky's study of the Coma cluster [34]. He calculated the velocity distribution of individual galaxies within the Coma cluster by observing the doppler shifts in the galactic spectra. A theoretical prediction about the velocity distribution could be given by

assuming mechanical equilibrium. For this the relation between the average kinetic energy $\overline{E}_{kin}$ and the average potential energy $\overline{E}_{pot}$ is given by the virial theorem

$$\overline{E}_{kin} = -\frac{1}{2}\overline{E}_{pot}. \tag{3.1}$$

Assuming that matter is evenly distributed over the Coma cluster, its mass can be estimated as approximately $M \sim 1.6 \times 10^{42}$ kg. With a cluster radius of about $R \sim 10^{22}$ m the total potential energy could be determined as

$$E_{pot} = -\frac{3}{5}G\frac{M^2}{R}, \tag{3.2}$$

with G being the gravitational constant. This leads to an average velocity of $\sqrt{\overline{v}^2} \sim 80\ \frac{\text{km}}{\text{s}}$.

If this result is compared to the redshift measurements, high discrepancies arise. Zwicky came to the conclusion that the Coma cluster must contain additional non-luminous matter in order to explain the observed mismatch. In addition, he concluded that dark matter must have a higher density than luminous matter.

3.1.2. Rotation Curves

The circular velocity distribution of stars as a function of their distance from the galactic center was investigated in several spiral galaxies. For illustration, the velocity distribution of the galaxy NGC 3198 is shown in Figure 3.1.

From Newtonian dynamics one would expect that the velocity v behaves as

$$v(r) = \sqrt{\frac{GM(r)}{r}}, \tag{3.3}$$

with the total mass of the galaxy up to the radius r is given as $M(r) = 4\pi \int_0^r dr' r'^2 \varrho(r')$, where $\varrho(r')$ is the mass density.

Based on the nearly constant mass $M(r)$ for large distances r, the velocity should decrease as $\sim \frac{1}{\sqrt{r}}$, as seen in Figure 3.1 (curve *disk*). However, the measured velocity (data points) shows a plateau. Assuming the presence of a halo of a invisible mass with the density distribution $\rho \sim \frac{1}{r^2}$, results in a rise of the velocity described by the curve *halo*. Adding the contribution of the halo to the disk (third line), the resulting curve describes well the measured velocities.

3.1.3. Bullet Cluster

If separation of baryonic matter and dark matter in a galaxy or galaxy cluster would be observed, this would be an indication of the existence of dark matter and speak

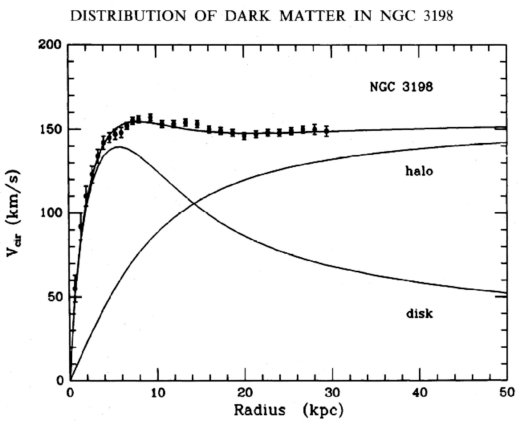

Figure 3.1.: The velocity distribution of the galaxy NGC 3198 is shown. The observed velocity distribution is represented by the data points. The expected velocity distribution of the baryonic matter corresponds to the curve marked as *disk*. A halo of an invisible matter with a density distribution $\rho \sim \frac{1}{r^2}$ gives the curve called *halo*. The sum of disk and halo gives the third curve that matches the data points of the observed velocity distribution. The image was taken from [35].

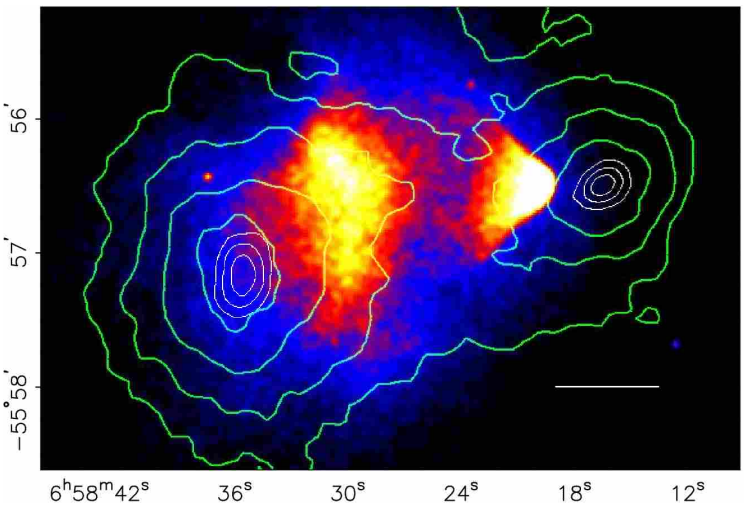

Figure 3.2.: The Bullet Cluster 1E0657-558 shown with different color codes for specific mass sources. The red area visualizes the X-ray emission observed by the Chandra telescope. The blue colored region shows the visible mass from the galaxies. The gravitational potential is reconstructed assuming gravitational lensing and visualized by the green lines. The image is taken from [36].

against a modification of the laws of gravity, which could be an alternative explanation for the rotation curve observations. With the observation of the Bullet Cluster by the Chandra telescope such an evidence for dark matter was found [36]. Fig. 3.2 shows the cluster 1E0657-558. While the galaxies are directly visible, the interstellar dust is detected by its X-ray radiation. In Fig. 3.2 the location of the interstellar dust is shown with red to white colored areas. The blue region highlights the position of the galaxies. While the galaxies pass without collision, the intergalactic hot plasma is slowed down by interaction between the respective clusters. In addition, the X-ray image shows the shape of an impact cone. The total amount of matter in the cluster can be investigated by gravitational lenses[1]. The gravitational potential determined by this method is shown in Fig. 3.2 with the green contour lines. If there is no other source for the gravitational potential, the dominant mass fraction of the clusters should lie in the plasma. This is not the case in cluster 1E0657-558. With a significance of 8σ the peak of the gravitational potential has an offset to the center of the baryonic mass. This offset can be explained by the presence of dark matter, which changes the gravitational potential. In addition, the maximum of the gravitational potential is aligned with the former cluster center and not slowed down, dark matter seems to react only weakly and is therefore not affected by the collision.

3.1.4. Cosmic Microwave Background

There is not only evidence for dark matter, but also astrophysical observations from which the total amount of dark matter in the Universe can be determined. Measurements of the *Cosmic Microwave Background* (CMB) allow the determination of the relic density with high accuracy. The CMB results from the time when the Universe became transparent. Shortly after the electrons and atoms recombined, the photons decoupled and spread without scattering forming the CMB. The CMB has an almost perfect blackbody spectrum at $T = 2.7255$ K [37] and is globally isotropic within $\mathcal{O}(10^{-5})$ K. In 1990 the isotropic blackbody spectrum was confirmed by the Cobe satellite [38, 39]. Later, the *Wilkinson Microwave Anisotropy Probe* (WMAP) [40] improved the accuracy of the measured density fluctuations in the early Universe. The most precise measurement to date was performed by the Planck Collaboration [23].

The temperature of the photons is influenced by fluctuations in the energy density of the photons at the time of the last scattering, Doppler shift, Sachse-Wolfe effect and the integrated Sachse-Wolfe effect[2] [42].

[1] Gravitational lensing is an effect where in the presence of heavy masses, the light is deflected by gravitational fields. This can be observed by blurred or distorted objects behind heavy masses. Statistical methods can be used to determine the mass of gravitational lenses [35].

[2] If the photon reaches the potential well, the wavelength is shifted. When leaving the well, the wavelength of the photon is shifted again, but the shifts do not compensate each other because the gravitational potential flattens out caused by the expansion of the Universe.

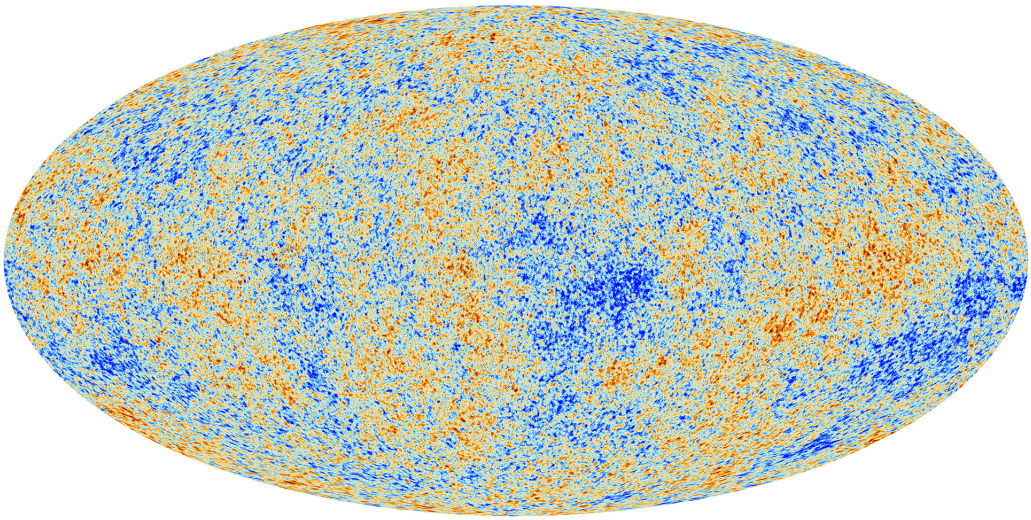

Figure 3.3.: Skymap of temperature fluctuations in the CMB, provided by the Planck Collaboration [41].

The observed temperature fluctuations can be described by a two-dimensional power spectrum [43].

$$\frac{\delta T}{T}(\theta,\phi) = \sum_{l=2}^{\infty} \sum_{m=-l}^{l} a_{lm} Y_{lm}(\theta,\phi), \tag{3.4}$$

with the multipole moment a_{lm} and the spherical harmonics $Y_{lm}(\theta,\phi)$. The polar angles θ and ϕ parameterize the sky.

The variance of the temperature fluctuations

$$\left\langle \left(\frac{\delta T}{T}\right)^2 \right\rangle = \frac{\int_0^{2\pi}\int_0^{\pi} \left(\frac{\delta T}{T}\right)^2 d\theta \sin\phi d\phi}{\int_0^{2\pi}\int_0^{\pi} d\theta \sin\phi d\phi} \tag{3.5}$$

can be integrated and

$$\left\langle \left(\frac{\delta T}{T}\right)^2 \right\rangle = \frac{1}{4\pi} \sum_{lm} \sum_{l'm'} \int_0^{2\pi}\int_0^{\pi} a_{lm} a_{l'm'} Y_{lm}(\theta,\phi) Y_{l'm'}(\theta,\phi) d\theta \sin\phi d\phi. \tag{3.6}$$

is obtained by exploiting the orthogonality relations of the spherical harmonics.

Based on the observations one can assume that the small temperature fluctuations are gaussian-like distributed. Using the definition of the variance C_l of a_{lm}

$$C_l = \langle a_{lm}^2 \rangle = \frac{1}{(2l+1)} \sum_{m=-1}^{l} a_{lm}^2 \tag{3.7}$$

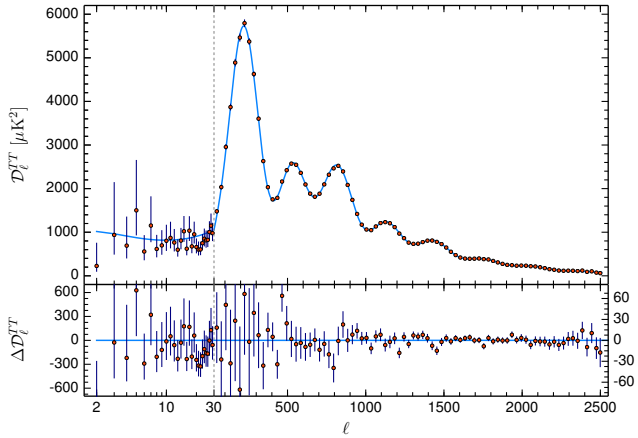

Figure 3.4.: Planck 2018 temperature power spectrum [23].

the variance of the thermal fluctuations reads

$$\begin{aligned}\left\langle\left(\frac{\delta T}{T}\right)^2\right\rangle &= \frac{1}{4\pi}\sum_{lm} a_{lm}a_{l'm'}\delta_{ll'}\delta_{mm'} \\ &= \frac{1}{4\pi}\sum_{l=2}^{\infty}\sum_{m=-l}^{l} a_{lm}^2 \\ &= \frac{1}{4\pi}\sum_{l=2}^{\infty}(2l+1)C_l.\end{aligned} \tag{3.8}$$

The power spectrum of the CMB in Figure 3.4 is plotted in terms of $l(l+1)C_l/(2\pi)$ as a function of the multipole moments l. The Planck data (red dots) is well described by the plotted spectrum.

The latest cosmological Standard Model Λ_{CDM} is based on a flat universe and fulfills the Friedmann-Lemaître-Robertson-Walker metric. This specific model describes cosmology using six different parameters, the so-called energy content of baryons $\Omega_b h^2$, the physical density of dark matter $\Omega_\chi h^2$, the Hubble expansion rate H_0 and the amplitude A_s of the power spectrum in $P_0(k) \sim A_s k^{n_s-1}$, which additionally contains the optical depth parameter τ and the spectral index n_s, which describes the initial perturbations.

By adjusting the Λ_{CDM} parameter to the observed data with a likelihood analysis, a precise value for the relic density can be determined. The latest results from Planck [23] give

$$\Omega_b h^2 = 0.02237 \pm 0.00015 \quad \Omega_\chi h^2 = 0.12 \pm 0.0012, \tag{3.9}$$

where h is the Hubble constant in units of $100\frac{km}{sMpc}$. The relic densities are given in terms of the critical density $\rho_c = \frac{3H^2}{8\pi G}$. Total densities equal one correspond to a perfectly flat universe. The dark energy content in the Universe results from $\sum\Omega = 1$.

3.1.5. N-Body Simulations

Based on its gravitational interaction, dark matter is expected to have a strong impact on the structure formation in the Universe. The cosmological information from the CMB, the temperature anisotropies and the corresponding density variations are used as a starting state in *N-body simulations* [44] to enable the simulation of structure formation in the Universe. Two well-known projects of this kind are the Millennium [45] and the Bolshoi [46] simulation. The simulations show that dark matter dominates structure formation. Due to the earlier clumping of dark matter, so-called dark gravitational centers can form, attracting baryonic matter, which would otherwise drift apart. Structure formation with purely non-relativistic dark matter (cold dark matter) would lead to a large number of small structures, like dwarf galaxies and subhalos. These objects exist in reality, but in a smaller quantity than predicted in these simulations. Therefore, small amounts of warm or hot dark matter might additionally be needed to avoid these discrepancies. This is known as the missing satellite problem [47].

3.2. Properties of Dark Matter

The observations and experiments not only provide evidence for dark matter and determine the relic density, but also reveal its properties. A short overview of these properties can be found here.

Non-baryonic From the observations of the Bullet Cluster and the CMB it is deduced that dark matter must be non-baryonic.

Stable The lifetime of the candidate for dark matter must at least exceed the age of the Universe. The Hubble Space Telescope Key Project determined this time to be $\tau \geq 4.3 \times 10^{17}$ s [48].

Neutral Dark matter is known to be non-luminous, therefore it has to be electrically neutral. Furthermore, a color charge is highly unlikely. If dark matter would be charged, this would have an impact on the stability of disks of spherical galaxies [49]. Charged particles would interfere with the CMB anisotropies [50]. From direct detection experiments it is known that dark matter can only have a small coupling to bosons charged under SU(2). Therefore, dark matter is proposed to be electrically neutral and a color singlet. Furthermore, from the observation on the Bullet Cluster, dark matter should be collision-less [36].

Cold Whether dark matter is hot or cold depends on whether it was relativistic or not during the decoupling phase. Dark matter with velocities in the range between relativistic and non-relativistic is called warm dark matter. The distance that dark matter covers until it is trapped gravitationally is called the free-streaming length. For hot dark matter the free-steaming length is large, so structure formation is

washed out at small scales. Only the fragmentation of large structures could lead to smaller ones. This contradicts the N-body simulation and the current observation of the age of galaxies and galaxy clusters. Therefore, hot dark matter is disfavored as the main candidate for dark matter [51]. In contrast, cold dark matter was non-relativistic long before the matter dominated time, and therefore has a short free-streaming length. The N-body simulations are in good agreement with today's observations. But there are still some discrepancies. One of them is the so-called missing satellite problem [47]: The number of predicted satellite halos in the Milky Way exceeds the number of observed galaxies. This leads to the assumption that warm dark matter must also be considered. The amount of warm dark matter is limited by the suppression of smaller structures, seen by studying the growth of structures in galaxy clusters and the Lymann-α-forest [52]. Cold dark matter is nevertheless the preferred candidate for dark matter.

Consistent with Big Bang Nucleosynthesis The predicted abundance of light elements produced within the first three minutes after the Big Bang is in very good agreement with the observations. The added candidate for dark matter should not influence this [53]. The changes in Big Bang Nucleosynthesis (BBN) due to the existence of additional relativistic particles would lead to a faster expansion rate and thus to an earlier freezing out of the neutron-to-proton ratio. This would lead to a higher He^4 abundance [54], also to particles decaying during BBN [55].

Consistent with stellar evolution Light, weakly interacting particles generated in the hot plasma of stars could escape without further interaction and cause a loss of energy that would alter the evolution of the star [56].

3.3. Dark Matter Candidates and Theories

There are various approaches to solve the problem of dark matter. One possibility is to modify the existing theory at the astrophysical level so that it is not necessary to introduce new particles. An example would be *Modified Newtonian Dynamics* (MOND) [57], motivated by the attempt to explain the observed discrepancies of the rotation curves without a dark matter particle. The assumption is that Newtonian mechanics is not valid for small accelerations. A constant a_0 is introduced into Newtonian mechanics with the dimension of an acceleration for such small accelerations to be consistent with the rotation curves. But this modified theory gives no explanation for the observations in the Bullet Cluster.

There are astronomical objects that can partially explain the content of dark matter in the Universe. These astronomical objects are the so-called *Massive Astrophysical Compact Halo Objects* (MACHOs) [58], which consist of baryonic matter, but emit no radiation (black holes, neutron stars and different kinds of dwarfs). Nevertheless, the amount of baryonic matter is limited by CMB measurements and large scale structures.

Therefore, a large part of the non-baryonic matter is still needed to explain the experimental observations. A suitable way to explain the observation is a particle dark matter candidate. In the following, we review a list of possible particle dark matter candidates.

Sterile Neutrinos Right-handed neutrinos can explain neutrino oscillations and baryon asymmetry, but can also provide a candidate for dark matter. They are called sterile because they are not involved in the weak interactions other than mixing with active neutrinos. Sterile neutrinos are considered quite heavy. Through a seesaw-like mechanism or some flavor symmetries, it is possible to produce a light sterile neutrino in the keV range that can be considered a candidate for dark matter. Yet, such a sterile neutrino would be warm dark matter and their relic density is therefore limited. Current restrictions for sterile neutrinos as candidates for dark matter can be found in [59].

Neutralinos We have already discussed the neutralino in the context of the MSSM. The neutralino is the lightest sparticle in a wide range of the SUSY parameter space and is stable due to the R-parity conservation. It is a suitable candidate for dark matter. Regarding its properties the neutralino belongs to the *weakly interacting massive particle*. (WIMP). In addition, the neutralino leads to the correct relic density in many MSSM scenarios.

Sneutrinos The sneutrino is the superpartner of the previously discussed neutrino. The left-handed sneutrinos are excluded as a dark matter candidate. Yet the right-handed sneutrinos are still a viable option. The light sneutrinos are excluded by the discovery of the Higgs boson. Heavy sneutrinos, on the other hand, are still viable - but highly restricted.

Gravitinos SUSY as a local symmetry can be used to formulate a quantum theory of gravitation - supergravity. In supergravity a new particle is formed, the gravitino, which is the superpartner of the graviton. This new particle can be the lightest SUSY particle and is stable.

This list of candidates for dark matter is far from complete. A complete list is outside the scope of this thesis. In Chapter 6 - we focus on the lightest neutralino as a dark matter candidate. In the next section, we will present WIMP dark matter searches.

3.4. Dark Matter Searches

The WIMP is a favored dark matter candidate and several experiments are carried out to search specifically for such a candidate. The search strategies are divided into three different types, these three options are shown in Figure 3.5 and briefly explained including a current status in the following.

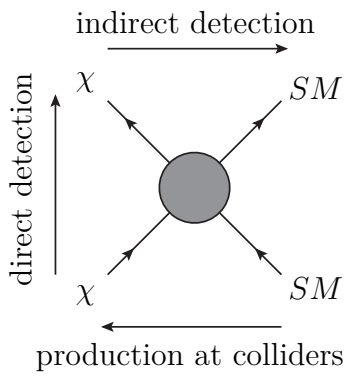

Figure 3.5.: Overview of the different search channels for dark matter. χ indicates the dark matter particle and SM a Standard Model particle. Indirect detection searches for SM particles that are created by the destruction of dark matter. Direct detection, on the other hand, attempts to detect collisions between SM particles and dark matter particles. In the context of the collider searches, the destruction product of the SM particles is examined for final states of dark matter due to missing energies.

3.4.1. Collider Searches

Collisions with sufficiently high energies such as the ones at the LHC can produce a pair of dark matter particles in a controlled collider environment. Dedicated LHC experiments ATLAS and CMS use 36.1 fb^{-1} of data at a center-of-mass energy of 13 TeV to look for signals of dark matter.

There are two general approaches to collider searches for dark matter. One is very model specific, taking into account every particle and interaction of the model. An example of such an approach is given in Sec. 2.5.1. Here we will outline a model-independent collider search based on an effective field approach.

In this approach used by the ATLAS collaboration all heavy particles apart from the DM particle and the necessary heavy gauge bosons are integrated out and their effects are included through the effective couplings.

Due to their weak interaction, if a pair of dark matter particles is produced at the LHC, it does not leave any signature in the detector. In order to highlight dark matter productions, one needs at least one visible particle being produced in the collision. The simplest signature are monojets or monophotons, where one single gluon or photon is radiated from the initial state. It is this visible particle which shows the missing momentum and energy carried by the invisible dark matter particle.

Within the analysis of ATLAS [60] the data were in good agreement with the Standard Model. The resulting exclusion limits for the pair production of weakly interacting dark matter candidates are model specific. The different models used in the analysis are

described in the following paragraphs.

The dark matter models are defined for Dirac fermion WIMPs (χ), which are generated via an s-channel exchange of a spin 1 mediator between two colliding quarks. Depending on the coupling, the mediator is either vector-like (Z_V), axial-vector-like (Z_A) or pseudoscalar-like (Z_p). These models are defined with four free parameters, the WIMP mass m_χ, the mediator mass m_{Z_A}, m_{Z_V}, m_{Z_p} and the coupling g_q to the quarks and g_χ to the WIMPs. A coupling with other SM particles is not considered. From this process a monojet signature is expected from the initial state radiating of a gluon.

Another production channel for WIMPs is mediated by a colored scalar, which is assumed to couple as a color triplet, SU(2) doublet to left-handed quarks. A new production mechanism via the u- and t-channel is considered with direct interaction between standard model particles and dark matter particles as well as s-channel exchange of two mediators. This model is defined with three free parameters, the WIMP mass m_χ, the mediator mass m_η and the mediator coupling to the Standard Model particle and WIMP $g_{q\chi}$. Only interactions with the quarks of the first two generations are considered.

Figure 3.6 shows the results of the ATLAS search for axial (top left), vector (top right) and colored scalar (bottom) mediators for dark matter production. The exclusion contours on the ratio of the measured signal cross section to the predicted ($\mu = \frac{\sigma}{\sigma}\sigma_{th}$) within a confidence level (C.L.) of 95 % are shown in the figures. The observed limits are marked by a black line with a 1σ band (dashed black lines) to take theoretical uncertainties (PDF, scale...) into account. The expected limits are indicated by a blue dashed line with the 1σ (green) and 2σ (yellow) band. The dashed black line shows the kinematic limit for on-shell production, where the mass of the mediator particles is twice the mass of the dark matter.

In the upper left corner of the Figure 3.6 the limits within the simplified model with an axial vector mediator and a Dirac WIMP with the couplings $g_q = \frac{1}{4}$ and $g_\chi = 1$ are shown in the $m_{Z_A} - m_\chi$ plane. An additional hashed region is marked which is excluded due to the violation of pertubative unitarity in the parameter region for $m_\chi > \sqrt{\frac{\pi}{2}} m_{Z_A}$. The cyan line shows earlier results of ATLAS [62] with an integrated luminosity of 3.2 fb^{-1} at 13 TeV. The red relic density line $\Omega_\chi h^2 = 0.12$, calculated from MadDM [61], crosses the exclusion region at $m_{Z_A} \sim 1200$ GeV and $m_\chi \sim 440$ GeV.

A vector mediator is considered in Figure 3.6 top right, with the same couplings as in the previous case. The boundaries are displayed in the plane $m_{Z_V} - m_\chi$ with the same color code as before. For light WIMPs, masses below 1.55TeV are excluded.

In the lower left figure the exclusion limits in the $m_\eta - m_\chi$ plane are shown for a colored scalar mediator with a coupling $g = 1$. Mediator masses below 1.67 TeV are excluded for light dark matter particles. Masses up to 620 GeV are excluded in the case of $m_\chi = m_\eta$.

The results of CMS [63], Figure 3.7, are similar to the discussed ATLAS results. The exclusion contours are displayed at 95 % C.L. in the $m_{med} - m_{DM}$ plane. The observed contours (red line) are displayed with a 1σ band (thin red solid lines), the expected

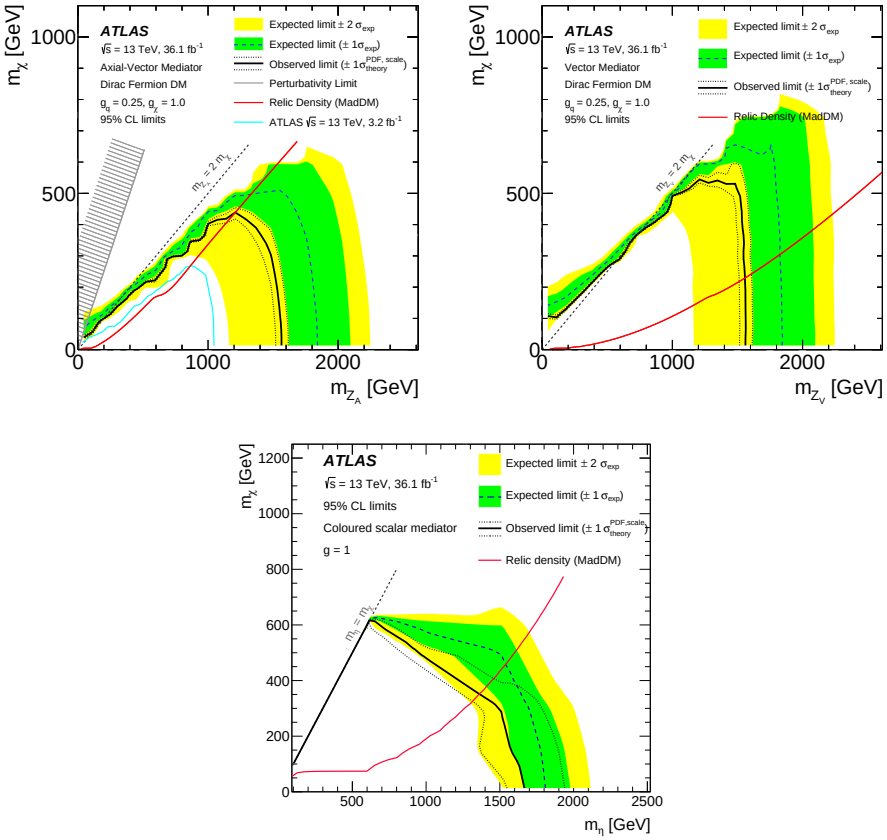

Figure 3.6.: ATLAS search for axial (top left), vector (top right) and colored scalar (bottom) mediator for DM production, showing the 95 % exclusion limits depending on mediator particle mass and dark matter particle mass. The shaded area is excluded due to perturbativity ($m_\chi > \sqrt{\frac{\pi}{2}} m_{Z_A}$) in case of the axial-vector mediator. The red line gives the kinematic limit for on-shell production($m_{Z_A}, m_{Z_V}, m_{Z_\eta} = 2m_\chi$). The solid black line is the observed limit within an 1σ band (dotted black lines), taking theoretical uncertainties into account. The blue dashed line indicates the expected limit with the 1σ (green) and the 2σ (yellow) band. The red line shows the relic density $\Omega_\chi h^2 = 0.12$ calculated by MadDM [61]. Figures taken from [60].

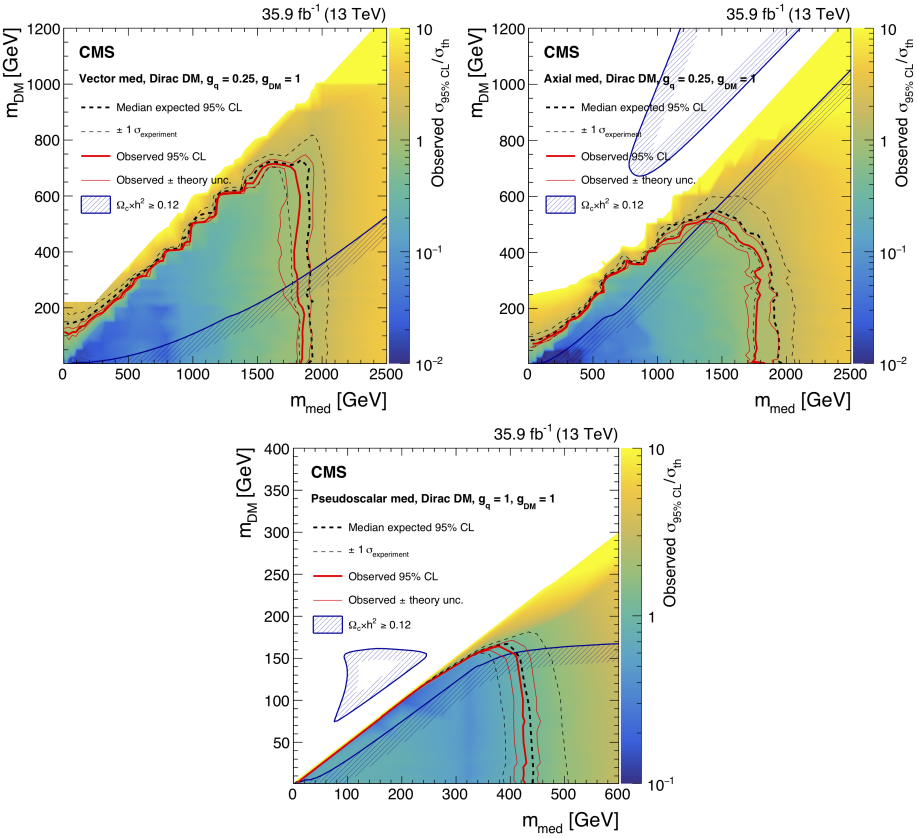

Figure 3.7.: CMS search for axial (upper left), vector (upper right) and pseudoscalar (lower) mediator within DM production. Exclusion contours are shown at 95 % C.L. in the $m_{med} - m_{DM}$ plane. The red solid line represents the observed contours with a 1σ band (thin red solid lines), the expected exclusion contour is shown by the black dashed line with corresponding 2σ band (thin dashed black lines). The dark blue contours (provided by MadDM [61]) gives the region where the Planck limit $\Omega_\chi h^2 = 0.12$ [23] is overstepped. Figures taken from [63].

exclusion contour (black dashed line) with a corresponding 2σ band (thin dashed black lines). The region where the relic density $\Omega_\chi h^2 = 0.12$ [23] is exceeded is represented by the dark blue contours (provided by MadDM [61]). For axial vector (top left) and vector (top right) models, mediator masses up to 1.8 TeV and dark matter particle masses up to 500 GeV and 700 GeV are excluded. The pseudoscalar mediator has limits for the mediator mass up to 400 GeV and for the dark matter mass up to 150 GeV.

Figure 3.8 shows exclusion limits at 90 % C.L. on spin dependent/spin independent cross section for the axial (top left) and vector-axial (top right) mediator model depending on the particle mass of the dark matter. The observed (solid red line) and the expected (dashed black line) limits are compared with the results of direct and indirect detection, CDMSLite [64], LUX [65], XENON1T [66], PANDAX-II [67] and CRESST-II [68] for vector-mediator and Picasso [69], PICO-60 [70], IceCube [71] and Super-Kamiokande [72] in case of axial-vector. In the case of the vector mediator, the biggest restrictions for masses below 5 GeV are provided by CMS, while for higher dark matter masses CDMSLite and CRESST-II place more severe limits. For the axial vector case, the strongest constraints are given by CMS up to a dark mass of 550 GeV, followed by IceCube $t\bar{t}$ and PICO-60 for higher masses.

In the lower Figure 3.8 the upper limits of the pseudoscalar mediator are translated into velocity averaged DM annihilation cross section ($\langle \sigma v \rangle$). The results are compared with those of the indirect detection experiment Fermi-LAT [73]. Again, CMS provides strongest constraints for low masses up to 150 GeV for the mass of dark matter. Since the scattering cross section between dark matter particles and SM quarks is suppressed at non-relativistic velocities for a pseudoscalar mediator, there are no comparable limits from direct detection experiments.

3.4.2. Indirect Detection

Indirect detection [74] is looking for products of WIMP-WIMP annihilation. The annihilation rate of WIMPs is proportional to the square of the dark matter density. Therefore, it is sensible to look for dark matter annihilation in regions with expected high WIMP densities, such as the sun, earth and the galactic center. Possible annihilation products contain gamma-rays, neutrinos and antimatter.

The annihilation of WIMPs can produce quark-anti-quark pairs, which produce particle jets. The resulting jets release gamma-rays. These processes are primarily expected to take place in the galactic center. Detection devices for gamma-rays are shielded by an anti-coincidence shield, to limit the amount of charged particles entering the detector. After passing the shield, the gamma-rays hit thin sheets of heavy nuclei, where the photons are converted to e^+e^- pairs. The energies of the positrons and electrons are tracked by calorimeters. If the anti-coincidence shield is not triggered, the registered energy is the signature of the gamma-ray event. IACT (Imaging Atmospheric Cherenkov Telescope), HESS [75], VERITAS [76] and the FERMI satellite [77] search for γ rays.

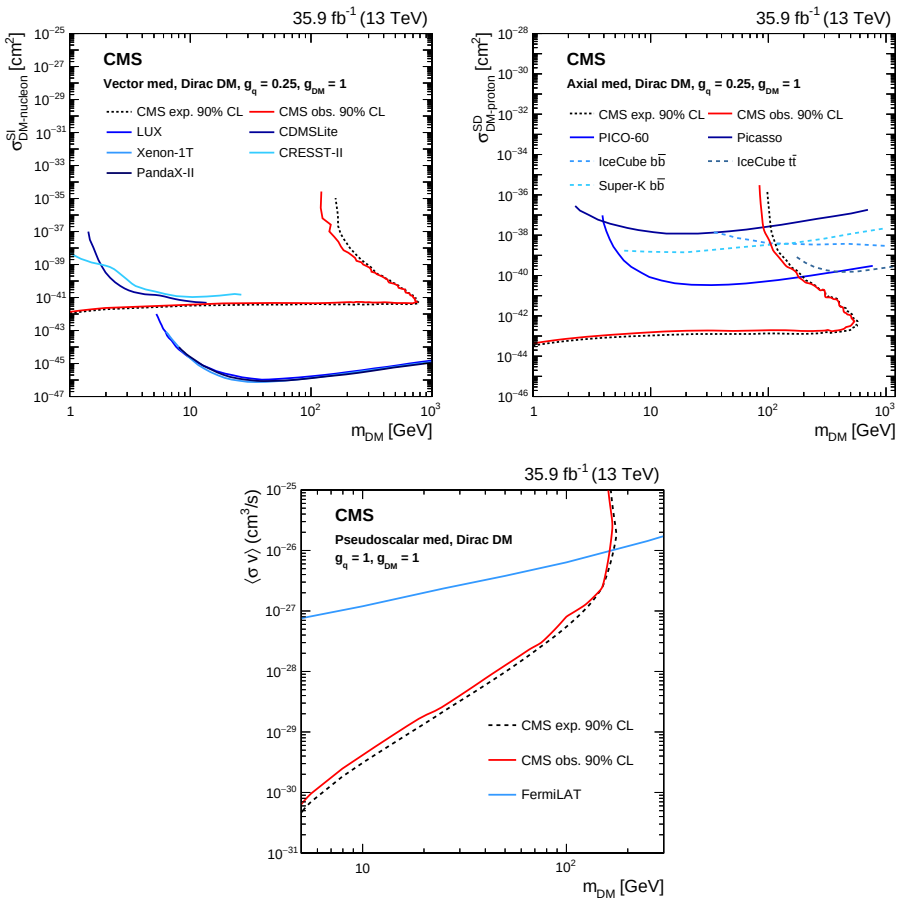

Figure 3.8.: CMS limits at 90 % C.L. on spin-depend/spin-independent cross section for axial (upper left), and vector (upper right) mediator models in dependence of the mass of the dark matter particle. The solid red line give the observed limits provided by CMS and the dotted black line the expected limits. Further limits for comparison are from CDMSLite [64], LUX [65], XENON1T [66], PANDAX-II [67] and CRESST-II [68] for vector mediator and Picasso [69], PICO-60 [70], IceCube [71], and Super-Kamiokande [72] are shown in case of the axial-vector. The velocity averaged dark matter cross section for the pseudoscalar mediator (lower) is compared to upper limits from Fermi-LAT [73]. Figures taken from [63].

Antimatter is cosmologically rare and therefore an excellent signal of WIMP-WIMP-annihilation. But unlike gamma-rays and neutrinos, antimatter is affected by magnetic fields and lose energy due to inverse Compton and synchroton processes, which makes it impossible to conclude on the annihilation origin. The antimatter particle flux is therefore studied as a whole. Experiments searching for antimatter must be located at the top of the earth's atmosphere. Experimental facilities searching for charged cosmic rays are PAMELA [78], FERMI [77] , HESS [75] and AMS [79].

Another important product of WIMP-WIMP annihilation is the neutrino. WIMPs passing through the sun may be slowed down by scattering so that the WIMPs are bound in the sun. These slow WIMPs accumulate to the center. This leads to an enhancement of the corresponding density and annihilation rate. Even though the annihilation products are most likely immediately absorbed, neutrinos wont. Neutrinos can cover long distances of dense matter without interaction, making them an interesting candidate for the indirect detection of dark matter, but also challenging to detect. Neutrinos can only be detected by secondary particles, as done in IceCube [71, 80] and Super-Kamiokande [72].

IceCube is a big neutrino telescope, located at the South Pole. The ice is used as a medium for the neutrino detection, due to its excellent optical qualities and the massive amount creating a large area for interaction. The secondary particles resulting from the neutrino interaction move through the ice, causing the emission of Cherenkov light. The Cherenkov photons are then detected by the photomultiplier tubes (PMTs), see also Chap. 4.

In the following current limits on dark matter are discussed focusing on the publication [71] and [80].

To set limits, it is assumed that dark matter annihilates to a certain final state with a canonical thermal annihilation cross section $\langle \sigma v \rangle = 3 \times 10^{-26}$ cm^{3}s^{-1}. In the IceCube analysis [80], `DarkSUSY` was used to calculate the predicted neutrino spectrum at the detector for each model and to obtain the dark matter population today. Figure 3.9 shows limits of the spin-dependent WIMP-proton cross section depending on the dark matter particle mass. On the left side the results of IceCube for different final state are shown. Soft final states like gluon (green dashed line) and bottom quark (red solid line) have weaker limits than the hard final state like neutrino (orange dashed line) and tau (solid blue line), which have stronger constraints. Furthermore, limits for Higgs boson (pink dashed line), top quark (solid yellow line), W boson (solid orange line) and Z boson (black dashed line) are displayed.

On the right side IceCube (orange) and Super-Kamiokande [72] (black) limits on bottom quark (dotted), W boson (dashed) and tau (solid) final states are shown. IceCube provides the strongest limits for WIMP masses above 200 GeV, while Super-Kamiokande provides a higher sensitivity for lower WIMP masses. The PICO experiments (blue and violet)[81, 82] provide the strongest limits compared to the indirect detection limits.

Due to the absence of significant dark matter signals, the data obtained by IceCube is translated into lower limits for the lifetime of a dark matter particle. This study was

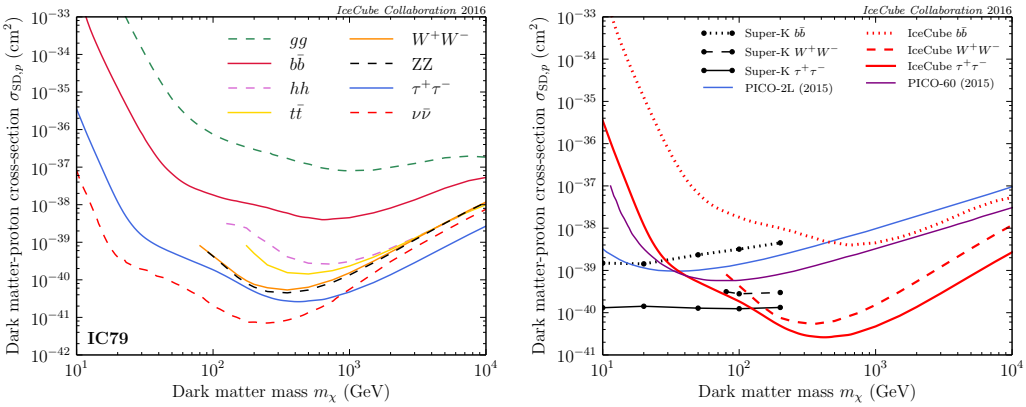

Figure 3.9.: Left: Limits by IceCube on spin-dependent WIMP-proton cross section depending on dark matter particle mass for different annihilation final states (gluon (dashed green), bottom quark (solid red), Higgs boson (dashed rose), top quark (solid yellow), W boson (solid orange), Z boson (dashed black), tau (solid blue) and neutrino (dashed red)). Right: Comparison of limits by IceCube (bottom quark dooted orange, W boson dashed orange, tau solid orange lines) to limits by Super-Kamiokande (bottom quark dooted black, W boson dashed black, tau solid black lines) [72] and PICO [81, 82] (PICO-2L blue, PICO-60 violet). Figures taken from [71].

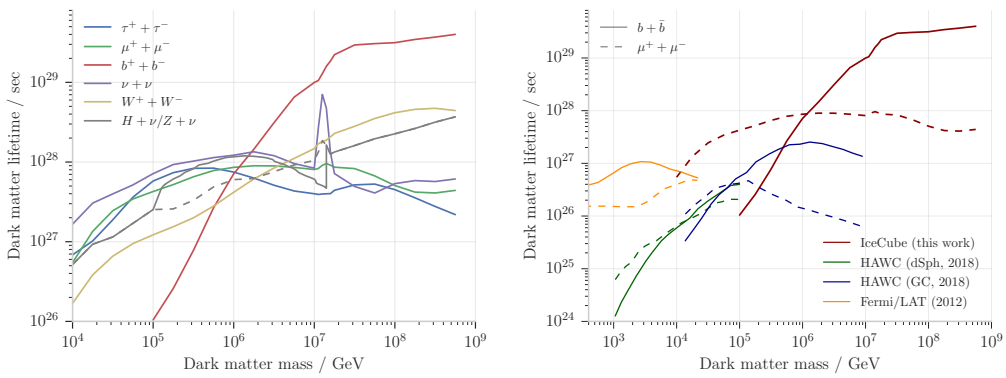

Figure 3.10.: Left: Limits on dark matter lifetime for specific decay channels from IceCube data [80] . Combined result for $Z + \nu$ and $H + \nu$ (solid grey line), due to the indistingluishable spectra within the energy resolution. Seperate results for $\tau^+ + \tau$ (blue), $\mu^+ + \mu$ (green), $b^+ + b$ (red), $\nu + \nu$ (violate), and $W^+ + W$(yellow) are shown. The dashed grey line represents the limit from cascade analysis. Right: Comparison of IceCube results on lower limits of dark matter lifetime towards gamma-ray telescopes: HAWC (Dwarf Spheroidal Galaxies) [83], HAWC (Galactic Halo) [84] and Fermi-LAT [85] . Figures taken from [80].

done by the IceCube collaboration [80], the results are shown in Figure 3.10. On the left side IceCube lifetime limits for dark matter are visualized for tau (blue), muon (green), bottom quark(red), neutrino (violet), W bosons (yellow) and combined Higgs-neutrino and Z boson-neutrino final states. The analysis of $H + \nu$ and $Z - \nu$ are treated as the same channel because the resulting neutrino spectra are indistinguishable within the energy resolution. The lower limit on the lifetime is not calculated in the $b^+ + b$ case for masses below $m_{DM} < 10^5$ GeV, due to the similarity of the decay spectrum with the atmospheric background fluxes.

The right figure shows that IceCube provides the strongest limits for dark matter lifetime for masses above 10^4 GeV (red lines) for bottom (solid) and muon (dashed) final states. The limits are compared with HAWC (Dwarf Speriodal Galaxies(dSph) [83] green, Galactic Halo (GC)[84] blue) and Fermi/LAT [85] (yellow). While Fermi/LAT provides the only constraints for dark matter masses below 1000 GeV, HWC provides the stronger limits in the mass range from 1000 GeV up to 10^7 GeV. IceCube provides the only limits for masses above 10^7 GeV. In the bottom final state, IceCube additionally gives the strongest limits in the mass range from about 10^5 GeV to $2 - 3 \times 10^5$ GeV.

3.4.3. Direct Detection

Assuming that our galaxy is embedded in a dark matter halo, as suggested by the rotation curves, the Earth would be exposed to a flux of dark matter as it orbits the Sun. Dark matter from this flux may interact with nuclei from target material. These interactions can lead to nuclear recoils, which produce a measurable signal.

Regarding the direct detection of dark matter [74], experiments are looking for the discussed recoil when a dark matter particle scatters with a SM particle. As background radiation could lead to similar signals, the experimental set-ups must be well shielded. For detection purpose different types of probes can be used, phonons, ionization and scintillation. All are sensitive in different regimes. With at least two of these channels, the best possible distinction between background and signal is obtained. Within direct detection, a distinction is made between spin-dependent (axial vector) and spin-independent (scalar) couplings.

One experiment in Gran Sasso is XENON, with the latest update of XENON1T [86, 87]. A tank full of liquid xenon gives a large target for scattering with dark matter particles. The nuclear recoils excite and ionize the liquid xenon, which de-excites under the emission of scintillation light. The scintillation is detected by photosensors installed at the top and bottom of the tank. Additionally, the ionization electrons are accelerated by an electric field to the top of the tank, where they pass from the liquid phase to the gas phase (which is on top of the liquid phase). Hence photons are emitted and can be detected as a secondary signal. The run time between both signals gives rise to the depth of the scattering. The interaction depth alongside the photodetector hit pattern allows to determine the precise coordinates of the interaction.

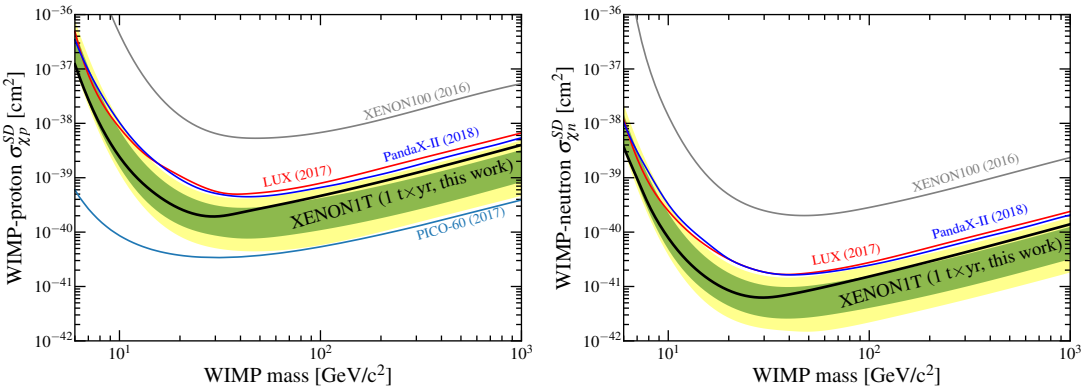

Figure 3.11.: Upper limits from XENON1T on spin dependent WIMP-proton(right) and WIMP-neutron (left) with 90 % C.L. [87] from one year measurements (black line). The green band indicates the expected sensitivity in a 1σ band and yellow the corresponding 2σ band. In addition the results from XENON100 [88] (gray), LUX [65] (red) and PandaX-II [89] (blue) are shown. For the WIMP-proton also results from PICO-60 [70] (light blue) are shown additionally.

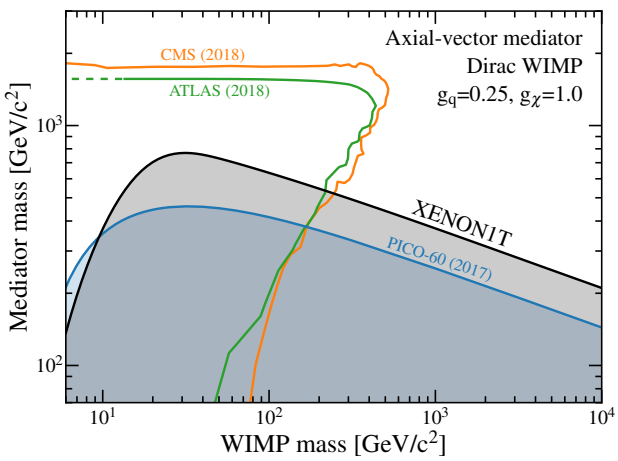

Figure 3.12.: Upper limit from XENON1T in the $m_{\text{med}} - m_\chi$ plane for a simplified iso-scalar model with 95 % C.L. The model contrains a Dirac WIMP with a coupling (g_χ) fixed to 1.0 and a axial-vector mediatorm where the mediator quark coupling (g_q) is fixed to 0.25 [87]. Again limits from PICO-60 [70] are shown. Furthermore the previosly discussed (Figure 3.6 and Figure 3.7 upper left) limits by ATLAS [60] and CMS [63] are shown.

Since the neutron and proton case data agree with the background hypothesis, upper limits for the WIMP-proton and WIMP-neutron cross-sections are defined. In [87] these upper limits are set for spin-dependent (SD) WIMP-proton (Figure 3.11 left) and WIMP-neutron (Figure 3.11 right) case. The Figure 3.11 shows the 90 % C.L. limits and the corresponding 1σ and 2σ sensitivity bands. The most stringent constraints from direct detection experiments apply to neutron-only limits for WIMP masses above 6 GeV/c^2, for a minimum of 6.3×10^{-42} cm^2 for a 30 GeV/c^2 WIMP. For the proton limit, PICO-60 [70] gives the highest constraints for the lower cross section limit. The minimum is reached at 4×10^{-41} cm^2 for a 30 GeV/c^{-2} WIMP.

The analysis by the XENON1T collaboration additionally contains a comparison of the direct detection results from the SD searches with the collider experiments ATLAS and CMS, see Section 3.4.1. The model containing a Dirac fermion WIMP of mass m_χ with a s-channel interaction with quarks and a spin-1 mediator of mass m_{med} with an axial-vector coupling to WIMP and quarks is considered. The upper limits can be transformed into the plane $m_{med} - m_\chi$ and directly compared with the collider experiments from section 3.4.1. The results from ATLAS (Figure 3.6 top left) and CMS (Figure 3.7 top left) are compared to the results from Xenon1T [87] and PICO-60 [70] in Figure 3.12. The shaded regions are excluded by ATLAS (green), CMS (red), PICO (blue) and XENON1T (black).Direct detection excludes additional parameter spaces.

3.4.4. Conclusion

Overall, no direct signal from dark matter was detected in the experiments under discussion. Combining the three different types of experiments – direct, indirect and collider searches – better constraints can be set for the annihilation cross section of dark matter.

3.5. Relic Density

The relic density Ω_χ of dark matter is known by the measurements of the CMB, see section 3.1.4. To investigate a theory that contains a candidate for dark matter for its reliability, predictions about the relic density have to be checked. The relic density is determined by solving the Boltzmann equation, which is discussed in detail in the following. The derivation of the Boltzmann equation follows [90]. In addition, co-annihilation within the Boltzmann equation and the thermal average of the cross section are discussed.

3.5.1. Boltzmann Equation

The Boltzmann equation [90]

$$L[f] = C[f]. \tag{3.10}$$

describes the evolution of the phase space density $f(\mathbf{p}, \mathbf{x}, t)$, assuming an interaction of at most two particles. L is the Liouville operator describing the change of the particle phase space density. The collision operator C takes into account the interaction of particles and the resulting changes in the number of particles per phase space volume. Considering the fact that the phase space density is homogeneous and isotropic, i.e. depends only on the particle energy E and the time t, the Liuoville operator becomes

$$L[f] = \frac{\partial f}{\partial t} - H \frac{|\mathbf{p}|^2}{E} \frac{\partial f}{\partial E}, \tag{3.11}$$

where $H = \dot{R}/R$ is the Hubble rate and R the scale factor of the Universe, with the corresponding derivative $\dot{R}$ in time. On the right side of the equation, the collision operator C counts the gained or lost particles by collisions with other particles. The particle number density n is defined as the integral of the phase space density over all momenta and the sum over all spins

$$n = \int \mathrm{d}n = \int f(E, t) \frac{g \, \mathrm{d}^3 p}{(2\pi)^3}. \tag{3.12}$$

g being the spin degrees of freedom and $f = f(E, t)$ the phase space distribution function of particles. The evolution function for the particle number density is given by the integrated Boltzmann equation over all particle momenta and summed over the spin degrees of freedom. For a $2 \to 2$ process ($12 \to 34$) the Liouville term becomes

$$g_1 \int L(f_1) \frac{\mathrm{d}^3 p_1}{(2\pi)^3} = \frac{1}{R} \frac{\mathrm{d}}{\mathrm{d}t} (R^3 n_1) = \dot{n}_1 + 3 H n_1. \tag{3.13}$$

For the collision term, only the inelastic terms survive the integration

$$\begin{aligned} g_1 \int C(f_1) \frac{\mathrm{d}^3 p_1}{(2\pi)^3} = &- \sum_{\text{Spin}} \int (f_1 f_2 (1 \pm f_3)(1 \pm f_4) |M_{12 \to 34}|^2 \\ &- f_3 f_4 (1 \pm f_1)(1 \pm f_2) |M_{34 \to 12}|^2) \cdot (2\pi)^4 \delta(p_1 + p_2 - p_3 - p_4) \\ &\cdot \frac{\mathrm{d}^3 p_1}{(2\pi)^3 2E_1} \frac{\mathrm{d}^3 p_2}{(2\pi)^3 2E_2} \frac{\mathrm{d}^3 p_3}{(2\pi)^3 2E_3} \frac{\mathrm{d}^3 p_4}{(2\pi)^3 2E_4}, \end{aligned} \tag{3.14}$$

with the invariant polarized amplitude M.

For identical initial particles a factor $\frac{1}{2}$ must be taken into account to avoid double counting and a factor 2 from the disappearance of two particles at each annihilation. Because of this cancellation of the factors, there is no additional factor for identical particles in the equation. Both f_3 and f_4 can be replaced by their equilibrium distributions f_3^{eq} and f_4^{eq}, omitted by the fact that the annihilation product is in equilibrium with the thermal background. The detailed balance allows the replacement

$$f_3^{\text{eq}} f_4^{\text{eq}} = f_1^{\text{eq}} f_2^{\text{eq}}. \tag{3.15}$$

By considering unitarity, the collision term simplifies

$$\sum_{\text{spin}} \int |M_{34\to 12}|^2 (2\pi)^4 \delta^4(p_1 + p_2 - p_3 - p_4) \frac{\mathrm{d}^3 p_3}{(2\pi)^3 2E_3} \frac{\mathrm{d}^3 p_4}{(2\pi)^3 2E_4} \tag{3.16}$$

$$= \sum_{\text{spin}} \int |M_{12\to 34}|^2 (2\pi)^4 \delta^4(p_1 + p_2 - p_3 - p_4) \frac{\mathrm{d}^3 p_3}{(2\pi)^3 2E_3} \frac{\mathrm{d}^3 p_4}{(2\pi)^3 2E_4}. \tag{3.17}$$

With the introduction of the unpolarized cross section $\sigma_{12\to 34}$ one obtains

$$\sum_{\text{spin}} \int |M_{12\to 34}|^2 (2\pi)^4 \delta^4(p_1 + p_2 - p_3 - p_4) \frac{\mathrm{d}^3 p_3}{(2\pi)^3 2E_3} \frac{\mathrm{d}^3 p_4}{(2\pi)^3 2E_4} = 4F g_1 g_2 \sigma_{12\to 34} \tag{3.18}$$

with $F = [(p_1 \cdot p_2)^2 - m_1^2 m_2^2]^{\frac{1}{2}}$. g_1 and g_2 are the averaged spin factors. To include all accessible final channels, $\sigma_{12\to 34}$ is replaced by the total annihilation cross section

$$g_1 \int C(f_1) \frac{\mathrm{d}^3 p_1}{(2\pi)^3} = - \int \sigma v_{\text{Møl}} (\mathrm{d}n_1 \mathrm{d}n_2 - \mathrm{d}n_1^{\text{eq}} \mathrm{d}n_2^{\text{eq}}). \tag{3.19}$$

n_1 and n_2 are the particle number densities and their equilibrium values are n_1^{eq} and n_2^{eq}. $\mathrm{d}n_1$ and $\mathrm{d}n_2$ are the momentum-space differentials. The Møller velocity[3] $v_{\text{Møl}} = \frac{F}{E_1 E_2}$ is defined in a way that $v_{\text{Møl}} n_1 n_2$ is invariant under Lorentz transformation. This product equals the product of the relative velocity v_{lab} with the particle densities $n_{1\text{lab}}$ and $n_{2\text{lab}}$. Using the Møller velocity, the invariant interaction rate per unit volume and unit time can be written in any reference frame as

$$\frac{\mathrm{d}^2 N}{\mathrm{d}V \mathrm{d}t} = \sigma v'_{\text{Møl}} n'_1 n'_2. \tag{3.20}$$

The chosen reference frame is symbolized by a prime on the velocity and the particle densities, σ is the invariant cross section. Choosing the cosmic comoving frame with the particle velocities $v_1 = \frac{p_1}{E_1}$ and $v_2 = \frac{p_2}{E_2}$, the Møller velocity becomes

$$v_{\text{Møl}} = \left[|v_1 - v_2|^2 - |v_1 \times v_2|^2 \right]^{\frac{1}{2}}. \tag{3.21}$$

By symmetry considerations it occurs that the distributions in kinematic equilibrium are proportional to those in chemical equilibrium, whereby the proportional factor is independent of the moment. The equation (3.19) with the comparison of the situation before and after decoupling leads to

$$g_1 \int C(f_1) \frac{\mathrm{d}^3 p_1}{(2\pi)^3} = - < \sigma v_{\text{Møl}} > (n_1 n_2 - n_1^{\text{eq}} n_2^{\text{eq}}). \tag{3.22}$$

[3]Note that in this case a lot of literature refers to the relative velocity, which was previously the assumption, but was corrected later on[91].

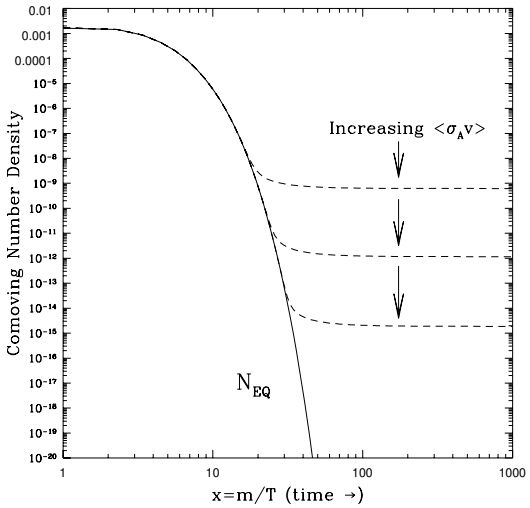

Figure 3.13.: Behavior of comoving number density in time. The solid line represents the behaviour of the comoving number density in equilibrium. When the chemical decoupling takes place, depending on $\langle \sigma v \rangle$, the comoving number density follows the dashed line on a plateau. This is happening at the so-called freeze-out Image taken from lecture notes [92], originally published in [93].

The thermally averaged total annihilation cross section multiplied by the Møller velocity is given by

$$< \sigma v_{\text{Møl}} >= \frac{\int \sigma v_{\text{Møl}} \mathrm{d}n_1^{\text{eq}} \mathrm{d}n_2^{\text{eq}}}{\int \mathrm{d}n_1^{\text{eq}} \int \mathrm{d}n_1^{\text{eq}}}. \tag{3.23}$$

Comparing Eq. (3.19) with Eq. (3.22) results in

$$\dot{n}_1 + 3Hn_1 = - < \sigma v_{\text{Møl}} > (n_1 n_2 - n_1^{\text{eq}} n_2^{\text{eq}}), \tag{3.24}$$

similar for n_2. For identical particles it follows

$$\dot{n} + 3Hn = - < \sigma v_{\text{Møl}} > (n^2 - n_{\text{eq}}^2). \tag{3.25}$$

Where σ is summed over final and averaged over initial spins with no additional factor for identical particles.

The behavior of the comoving number density in time is given by the Boltzmann equation shown in Figure 3.13. The solid line indicates the equilibrium value. Starting at high temperatures, shortly after the Big Bang, the Hubble parameter term in the Boltzmann equation was negligibly small. Annihilation and production of dark matter were in equilibrium. The comoving number density remained constant until the production of dark matter was reduced, which was caused by the decreasing temperature.

There was not enough energy left to produce new particles of dark matter. The comoving number density decreased until the dark matter annihilation rate became too small due to the expansion of the Universe. This is the point of freeze-out, where the comoving number density reached the plateau. The freeze-out depends on the cross section of the corresponding annihilation of dark matter. With increasing cross section the time of freeze-out also increases.

3.5.2. Coannihilation within the Boltzmann Equation

In the previous section, the Boltzmann equation has already been discussed for non-identical particles. This is important because the co-annihilation depends on the Boltzmann factor

$$\frac{n_i^{\mathrm{eq}}}{n_\chi^{\mathrm{eq}}} \sim \exp\left(-\frac{m_i - m_\chi}{T}\right), \tag{3.26}$$

with the dark matter equilibrium number density n_χ^{eq} and the corresponding mass m_χ and the equilibrium number density of the other co-annihilating particle i. T is the freeze out temperature. When the particles are non-degenerated in mass, co-annihilation is suppressed by the Boltzmann factor, but for nearly mass degenerated particles co-annihilation can have a large impact on the annihilation cross section. Furthermore, the annihilation of the mass degenerated particles can even be the leading contribution to the relic density. In case of Supersymmetry, a candidate for the LSP can be the lightest stop. This is not only limited to the next lightest sparticle (NLSP), but is true for all mass degenerated particles. A further discussion of the importance of the annihilation of the mass degenerated particles is performed in Chapter 6.

3.5.3. Thermal Averaging

Next, we will concentrate on the relevant expressions for the calculation of the thermal average of the cross section times Møller velocity, which is relevant for the relic density calculation. In the following, the index Møl is omitted from the velocity, the Møller velocity is simply denoted as v. The total number density in equilibrium is given as

$$n^{\mathrm{eq}} = \sum_i n_i^{\mathrm{eq}} = \sum_i \frac{g_i}{(2\pi)^3} \int \mathrm{d}^3 p_i e^{\frac{E_i}{T}} = \frac{T}{2\pi^2} \sum_i g_i m_i^2 K_2\left(\frac{m_i}{T}\right), \tag{3.27}$$

with K_2 being the modified Bessel function of second kind of order two [94]. Assuming the Boltzmann statistics, holding for non-relativistic dark matter particles, the previous formula can be rewritten as

$$\sum_{ij} \langle \sigma_{ij} v_{ij} \rangle n_i^{\mathrm{eq}} n_j^{\mathrm{eq}} = \sum_{ij} \int W_{ij} g_i g_j e^{-\frac{E_i}{T}} e^{-\frac{E_j}{T}} \frac{\mathrm{d}^3 p_i}{(2\pi)^3 2E_i} \frac{\mathrm{d}^3 p_j}{(2\pi)^3 2E_j}, \tag{3.28}$$

with the annihilation rate per unit volume $W_{ij} = 4E_iE_j\sigma_{ij}v_{ij}$. Performing the first integration and reformulating the expression, we derive

$$\sum\langle\sigma_{ij}v_{ij}\rangle n_i^{\mathrm{eq}}n_j^{\mathrm{eq}} = \frac{T}{32\pi^4}\sum_{ij}\int_{(m_i+m_j)^2}^{\infty}\mathrm{d}s g_i g_j p_{ij} W_{ij} K_1\left(\frac{\sqrt{s}}{T}\right), \tag{3.29}$$

p_{ij} stands for the momentum of the particle χ_i (or χ_j) in the center-of-mass frame of the pair $\chi_i\chi_j$. The effective annihilation rate W_{eff} is defined as

$$\sum_{ij} g_i g_j p_{ij} W_{ij} = g_\chi^2 p_{\mathrm{eff}} W_{\mathrm{eff}} \tag{3.30}$$

further using the definition of

$$p_{\mathrm{eff}} = p_{11} = \frac{1}{2}\sqrt{s-4m_1^2}. \tag{3.31}$$

To sum it up, we end with

$$\sum\langle\sigma_{ij}v_{ij}\rangle n_i^{\mathrm{eq}}n_j^{\mathrm{eq}} = \frac{g_\chi^2 T}{4\pi^2}\int_o^{\infty}\mathrm{d}p_{\mathrm{eff}}p_{\mathrm{eff}}^2 W_{\mathrm{eff}} K_1\left(\frac{\sqrt{s}}{T}\right). \tag{3.32}$$

Finally the thermal average of the cross section times velocity can be written as

$$\langle\sigma_{eff}v\rangle = \frac{\int_0^\infty \mathrm{d}p_{\mathrm{eff}}p_{\mathrm{eff}}^2 W_{\mathrm{eff}} K_1\left(\frac{\sqrt{s}}{T}\right)}{m_\chi^4 T\left[\sum_i \frac{g_i}{g_\chi}\frac{m_i^2}{m_\chi^2}K_2\left(\frac{m_i}{T}\right)\right]^2}, \tag{3.33}$$

where annihilation and coannihilation processes are considered.

3.5.4. Computation of the Relic Density

In the following, only identical particles are considered to illustrate the schematic calculation. The expansion of the Universe corresponds to the ratio of the number of particles to the entropy $Y = \frac{n}{s}$, where s is the total entropy density of the Universe to implicitly treat the decrease in density. The total entropy per comoving frame is given by $S = R^3 s$. This value is constant as long as there is no change in entropy. Dividing (3.25) by S, results in

$$\dot{Y} = -s < \sigma v_{\mathrm{Møl}} > (Y^2 - Y_{\mathrm{eq}}^2). \tag{3.34}$$

Y_{eq} is the equilibrium abundance determined by

$$Y_{\mathrm{eq}} = \frac{45gx^2K_2(x)}{4\pi^4 h_{\mathrm{eff}}(\frac{m}{x})}. \tag{3.35}$$

The degrees of freedom of the initial particles is given by g and h_{eff} denotes the effective degrees of freedom for the entropy. The scale factor R is a time variable, such that

$$\frac{\mathrm{d}Y}{\mathrm{d}R} = \frac{s < \sigma v_{\text{Møl}} >}{RH}(Y^2 - Y_{\text{eq}}^2). \tag{3.36}$$

$H = (\frac{8}{3}\pi G\rho)^{\frac{1}{2}}$ is the Hubble parameter, G the gravitational constant and ρ the total energy density. Rewriting (3.36) in terms of the parameter $x = \frac{T}{m}$, results in

$$\frac{\mathrm{d}Y}{\mathrm{d}x} = \frac{1}{3H}\frac{\mathrm{d}s}{\mathrm{d}x} < \sigma v_{\text{Møl}} > (Y^2 - Y_{\text{eq}}^2), \tag{3.37}$$

with T being the photon temperature. In the following step the effective degrees of freedom for the energy g_{eff} and the entropy h_{eff} density are introduced

$$\rho = g_{\text{eff}}(T)\frac{\pi^2}{30}T^4, \qquad s = h_{\text{eff}}(T)\frac{2\pi^2}{45}T^3. \tag{3.38}$$

For relativistic particles with only one internal degree of freedom, the effective degrees of freedom for the energy and the entropy equal one $g_{\text{eff}}(T) = h_{\text{eff}} = 1$. Using Eq. (3.38) in (3.37), the final result for the Boltzmann equation reads

$$\frac{dY}{dx} = -\sqrt{\frac{\pi}{45G}}\frac{g^{*\frac{1}{2}}m}{x^2} < \sigma v_{\text{Møl}} > (Y^2 - Y_{\text{eq}}^2). \tag{3.39}$$

The content of the Universe is given by the degrees of freedom parameter

$$g^{*\frac{1}{2}} = \frac{h_{\text{eff}}}{g_{\text{eff}}^{\frac{1}{2}}}\left(1 + \frac{1}{3}\frac{T}{h_{\text{eff}}}\frac{dh_{\text{eff}}}{dT}\right). \tag{3.40}$$

As long as the statistical and mechanical factors are negligible, Eq. (3.39) is valid. The annihilation products are in thermal equilibrium, the considered species remain in kinematic equilibrium after decoupling and the initial chemical potential of the species is negligible.

4 Influence of External Components in the Vicinity of a PMT on Its Electric Field

The previously mentioned experiment IceCube [95] also researches in the direction of dark matter, but its main focus is on the detection of high energy cosmic neutrinos, where the data can be analyzed in regard to dark matter. Since neutrinos only interact weakly they are not directly detectable. IceCube uses the ice at the South Pole as a large medium for interactions with cosmic neutrinos. If such an interaction takes place, charged particles are formed, which in turn emit Cherenkov light. The detection of this light not only identifies the neutrino, but also allows analyses to be carried out with regard to the origin, direction and energy of the neutrino.

The existing detector of IceCube will now be upgraded [96], where additional strings, equipped with optical modules featuring an array of several small photomultiplieres, so-called multi-PMT digital optical modules (mDOMs), for the detection of the Cherenkov light, will be added to the inner core of the detector. The Hamamatsu R12199-01 HA MOD photomultiplier tube will be the baseline PMT for this extension. An important aspect for this PMT is a low background rate, since in the deep ice at the South Pole only negligible optical noise reaches the PMT. Since the PMT is contained in the mDOM, several other components are located near the PMT. For this the influence of external components on the electric field in the PMT has to be taken into account, such as a shielding of the dynode structure by the so-called HA-coating and reflectors near photocathodes.

In the following, an introduction to basic functionality, operation principles and in particular noise mechanisms of the photomultiplier tube is given. Furthermore the influence of external components in the vicinity of the PMT on its electric field will be investigated using finite element simulations. This simulation contributed to publication

[97].

4.1. Photomultiplier Tubes

Photomultiplier tubes (PMT) [98, 99] are devices that convert photons into measurable electrical signals. Due to their high sensitivity, it is possible to detect signals from individual photons.

Figure 4.1 sketches such a PMT. When a photon hits the photocathode, an electron is released from the thin photocathode layer by the photoelectric effect.Inside the glass there is a vacuum so that the electron can move freely. These photoelectrons are accelerated to the electron multiplier by an applied electrical potential. The electron multiplier consists of an arrangement of several electrodes (dynodes). When the electron hits the first dynode, secondary electrons are released. Due to the electrical potential differences between the dynodes, the electrons are further accelerated to the second dynode. Secondary electrons are also released here. This process is repeated until the electrons hit the anode. An output signal is generated. The signal is amplified by the generation of secondary electrons.

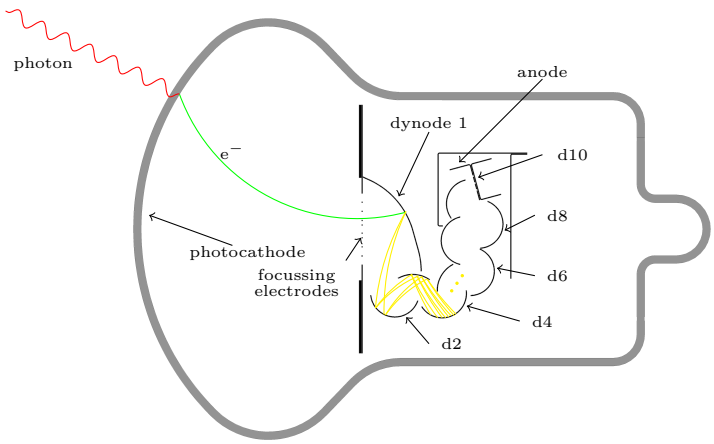

Figure 4.1.: Schematic representation of a photomultiplier tube. The photon (red) hits the surface of the photocathode and an electron (green) is released. The electron is accelerated towards the first dynode. On impact, secondary electrons (yellow) are released, which are accelerated to the next dynode and release further electrons. Due to the dynode structure, the signal is amplified by the multiplication of the electrons. At the end, the electrons reach the anode that outputs the signal.

There are two possibilities to convert the incoming electrons at the anode into a signal. A distinction is made between a current signal and a voltage signal. With a current signal the incoming charge signals of the PMT are integrated in a certain period of time with a current value as result. This mode is called current or analog mode. This mode is used when the PMT is permanently exposed to a light source or when the time information of individual signals is not needed. In pulse or photon counting mode, the output is connected to a resistor, resulting in voltage pulses. These can be read-out with an oscilloscope. This way individual pulses can be analyzed and maximum information about the photon flux can be obtained. This mode is advantageous by low light intensities.

Even in complete darkness, the PMT delivers a measurable signal. This so-called dark rate (or dark current in analog mode) has different origins. In the following the possible sources for dark rates are briefly discussed. We start with the thermal noise, which is caused by the spontaneous emission of electrons. These enter the dynode system and are amplified like a photoelectron. The spontaneous emission is strongly temperature dependent. This main source of dark rates can be suppressed by cooling. Field emission is the emission of electrons induced by the electric field by the voltages applied to the dynodes. Leakage current refers to the constant flow of charge through materials that are not perfectly insulated. Other sources can also be emissions from isotopes within the PMT, as well as cosmic rays.

There are also noise pulses that originate from the signal itself. Late pulses are pulses that are measured nanoseconds after the actual signal, e.g. resulting from the backscattering of the photoelectron at the first dynode. Photons can also be emitted from the last dynode or anode, which can begin to scintillate under strong electron bombardment.

Afterpulses are signals that are measured a few microseconds after the actual signal. These can be triggered by photoelectrons, which ionize the remaining gas in the PMT on their way to the first dynode.

Finally, photons can also pass through the photocathode without being absorbed. These generate electrons not until the first dynode. Since one dynode is missing during amplification, the signal is correspondingly smaller than a typical signal of a correctly measured photon.

4.2. Simulation

PMTs operated at negative high voltage have a higher dark rate due to the influence of external electric fields [100]. It is necessary to avoid conductive objects such as reflectors near the PMT, especially if they are additionally grounded. A common method to reduce these influences is to use a conductive coating around the PMT connected to the photocathode potential of the PMT. Another approach investigated in [101] is the coating of PMT with insulating varnish, which prevents possible discharges between sur-

rounding objects and the tube. However, such a coating does not protect the particularly sensitive photocathode [100].

For a realistic simulation of the influence of electric potentials close to the PMT, a realistic model of the PMT is required. A non-functional PMT was removed from its glass shell and modeled with Autodesk Inventor® [102] in realistic dimensions including all components. Fig. 4.2 shows the photo of the PMT (top left), the corresponding complete model (bottom) and the model in the same view as in the photo (top right). The effects of electrical potentials in the vicinity of the PMT were simulated using COMSOL Multiphysics® [103].

Fig. 4.3 on the bottom left shows the cut plane of the PMT, depicting the field of interest for the simulation of the influence of the reflector (blue box) and the HA-coating (red box). Corresponding to a cathode-anode voltage of -1300 V, the electric potential was assigned to each component of the PMT.

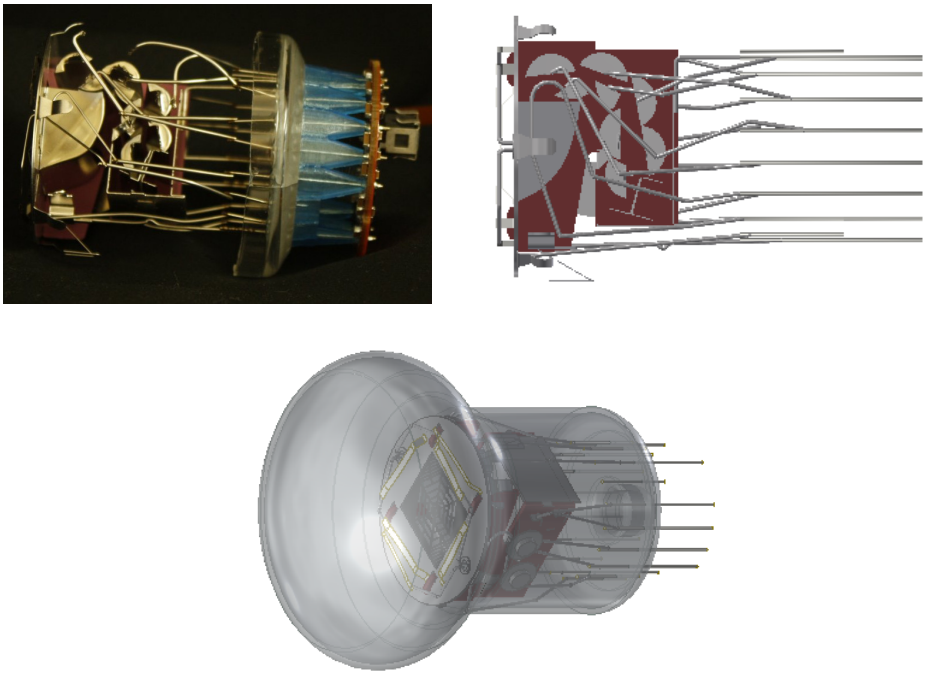

Figure 4.2.: Top left: Photo of a PMT without the glass and the ceramic plate on one side. Top right: The model of the PMT with almost the same view as on the left photo. Bottom: View of the complete model of the PMT.

The photoelectrons and secondary electrons can be disturbed by external fields on their way through the dynode system. These can be caused by grounded conductive materials in the vicinity of the PMT. If electrons are deflected in such a way that they hit the glass envelope of the PMT, scintillation light is emitted which can reach the photocathode, leading to increased dark rates of the PMT [101].

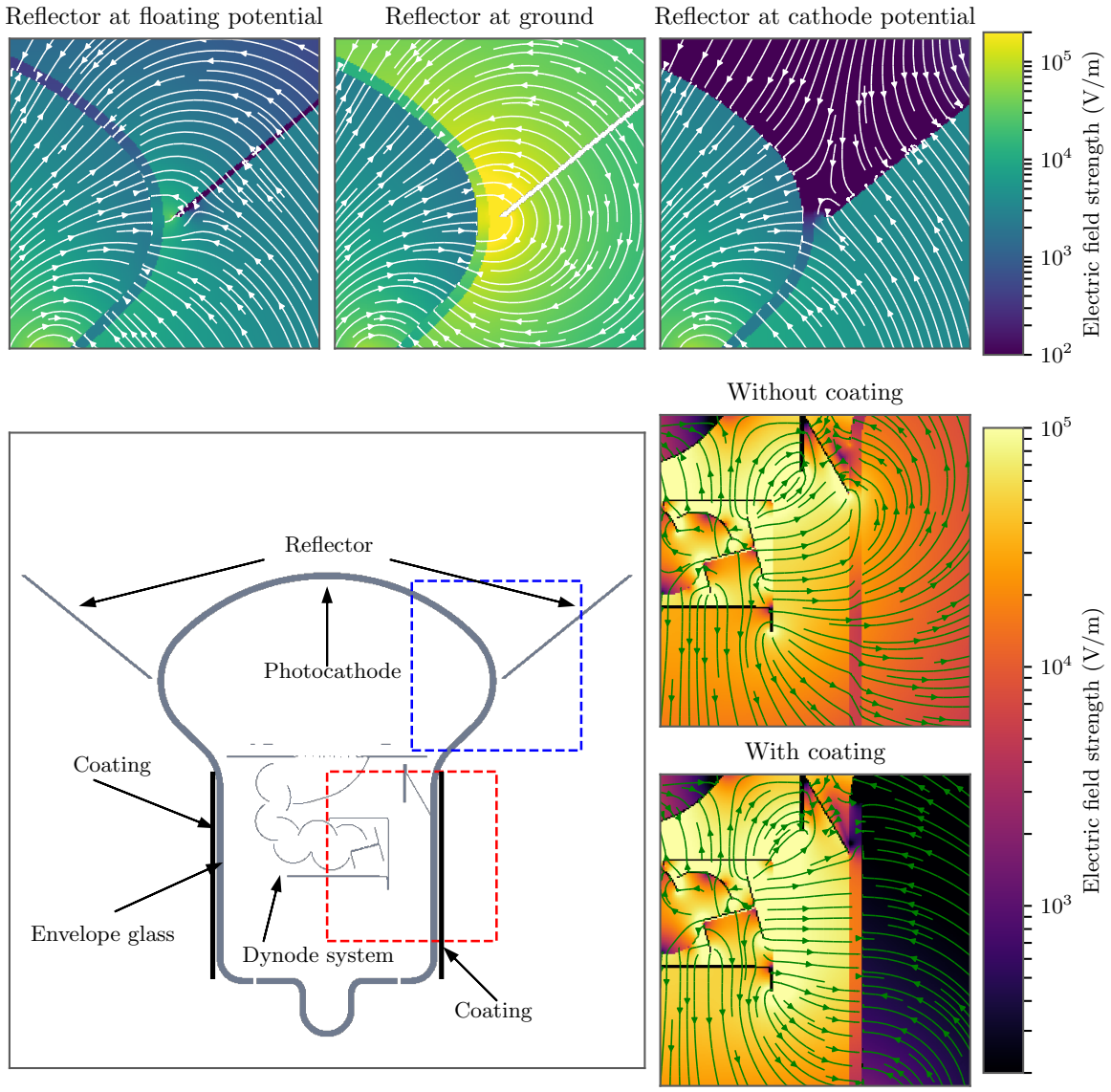

Figure 4.3.: Buttom left: Cut plane through the simulated geometry of the PMT. The blue dashed square indicates the region of the diagrams in the top and the red square depicts the region of the two diagrams in the lower right. The coating thickness has been increased for visibility. Top: Finite-element simulation of the electric field around the PMT window with the reflector on floating potential (left), ground (center) and photocathode potential (right). Bottom right: Electric field around the envelope of the tube with and without coating at photocathode potential. The color scale indicates the electric field strength in V/m and the arrows indicate the direction of the field in the plane.

In the following we investigate the effect of shielding around the PMT tube with an inner conductive layer placed on the potential of the photocathode. This is coated with an insulating layer. Figure 4.3 (bottom left) shows this layer, labeled as coating. On the right side, in the lower two diagrams the resulting electric field is shown near the dynode system with and without coating. The coating increases the electric field between the dynode system and the glass by approximately 80%. By increasing the electric field, a repulsive field prevents electrons from escaping the dynode system and impacting the glass, resulting in a reduction of the background rate. Likewise, the dynode system is shielded from external fields.

To increase the effective area of a PMT, aluminium reflectors are used (such as in KM3NET [104], MAGIC [105], H.E.S.S [106]). The reflectors are located directly at the window of the PMT, near the photocathode, where there is no possibility to shield the PMT from external fields. However, since these reflectors are conductive, they can have a significant influence on the electric field.

Investigating the electric field in vicinity of the photocathode is a crucial aspect, as the electric field acts on the band structure in the semiconductor and leads to the emission of electrons In Fig. 4.3, top row, we show the resulting electric fields for three different configurations of the reflector in the region of the red box (bottom left). From the left, the reflector is set to floating potential. In the glass of the PMT there is a strong electric field that has a maximum of 4.6 kV/m at the point where the reflector is closest to the glass (∼1 mm distance). If the reflector is grounded (center diagram) the electric field strength increases dramatically up to 0.14 MV/m. Both configurations also feature high electric fields in regions further away from the reflector. At the center of the photocathode, the surface of the glass still has values of 12 kV/m (ground) and 0.4 kV/m (floating).

If the reflector is set to the potential of the photocathode (right), the electric field in the glass varies only between ∼5 V/m and ∼25 V/m, which would be the preferred use.

All in all, this analysis provided a deeper understanding of the noise mechanism and what kind of counter measurements can reduce those.

5 DM@NLO

Dark Matter at next-to-leading order (DM@NLO) is a tool that provides predictions for the relic density of dark matter in MSSM models including higher order QCD corrections. There are other existing public tools for the calculation of the relic density, like micrOMEGAs [107] and DarkSUSY [108].

Björn Herrmann, Michael Klasen and Karol Kovařík have created DM@NLO 2006. Since then, the tool has been constantly developed further. In the following we give an overview on the current status of DM@NLO, in addition the tool chain of DM@NLO with the interface to micrOMEGAs is explained.

5.1. Status of DM@NLO

Over the years, many new processes have been implemented in DM@NLO that contribute to the annihilation cross section for the calculation of relic density. Figure 5.1 gives a schematic overview of already implemented and analyzed processes, ongoing work and future projects.

The first diagram shows the first implemented process, the annihilation of the lightest neutralinos into heavy quark final states. In the first publication [109] the focus was on the Higgs funnel. This was the dominant process in regions of minimal supergravity (mSUGRA)[1] parameter space at large $\tan\beta$, which was theoretically favored at that time by the unification of the Yukawa couplings in the GUT. The analysis showed a strong influence of the corrections on the extraction of SUSY mass parameters from cosmological data.

In 2009, the same process was additionally analyzed with respect to the full QCD and SUSY-QCD corrections [110]. Omitting the fact that the light quark final states do not lead to significant contributions in the analyzed mSUGRA, only heavy quark anti-quark final states were considered. Again, there was a significant influence on the annihilation cross section and further on the extraction of SUSY mass parameters from

[1] The number of free parameters in MSSM is reduced to $(m_0,\ A_0, m_{1/2},\ \tan\beta,\ \mathrm{sgn}(\mu))$ with the additional constrains $b_0 = A_0 m_0$, $m_{3/2} = m_0$. Meanwhile, mSUGRA is largely excluded as a viable SUSY model.

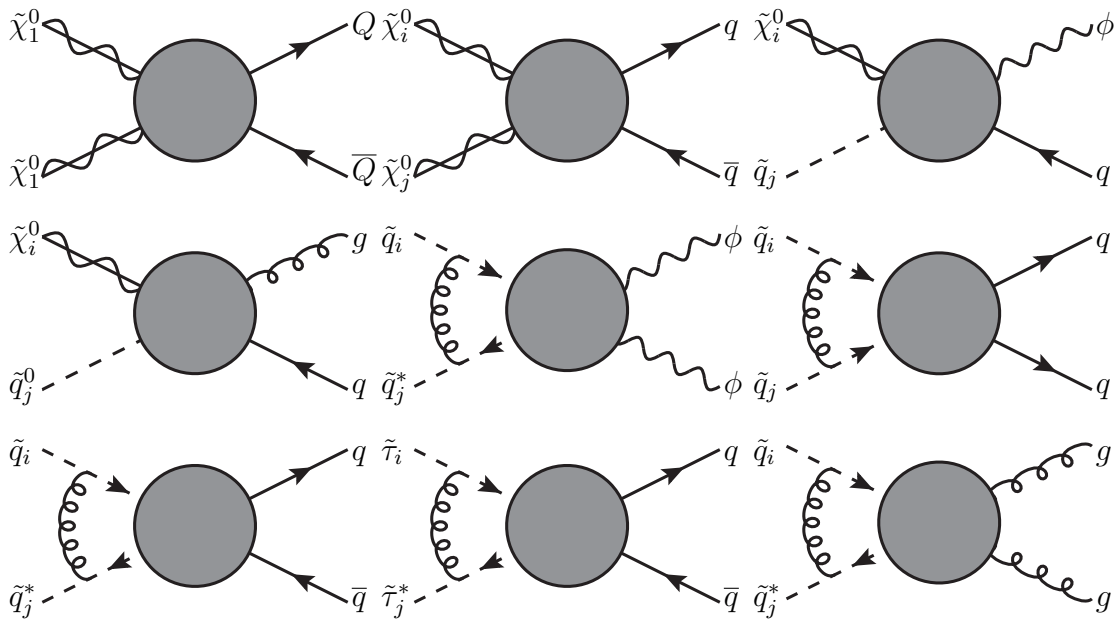

Figure 5.1.: Schematic overview of included processes and future processes of DM@NLO, with $\phi = H, V$. The grey circle symbolizes the $\mathcal{O}\alpha_S$ SUSY-QCD corrections, while the gluon lines between the particles indicate included Sommerfeld enhancement effects. The focus on this work lies on the processes $\tilde{q}_i\tilde{q}_j \to qq$ and $\tilde{q}_i\tilde{q}_j^* \to q\overline{q}$.

cosmological data. The observed differences were in the same order of magnitude as the experimental error from cosmological precision measurements. In a further step, scenarios without scalar and gaugino mass unification were analyzed [111, 112] with an effect on the annihilation cross section of 20 to 50% and a shift between 5 GeV to 50 GeV for the extracted SUSY mass parameters.

Within 2014, the previously discussed process was expanded so that all gaugino's annihilations and co-annihilations into heavy and light quark-anti-quark final states were considered [113]. The analysis was not based on mSUGRA, like the previous ones, but focused on the pMSSM, Section 2.3.2. Three reference scenarios with a variety of annihilation and co-annihilation channels for gauginos were investigated. The resulting neutralino relic density was shifted by up to 10% relative to the tree level. In particular, these shifts are greater than Planck's experimental uncertainty.

The co-annihilation of gauginos with squarks was published in 2012 [114, 115] with a focus on the full $\mathcal{O}(\alpha_S)$ SUSY-QCD corrections for neutralino-stop co-annihilation in quark and electroweak vector or Higgs boson final states. The analysis was performed on scenarios within the pMSSM considering the limits of the WMAP relic density data. The one-loop corrections had an influence on the annihilation cross section of about 30%,

the relic density received an influence of about 9%. Only two years later the extension of co-annihilation into top quark-gluon final state was published [116]. By corrections to 80% of the contributing processes in the example scenario, a relative correction to the default micrOMEGAs relic density of about 20% was achieved, leading to a significant shift of the 2σ relic density band of the experimental Planck value.

Since stop annihilation also has non-neglectable contributions to relic density, the annihilation was implemented in electroweak final states in DM@NLO with almost degenerated masses of stop and lightest neutralino. In 2014, the effect of the full $\mathcal{O}(\alpha_S)$ SUSY-QCD corrections of stop-antistop annihilation was published [117], including additionally the coulomb corrections by gluon exchange between incoming stops. Substantial corrections were identified in three reference scenarios.

With the annihilation channels discussed in the meantime a study on the theoretical uncertainty of the supersymmetric relic density of dark matter from scheme and scale variation was carried out by DM@NLO [118]. To illustrate the effects of the higher order SUSY-QCD corrections and their scale uncertainties, three different scenarios were examined. The theoretical uncertainties have been reduced in many cases and can be compared with the size of the experimental ones in some scenarios.

Now we come to a process considered in this thesis [119] a precision analysis of the annihilation of squark pairs in quark end states is performed with full $\mathcal{O}(\alpha_S)$ SUSY-QCD corrections, including Sommerfeld enhancement effects. Details of the calculation are described in the following chapters. The numerical results are discussed in detail in the Chap. 11.

In addition, the processes that take into account the annihilation and co-annihilation of squark-anti-squark in quark-anti-quark final states will be investigated. The current status is given in the Chap. 11 showing preliminary results for the end states top-anti-top and top-anti-bottom. Open questions corresponding to the bottom-anti-bottom-final state are also discussed.

To complete the most relevant squark-annihilations that contribute to the annihilation cross section, squark-anti-squark annihilation into gluon final state should be considered as a next step. Furthermore the annihilation of gluinos and co-annihilation of gluinos with scalar top quarks are interesting processes within scenarios, where the gluino or both stop and gluino are almost mass degenerated to the neutralino.

Another part of DM@NLO is the implementation of SUSY-QCD corrections for the direct detection of neutralino dark matter in 2016 [120, 121]. A complete NLO-QCD calculation of neutralino scattering on protons or neutrons in the MSSM was performed. By adapting the results of the NLO-QCD calculation to the scalar and axial vector operators in the effective field theory approach, predictions could be made about the spin-independent and spin-dependent detection rates. The NLO-QCD effects are proven to be at least equal and sometimes greater than the currently estimated nuclear uncertainties.

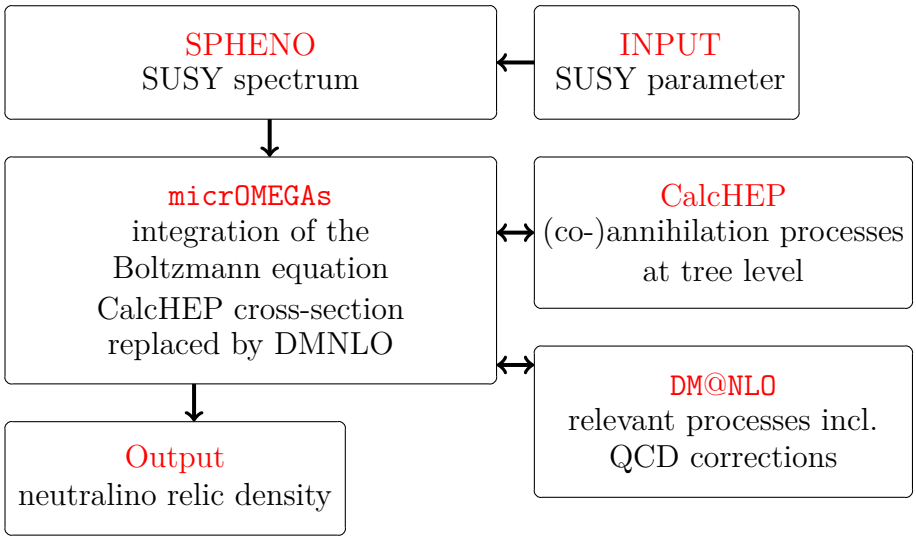

Figure 5.2.: Visualization of the software chain with an interface of DM@NLO to micrOMEGAs for the calculation of the dark matter relic density.

5.2. Structure of the Tool

DM@NLO is a FORTRAN-based code that provides the (co-)annihilation cross section including NLO SUSY-QCD corrections within the MSSM of previously discussed processes relevant to the calculation of the relic density of dark matter.

A schematic overview of the relic density calculation involving DM@NLO is given in figure 5.2. DM@NLO is a program, providing the annihilation cross section within next-to-leading order calculations. For the determination of the relic density, DM@NLO is linked through an interface to micrOMEGAs, which solves the Boltzmann equation. Processes, which are not yet implemented in DM@NLO are provided by the internal version of CalcHEP within micrOMEGAs. CalcHEP includes the calcualtion of the annihilation cross section at leading order containing effective couplings[2] in special cases. As Input the SUSY spectrum is needed, which is taken from a spectrum file in SUSY Les Houches Accord 2 [122]. In our case the scenario is defined through the 19 free parameters of the pMSSM at a scale Q_{SUSY}. These 19 parameter and the scale are used as the input for the spectrum calculator SPheno [123, 124], which determines the spectrum and hands it over to micrOMEGAs in SUSY Les Houches Accord 2.

A further interface to DarkSUSY is currently under development.

A schematic overview of the calculation of the relic density with DM@NLO is shown in the figure 5.2. DM@NLO is a program that provides the annihilation cross section within the next leading order calculations. To determine the relic density, DM@NLO is linked to micrOMEGAs via an interface. micrOMEGAs determines the solution of the Boltzmann

[2]Effective couplings only contains part of NLO calculations and do not feature full NLO result.

equation. Processes not yet implemented in DM@NLO are provided by the internal version of CalcHEP within micrOMEGAs˙CalcHEP contains the calculation of the annihilation cross section in leading order with effective couplings[3]. As input the SUSY spectrum is needed, which is taken from a spectrum file in SUSY Les Houches Accord 2 [122]. In our case, the scenario is defined by the 19 free parameters of the pMSSM on a Q_{SUSY} scale. These 19 parameters and the scale are used as input for the spectral calculator SPheno [123, 124], which determines the spectrum and passes it on to micrOMEGAs in SUSY Les Houches Accord 2.

Another interface to DarkSUSY is currently under development.

[3]Effective couplings contain only a part of the NLO calculations and does not contain the full NLO results.

6 Squark Annihilation into Quark Final States

The analysis presented in this thesis focuses on the contribution of squark-pair and squark-anti-squark annihilations to the total annihilation cross section σ_{ann} of neutralino dark matter. Scenarios are investigated in the pMSSM in which the processes

$$\tilde{t}_1\tilde{t}_1 \to tt, \qquad \tilde{b}_1\tilde{b}_1 \to bb, \qquad \tilde{t}_1\tilde{b}_1 \to tb, \tag{6.1}$$

$$\tilde{t}_1\tilde{t}_1^* \to t\bar{t}, \qquad \tilde{t}_1\tilde{t}_1^* \to b\bar{b}, \qquad \tilde{t}_1\tilde{b}_1^* \to t\bar{b}, \tag{6.2}$$

are important for the determination of the relic density. As already mentioned, the annihilation and co-annihilation of the NLSP can make a dominant contribution to the annihilation cross section entering the relic density calculation. To illustrate the relevance of both annihilations, a set of parameter points was generated, with the lightest neutralino as the LSP and the lightest top squark as the NLSP. The other parameters are chosen so that other particles do not contribute to the annihilation cross section.

The contribution of annihilation $\tilde{\chi}_1^0\tilde{\chi}_1^0 \to t\bar{t}$, $\tilde{t}_1\tilde{t}_1 \to tt$, $\tilde{t}_1\tilde{t}_1^* \to t\bar{t}$ and co-annihilation $\tilde{\chi}_1^0\tilde{t} \to tg$ to the total cross section depending on the mass difference between the stop and the neutralino is shown in Fig. 6.1. ΔM is defined as the ratio between the mass difference of the stop and neutralino mass in respect to the neutralino mass

$$\Delta M = \frac{m_{\tilde{t}_1} - m_{\tilde{\chi}_1^0}}{m_{\tilde{\chi}_1^0}} \,. \tag{6.3}$$

This variable is motivated by the Boltzmann factor Eq. (3.26)

$$\frac{n_i^{\text{eq}}}{n_j^{\text{eq}}} = \exp\left(-\frac{m_i - m_\chi}{T}\right) = \exp\left(-\frac{m_i - m_\chi}{m_\chi x}\right) \tag{6.4}$$

that contributes to the annihilation cross section. The importance of the cross section of the NLSP depends on ΔM entering through (6.4)

$$\langle \sigma v \rangle = \sum_{ij} \langle \sigma_{ij} v_{ij} \rangle \frac{n_i^{\text{eq}}}{n_\chi^{\text{eq}}} \frac{n_j^{\text{eq}}}{n_\chi^{\text{eq}}} \,. \tag{6.5}$$

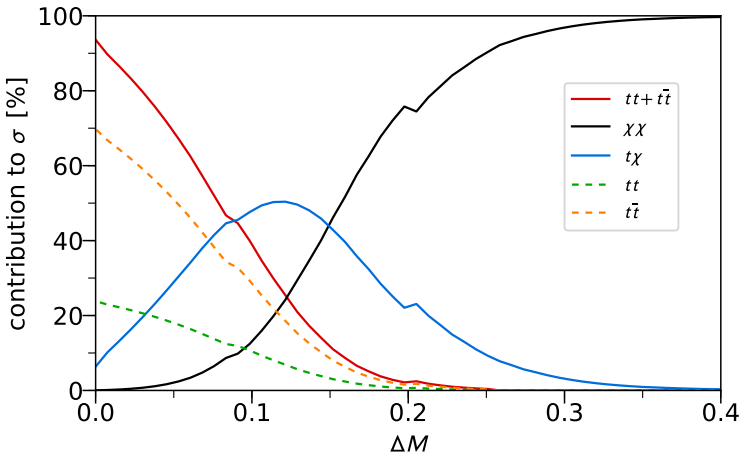

Figure 6.1.: Contribution of stop (red), neutralino (black) annihilation and neutralino stop co-annihilation (blue) to the annihilation cross section σ as a function of $\Delta M = \frac{m_{\tilde{t}_1} - m_{\tilde{\chi}_1^0}}{m_{\tilde{\chi}_1^0}}$. The dashed lines show the $\tilde{t}_1\,\tilde{t}_1$ (green) and $\tilde{t}_1\,\tilde{t}_1^*$ (orange) contribution of the stop annihilation.

The black solid line shows the contribution of pure neutralino annihilation, which increases with increasing mass differences. When the stop mass is about 1.4 times the neutralino mass, 100 % of the annihilation cross section depends on the neutralino annihilation. With decreasing mass difference the stop annihilation (red solid line) is the most important process, which reaches more than 90 % for equal mass of stop and neutralino. This contribution can be divided into stop-anti-stop (orange dotted line) and stop-stop annihilation (green dotted line). The co-annihilation of neutralino and stop has a non vanishing contribution at $\Delta M = 0$. The co-annihilation contribution increases for higher ΔM with a maximum at $\Delta M \approx 0.12$, the point, where the stop and neutralino contribution lines cross. From there the contribution decreases until it vanishes.

Summarizing, for ΔM in the range of 0 and 0.08, the stop annihilation is the leading contribution, by $\Delta M \approx 0.08$ until 0.15 the co-annihilation leads, then the neutralino annihilation is the leading contribution. At $\Delta M \approx 0.25$ the stop annihilation no longer contributes to the relic density calculation.

In order to consider the most important experimental constrains on the pMSSM, the previously discussed results of the ATLAS analysis, Sec. 2.5.1, were used to find suitable scenarios in the parameter space. The analysis of ATLAS contained 5×10^8 parameter points, after the applied constraints from various searches of ATLAS and other experiments survived a subset of about 300,000 viable scenario points.

The subset of points is shown in Fig. 6.2 in the $m_{\tilde{\chi}_1^0} - m_{\tilde{t}_1}$ plane. The diagram distinguishes the type of neutrinos within the color code. Most ATLAS points contain

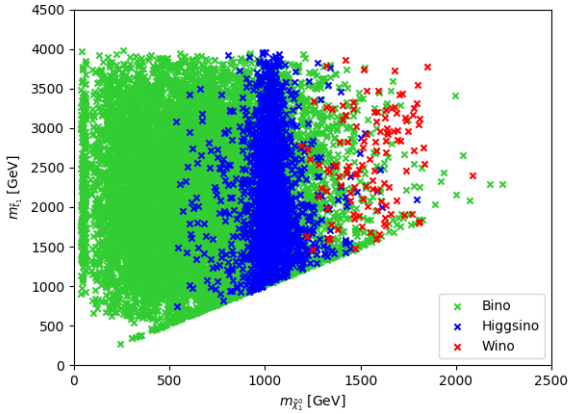

Figure 6.2.: ATLAS points with higgsino-like (blue), bino-like (green) and wino-like (red) lightest neutralino in the $m_{\chi_1^0} - m_{t_1}$ plane.

a bino-like neutralino (green). Higgsino-like neutralinos (blue) are centered around the neutralino mass $\sim 1000\,\text{GeV}$. Wino-like neutralinos (red dots) are rare. At in the range of almost generated masses, several scenario points are viable.

In the following, we will take a closer look at the viable points to examine the regions of the parameter space in which the processes (6.1),(6.2) contribute significantly. As already discussed, the mass of the particle must be almost mass degenerate to the LSP mass in order to contribute to the annihilation cross section. For the third squark it is not an unnatural requirement. To explain the Higgs boson of the Standard Model within the MSSM, a light scalar top squark is required. In addition, mass degeneration makes the testing in colliders more difficult due to different topologies, making their exclusion less likely.

Moreover most of the viable points are bino-like, see Fig. 6.2. Whereas higgsino-like and wino-like lightest neutralinos most likely lead to scenarios with other gauginos as the NLSP, bino-like lightest neutralinos need an enhancement mechanism to be consistent with the relic density (3.9). The pure annihilation of the LSP is not efficient enough. Such kind of enhancement is provided by the LSP-NLSP co-annihilation and NLSP annihilation.

Fig. 6.3 shows the number of scenarios for the corresponding contribution percentages for the processes (6.1) and (6.2). Contributions below 1% were neglected. First it is to mentioned that most of the scenarios relevant here contain a bino-like lightest neutralino as the LSP.

The first figure shows the contributions of stop annihilation to a top pair. This process contributes up to 30% to the cross section. Altogether the process contributes to about 490 scenarios of the ATLAS points. Most scenarios receive a contribution of up to 10%, 60 scenarios even receive a contribution of more than 10% and up to 15%. 6 scenarios

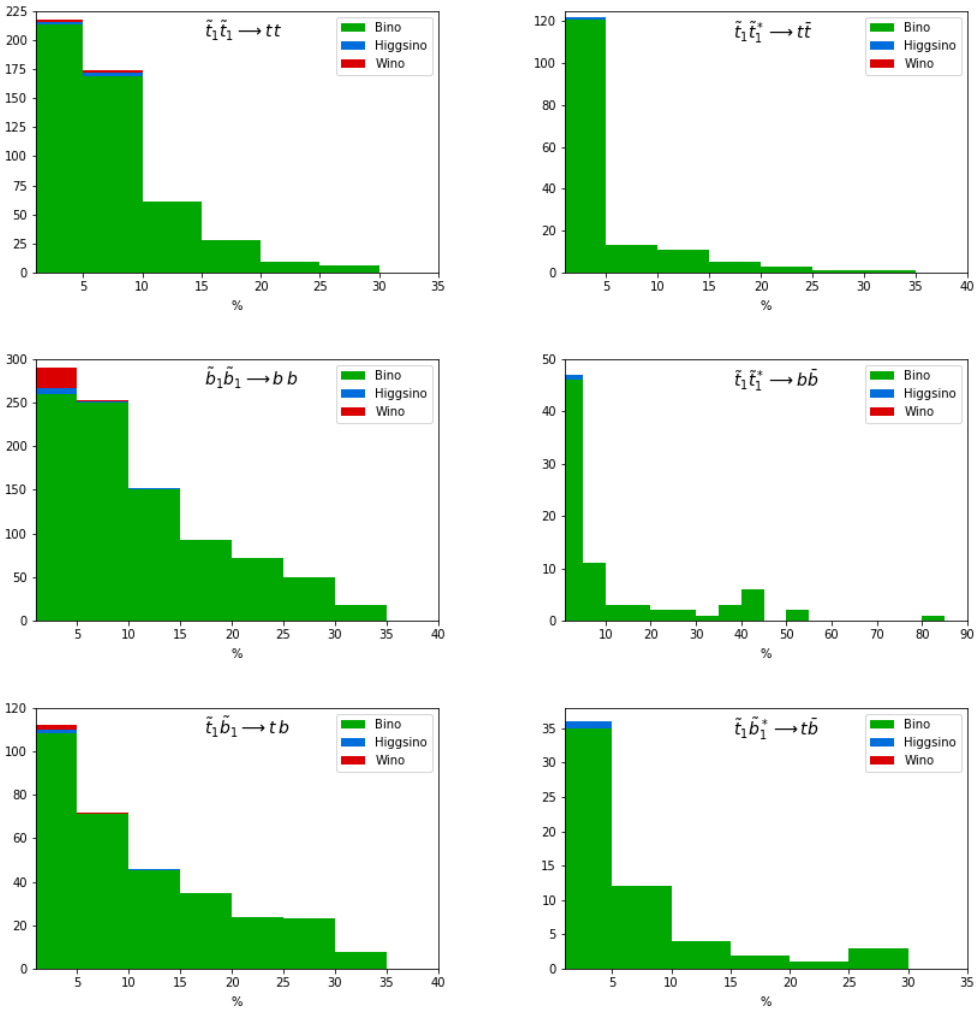

Figure 6.3.: Relevant contributions of $\tilde{q}\tilde{q} \to qq$ and $\tilde{q}\tilde{q}^* \to q\bar{q}$ to the relic density of the ATLAS points. First: $\tilde{t}_1\tilde{t}_1 \to tt$, second: $\tilde{t}_1\tilde{t}_1^* \to t\,\bar{t}$, third: $\tilde{b}_1\tilde{b}_1 \to bb$, fourth: $\tilde{t}_1\tilde{t}_1^* \to b\,\bar{b}$, fifth: $\tilde{t}_1\tilde{b}_1 \to tb$, sixth: $\tilde{t}_1\tilde{b}_1^* \to t\,\bar{b}$

actually receive a contribution of up to 30%.

The next figure illustrate the contributions of stop-anti-stop annihilation to top-anti-top final states. This process contributes to about 150 scenarios. Contributions of up to 30% are possible. In most scenarios the process contributes up to 5% to the annihilation cross section.

With contributions to nearly 900 scenarios, the sbottom annihilation is the most strongly represented process. Contributions of up to 35% still occur in 18 scenarios. Almost half of the points get contributions of over 10% from this process.

The stop-anti-stop annihilation has an interesting scenario, where in one scenario point the process contributes more than 80% to the cross section. In total, the process contributes to about 80 scenarios.

The last line of the figure shows the stop-sbottom and stop-anti-sbottom contributions. While stop-sbottom co-annihilation is relevant for about 320 scenarios, stop-anti-sbottom has about 60 scenarios influenced by the process.

In summary, it can be said that there are a large number of viable scenarios to which the considered processes give large contributions. It is expected that the NLO corrections of these processes will make an important contribution to the calculation of the relic density.

6.1. Reference Scenarios

The numerical part of the presented study will be based on three reference scenarios following the study by ATLAS [1]. Three pMSSM scenarios were chosen, the relevant soft-breaking parameters and particle masses are listed in Tab. 6.1. It is to mention, even by taking identical input soft mass parameters, the resulting physical masses slightly differ to those in the ATLAS study. This results from a different computational setup, used here. Despite the small changes in the physical masses, all experimental constrains are still satisfied and the phenomenology is not altered.

The scenarios feature bino-like neutralinos as the lightest sparticle. This results from the bino mass parameter M_1, which is smaller than the wino and higgsino mass parameter M_2 and $|\mu|$. The masses of the third-generation squarks are depending on the "left-handed" stop and sbottom mass parameter $M_{\tilde{q}_L}$ and the "right-handed" ones $M_{\tilde{t}_R}$ and $M_{\tilde{b}_R}$. The squarks of the first and second generation, the sleptons, and other electroweak gauginos are heavier such that they do not influenced the phenomenology discussed here. As discussed in Sec. 5.2 the soft-breaking terms defined at scale Q_{SUSY}, see Tab. 6.1, are handed to the spectrum calculator `SPehno3.3.3` [123, 124] to obtain the physical mass spectrum. The mass spectrum is then given to `micrOMEGAs2.4.1` [107, 125] using the SUSY Les Houches Accord 2 [122]. In addition to the calculation of the relic density, `micrOMEGAs` provides the contribution of all individual channels contributing to σ_{ann} given in Tab. 6.2.

The processes given in Eqs. 6.1 and 6.2 have significant contribution. More precisely,

Scenario	M_1	M_2	M_3	$M_{\tilde{q}_L}$	$M_{\tilde{t}_R}$	$M_{\tilde{b}_R}$
I	1278.5	2093.5	1267.2	2535.1	1258.7	3303.8
II	1629.2	3613.4	1720.8	1513.2	3964.9	3871.5
III	1106.0	2121.4	3790.9	1310.3	2001.94	1473.3

Scenario	A_t	A_b	μ	m_{A^0}	$\tan\beta$	Q_{SUSY}
I	2755.3	2320.9	-3952.6	3624.8	15.5	1784.64
II	-4434.9	2201.7	2615.4	3451.3	53.1	2447.96
III	3307.8	2683.2	2590.7	2451.4	6.0	1615.85

	$m_{\tilde{\chi}_1^0}$	$m_{\tilde{\chi}_2^0}$	$m_{\tilde{\chi}_1^\pm}$	$m_{\tilde{t}_1}$	$m_{\tilde{b}_1}$	$m_{\tilde{g}}$	m_{h^0}	m_{H^0}	$\Omega_{\tilde{\chi}_1^0}h^2$
I	1279.7	2153.6	2153.5	1301.9	2554.2	1495.5	125.8	3625.6	0.12
II	1624.4	2606.6	2606.6	1652.0	1654.9	1944.9	127.8	3451.2	0.12
III	1101.0	2127.8	2128.0	1192.9	1222.9	3680.7	122.9	2450.9	0.12

Table 6.1.: Reference scenarios within the phenomenological MSSM for our numerical study. Note that only the parameters which are relevant for our analysis are given here. All dimensional quantities are given in GeV.

in Scenario I, the annihilation of stop quark pairs is second most important process. With previously analyzed processes, Sec. 5.1 `DM@NLO` can provide 45% of the total annihilation cross section. Around 30% corresponds to the stop pair annihilation, the other 15% came from the stop neutralino co-annihilation. The NLSP is the mostly "right-handed" scalar top $\tilde{t}_1$ with a mass difference of about 20 GeV compared to the LSP. Moreover, the process is enhanced by the relatively low gluino mass $m_{\tilde{g}}$. The bottom squark are heavy, therefore the corresponding annihilation channels are negligible. In Fig. 6.4 the importance of different relevant contributions to the annihilation cross section in and around this scenario is shown. The part of the parameter space, where the neutralino is not the LSP is indicated by the grey region. In this region the stop is lighter than the neutralino and therefore the LSP and would be the dark matter candidate. The shades of green indicates the contribution of the different processes towards the annihilation cross section. The red point gives the location of Scenario I. The first plot shows the complete contribution of `DM@NLO` to the annihilation cross section. The other five figures show the contribution of specific processes of LSP-NLSP co-annihilation and NLSP annihilation. In general the co-annihilation is most important, when the mass splitting between LSP and NLSP is about 150 GeV. The parameter region where the dark matter relic density is within 2σ of the experimental value (3.9) is highlighted in orange. The relic density is computed using `micrOMEGAs`. We see that around Scenario

Contributing processes	Scenario I	Scenario II	Scenario III
$\tilde{t}_1\,\tilde{t}_1 \;\to\; t\,t$	30.5%	8.8%	–
$\tilde{b}_1\,\tilde{b}_1 \;\to\; b\,b$	–	7.4%	–
$\tilde{t}_1\,\tilde{b}_1 \;\to\; t\,b$	–	34.0%	–
$\tilde{t}_1\,\tilde{t}_1^* \;\to\; t\,\bar{t}$	3.1%	–	32.1%
$\tilde{t}_1\,\tilde{t}_1^* \;\to\; b\,\bar{b}$	–	2.4%	9.7%
$\tilde{t}_1\,\tilde{b}_1^* \;\to\; t\,\bar{b}$	–	4.0%	39.6%
$\tilde{\chi}_1^0\,\tilde{\chi}_1^0 \;\to\; q\,\bar{q}$	–	–	–
$\tilde{\chi}_1^0\,\tilde{t}_1 \;\to\; t\,g$	9.3%	–	–
$\tilde{\chi}_1^0\,\tilde{t}_1 \;\to\; q\,V\,, q\,\phi$	5.8%	–	3.0%
$\tilde{\chi}_1^0\,\tilde{b}_1 \;\to\; q\,V\,, q\,\phi$	–	–	1.2%
$\tilde{t}_1\,\tilde{t}_1^* \;\to\; g\,g$	38.7%	9.8%	2.3%
$\tilde{b}_1\,\tilde{b}_1^* \;\to\; g\,g$	–	8.1%	–
$\tilde{q}\,\tilde{q}^* \;\to\; g\,V$	5.6%	19.1%	1.3%
$\tilde{q}\,\tilde{q}^* \;\to\; EW$	–	–	3.9%
$\tilde{\chi}_1^0\,\tilde{g} \;\to\; X$	3%	–	–
$\tilde{g}\,\tilde{g} \;\to\; X$	–	–	–
`DM@NLO` current analysis	30.5%	50.2%	71.7%
`DM@NLO` total [109, 110, 111, 113, 114, 116, 117]	45.6%	50.2%	79.8%

Table 6.2.: Dominant annihilation channels contributing to σ_{ann} and thus to the neutralino relic density in the two reference scenarios given in Tab. 6.1. Here, $V = \gamma, Z^0, W^\pm$, $\phi = h^0, H^0, A^0, H^\pm$ and EW includes all pure electroweak final states including $VV, \phi\phi, \phi V, l\bar{l}$ and $\nu_l\bar{l}$. Further contributions below 1% are omitted.

I, the line for the relic density lies in the region with dominant contribution of stop annihilation. For lighter neutralino and stop masses as in the reference Scenario I the same processes contribute to the annihilation cross section. For higher masses, new processes occur. We reach a point, where the LSP and NLSP are of the same mass as the light gluino ($m_{\tilde{g}} = 1495.5\,\text{GeV}$). In these parameter space, three particles are almost mass degenerated and gluino annihilation and gluino-stop co-annihilation dominate the total annihilation cross section.

We have a slightly different situation in Scenario II. Here, the "left-handed" mass parameter $M_{\tilde{q}_L}$ is much smaller than the "right-handed" masses $M_{\tilde{t}_R}$ and $M_{\tilde{b}_R}$, resulting in mainly "left-handed" physical states $\tilde{t}_1$ and $\tilde{b}_1$ with almost mass degenerated masses. The mass differences between them and the lightest neutralino is around 30 GeV. Processes containing stop and sbottom contribute to the total annihilation cross section, see Tab. 6.2. The three processes (6.1) contribute to more than 50% of the total annihilation cross section. The mixed annihilation $\tilde{t}_1\tilde{b}_1 \to tb$ dominates compared to stop-pair and sbottom-pair annihilation, discussed further in the next section. In Fig. 6.5 the relative importance of the channels of Scenario II are shown. As before, the 2σ relic density limit by Planck closely follows the border, where the neutralino is no longer the LSP. Differently to Scenario I, when the stop mass reaches $\sim$ 1600 GeV, which is around half of the heavy Higgs mass $m_{H^0} = 3451.2\,\text{GeV}$ the composition of the contribution of the processes changes. The stop-anti-stop annihilation, enhanced by the exchange of the Higgs, grows. Another differences is seen in higher stop and neutralino masses, where the annihilation and co-annihilation processes are not efficient enough to reach the observed relic density. For this region, the relic density 3.9 lies in the region, where the stop is the LSP and therefore the dark matter candidate. Meaning that for $M_1 \gtrsim 1800\,\text{GeV}$ the neutralino would be excluded as a dark matter candidate.

In Scenario III as in Scenario II, we have three almost mass degenerate particles, the neutralino as the LSP and the stop and sbottom as NLSP and NNLSP, omitted by the small parameter $M_{\tilde{q}_L}$ compared to the "right-handed" mass parameters. The phenomena that the Higgs mass is around twice the size of the NLSP and NNLSP enhances the squark-anti-squark (co-)annihilation in the close region around the reference scenario. The main contribution is given by the co-annihilation of the lightest stop and the lightest sbottom, centered around the Higgs resonance dominated region. The second most contribution process is given by the annihilation of the lightest stop-anti-stop to top-anti-top final state. The bottom-anti-bottom final state is also enhanced by the Higgs resonance. Around the reference scenario, the annihilation of the neutralino contributes to the relic density with an enhancement around $M_1 \sim 1230\,\text{GeV}$ and $M_{\tilde{q}_L} \gtrsim 1370\,\text{GeV}$. This enhancement is again due to a Higgs resonance, where the neutralino mass equals half of the heavy Higgs mass. Around the border, where the neutralino is no longer the LSP, except the Higgs resonance region, the dominant annihilation channel is given by the stop-anti-stop annihilation into gluon final state.

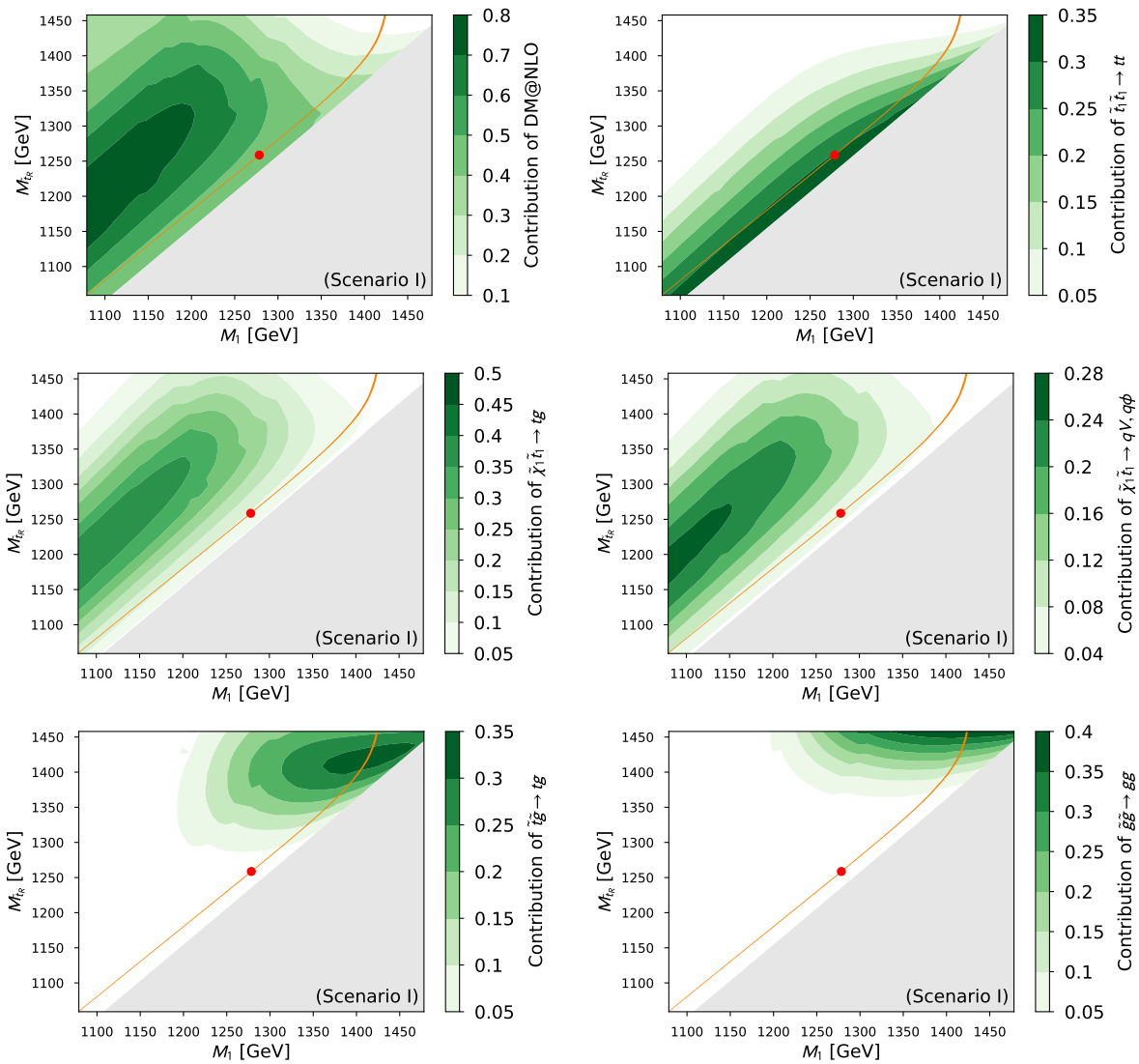

Figure 6.4.: Contribution of selected processes to the total annihilation cross section σ_{ann} in the M_1-$M_{\tilde{t}_R}$ plane around reference Scenario I. The orange band indicates the parameter region in agreement with the *Planck* limit given in Eq. (3.9) at the 2σ confidence level. The green levels indicate the relative importance of the processes that can be corrected by `DM@NLO` (first and fifth plot) and of selected individual processes (remaining plots). The grey region corresponds to $m_{\tilde{t}_1} < m_{\tilde{\chi}_1^0}$. The red dots indicate Scenarios I of Tab. 6.1.

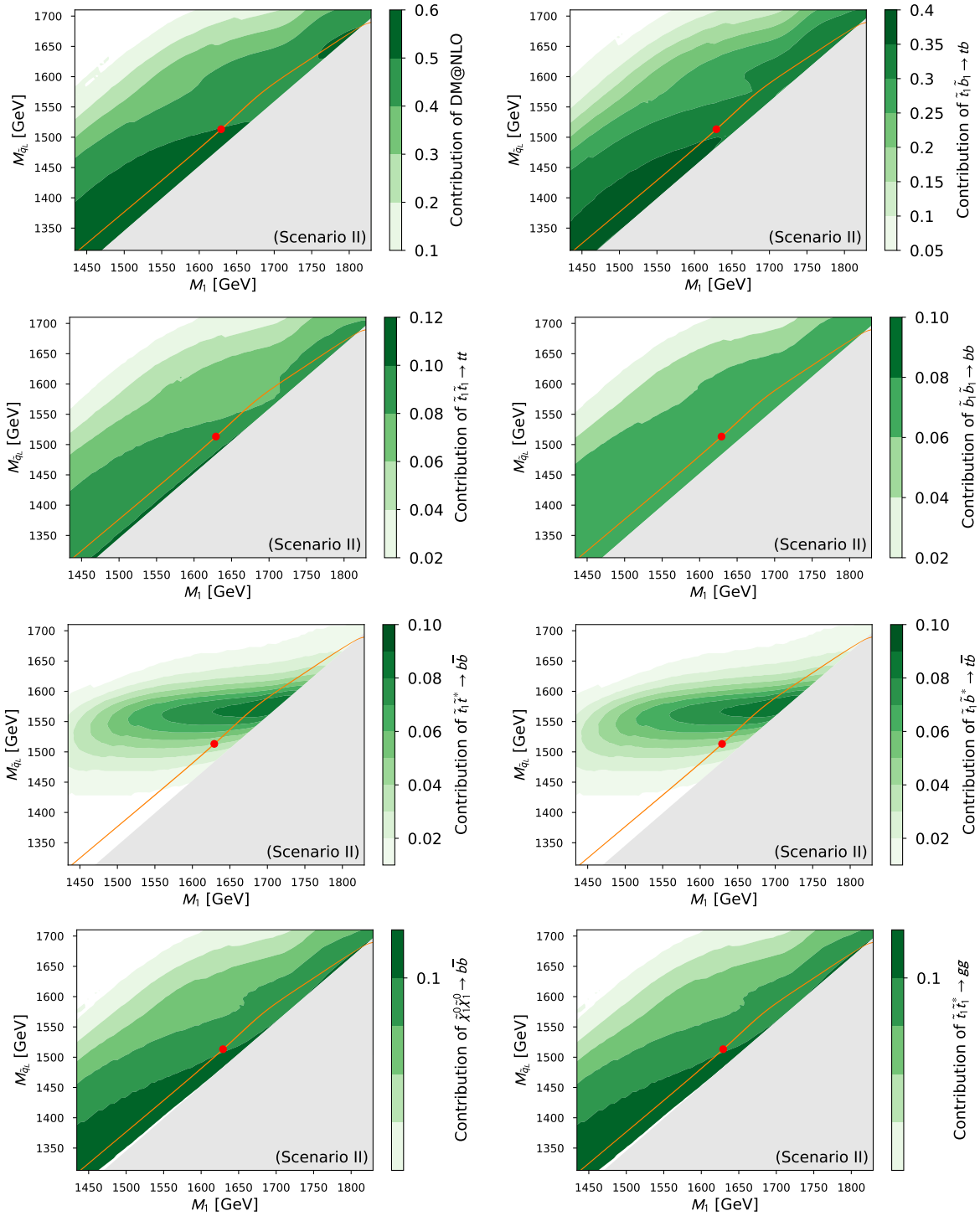

Figure 6.5.: Contribution of selected processes to the total annihilation cross section σ_{ann} in the M_1-$M_{\tilde{q}_L}$ plane around reference Scenario II of Tab. 6.1. The same color scheme as in the previous Fig. 6.4 is used.

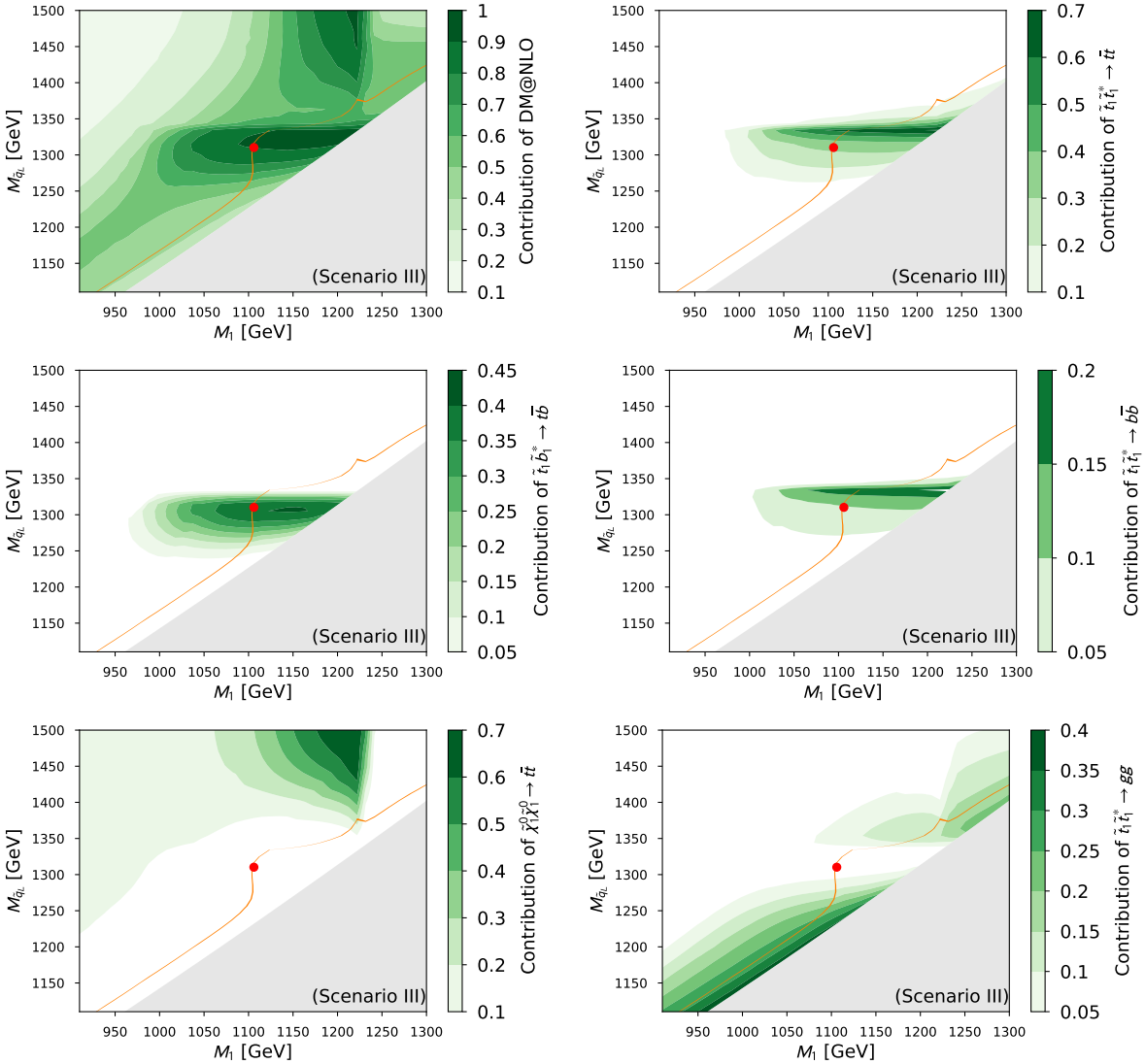

Figure 6.6.: Contribution of selected processes to the total annihilation cross section σ_{ann} in the M_1-$M_{\tilde{q}_L}$ plane around reference Scenario III of Tab. 6.1. The same color scheme as in the previous Fig. 6.4 is used.

6.2. Leading Order Cross Section

Having shown that the processes in Eq. (6.1) are important in large regions around the first two scenarios and Eq. (6.2) in the third scenario, introduced in the previous section, we now turn to review important features of the leading-order cross sections of these processes. The Feynman diagrams for the processes in question are shown in Figs. 6.2 and 6.2. The matrix elements of all three processes of Eq. (6.1) have contributions from t-channel or u-channel exchanges of strongly interacting gluinos as well as from electroweak gauginos. The matrix elements of the processes (6.2) have no contribution from u-channel, but additionally has contributions from s-channel with the exchange of gluon, vector boson and Higgs. Therefore the cross sections can be symbolically written as

$$\sigma = \sigma_s\Big(\alpha_s^2\Big) + \sigma_{se}\Big(\alpha_s\,\alpha_e\Big) + \sigma_e\Big(\alpha_e^2\Big)\,, \tag{6.6}$$

where σ_s is the cross section proportional to the square of the strong coupling constant α_s^2, σ_{se} is the cross section originating from the interference of the strong and electroweak interacting parts of the scattering amplitude and σ_e is the purely electroweak cross section proportional to the square of the electromagnetic coupling constant α_e^2.

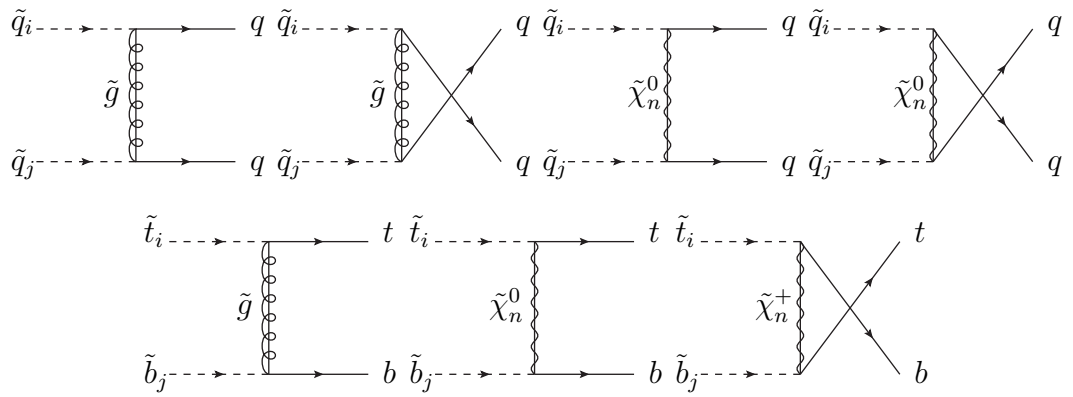

Figure 6.7.: Tree-level Feynman diagrams for squark annihilation into quark pairs for the case of squarks of identical (upper row) and different (lower row) type.

The decomposition of the total cross section into contributions from different channels and interferences of the three processes (6.1), is shown in Fig. 6.9. The cross sections for $\tilde{t}_1\tilde{t}_1 \to tt$ and $\tilde{b}_1\tilde{b}_1 \to bb$ in the top left, top right and bottom right panels in Fig. 6.9 show the expected hierarchy, in which the gluino t-channel and u-channel exchanges dominate the cross section and are about an order of magnitude larger than the next largest contribution which is the interference of the gluino exchange with the electroweak t- and u-channels. The contribution from the interference between the gluino exchange diagrams and the gaugino exchange diagrams is yet another order of magnitude larger than the purely electroweak contribution. As argued before, in scenarios where the

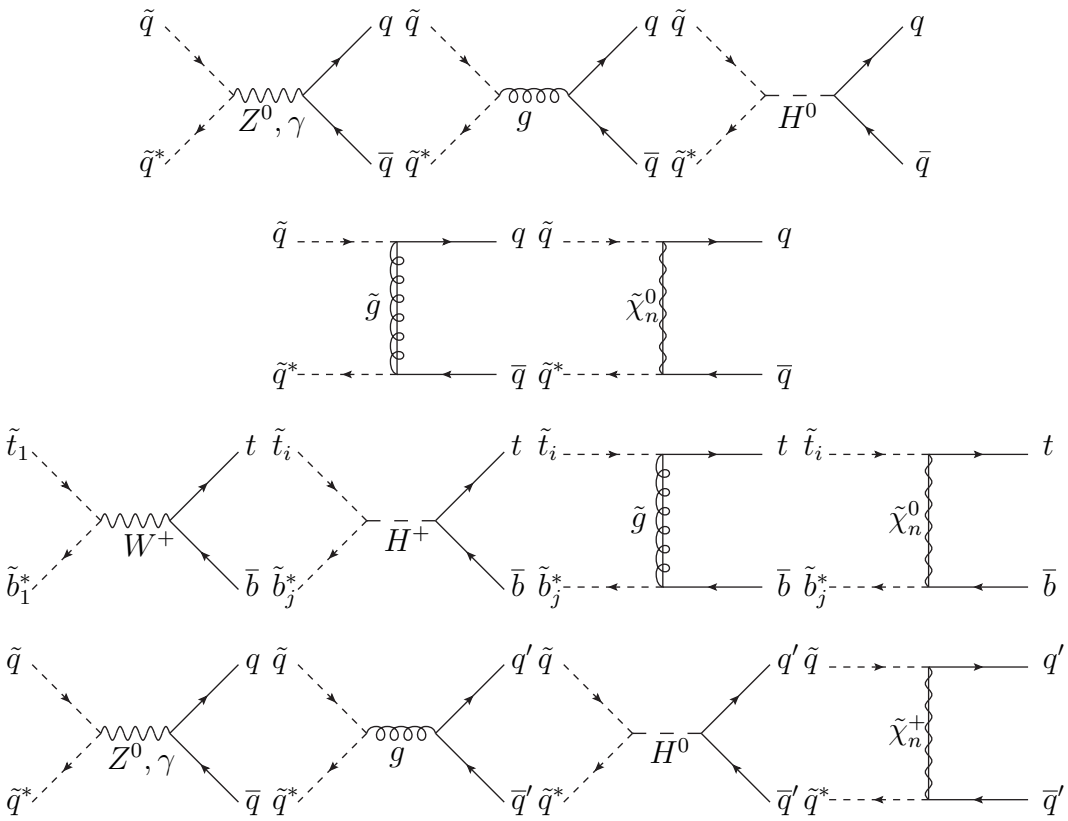

Figure 6.8.: Tree-level Feynman diagrams for the squark-anti-squark annihilation into quark-anti-quark final state for the case of identical types of squark and quarks (first two rows), stop-anti-sbottom (third row) and identical squarks annihilating into different type of quarks (fourth row).

processes in Eq. (6.1) are important, the lightest neutralino is bino-like and the gluino mass is relatively small. These facts imply that the neutralino-squark-quark coupling and the gluino-squark-quark coupling differ mainly by the coupling constant. Therefore, the hierarchy observed in Fig. 6.9 is simply due to the ratio of the different coupling constants $\alpha_s(\sqrt{m_{\tilde{t}_1} m_{\tilde{t}_2}})/\alpha_e(m_Z)$.

The only process where this hierarchy is not present is the annihilation $\tilde{t}_1\tilde{b}_1 \to tb$. Here the hierarchy observed in the other two processes is modified due to a few factors. First, there is no gluino u-channel exchange. Then, the gluino mass in this scenario is larger, and this processes proceeds also through a chargino u-channel exchange. The larger gluino mass together with the missing u-channel suppresses the gluino contribution compared to the other two processes. Moreover, in the case of the higgsino-like chargino exchange, the Yukawa component of the chargino-squark-quark coupling is not suppressed as in the case of bino-like neutralino. The combination of these effects results in the interference between the gluino and the chargino exchange being suppressed with

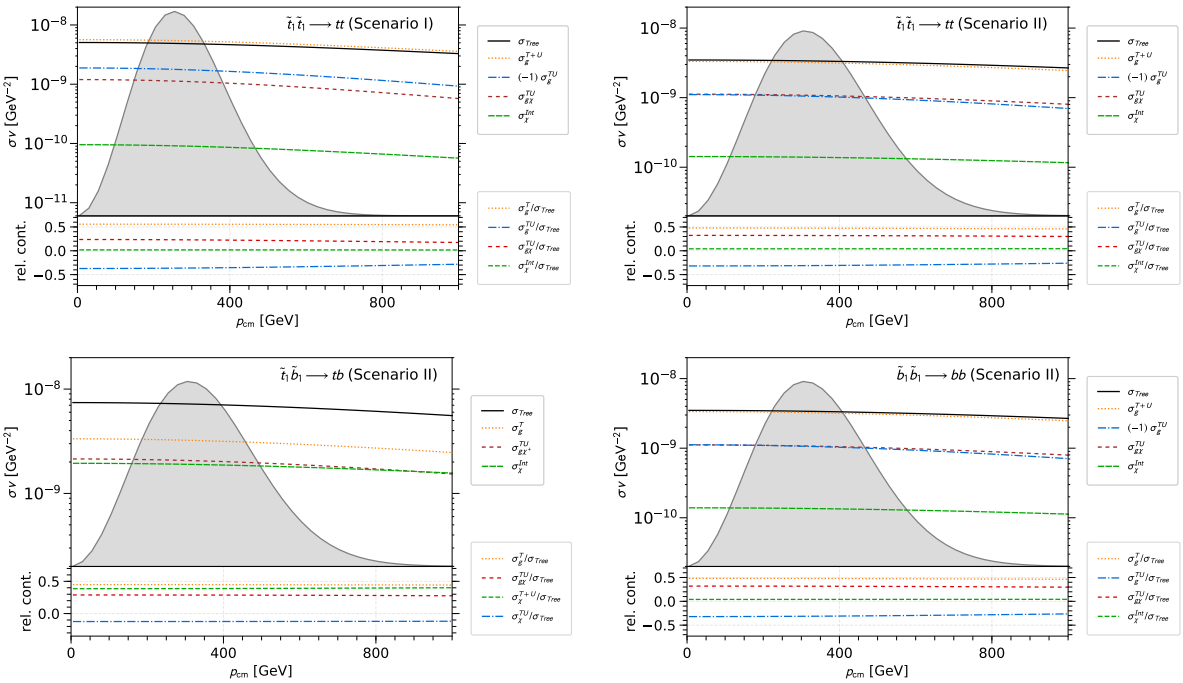

Figure 6.9.: Upper part: Leading-order cross section σv as a function of the center-of-mass momentum p_{cm} into different sub-channels according to Fig. 6.2 in the two pMSSM scenarios I and II of Tab. 6.1. In the legend, $\sigma_{\mathrm{T}ree}$ denotes the total tree-level cross section, the subscripts g, χ and $g\chi$ correspond to gluino exchange squared, gaugino exchange squared, and gluino-gaugino interference. The superscripts indicate squared t-channel (T), squared u-channel (U), the sum of both (T+U) and the t-u interference contributions (TU). For the gaugino exchange, the superscript "Int" refers to the sum of all involved diagrams. Lower part: Contributions relative to the total tree-level result $\sigma_{\mathrm{T}ree}$.

respect to the pure gluino contribution only by a factor of about two. On top of that, the electroweak contribution is comparable with the gluino-chargino interference.

The decomposition of the total cross section into contributions from different channels and interferences of the three processes (6.2), is shown in Fig. 6.10. The heavy Higgs boson mass is of the order of two times the lightest stop mass, leading to an enhancement of the s-channel Higgs contribution by the resonance. Within all three panels a peak is visible increasing the cross section about some order of magnitudes. The cross sections for $\tilde{t}_1\tilde{t}_1^* \to t\bar{t}$ in the upper left panel shows the gluino t-channel as the second most contributing channel. Around a center-of-mass momentum of 400 GeV the gluon s-channel contributes more than the gluino t-channel. Around $p_{cm} \sim 850,\mathrm{GeV}$ the gluon s-channel is the dominating contribution. But indicated by the grey shaded region, the

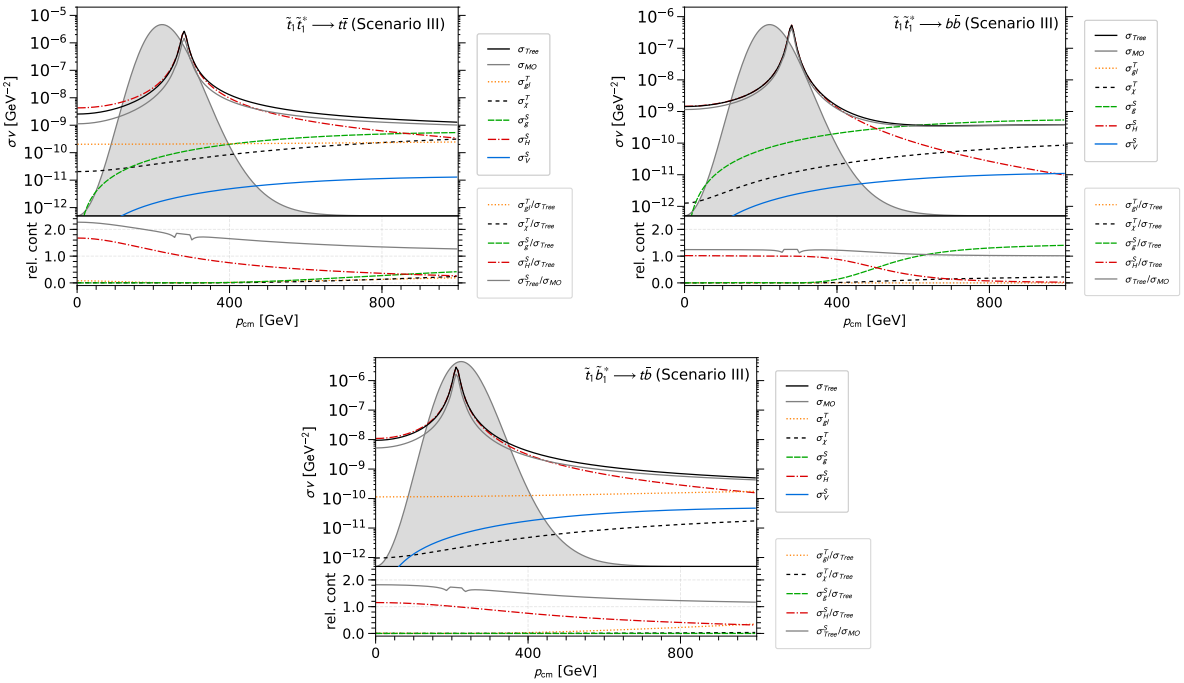

Figure 6.10.: Upper part: Leading-order cross section σv as a function of the center-of-mass momentum p_{cm} into different sub-channels according to Fig. 6.2 in the scenario III of Tab. 6.1. In the legend, $\sigma_{\mathrm{T}ree}$ denotes the total tree-level cross section, the subscripts g, χ, g, H and V correspond to gluino, gaugino, gluon, Higgs boson and vector boson exchange squared. The superscripts indicate squared t-channel (T) and squared s-channel (S). Lower part: Contributions relative to the total tree-level result $\sigma_{\mathrm{T}ree}$.

velocity distribution, which will be multiplied to the cross section σv, when taking the thermal average, only contributions up to around $p_{cm} \sim 700\,\mathrm{GeV}$ are important. The neutralino t-channel contributes is an order of magnitude less than the gluino t-channel. The contribution of the vector boson s-channel is more than three orders of magnitude suppressed.

In the case of $\tilde{t}_1\tilde{t}_1^* \to b\bar{b}$ in the top right panel in Fig. 6.10 a similar hierarchy as in the left panel is shown, except the fact that no gluino t-channel contributes to the cross section. The gluon s-channel contribution dominates already at a center-of-mass momentum $p_{cm} \sim 500\,\mathrm{GeV}$. The Higgs s-channel contribution decreases more strongly with increasing p_{cm}. Again the contribution of the vector boson s-channel is orders of magnitude smaller.

For the annihilation channel $\tilde{t}_1\tilde{b}_1^* \to t\bar{b}$ the lower panel, again the Higgs s-channel is the dominant channel, caused by the Higgs resonance. Followed by the gluino t-channel contribution. The contribution of the vector boson is greater by the exchange of a W^+

boson. The contribution of the neutralinos contributes the least.

6.3. Color Decomposition

Another important aspect of the processes we investigate is the fact that both initial and final state particles carry color. The color structure of the initial and final state will be extremely relevant later in the discussion of the next-to-leading SUSY-QCD corrections and their resummation. The color decomposition is discussed in greater detail for the squark annihilation, the squark-anti-squark annihilation will be briefly summarized.

In case of the squark annihilation both scalar quarks in the initial state (and also the quarks in the final state) transform under the fundamental representation of the $SU(3)$ group (denoted here as $\mathbf{3}$ due to the dimensionality of the representation). The two particle system however transforms under a tensor product of the corresponding representations $\mathbf{3} \otimes \mathbf{3}$ which can be decomposed via a Clebsch-Gordan decomposition into $SU(3)$-invariant subspaces as

$$\mathbf{3} \otimes \mathbf{3} = \overline{\mathbf{3}} \oplus \mathbf{6}\,. \tag{6.7}$$

In order to construct a color basis adapted to our matrix element, we can use the Clebsch-Gordan coefficients of the decomposition

$$C^{\{\overline{\mathbf{3}}\}}_{\alpha\, a_1 a_2} = \frac{1}{\sqrt{2}}\epsilon_{\alpha a_1 a_2}\,, \qquad \alpha = 1,2,3\,, \tag{6.8}$$

$$C^{\{\mathbf{6}\}}_{\alpha\, a_1 a_2} = \frac{1}{2}\left(\delta_{\alpha_1 a_1}\delta_{\alpha_2 a_2} + \delta_{\alpha_1 a_2}\delta_{\alpha_2 a_1}\right)\,, \qquad \alpha_i = 1,\ldots,6\,, \tag{6.9}$$

where the indices $a_{1,2}$ can take the values 1 to 3 (for details see Ref. [126]). The basis is constructed by considering that $SU(3)$ color symmetry is an exact symmetry of the theory and so the color is conserved between the initial and final states. That means if a pair of initial state particles transforms in an irreducible representation of the $SU(3)$ group, the pair of final state particles must transform in the same representation. After proper normalization, we can combine the Clebsch-Gordan coefficients into the following basis relevant for our processes

$$C^{\{\overline{\mathbf{3}},\overline{\mathbf{3}}\}}_{a_1 a_2 a_3 a_4} = \frac{1}{\sqrt{2N_c(N_c-1)}}\left(\delta_{a_1 a_3}\delta_{a_2 a_4} - \delta_{a_1 a_4}\delta_{a_2 a_3}\right)\,, \tag{6.10}$$

and

$$C^{\{\mathbf{6},\mathbf{6}\}}_{a_1 a_2 a_3 a_4} = \frac{1}{\sqrt{2N_c(N_c+1)}}\left(\delta_{a_1 a_3}\delta_{a_2 a_4} + \delta_{a_1 a_4}\delta_{a_2 a_3}\right)\,. \tag{6.11}$$

The matrix element can be expanded in this basis as

$$M_{stij} = M_{\overline{\mathbf{3}}}\, C^{\{\overline{\mathbf{3}},\overline{\mathbf{3}}\}}_{stij} + M_{\mathbf{6}}\, C^{\{\mathbf{6},\mathbf{6}\}}_{stij}\,, \tag{6.12}$$

where s, t, i and j are the color indices of the incoming and the outgoing particles. Given the orthonormality of the basis, the triplet and sextet parts of the amplitude can be determined as

$$M_{\overline{\mathbf{3}}} = M_{stij} C^{\{\overline{\mathbf{3}},\overline{\mathbf{3}}\}}_{stij}, \qquad M_{\mathbf{6}} = M_{stij} C^{\{\mathbf{6},\mathbf{6}\}}_{stij} \,. \tag{6.13}$$

In the case of the annihilation process $\tilde{t}_1\tilde{t}_1 \to tt$ or $\tilde{b}_1\tilde{b}_1 \to bb$, the triplet and the sextet matrix elements are a linear combination of the gluino and gaugino t-channel and u-channel exchanges. At tree-level the explicit expression for the triplet part of the matrix element is

$$\begin{aligned} M_{\overline{\mathbf{3}}} = \frac{(N_c^2-1)}{2\sqrt{2N_c(N_c-1)}}(-M^t_{\tilde{g}} + M^u_{\tilde{g}}) \\ + \frac{N_c(N_c-1)}{\sqrt{2N_c(N_c-1)}}(M^t_{\tilde{\chi}} - M^u_{\tilde{\chi}}) \,. \end{aligned} \tag{6.14}$$

Analogously, the sextet part of the matrix element is

$$\begin{aligned} M_{\mathbf{6}} = \frac{(N_c^2-1)}{2\sqrt{2N_c(N_c+1)}}(M^t_{\tilde{g}} + M^u_{\tilde{g}}) \\ + \frac{N_c(N_c+1)}{\sqrt{2N_c(N_c+1)}}(M^t_{\tilde{\chi}} + M^u_{\tilde{\chi}}) \,. \end{aligned} \tag{6.15}$$

The same decomposition can be performed for the process $\tilde{t}_1\tilde{b}_1 \to tb$ and the explicit results given in Eqs. (6.14) and (6.15) can be used after setting $M^u_{\tilde{g}} = 0$ and interpreting $M^u_{\tilde{\chi}}$ as the u-channel chargino exchange. The squared amplitude is then in all cases given simply by

$$|M|^2 = |M_{\overline{\mathbf{3}}}|^2 + |M_{\mathbf{6}}|^2 \,, \tag{6.16}$$

where due to the orthonormality of the color basis, there is no interference between the triplet and the sextet matrix elements.

The leading order triplet and sextet cross sections for the relevant processes are shown in Fig. 6.11. The general behavior of the color decomposed cross sections for the processes $\tilde{t}_1\tilde{t}_1 \to tt$ and $\tilde{b}_1\tilde{b}_1 \to bb$ is very similar. Both processes contain identical particles in the initial state and are symmetric with respect to their interchange. Given that the color basis vector $C^{\{\overline{3},\overline{3}\}}$ is anti-symmetric with respect to the same interchange, the partial wave of the the triplet cross section is a p-wave, making its contribution to the relic density subdominant. For these two processes only the sextet color combination contributes. In the case of the last process $\tilde{t}_1\tilde{b}_1 \to tb$, the symmetry argument does not apply and both color combinations contain an s-wave and contribute equally to the relic density.

The analog procedure was proceeded on the squark-anti-squark annihilation. As before the scalar quark and anti-quark in the initial state (and also the quark and anti-quark

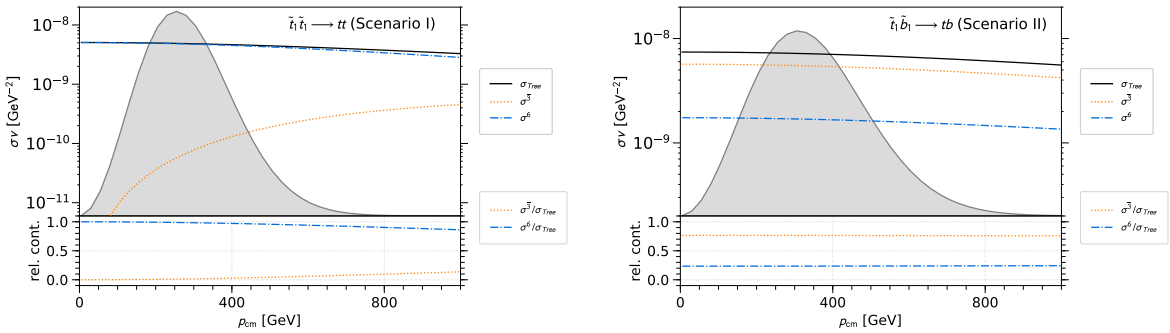

Figure 6.11.: Upper part: Decomposition of the leading order cross section into color basis in typical pMSSM scenarios for identical (left) and nonidentical (right) incoming particles. The superscripts $\overline{\mathbf{3}}$ and $\mathbf{6}$ refer to the respective color representation. Lower part: Contributions relative to the total tree-level cross section σ_{Tree}.

in the final state) transform under the fundamental representation of the $SU(3)$ group (denoted here as $\mathbf{3}$ due to the dimensionality of the representation). This time the two particle system however transforms under a tensor product of the corresponding representations $\mathbf{3} \otimes 3$ which can be decomposed as

$$\mathbf{3} \otimes \overline{\mathbf{3}} = \mathbf{1} \oplus \mathbf{8}\,. \tag{6.17}$$

In order to construct a color basis adapted to our matrix element, we can use the Clebsch-Gordan coefficients

$$C^{\{\mathbf{1}\}}_{a_1 a_2} = \frac{1}{\sqrt{N_c}}\delta_{a_1 a_2}\,, \tag{6.18}$$

$$C^{\{\mathbf{8}\}}_{\alpha\, a_1 a_2} = \sqrt{2}T^{\alpha}_{a_1 a_2}\alpha = 1,2,3\,. \tag{6.19}$$

After proper normalization, we can combine the Clebsch-Gordan coefficients into the following basis relevant for our processes

$$C^{\{\mathbf{1},\mathbf{3}\}}_{a_1 a_2 a_3 a_4} = \frac{1}{\sqrt{N_c}}\delta_{a_1 a_2}\delta_{a_3 a_4}\,, \tag{6.20}$$

and

$$C^{\{\mathbf{8},\mathbf{8}\}}_{a_1 a_2 a_3 a_4} = \frac{1}{\sqrt{N_c^2-1}}\left(\delta_{a_1 a_3}\delta_{a_4 a_2} - \frac{1}{N_c}\delta_{a_1 a_2}\delta_{a_4 a_3}\right)\,. \tag{6.21}$$

The matrix element can be expanded in this basis as

$$M_{stij} = M_{\mathbf{1}}\, C^{\{\mathbf{1},\mathbf{1}\}}_{stij} + M_{\mathbf{8}}\, C^{\{\mathbf{8},\mathbf{8}\}}_{stij}\,. \tag{6.22}$$

Given the orthonormality of the basis, the triplet and sextet parts of the amplitude can be determined as

$$M_{\mathbf{1}} = M_{stij} C_{stij}^{\{\mathbf{1},\mathbf{1}\}}, \qquad M_{\mathbf{8}} = M_{stij} C_{stij}^{\{\mathbf{8},\mathbf{8}\}} . \tag{6.23}$$

In the case of the annihilation process $\tilde{t}_1 \tilde{t}_1^* \to t\bar{t}$, the singlet and the octet matrix elements are a linear combination of the gluino and gaugino t-channel and either Higgs (singlet) or gluon (octet) s-channel exchanges. At tree-level the explicit expression for the singlet part of the matrix element is

$$M_{\mathbf{1}} = N_c M_H + M_{\tilde{\chi}} + \frac{N_c^2 - 1}{2N_c} M_{\tilde{g}} \tag{6.24}$$

Analogously, the octet part of the matrix element is

$$M_{\mathbf{8}} = \frac{\sqrt{N_c^2 - 1}}{2} M_g + \sqrt{N_c^2 - 1} M_{\tilde{\chi}} + (-\frac{1}{2N_c})\sqrt{N_c^2 - 1} M_{\tilde{g}} \tag{6.25}$$

The same decomposition can be performed for the process $\tilde{t}_1 \tilde{b}_1^* \to t\bar{b}$ and the explicit results given in Eqs. (6.24) and (6.25) can be used after setting $M_g^s = 0$ and for the process $\tilde{t}_1 \tilde{t}_1^* \to b\bar{b}$ interpreting $M_{\tilde{\chi}}^t$ as the t-channel chargino exchange and setting $M_{\tilde{g}}^t = 0$. The squared amplitude is then in all cases given simply by

$$|M|^2 = |M_{\mathbf{1}}|^2 + |M_{\mathbf{8}}|^2 , \tag{6.26}$$

where due to the orthonormality of the color basis, there is no interference between the singlet and the octet matrix elements.

The leading order singlet and octet cross sections for the relevant processes are shown in Fig. 6.12. It is worth mentioning that by the Higgs resonance the singlet is the dominant contribution. Only in the bottom-anti-bottom case, the octet enhanced by the gluon s-channel becomes dominant at a pcm of $> 500\,\mathrm{GeV}$. In the case of $\tilde{t}_1 \tilde{b}_1^* \to t\bar{b}$ where no gluon s-channel exists, the octet contribution is even smaller and has lost its p-wave form, whereas in the case of top-anti-top and bottom-anti-bottom the octet has a unique p-wave dominated shape.

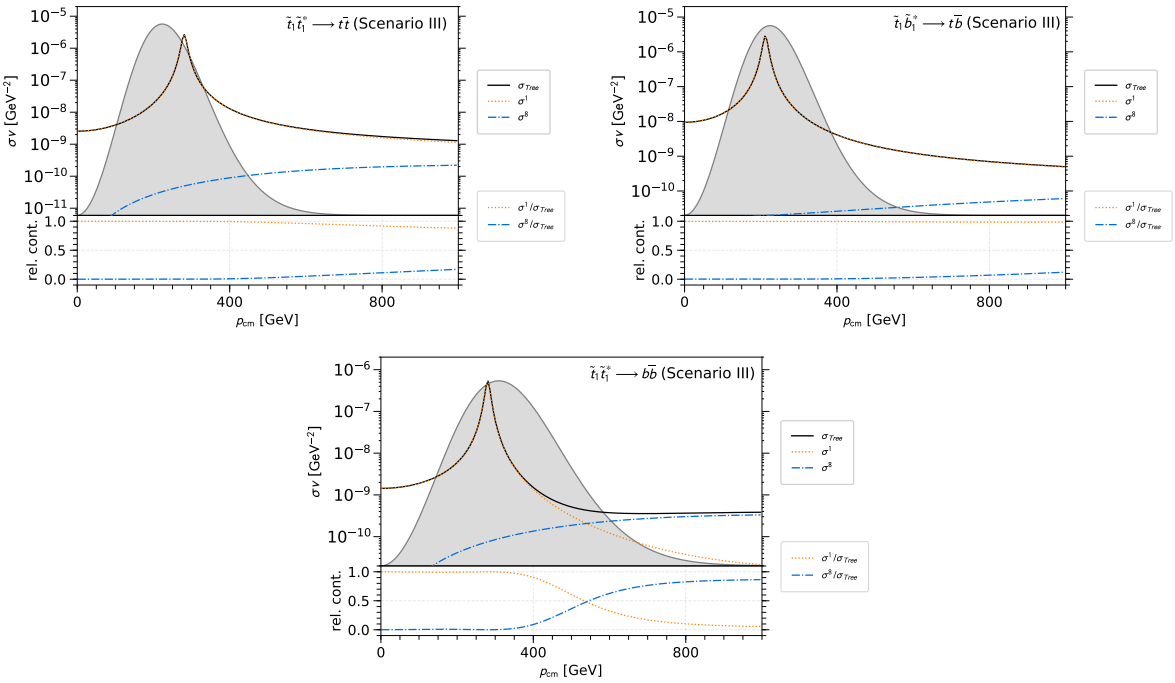

Figure 6.12.: Upper part: Decomposition of the leading order cross section into color basis in typical pMSSM scenarios for identical (left) and nonidentical (right) incoming particles. The superscripts **1** and **8** refer to the respective color representation. Lower part: Contributions relative to the total tree-level cross section σ_{Tree}.

7 Virtual Corrections

For the calculation of the NLO corrections to the respective tree level diagrams, Fig. (6.2) and (6.2), all virtual and real contributions (Chapter 9) are needed. The virtual corrections are characterized by the fact that they have the same initial and final states. Only the internal exchange of particles by additional virtual particles differs. Therefore, the same kinematics and phase space are used as for the tree level calculation. We distinguish between three different virtual contributions, self-energies (2-point functions), vertex corrections (3-point functions) and box diagrams (4-point functions). In our calculations we consider all SUSY-QCD corrections, whereby the virtual particles to be exchanged are limited to squarks, quarks, gluons and gluinos. Through the exchange of these virtual particles, there are divergences in the contributions that need to be specifically addressed. In general, taking into account all virtual and real contributions, these divergences are generally canceled out.

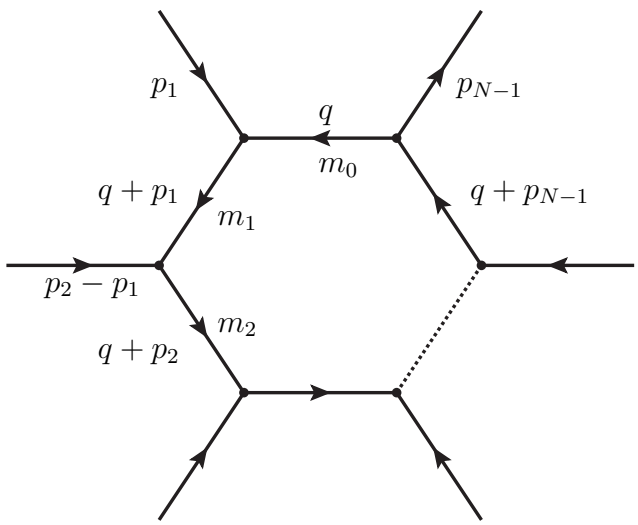

Figure 7.1.: N-loop diagram. The kinematic can be fixed by the external momenta, only the momentum q stays unconstrained

The diagrams that contain such virtual corrections are also called loop diagrams.

Such a N-loop diagram can be seen in Fig. 7. The loop contains a virtual undefined momentum q, which is integrated over the entire phase space. In general, such a loop diagram has the general form

$$\int \frac{d^4q\, d^4(q+p_1)\, \ldots d^4(q+p_{N-1})}{(\not{q}-m_0)^2+((\not{q}+\not{p}_1)-m_1)^2+\ldots+((\not{q}+\not{p}_{N-1})-m_{N-1})} \tag{7.1}$$

Since the propagator contains the momentum q, it can become infinite, causing divergences. Even though the full calculation becomes finite in the end, the individual contributions must be manageable. Therefore it is important to extract the divergences. There are several ways to do this. One possibility is the so-called dimensional regularization, which we consider in the following.

7.1. Dimensional Regularization

Let us first consider the simple divergent integral

$$\int_a^\infty \frac{1}{r^2} d^3r. \tag{7.2}$$

This integral has a linear divergence. If the integration is reduced by one dimension

$$\int_a^\infty \frac{1}{r^2} d^2r, \tag{7.3}$$

the integral has only a logarithmic divergence. If the integration is reduced by another dimension, we get a convergent integral

$$\int_a^\infty \frac{1}{r^2} dr. \tag{7.4}$$

For the calculation of divergent integrals in four dimensions, the integration is transformed into D dimensions. After the integration the limes $D \to 4$ can be performed and the pole of the integral becomes visible again in the final result. The advantage of dimensional regularization is the conservation of Lorentz invariance, gauge invariance and unitarity. In the following we consider the extraction of divergence more closely.

Extraction of Divergences

Each diagram in the calculation of the virtual corrections contains a slightly modified loop integral. A great benefit are the calculations by Passarino and Veltman [127], who reduced the loop integral to a few calculable integrals.

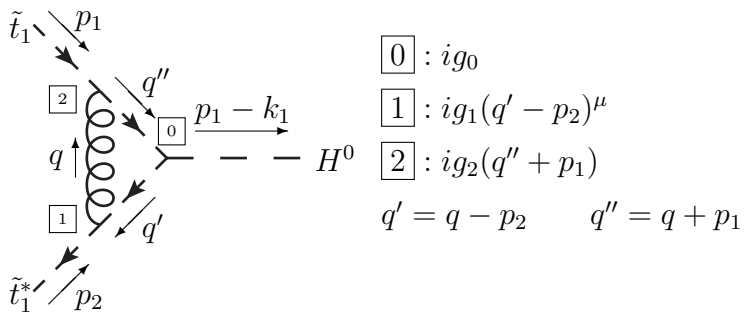

Figure 7.2.: Vertex correction for stop-anti-stop-Higgs vertex containing virtual exchange of a gluon between initial particles.

This strategy will be illustrated in the following example. For this we consider the vertex from stop-anti-stop to Higgs with an exchange of a gluon between the initial particles, see Fig. 7.2. This three point function contains the integral

$$\mathcal{M} = i^6 \mu^{3\left(\frac{4-D}{2}\right)} g_0 g_1 g_2 \int \frac{d^D q}{(2\pi)^D} \frac{(q+2p_1)^\mu (q-2p_2)^\nu}{q^2\left[(q+2p_1)^2 - m_1^2\right]\left[(q-2p_2)^2 - m_2^2\right]} (-\mathrm{g}^{\mu\nu}). \tag{7.5}$$

The coupling constants $g_{0,1,2}$ contain the color structure of the respective vertices, since these are currently not relevant for the consideration of divergences. The momentum q to be integrated is also contained in different orders in the numerator. Therefore we decompose the integral into integrals sorted by the order in q

$$\begin{aligned}\mathcal{M} = \mu^{3\left(\frac{4-D}{2}\right)} g_0 g_1 g_2 \mathrm{g}^{\mu\nu} \Bigg[& \int \frac{d^D q}{(2\pi)^D} \frac{q^\mu q^\nu}{q^2\left[(q+2p_1)^2 - m_1^2\right]\left[(q-2p_2)^2 - m_2^2\right]} \\ & \int \frac{d^D q}{(2\pi)^D} \frac{2p_1^\mu q^\nu}{q^2\left[(q+2p_1)^2 - m_1^2\right]\left[(q-2p_2)^2 - m_2^2\right]} \\ & \int \frac{d^D q}{(2\pi)^D} \frac{-2q^\mu p_2^\nu}{q^2\left[(q+2p_1)^2 - m_1^2\right]\left[(q-2p_2)^2 - m_2^2\right]} \\ & \int \frac{d^D q}{(2\pi)^D} \frac{-4p_1^\mu p_2^\nu}{q^2\left[(q+2p_1)^2 - m_1^2\right]\left[(q-2p_2)^2 - m_2^2\right]} \Bigg].\end{aligned} \tag{7.6}$$

The numerator factorizes with the spinor structure so that it is irrelevant for the integral and only the order in q plays a role. Altogether we get three different integral loops for loops with three external legs. If these integrals are calculated in advance, they can be reused for each integral of this form. Looking at the other contributions of the virtual corrections, the self-energies have two external legs, with two propagators and the box diagrams have four propagators with four external legs. Extending this to a general form for one-loop diagrams with N propagators and M loop momenta, this

results in

$$T^N_{\mu_1,\ldots,\mu_M}(p_1,\ldots p_{N-1},m_0,\ldots,m_{N-1}) = \frac{(2\pi\mu)^{4-D}}{i\pi^2} \tag{7.7}$$
$$\int d^D \frac{q_{\mu_1}\ldots q_{\mu_N}}{(q^2-m_0^2+i\epsilon)[(q+p_1)^2-m_1^2+i\epsilon]\ldots[(q+p_{N-1})^2-m_{N-1}^2+i\epsilon]}.$$

The constant $\frac{(2\pi)^4}{i\pi^2}$ is set for conventional reasons. The momenta are shown in Figure 7. In the following we adopt the usual naming convention and refer to the tensor integrals as

$$T^1 \to A \quad T^2 \to b \quad T^3 \to C \quad T^4 \to D \tag{7.8}$$

depending on the number of propagators. The scalar integrals A_0, B_0, C_0, D_0, which contain no loop momenta in the numerator and therefore no Lorentz indices, have been developed by t'Hoft and Veltman [128]. In the following we will deal with the generic integral and later on with the example of the scalar integral A_0 in more detail.

7.1.1. Generic Integral

The scalar integrals can be reduced to the generic structure

$$I_n(A) = \int d^D q \frac{1}{(q^2-A+i\epsilon)^n} \tag{7.9}$$

Whether the integral is convergent or not depends on the dimension D and the power n. In the case $A > 0$ (since A stands for a mass, this can generally be assumed) converges the integral for $D < 2n$. The function that is integrated is generally complex and has a scalar pole at

$$0 = q^2 - A + i\epsilon \tag{7.10}$$
$$\Rightarrow q_0 = \pm\sqrt{\vec{q}^{\,2}+A} \mp i\epsilon \tag{7.11}$$

The position of the pole is shown in Figure 7.3 by the crossing lines.

By the application of the Cauchy theorem, it is possible to shift the integration along the real axis to an integration along the imaginary axis. The change of direction of integration is known as the Wick rotation. With the transformation to the Euclidean metric using the new variables

$$q_0 = iq_{E,0}\,, \qquad q^k = q_E^k\,, \tag{7.12}$$
$$q^2 = q_0^2 - \vec{q}^{\,2} = -q_{E,0}^2 - \vec{q}_E^{\,2} = -q_E^2 \leq 0\,, \tag{7.13}$$

the integral can be expressed in dependence of q_E as

$$\begin{aligned} I_n(A) &= i\int_{-\infty}^{\infty} \mathrm{d}q_{E,0} \int \mathrm{d}^{D-1}q_E(-q_{E,0}^2 - \vec{q}_E^{\,2} - A + i\epsilon)^{-n} \\ &= i\int \mathrm{d}^D q_E\ (-1)^n\ (q_E^2 + A - i\epsilon)^{-n}\,. \end{aligned} \tag{7.14}$$

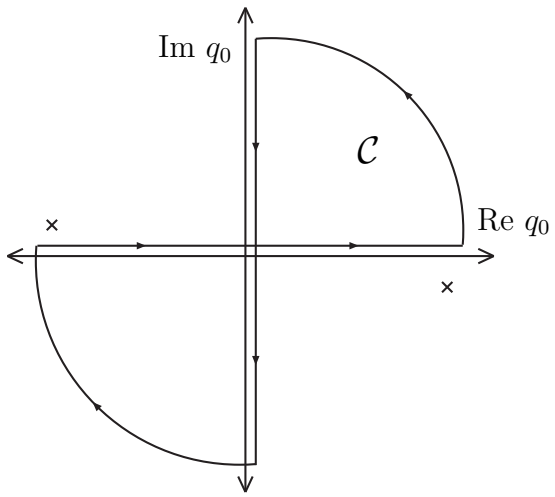

Figure 7.3.: Visualisation of the position of pole within the complex plane. Figure taken from [129].

This integral in terms of q_E is spherical symmetric in D dimensions. For further consideration, proceed as we do with 2 or 3 dimensional integrals, where in this case polar coordinates or spherical coordinates are introduced. For this we use the definition of the solid angle

$$\Omega_{D-1} = \frac{2\pi^{D/2}}{\Gamma\Big(D/2\Big)} \,. \tag{7.15}$$

in D dimensions with the Euler Γ function. By the spherical coordinates

$$\int \mathrm{d}^D q_E = \int \mathrm{d}\Omega_D \int_0^\infty \mathrm{d}q_E \, q_E^{D-1} = \int \mathrm{d}\Omega_D \int_0^\infty \mathrm{d}q_E^2 \, \frac{1}{2} \, (q_E^2)^{D/2-1} \,. \tag{7.16}$$

the generic integral to

$$I_n(A) = i \, (-1)^n \, \pi^{D/2} \, \frac{\Gamma(n - D/2)}{\Gamma(n)} \, (A - i\epsilon)^{D/2-n} \,. \tag{7.17}$$

can be determined. Formula (7.17) was determined for the convergent case $D < 2n$, but since Γ is defined in the full complex plane with the exception of the poles at $z = 0, -1, -2 \ldots$, the limes $D \to 4$ can be performed. The two possible divergent integrals I_1 and I_2 are divergent by the poles of Γ in I_1 and I_2 resulting in the ultraviolet (UV) divergences in the dimensional regularization.

7.1.2. The Scalar Integral A_0

As an example for a real loop integral we consider

$$A_0(m^2) = \frac{(2\pi\mu)^{4-D}}{i\pi^2} \int \mathrm{d}^D q \, \frac{1}{q^2 - m^2 + i\epsilon} \,, \tag{7.18}$$

the other integrals are not discussed in detail. The parameter μ has the dimension of energy. The coefficient μ^{4-D} ensures that the dimension of the integral does not depend on D. The other integrals are not discussed in detail. With the solution for the generic integral (7.17), the expression for A_0 can be expressed as

$$\begin{aligned} A_0(m^2) &= \frac{(2\pi\mu)^{4-D}}{i\pi^2} \, I_1(m^2) \\ &= -(m^2 - i\epsilon) \left(\frac{m^2 - i\epsilon}{4\pi\mu^2}\right)^{\frac{D-4}{2}} \Gamma\!\left(\frac{2-D}{2}\right). \end{aligned} \tag{7.19}$$

The Euler Γ function has a pole for $D \to 4$ which makes A_0 divergent. To determine the expansion of A_0 around this pole, a new variable $\epsilon = \frac{4-D}{2}$ is introduced

$$A_0(m^2) = -(m^2 - i\epsilon) \left(\frac{m^2 - i\epsilon}{4\pi\mu^2}\right)^{-\epsilon} \Gamma(\epsilon - 1) \,. \tag{7.20}$$

For extraction of the pole, the relation

$$\Gamma(z+1) = z\,\Gamma(z) \tag{7.21}$$

of the Euler Γ function is used. In addition, the factor

$$c_\epsilon = (4\pi)^\epsilon \, \Gamma(1+\epsilon) \tag{7.22}$$

is extracted, so that we obtain

$$A_0(m^2) = -c_\epsilon (m^2 - i\epsilon) \left(\frac{m^2 - i\epsilon}{\mu^2}\right)^{-\epsilon} \frac{1}{\epsilon\,(\epsilon - 1)} \,. \tag{7.23}$$

If the terms $\left(\frac{m^2 - i\epsilon}{\mu^2}\right)^{-\epsilon}$ and $\frac{1}{\epsilon\,(\epsilon-1)}$ for $\epsilon = 0$ are expanded in Taylor series and the small imaginary part $i\epsilon$ is neglected,

$$A_0(m^2) = m^2 \left(\frac{c_\epsilon}{\epsilon} - \ln\left(\frac{m^2}{\mu^2}\right) + 1 + \mathcal{O}(\epsilon)\right) \,, \tag{7.24}$$

results. If additionally the factor c_ϵ is expanded and the conventional notation

$$\Delta = \frac{1}{\epsilon} - \gamma_E + \ln(4\pi) \,, \tag{7.25}$$

is used, where γ_E is the Euler-Mascharoni constant. The final result for the scalar integral is

$$A_0(m^2) = m^2 \left(\Delta - \ln\left(\frac{m^2}{\mu^2}\right) + 1 + \mathcal{O}(\epsilon)\right) \,. \tag{7.26}$$

The integral contains an ultraviolet divergence expressed in the limit $\epsilon \to 0$.

7.1.3. The Scalar Integral B_0

The scalar integral

$$B_0(p_1^2, m_0^2, m_1^2) = \frac{(2\pi\mu)^{4-D}}{i\pi^2} \int \mathrm{d}^D q \, \frac{1}{(q^2 - m_0^2 + i\epsilon)[(q+p_1)^2 - m_1^2 + i\epsilon]} \,. \tag{7.27}$$

appears at two point functions. By the Feynman parametrization

$$\frac{1}{ab} = \int_0^1 \mathrm{d}x \, \frac{1}{\Big(a(1-x) + bx\Big)^2} \,. \tag{7.28}$$

identifying

$$a = q^2 - m_0^2 + i\epsilon \,, \qquad b = (q+p_1)^2 - m_1^2 + i\epsilon \,. \tag{7.29}$$

and the parametrization

$$q' = q + xp_1 \,, \qquad \mathrm{d}q = \mathrm{d}q' \,, \qquad A = x^2 p_1^2 - x\,(p_1^2 - m_1^2 + m_0^2) + m_0^2 \,. \tag{7.30}$$

(7.27) can be written as

$$B_0(p_1^2, m_0^2, m_1^2) = \frac{(2\pi\mu)^{4-D}}{i\pi^2} \int_0^1 \mathrm{d}x \, I_2(A) \,, \tag{7.31}$$

with the integral

$$I_2(A) = i\pi^{D/2} \frac{\Gamma\Big(\frac{4-D}{2}\Big)}{\Gamma(2)} \, (A - i\epsilon)^{D/2-2} \,. \tag{7.32}$$

The parameter $\epsilon = \frac{4-D}{2}$ is introduced again and the relation

$$\Gamma(\epsilon) = \frac{1}{\epsilon} \, \Gamma(1+\epsilon) \,. \tag{7.33}$$

for the Euler Γ function is used. If the result is expanded around $\epsilon = 0$, the result is

$$B_0(p_1^2, m_0^2, m_1^2) = \left(\frac{c_\epsilon}{\epsilon} - \int_0^1 \mathrm{d}x \, \ln \left(\frac{x^2 p_1^2 - x\,(p_1^2 - m_1^2 + m_0^2) + m_0^2 - i\epsilon}{\mu^2} \right) + \mathcal{O}(\epsilon) \right) . \tag{7.34}$$

We again encounter the factor c_ϵ which when expanded transforms the pole $\frac{1}{\epsilon}$

$$\frac{c_\epsilon}{\epsilon} = \Delta = \frac{1}{\epsilon} - \gamma_E + \ln 4\pi \,. \tag{7.35}$$

An additional feature of the scalar integral B_0 is that the argument can become negative in the logarithm for certain parameter sets of the arguments. Therefore the logarithm in the complex plane must be considered for such a case. As an example we very briefly

discuss $B_0(0,0,0)$. Here the logarithm results in a further divergence which can be identified as infrared divergence. This specific loop can be expressed as

$$B_0(0,0,0) = \frac{1}{\epsilon_{\mathrm{UV}}} - \frac{1}{\epsilon_{\mathrm{IR}}}. \tag{7.36}$$

Infrared divergences occur through the exchange of mass less particles, like in our case the gluon. While the UV divergences are canceled by the respective counterterms, Chapter 8, the IR divergences are canceled by diagrams emitting an additional gluon. This is discussed in greater detail in Chapter 9.

7.1.4. Tensor Reduction

So far we have only considered scalar integrals. As seen in the vertex correction in Eq.(7.6), the numerator can also contain any order of q. Therefore we need also non-scalar integrals. We look at these occurring tensors using the example of the 2-point functions. With the order q in the numerator the tensor B^μ can occur, with the factor $q^\mu q^\nu$ the tensor $B^{\mu\nu}$ occurs. These tensors can be represented as follows

$$B^\mu = p_1^\mu B_1\,, \tag{7.37}$$

$$B^{\mu\nu} = \mathrm{g}^{\mu\nu} B_{00} + p_1^\mu p_1^\nu B_{11}\,. \tag{7.38}$$

Let us take a closer look at B^μ and multiply on both sides of the Eq. (7.37) the only external 4-momentum p_1

$$p_1^\mu B_1 = \frac{(2\pi\mu)^{4-D}}{i\pi^2} \int \mathrm{d}^D q \frac{p_1.q}{[q^2 - m_0^2 + i\epsilon][(q-p_1)^2 - m_1^2 + i\epsilon]} = p_1^2 B_1. \tag{7.39}$$

The product $p_1.q$ can be factorized with the respective denominators

$$p_1.q = \frac{1}{2}([(q+p_1)^2 - m_1^2 + i\epsilon] - [q^2 - m_0^2 + i\epsilon] - [p_1^2 - m_1^2 + m_0^2]) \tag{7.40}$$

By this trick the integral in Eq.(7.37) can be decomposed into already known scalar integrals

$$\begin{aligned} p_1^2 B_1 = \frac{(2\pi\mu)^{4-D}}{i\pi^2} \Big(& \int \mathrm{d}^D q \frac{1}{q^2 - m_0^2 + i\epsilon} - \int \mathrm{d}^D q \frac{1}{(q-p_1)^2 - m_1^2 + i\epsilon} \\ & - (p_1^2) - m_1^2 + m_0^2) \int \mathrm{d}^D q \frac{1}{[q^2 - m_0^2 + i\epsilon][(q-p_1)^2 - m_1^2 + i\epsilon]} \\ & = \frac{1}{2}[A_0(m_0^2) - A_0(m_1^2) - (p_1^2 - m_1^2 + m_0^2) B_0(p_1^2, m_0^2, m_1^2)] \Big). \end{aligned} \tag{7.41}$$

The factor B_1 for the integral Eq.(7.37) is

$$B_1 = \frac{1}{2p_1^2}[A_0(m_0^2) - A_0(m_1^2) - (p_1^2 - m_1^2 + m_0^2) B_0(p_1^2, m_0^2, m_1^2)]. \tag{7.42}$$

The divergence of

$$B_1(p_1^2, m_0^2, m_1^2) \sim -\frac{1}{2}\Delta + \text{finite terms} \tag{7.43}$$

can be determined from the scalar integrals. Analogously, the coefficients

$$\begin{aligned} B_{00}(p_1^2, m_0^2, m_1^2) = \frac{1}{2(D-1)} &[A_0(m_1^2) + 2m_0^2 B_0(p_1^2, m_0^2, m_1^2) \\ &+ (p_1^2 - m_1^2 + m_0^2) B_1(p_1^2, m_0^2, m_1^2)], \end{aligned} \tag{7.44}$$

$$\begin{aligned} B_{11}(p_1^2, m_0^2, m_1^2) = \frac{1}{2(D-1)} &[(D-2)A_0(m_1^2) - 2m_0^2 B_0(p_1^2, m_0^2, m_1^2) \\ &- D(p_1^2 - m_1^2 + m_0^2) B_1(p_1^2, m_0^2, m_1^2)] \end{aligned} \tag{7.45}$$

for Eq.(7.38) can be determined. Where the factors $\frac{1}{2(D-1)}$ have to be expanded in terms of ϵ to show the divergences explicitly

$$\frac{1}{2(D-1)} = \frac{1}{6}\frac{1}{(1-\frac{2}{3}\epsilon} = \Big(1 + \frac{2}{3}\epsilon + \mathcal{O}(\epsilon)\Big). \tag{7.46}$$

Resulting in the corresponding divergent proportions

$$B_{00}(p_1^2, m_0^2, m_1^2) \sim -\frac{1}{12}(p_1^2 - 3(m_0^2 + m_1^2))\Delta + \text{finiteterms} \tag{7.47}$$

$$B_{11}(p_1^2, m_0^2, m_1^2) \sim \frac{1}{3}\Delta + \text{finiteterms}. \tag{7.48}$$

7.2. Calculation of Virtual Corrections

Before we discuss specific details of the next-to-leading order calculation, we will address the systematics of SUSY-QCD corrections to processes which at leading order have both strong and electroweak contributions (see Eq. (6.6)). If we consider any radiative corrections (SUSY-QCD or electroweak) to the processes in question, the cross section including the next-to-leading order corrections can be symbolically written as

$$\begin{aligned} \sigma^{\text{NLO}} = \sigma^{\text{Tree}} &+ \Delta\sigma_s^{\text{NLO}}\Big(\alpha_s^3\Big) + \Delta\sigma_{se}^{\text{NLO}}\Big(\alpha_s^2\alpha_e\Big) \\ &+ \Delta\sigma_e^{\text{NLO}}\Big(\alpha_s\alpha_e^2\Big) + \Delta\sigma_{ee}^{\text{NLO}}\Big(\alpha_e^3\Big). \end{aligned} \tag{7.49}$$

The SUSY-QCD corrections contribute to the $\Delta\sigma_s^{\text{NLO}}$, $\Delta\sigma_{se}^{\text{NLO}}$ and $\Delta\sigma_e^{\text{NLO}}$ parts of the NLO cross section whereas the electroweak corrections would contribute to the $\Delta\sigma_{se}^{\text{NLO}}$, $\Delta\sigma_e^{\text{NLO}}$ and $\Delta\sigma_{ee}^{\text{NLO}}$ parts. Both classes of corrections, the SUSY-QCD and the electroweak, are ultraviolet and infrared finite and gauge independent by themselves making them formally consistent.

The first and leading term in the NLO correction is $\Delta\sigma_s^{\text{NLO}}\Big(\alpha_s^3\Big)$ which receives contributions only from SUSY-QCD corrections. In particular these are the SUSY-QCD

corrections to the gluino exchange diagrams interfered with the gluino tree-level contribution. These corrections are the main result of this analysis.

The following term $\Delta\sigma_{se}^{\mathrm{NLO}}\left(\alpha_s^2\alpha_e\right)$ receives contributions from three sources - from the interference of the SUSY-QCD corrected gluino exchange with the electroweak gaugino exchange, from the interference of the SUSY-QCD corrected electroweak gaugino exchange with the gluino diagrams and the last contribution would come from electroweak corrections to the gluino exchange interfered with the gluino tree-level. The last contribution is not included in this analysis and even though it is formally of the same order, due to the small size of the electroweak corrections which are typically a factor 10 smaller than SUSY-QCD ones this last contribution is the smallest of the three. This way our analysis provides also the leading corrections in the term $\Delta\sigma_{se}^{\mathrm{NLO}}\left(\alpha_s^2\alpha_e\right)$.

The third term $\Delta\sigma_{e}^{\mathrm{NLO}}\left(\alpha_s\alpha_e^2\right)$ contains the interference of the SUSY-QCD corrected electroweak gaugino exchange with the leading order electroweak gaugino diagrams as well as electroweak corrections to both parts of the interference between the gluino and the electroweak gaugino exchange.

The last term $\Delta\sigma_{ee}^{\mathrm{NLO}}\left(\alpha_e^3\right)$ is not considered here as it contains only electroweak corrections to the electroweak parts of the cross section.

The analysis presented here does not consider electroweak corrections as they are for the most part subleading and contribute about 1% to 3% correction [130, 131]. In some instances however, the electroweak corrections and specifically the Yukawa corrections can become important [132]. Even though we do not calculate electroweak corrections in this analysis, the leading effects of the enhanced Yukawa corrections are taken into account as described in [114]. In particular, these become relevant in the case of chargino exchange in the Scenario II (neutralino exchanges are not as enhanced due to the lightest neutralino being a pure bino in both scenarios).

As the discussion below shows, the SUSY-QCD corrections presented here are the dominant corrections even in scenarios with large $\tan\beta$ and are even more dominant owing to the presence of the Sommerfeld enhancement.

The one-loop SUSY-QCD corrections receive contributions from propagator-, vertex-corrections and box diagrams

$$\Delta\sigma^{\mathrm{NLO}} = \Delta\sigma_1^{\mathrm{vert}} + \Delta\sigma_2^{\mathrm{vert}} + \Delta\sigma^{\mathrm{prop}} + \Delta\sigma^{\mathrm{box}}\,. \tag{7.50}$$

In order to provide a powerful tool for SUSY-QCD corrections, a generic extendable structure is chosen. In the following we demonstrate the calculation on chosen examples. First we investigate the propagator corrections with a more detailed view on the gluino propagator corrections [133]. The calculation of the vertex corrections will be discussed by the vertex corrections depicted in Fig. 7.2. Furthermore the generic structures of all contributing vertex corrections are summarized. As a last step, the generic box diagrams are briefly discussed.

7.2.1. Propagator Corrections

The gluino propagator corrections receives contributions of three self energy diagrams depicted in Fig. 7.4. Due to the majorana nature of the gluino, the third diagram containing an anti-quark and anti-squark (the opposite fermion flow to the second diagram) has to be taken into account.

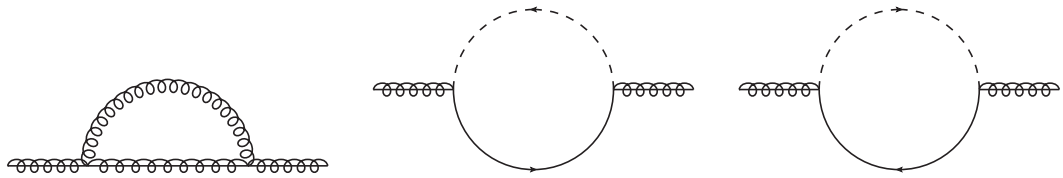

Figure 7.4.: Contributing self energy diagrams for the propagator corrections of the gluino.

We start with the calculation of the first loop diagram Fig. 7.5 containing a gluino and a gluon. The coupling constants g_0 and g_1 are just constants defined by the corresponding Feynman rules (B.3). The matrix element is given by

$$\begin{aligned}
\mathcal{M}^{\text{prop}}_{\tilde{g}_1} =& \overline{u}(p)\mu^{4-D}\int_q \frac{d^Dq}{(2\pi)^D}\, i\boxed{1}\frac{(\not{p}+\not{q}+M_1)}{\mathcal{D}_1}\, i\boxed{0}\,\frac{-i\mathrm{g}^{\mu\nu}}{\mathcal{D}_0}u(p)\\
=& -\overline{u}(p)\mu^{4-D}\int_q \frac{d^Dq}{(2\pi)^D} g_0 g_1 (i\mathrm{f}^{abc})(i\mathrm{f}^{acb})\gamma^\nu \frac{(\not{p}+\not{q}+M_1)}{\mathcal{D}_1}\gamma^\mu \frac{\mathrm{g}^{\mu\nu}}{\mathcal{D}_0}u(p)\\
=& -N^2\overline{u}(p)\mu^{4-D}\int_q \frac{d^Dq}{(2\pi)^D}\frac{g_0g_1}{\mathcal{D}_0\mathcal{D}_1}\Big[-(D-2)(\not{p}+\not{q})+DM_1\Big]u(p)\\
=& \frac{iN^2}{(4\pi)^2}\overline{u}(p)g_0g_1\Big[(D-2)(\not{p}B_0+\not{p}B_1)-DM_1B_0\Big]u(p)\,,
\end{aligned} \tag{7.51}$$

with N^2 from the color structure of the diagram. The matrix element leads to the generic form

$$\mathcal{M}^{\text{prop}}_{\tilde{g}} = \frac{i}{(4\pi)^2}\overline{u}(p)\Big[m_{\tilde{g}}(\Pi^{S,L}P_L+\Pi^{S,R}P_R)+\not{p}(\Pi^{f,L}P_L+\Pi^{f,R}P_R)\Big]u(p)\,, \tag{7.52}$$

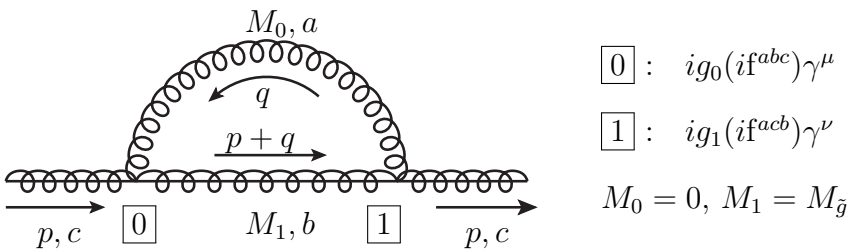

Figure 7.5.: Self energy containing a gluon and a gluino in the loop.

having $\Pi_1^{S,L} = \Pi_1^{S,R} = \Pi^{g,S}$ and $\Pi_1^{f,L} = \Pi^{g,L} = \Pi_1^{f,R} = \Pi^{g,R}$ in the case of Eq. 7.51 with

$$\Pi^{g,S} = -N^2 D g_0 g_1 \frac{M_1}{m_{\tilde{g}}} B_0 \tag{7.53}$$

$$\Pi^{g,L} = N^2 (D-2) g_0 g_1 (B_0 + B_1)\,. \tag{7.54}$$

The arguments of the tensor reduction are

$$B_0(p^2, M_0^2, M_1^2)\,, \tag{7.55}$$

$$B_1(p^2, M_0^2, M_1^2)\,. \tag{7.56}$$

With the use of the generic masses M_0 and M_1 and the momentum p^2 this set of arguments is true for all self energies contributing to the gluino propagator correction in t- and u-channel.

The second self energy contributing to the propagator correction of the gluino is the loop containing a quark and a squark Fig.7.6. The coupling constants $g_0^{L/R}$ and $g_1^{L/R}$ are given by (B.8) and (B.9). The matrix element is

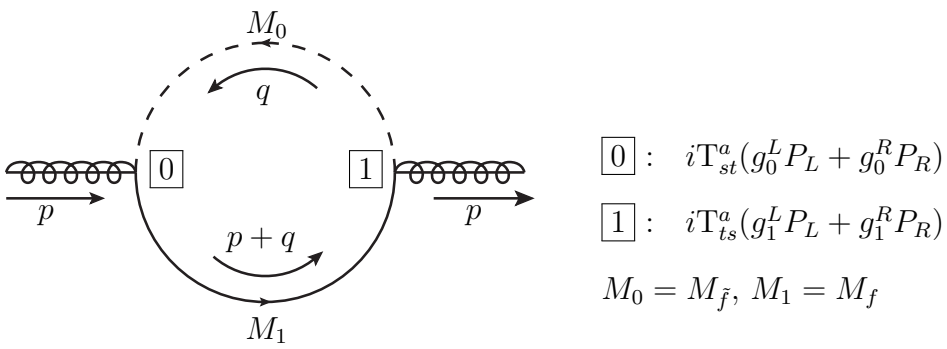

Figure 7.6.: Self energy of gluino, containing a quark and a squark in the loop.

$$\mathcal{M}^{\text{prop}}_{\tilde{g}_2} = \overline{u}(p)\mu^{4-D} \int_q \frac{d^D q}{(2\pi)^D}\, i\boxed{1} \frac{i(\not{p} + \not{q} + M_1)}{\mathcal{D}_1}\, i\boxed{0} \frac{i}{\mathcal{D}_0} u(p) \tag{7.57}$$

$$= \overline{u}(p)\mu^{4-D} \int_q \frac{d^D q}{(2\pi)^D} \frac{1}{\mathcal{D}_0 \mathcal{D}_1} \left[(\not{p}_0 + \not{p} B_1) \overleftrightarrow{\boxed{1}} + M_1 B_0 \boxed{1} \right] \boxed{0}\, u(p)\,, \tag{7.58}$$

with the coefficient identified by comparison with Eq. (7.52) as

$$\Pi_2^{S,L} = \frac{N}{2} g_0^L g_1^L \frac{M_1}{m_{\tilde{g}}} B_0 \tag{7.59}$$

$$\Pi_2^{f,L} = \frac{N}{2} g_0^L g_1^R (B_0 + B_1)\,. \tag{7.60}$$

The factor $\frac{N}{2}$ comes from the color structure. The right chiral parts can be obtained by switching the chiral components of the couplings

$$\Pi^{S,R} = \Pi^{S,L}(g_i^L \leftrightarrow g_i^R)\,, \tag{7.61}$$
$$\Pi^{f,R} = \Pi^{f,L}(g_i^L \leftrightarrow g_i^R)\,. \tag{7.62}$$

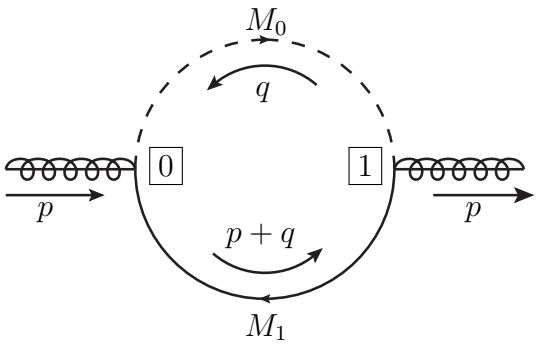

$\boxed{0}$: $iT^a_{ts}(g_0^R P_L + g_0^L P_R)$

$\boxed{1}$: $iT^a_{st}(g_1^R P_L + g_1^L P_R)$

$M_0 = M_{\tilde{f}},\ M_1 = M_f$

Figure 7.7.: Self energy of gluino, containing a anti-quark and a anti-squark in the loop.

The only differences in the calculation of the third diagram with a anti-quark and anti-squark in the loop to the previous calculation is the change of left and right handed part in the couplings due to the opposite fermion flow and a minus sign for the fermionic coupling. Therefore this diagram results in

$$\Pi_3^{S,L} = \frac{N}{2} g_0^R g_1^R \frac{M_1}{m_{\tilde{g}}} B_0 \tag{7.63}$$
$$\Pi_3^{f,L} = -\frac{N}{2} g_0^R g_1^L (B_0 + B_1) \tag{7.64}$$

The total matrix element is given by

$$\Pi^{S,L} = \sum_{i=1,3} \Pi_i^{S,L}\,, \qquad \Pi^{S,R} = \sum_{i=1,3} \Pi_i^{S,R}\,, \tag{7.65}$$
$$\Pi^{f,L} = \sum_{i=1,3} \Pi_i^{f,L}\,, \qquad \Pi^{f,R} = \sum_{i=1,3} \Pi_i^{f,R}\,. \tag{7.66}$$

The generic amplitudes corresponding to the different processes containing a gluino

propagator are

$$\begin{aligned}\mathcal{M}^t_{\text{prop},\tilde{q}\tilde{q}\to qq} =& \frac{i}{(t-m_{\tilde{g}})^2}(\bar{u}(k_1)(g_1^L P_L + g_1^R P_R)(-\not{p}_1 + \not{k}_1 + m_{\tilde{g}})((-\not{p}_1 + \not{k}_1) \\ &\times (\Pi^{F,L}P_L + \Pi^{F,R}P_R) + m_{\tilde{g}}(\Pi^{S,L}P_L + \Pi^{S,R}P_R))(-\not{p}_1 + \not{k}_1 + m_{\tilde{g}}) \\ &\times (g_2^L P_L + g_2^R P_R)v(k_2)\,, \end{aligned} \tag{7.67}$$

$$\begin{aligned}\mathcal{M}^u_{\text{prop},\tilde{q}\tilde{q}\to qq} =& \frac{i}{(u-m_{\tilde{g}})^2}(\bar{u}(k_1)(g_1^L P_L + g_1^R P_R)(-\not{p}_2 + \not{k}_1 + m_{\tilde{g}})((-\not{p}_2 + \not{k}_1) \\ &\times (\Pi^{F,L}P_L + \Pi^{F,R}P_R) + m_{\tilde{g}}(\Pi^{S,L}P_L + \Pi^{S,R}P_R))(-\not{p}_2 + \not{k}_1 + m_{\tilde{g}}) \\ &\times (g_2^L P_L + g_2^R P_R)v(k_2)\,, \end{aligned} \tag{7.68}$$

$$\begin{aligned}\mathcal{M}^t_{\text{prop},\tilde{q}\tilde{q}^*\to q\bar{q}} =& \frac{i}{(t-m_{\tilde{g}})^2}(\bar{u}(k_1)(g_1^L P_L + g_1^R P_R)(-\not{p}_1 + \not{k}_1 + m_{\tilde{g}})((-\not{p}_1 + \not{k}_1) \\ &\times (\Pi^{F,L}P_L + \Pi^{F,R}P_R) + m_{\tilde{g}}(\Pi^{S,L}P_L + \Pi^{S,R}P_R))(-\not{p}_1 + \not{k}_1 + m_{\tilde{g}}) \\ &\times (g_2^R P_L + g_2^L P_R)v(k_2)\,. \end{aligned} \tag{7.69}$$

The amplitude squared including propagator corrections is then written as

$$\begin{aligned}|\mathcal{M}^2|^{\text{prop}}_{\tilde{q}\tilde{q}\to qq} =& \, 2\Re(\mathcal{M}^t_{\text{prop},\tilde{q}\tilde{q}\to qq}\mathcal{M}^t_{\tilde{g}}) + 2\Re(\mathcal{M}^t_{\text{prop},\tilde{q}\tilde{q}\to qq}\mathcal{M}^u_{\tilde{g}}) \\ &+ 2\Re(\mathcal{M}^t_{\text{prop},\tilde{q}\tilde{q}\to qq}\mathcal{M}^t_{\tilde{\chi}}) + 2\Re(\mathcal{M}^t_{\text{prop},\tilde{q}\tilde{q}\to qq}\mathcal{M}^u_{\tilde{\chi}}) \\ &+ 2\Re(\mathcal{M}^u_{\text{prop},\tilde{q}\tilde{q}\to qq}\mathcal{M}^t_{\tilde{g}}) + 2\Re(\mathcal{M}^u_{\text{prop},\tilde{q}\tilde{q}\to qq}\mathcal{M}^u_{\tilde{g}}) \\ &+ 2\Re(\mathcal{M}^u_{\text{prop},\tilde{q}\tilde{q}\to qq}\mathcal{M}^t_{\tilde{\chi}}) + 2\Re(\mathcal{M}^u_{\text{prop},\tilde{q}\tilde{q}\to qq}\mathcal{M}^u_{\tilde{\chi}})\,, \end{aligned} \tag{7.70}$$

$$\begin{aligned}|\mathcal{M}^2|^{\text{prop}}_{\tilde{q}\tilde{q}^*\to q\bar{q}} =& \, 2\Re(\mathcal{M}^t_{\text{prop},\tilde{q}\tilde{q}^*\to q\bar{q}}\mathcal{M}^s_{g}) + 2\Re(\mathcal{M}^t_{\text{prop},\tilde{q}\tilde{q}^*\to q\bar{q}}\mathcal{M}^s_{H}) \\ &+ 2\Re(\mathcal{M}^t_{\text{prop},\tilde{q}\tilde{q}^*\to q\bar{q}}\mathcal{M}^s_{V}) + 2\Re(\mathcal{M}^t_{\text{prop},\tilde{q}\tilde{q}^*\to q\bar{q}}\mathcal{M}^t_{\tilde{g}}) \\ &+ 2\Re(\mathcal{M}^t_{\text{prop},\tilde{q}\tilde{q}^*\to q\bar{q}}\mathcal{M}^t_{\tilde{\chi}})\,. \end{aligned} \tag{7.71}$$

7.2.2. Vertex Corrections

We start with the process $\tilde{q}\tilde{q}^* \to q\bar{q}$, reconsidering the vertex correction Fig. 7.2 of the s-channel with a Higgs in the propagator the amplitude can be rewritten to a generic form for the amplitude

$$\mathcal{M}^s_{H,1} = \frac{-i}{s-m_H} g_H \bar{u}(k_1)(g_L P_L + g_R P_R)v(k_2)\,, \tag{7.72}$$

with a redefined coupling constant g_H. By performing the tensor reduction in Eq. (7.6) the redefined coupling constants resolves in

$$\begin{aligned} g_H =& C_F g_0 g_1 g_2 \Big(B_0 + \Big(C_1(-s+3m_1^2+m_2^2) + C_2(-s+m_1^2+3m_2^2)\Big) \\ &+ C_0\Big(M_0^2 + 2(-s+m_1^2+m_2^2)\Big)\Big)\,, \end{aligned} \tag{7.73}$$

with $M_0 = 0$ as the gluon mass, M_1 and M_2 are the corresponding sfermion masses, the couplings g_1 and g_2 correspond to the Feynman rules (B.4) and g_0 is given by the Feynman rule (B.21). The tensors having the argument set

$$C_i(m_1^2, s, m_2^2, M_0^2, M_1^2, M_2^2) \tag{7.74}$$

$$B_i(s, M_1^2, M_2^2)\,. \tag{7.75}$$

By setting g_H back on the tree level coupling, the tree level amplitude would be restored. In general divergences only occur in parts of the amplitude proportional to the tree level amplitude. Occurring divergences in non tree level structures already cancel within the amplitude.

In total, the s-channel diagrams contributing to the process $\tilde{q}\tilde{q}^* \to q\bar{q}$ contain scalar (index H) and vector (index g) propagators. The introduced generic forms of the amplitudes to model the vertex corrections receive a one as an index for the vertex correction on the initial state side and a two for the final state side. The corresponding generic amplitudes are given by Eqs. (7.72) and

$$\mathcal{M}^s_{g,1} = \frac{i}{s}\Big(A_{p_1-p_2}(p_1^\mu - p_2^\mu) + A_{p_1+p_2}(p_1^\mu + p_2^\mu)\Big)\bar{u}(k_1)\gamma^\mu(g^L P_L + g^R P_R)v(k_2)\,, \tag{7.76}$$

$$\begin{aligned}
\mathcal{M}^s_{g,2} = {} & \frac{ig}{s}(p_1^\mu - p_2^\mu)\mathrm{g}^{\mu\nu}\bar{u}(k_1)\Big(\gamma^\nu(A_1^L P_L + A_1^R P_R) + (k_1^\nu - k_2^\nu)(A_2^L P_L + A_2^R P_R) \\
& + (k_1^\nu + k_2^\nu)(A_3^L P_L + A_3^R P_R) + \gamma^\nu(B_1^L P_L + B_1^R P_R)(\not{k}_2 - m_4) \\
& + (k_1^\nu - k_2^\nu)(B_2^L P_L + B_2^R P_R)(\not{k}_2 - m_4) + (k_1^\nu + k_2^\nu)(B_3^L P_L + B_3^R P_R)(\not{k}_2 - m_4) \\
& + (\not{k}_1 - m_3)\gamma^\nu(C_1^L P_L + C_1^R P_R) + (\not{k}_1 - m_3)(k_1^\nu - k_2^\nu)(C_2^L P_L + C_2^R P_R) \\
& + (\not{k}_1 - m_3)(k_1^\nu + k_2^\nu)(C_3^L P_L + C_3^R P_R) + (\not{k}_1 - m_3)\gamma^\nu(D_1^L P_L + D_1^R P_R)(\not{k}_2 - m_4) \\
& + (\not{k}_1 - m_3)(k_1^\nu - k_2^\nu)(D_2^L P_L + D_2^R P_R)(\not{k}_2 - m_4) \\
& + (\not{k}_1 - m_3)(k_1^\nu + k_2^\nu)(D_3^L P_L + D_3^R P_R)(\not{k}_2 - m_4)\Big)v(k_2)\,,
\end{aligned} \tag{7.77}$$

$$\begin{aligned}
\mathcal{M}^s_{H,2} = {} & \frac{-i}{s - m_H} g\bar{u}(k_1)\Big((A_L P_L + A_R P_R) + (B_L P_L + B_R P_R)(\not{k}_2 - m_4)\,, \\
& + (\not{k}_1 - m_3)(C_L P_L + C_R P_R) + (\not{k}_1 - m_3)(D_L P_L + D_R P_R)(\not{k}_2 - m_4)\Big)v(k_2)
\end{aligned} \tag{7.78}$$

$$\begin{aligned}
\mathcal{M}^t_{\tilde{g},1} = {} & \frac{-i}{t - m_{\tilde{g}}}\bar{u}(k_1)\Big((A_L P_L + A_R P_R) + (B_L P_L + B_R P_R)(\not{p}_1 - \not{k}_1 - m_{\tilde{g}}) \\
& + (\not{k}_1 - m_3)(C_L P_L + C_R P_R) + (k_1 - m_3)(D_L P_L + D_R P_R)(\not{p}_1 - \not{k}_1 - m_{\tilde{g}})\Big) \\
& \times (-\not{p}_1 + \not{k}_1 - m_{\tilde{g}})(g_R P_L + g_L P_R)v(k_2)\,,
\end{aligned} \tag{7.79}$$

$$\begin{aligned}
\mathcal{M}^t_{\tilde{g},2} = {} & \frac{-i}{t - m_{\tilde{g}}}\bar{u}(k_1)(g_L P_L + g_R P_R)(-\not{p}_1 + \not{k}_1 - m_{\tilde{g}})\Big((A_L P_L + A_R P_R) \\
& + (B_L P_L + B_R P_R)(-\not{k}_2 - m_4) + (\not{p}_2 - \not{k}_2 - m_{\tilde{g}})(C_L P_L + C_R P_R) \\
& + (\not{p}_2 - \not{k}_2 - m_{\tilde{g}})(D_L P_L + D_R P_R)(-\not{k}_2 - m_4)\Big)v(k_2)\,.
\end{aligned} \tag{7.80}$$

The corresponding loop diagrams for the vertex corrections of $\mathcal{M}^s_{H,1}$ and $\mathcal{M}^s_{H,2}$ are depicted in Fig. 7.8. The vertex corrections of the gluon propagator are depicted in Figs. 7.9 and 7.10. The fermionic propagator in the t-channels and u-channels of the processes $\tilde{q}\tilde{q}^* \to q\bar{q}$ and $\tilde{q}\tilde{q} \to qq$ differ in color factor, coupling constant and mass for gauginos (neutralino and chargino) and gluino, but receive same the generic structure in the amplitudes. In case of the t-channel in $\tilde{q}\tilde{q}^* \to q\bar{q}$ the generic amplitudes are given in Eqs. (7.79) and (7.80) with the corresponding loop diagrams depicted in Fig. 7.11. Here, for the vertex correction of the lower vertex the opposite fermion flow has to be taken into account.The same diagrams contribute for the t- and u-channel of $\tilde{q}\tilde{q} \to qq$ with the generic amplitudes Eqs.(7.81) and (7.82). For the u-channel the amplitudes are given by Eqs. (7.83) and (7.84)

$$\begin{aligned}
\mathcal{M}^{\tilde{q}\tilde{q}\to qq,t}_{\text{vert},\tilde{g},1} =& \frac{-i}{t-m_{\tilde{g}}}\bar{v}(k_1)\Big((A_LP_L + A_RP_R) + (B_LP_L + B_RP_R)(\not{p}_1 - \not{k}_1 - m_{\tilde{g}}) \\
&+ (\not{k}_1 - m_3)(C_LP_L + C_RP_R) + (\not{k}_1 - m_3)(D_LP_L + D_RP_R) \\
&\times (\not{p}_1 - \not{k}_1 - m_{\tilde{g}})\Big)(-\not{p}_1 + \not{k}_1 + m_{\tilde{g}})(g_2^LP_L + g_2^RP_R)v(k_2)\,, \qquad (7.81)\\
\mathcal{M}^{\tilde{q}\tilde{q}\to qq,t}_{\text{vert},\tilde{g},2} =& \frac{-i}{t-m_{\tilde{g}}}\bar{v}(k_1)(g_1^LP_L + g_1^RP_R)(-\not{p}_1 + \not{k}_1 + m_{\tilde{g}}) \\
&\times \Big((A_LP_L + A_RP_R) + (-\not{p}_2 + \not{k}_2 - m_{\tilde{g}})(B_LP_L + B_RP_R) \\
&+ (C_LP_L + C_RP_R)(-\not{k}_2 - m_4) + (-\not{p}_2 + \not{k}_2 - m_{\tilde{g}})(D_LP_L + D_RP_R) \\
&\times (-\not{k}_2 - m_4)\Big)v(k_2)\,, \qquad (7.82)\\
\mathcal{M}^{\tilde{q}\tilde{q}\to qq,u}_{\text{vert},\tilde{g},1} =& \frac{-i}{u-m_{\tilde{g}}}\bar{v}(k_1)\Big((A_LP_L + A_RP_R) + (B_LP_L + B_RP_R)(\not{p}_2 - \not{k}_1 - m_{\tilde{g}}) \\
&+ (\not{k}_1 - m_3)(C_LP_L + C_RP_R) + (\not{k}_1 - m_3)(D_LP_L + D_RP_R) \\
&\times (\not{p}_2 - \not{k}_1 - m_{\tilde{g}})\Big)(-\not{p}_2 + \not{k}_1 + m_{\tilde{g}})(g_2^LP_L + g_2^RP_R)v(k_2)\,, \qquad (7.83)\\
\mathcal{M}^{\tilde{q}\tilde{q}\to qq,u}_{\text{vert},\tilde{g},2} =& \frac{-i}{u-m_{\tilde{g}}}\bar{v}(k_1)(g_1^LP_L + g_1^RP_R)(-\not{p}_2 + \not{k}_1 + m_{\tilde{g}}) \\
&\times \Big((A_LP_L + A_RP_R) + (-\not{p}_1 + \not{k}_2 - m_{\tilde{g}})(B_LP_L + B_RP_R) \\
&+ (C_LP_L + C_RP_R)(-\not{k}_2 - m_4) + (-\not{p}_1 + \not{k}_2 - m_{\tilde{g}})(D_LP_L + D_RP_R) \\
&\times (-\not{k}_2 - m_4)\Big)v(k_2)\,. \qquad (7.84)
\end{aligned}$$

Summing up, the squared amplitude containing all loop contributions up till now for $\tilde{q}\tilde{q} \to qq$ reads

$$
\begin{aligned}
|\mathcal{M}^2|^{\text{vertex}}_{\tilde{q}\tilde{q}\to qq} &= 2\Re(\mathcal{M}^{\tilde{q}\tilde{q}\to qq,t}_{\text{vert},\tilde{g},1}\mathcal{M}^{t*}_{\tilde{g}}) + 2\Re(\mathcal{M}^{\tilde{q}\tilde{q}\to qq,t}_{\text{vert},\tilde{g},1}\mathcal{M}^{u*}_{\tilde{g}}) + 2\Re(\mathcal{M}^{\tilde{q}\tilde{q}\to qq,u}_{\text{vert},\tilde{g},1}\mathcal{M}^{u*}_{\tilde{g}}) \\
&+ 2\Re(\mathcal{M}^{\tilde{q}\tilde{q}\to qq,u}_{\text{vert},\tilde{g},1}\mathcal{M}^{t*}_{\tilde{g}}) + 2\Re(\mathcal{M}^{\tilde{q}\tilde{q}\to qq,t}_{\text{vert},\tilde{g},1}\mathcal{M}^{t*}_{\tilde{\chi}}) + 2\Re(\mathcal{M}^{\tilde{q}\tilde{q}\to qq,t}_{\text{vert},\tilde{g},1}\mathcal{M}^{u*}_{\tilde{\chi}}) \\
&+ 2\Re(\mathcal{M}^{\tilde{q}\tilde{q}\to qq,u}_{\text{vert},\tilde{g},1}\mathcal{M}^{u*}_{\tilde{\chi}}) + 2\Re(\mathcal{M}^{\tilde{q}\tilde{q}\to qq,u}_{\text{vert},\tilde{g},1}\mathcal{M}^{t*}_{\tilde{\chi}}) + 2\Re(\mathcal{M}^{\tilde{q}\tilde{q}\to qq,t}_{\text{vert},\tilde{\chi},1}\mathcal{M}^{t*}_{\tilde{\chi}}) \\
&+ 2\Re(\mathcal{M}^{\tilde{q}\tilde{q}\to qq,t}_{\text{vert},\tilde{\chi},1}\mathcal{M}^{u*}_{\tilde{\chi}}) + 2\Re(\mathcal{M}^{\tilde{q}\tilde{q}\to qq,u}_{\text{vert},\tilde{\chi},1}\mathcal{M}^{u*}_{\tilde{\chi}}) + 2\Re(\mathcal{M}^{\tilde{q}\tilde{q}\to qq,u}_{\text{vert},\tilde{\chi},1}\mathcal{M}^{t*}_{\tilde{\chi}}) \\
&+ 2\Re(\mathcal{M}^{\tilde{q}\tilde{q}\to qq,t}_{\text{vert},\tilde{\chi},1}\mathcal{M}^{t*}_{\tilde{g}}) + 2\Re(\mathcal{M}^{\tilde{q}\tilde{q}\to qq,t}_{\text{vert},\tilde{\chi},1}\mathcal{M}^{u*}_{\tilde{g}}) + 2\Re(\mathcal{M}^{\tilde{q}\tilde{q}\to qq,u}_{\text{vert},\tilde{\chi},1}\mathcal{M}^{u*}_{\tilde{g}}) \\
&+ 2\Re(\mathcal{M}^{\tilde{q}\tilde{q}\to qq,u}_{\text{vert},\tilde{\chi},1}\mathcal{M}^{t*}_{\tilde{g}})\,. \qquad (7.85)
\end{aligned}
$$

In case of $\tilde{q}\tilde{q}^* \to q\bar{q}$ the squared amplitude is given by

$$
\begin{aligned}
|\mathcal{M}^2|^{\text{vertex}}_{\tilde{q}\tilde{q}^*\to q\bar{q}} &= 2\Re(\mathcal{M}^{\tilde{q}\tilde{q}^*\to q\bar{q},s}_{\text{vert},H,1}\mathcal{M}^{s*}_{H}) + 2\Re(\mathcal{M}^{\tilde{q}\tilde{q}^*\to q\bar{q},s}_{\text{vert},H,2}\mathcal{M}^{s*}_{H}) + 2\Re(\mathcal{M}^{\tilde{q}\tilde{q}^*\to q\bar{q},s}_{\text{vert},g,1}\mathcal{M}^{s*}_{H}) \\
&+ 2\Re(\mathcal{M}^{\tilde{q}\tilde{q}^*\to q\bar{q},s}_{\text{vert},g,2}\mathcal{M}^{s*}_{H}) + 2\Re(\mathcal{M}^{\tilde{q}\tilde{q}^*\to q\bar{q},t}_{\text{vert},\tilde{g},1}\mathcal{M}^{s*}_{H}) + 2\Re(\mathcal{M}^{\tilde{q}\tilde{q}^*\to q\bar{q},t}_{\text{vert},\tilde{g},2}\mathcal{M}^{s*}_{H}) \\
&+ 2\Re(\mathcal{M}^{\tilde{q}\tilde{q}^*\to q\bar{q},t}_{\text{vert},\tilde{\chi},1}\mathcal{M}^{s*}_{H}) + 2\Re(\mathcal{M}^{\tilde{q}\tilde{q}^*\to q\bar{q},t}_{\text{vert},\tilde{\chi},2}\mathcal{M}^{s*}_{H}) \\
&+ 2\Re(\mathcal{M}^{\tilde{q}\tilde{q}^*\to q\bar{q},s}_{\text{vert},H,1}\mathcal{M}^{s*}_{V}) + 2\Re(\mathcal{M}^{\tilde{q}\tilde{q}^*\to q\bar{q},s}_{\text{vert},H,2}\mathcal{M}^{s*}_{V}) + 2\Re(\mathcal{M}^{\tilde{q}\tilde{q}^*\to q\bar{q},s}_{\text{vert},g,1}\mathcal{M}^{s*}_{V}) \\
&+ 2\Re(\mathcal{M}^{\tilde{q}\tilde{q}^*\to q\bar{q},s}_{\text{vert},g,2}\mathcal{M}^{s*}_{V}) + 2\Re(\mathcal{M}^{\tilde{q}\tilde{q}^*\to q\bar{q},t}_{\text{vert},\tilde{g},1}\mathcal{M}^{s*}_{V}) + 2\Re(\mathcal{M}^{\tilde{q}\tilde{q}^*\to q\bar{q},t}_{\text{vert},\tilde{g},2}\mathcal{M}^{s*}_{V}) \\
&+ 2\Re(\mathcal{M}^{\tilde{q}\tilde{q}^*\to q\bar{q},t}_{\text{vert},\tilde{\chi},1}\mathcal{M}^{s*}_{V}) + 2\Re(\mathcal{M}^{\tilde{q}\tilde{q}^*\to q\bar{q},t}_{\text{vert},\tilde{\chi},2}\mathcal{M}^{s*}_{V}) \\
&+ 2\Re(\mathcal{M}^{\tilde{q}\tilde{q}^*\to q\bar{q},s}_{\text{vert},H,1}\mathcal{M}^{t*}_{\tilde{g}}) + 2\Re(\mathcal{M}^{\tilde{q}\tilde{q}^*\to q\bar{q},s}_{\text{vert},H,2}\mathcal{M}^{t*}_{\tilde{g}}) + 2\Re(\mathcal{M}^{\tilde{q}\tilde{q}^*\to q\bar{q},s}_{\text{vert},g,1}\mathcal{M}^{t*}_{\tilde{g}}) \\
&+ 2\Re(\mathcal{M}^{\tilde{q}\tilde{q}^*\to q\bar{q},s}_{\text{vert},g,2}\mathcal{M}^{t*}_{\tilde{g}}) + 2\Re(\mathcal{M}^{\tilde{q}\tilde{q}^*\to q\bar{q},t}_{\text{vert},\tilde{g},1}\mathcal{M}^{t*}_{\tilde{g}}) + 2\Re(\mathcal{M}^{\tilde{q}\tilde{q}^*\to q\bar{q},t}_{\text{vert},\tilde{g},2}\mathcal{M}^{t*}_{\tilde{g}}) \\
&+ 2\Re(\mathcal{M}^{\tilde{q}\tilde{q}^*\to q\bar{q},t}_{\text{vert},\tilde{\chi},1}\mathcal{M}^{t*}_{\tilde{g}}) + 2\Re(\mathcal{M}^{\tilde{q}\tilde{q}^*\to q\bar{q},t}_{\text{vert},\tilde{\chi},2}\mathcal{M}^{t*}_{\tilde{g}}) \\
&+ 2\Re(\mathcal{M}^{\tilde{q}\tilde{q}^*\to q\bar{q},s}_{\text{vert},H,1}\mathcal{M}^{t*}_{\tilde{\chi}}) + 2\Re(\mathcal{M}^{\tilde{q}\tilde{q}^*\to q\bar{q},s}_{\text{vert},H,2}\mathcal{M}^{t*}_{\tilde{\chi}}) + 2\Re(\mathcal{M}^{\tilde{q}\tilde{q}^*\to q\bar{q},s}_{\text{vert},g,1}\mathcal{M}^{t*}_{\tilde{\chi}}) \\
&+ 2\Re(\mathcal{M}^{\tilde{q}\tilde{q}^*\to q\bar{q},s}_{\text{vert},g,2}\mathcal{M}^{t*}_{\tilde{\chi}}) + 2\Re(\mathcal{M}^{\tilde{q}\tilde{q}^*\to q\bar{q},t}_{\text{vert},\tilde{g},1}\mathcal{M}^{t*}_{\tilde{\chi}}) + 2\Re(\mathcal{M}^{\tilde{q}\tilde{q}^*\to q\bar{q},t}_{\text{vert},\tilde{g},2}\mathcal{M}^{t*}_{\tilde{\chi}}) \\
&+ 2\Re(\mathcal{M}^{\tilde{q}\tilde{q}^*\to q\bar{q},t}_{\text{vert},\tilde{\chi},1}\mathcal{M}^{t*}_{\tilde{\chi}}) + 2\Re(\mathcal{M}^{\tilde{q}\tilde{q}^*\to q\bar{q},t}_{\text{vert},\tilde{\chi},2}\mathcal{M}^{t*}_{\tilde{\chi}})\,. \qquad (7.86)
\end{aligned}
$$

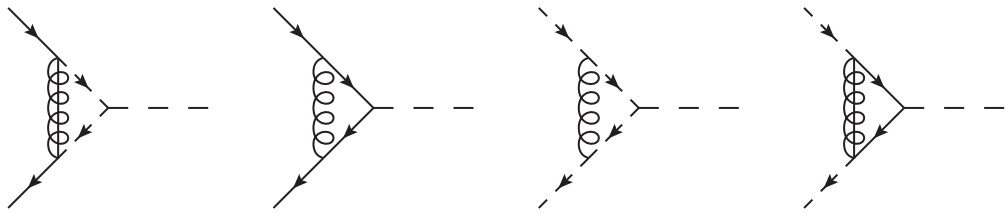

Figure 7.8.: Vertex correction of Higgs-fermion-femion and Higgs-sfermion-sfermion vertex.

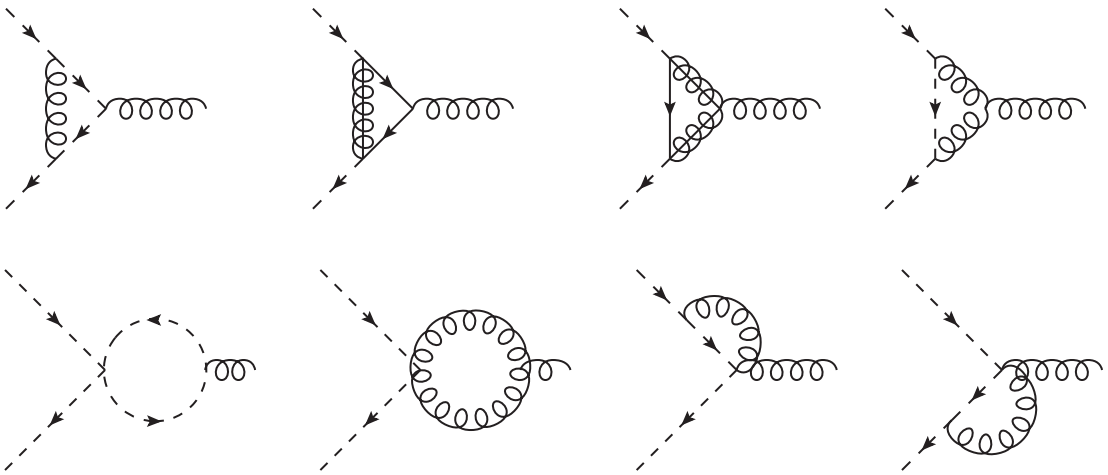

Figure 7.9.: Vertex-correction of the squark-squark-gluon vertex.

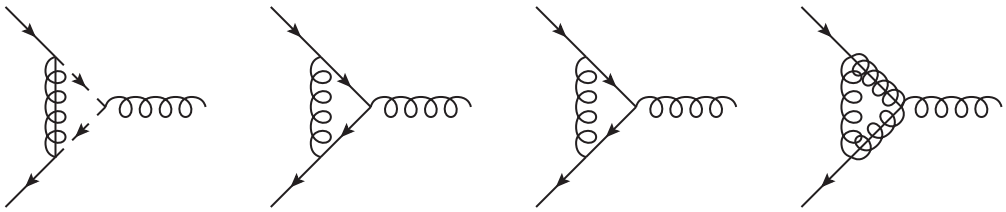

Figure 7.10.: Vertex correction of Gluon fermion femion.

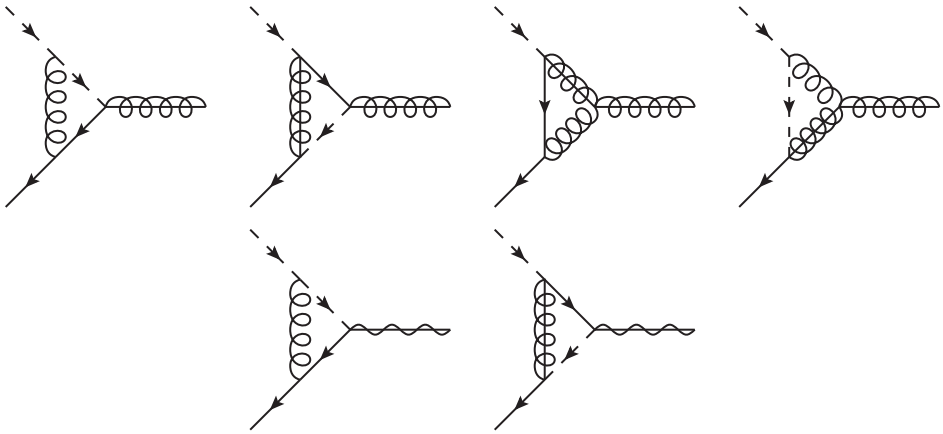

Figure 7.11.: Vertex-correction of the squark-quark-gluino vertex in the first line, vertex-correction of the squark-quark-neutralino vertex in the second line.

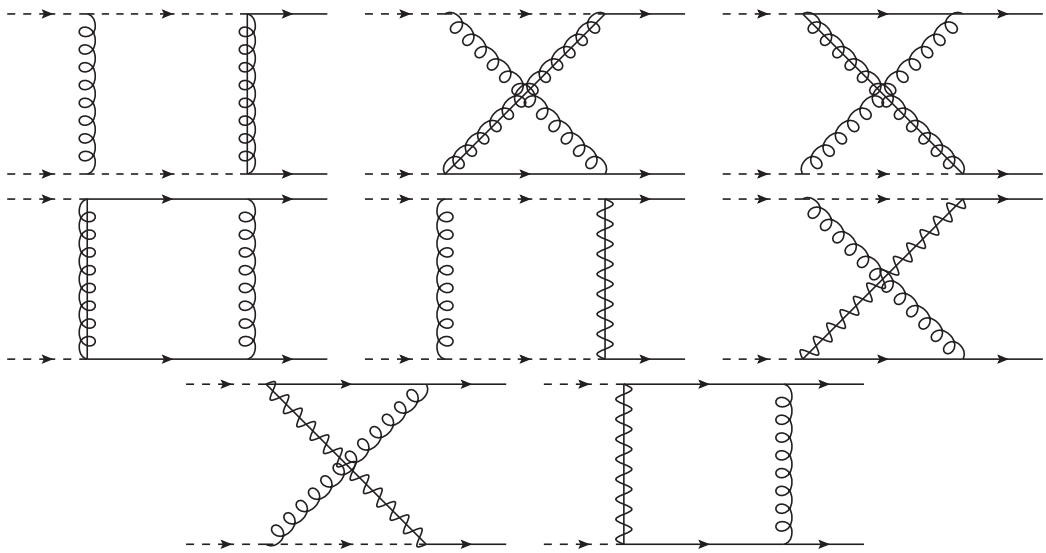

Figure 7.12.: Box-correction for $\tilde{q}\tilde{q} \to qq$.

7.2.3. Box Corrections

The last piece which is missing of the virtual corrections are the contributions of the box diagrams. Box contributions in case of the process $\tilde{q}\tilde{q} \to qq$ are represented in Fig. 7.12. The process $\tilde{q}\tilde{q}^* \to q\bar{q}$ have similar box diagrams resulting from the t-channel contributions of the gluino exchange Fig. 7.13 with additional diagrams from the s-channel gluon exchange. Further box diagrams from s-channel Higgs exchange are depicted in Fig. 7.14. Diagrams resulting from t-channel neutralino exchange are shown in Fig. 7.15.

All box diagrams can be expressed with the generic amplitude

$$\begin{aligned}\mathcal{M}_{\text{box}} =& i\bar{\text{u}}(k_1)\Big(\not{k}_1(C_L^{k_1}P_L + C_R^{k_1}P_R + D^{k_1}) + \not{k}_2(C_L^{k_2}P_L + C_R^{k_2}P_R + D^{k_2}) \\ &+ \not{p}_1(C_L^{p_1}P_L + C_R^{p_1}P_R + D^{p_1}) + (B_L P_L + B_R P_R) + A\Big)\text{v}(k_2)\,. \end{aligned} \tag{7.87}$$

The full squared matrix amplitude of the box contribution then reads

$$\begin{aligned}|\mathcal{M}^2|^{\text{box}}_{\tilde{q}\tilde{q}^*\to q\bar{q}} &= 2\Re(\mathcal{M}_{\text{box}}\mathcal{M}_H^{s*}) + 2\Re(\mathcal{M}_{\text{box}}\mathcal{M}_V^{s*}) \\ &+ 2\Re(\mathcal{M}_{\text{box}}\mathcal{M}_{\tilde{g}}^{t*}) + 2\Re(\mathcal{M}_{\text{box}}\mathcal{M}_{\tilde{\chi}}^{t*})\,, \end{aligned} \tag{7.88}$$

$$\begin{aligned}|\mathcal{M}^2|^{\text{box}}_{\tilde{q}\tilde{q}\to qq} &= 2\Re(\mathcal{M}_{\text{box}}\mathcal{M}_{\tilde{g}}^{t*}) + 2\Re(\mathcal{M}_{\text{box}}\mathcal{M}_{\tilde{\chi}}^{t*}) \\ &+ 2\Re(\mathcal{M}_{\text{box}}\mathcal{M}_{\tilde{g}}^{u*}) + 2\Re(\mathcal{M}_{\text{box}}\mathcal{M}_{\tilde{\chi}}^{u*})\,. \end{aligned} \tag{7.89}$$

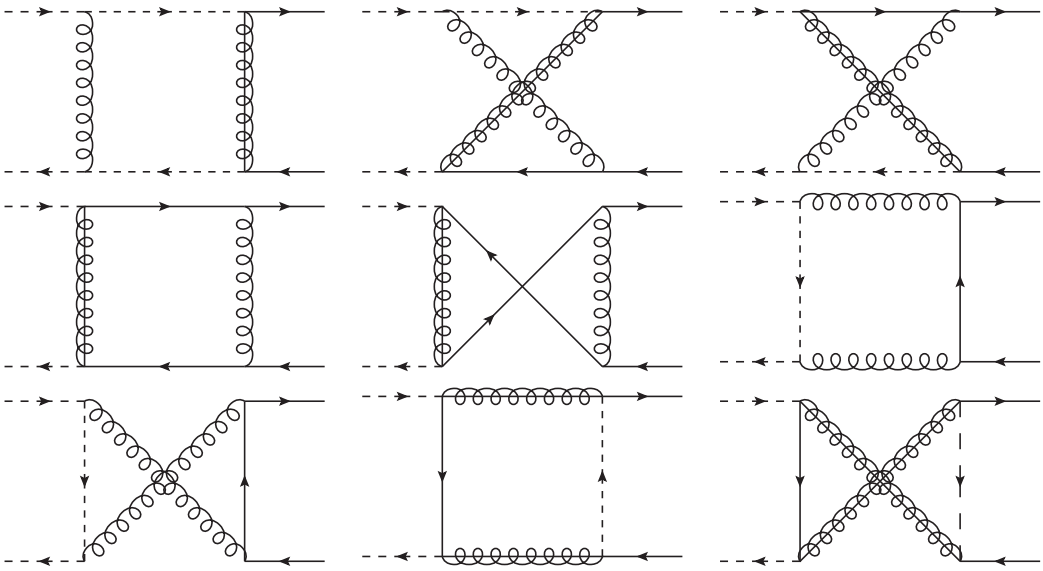

Figure 7.13.: Box-correction for $\tilde{q}\tilde{q}^* \to q\bar{q}$ of the pure strong interaction.

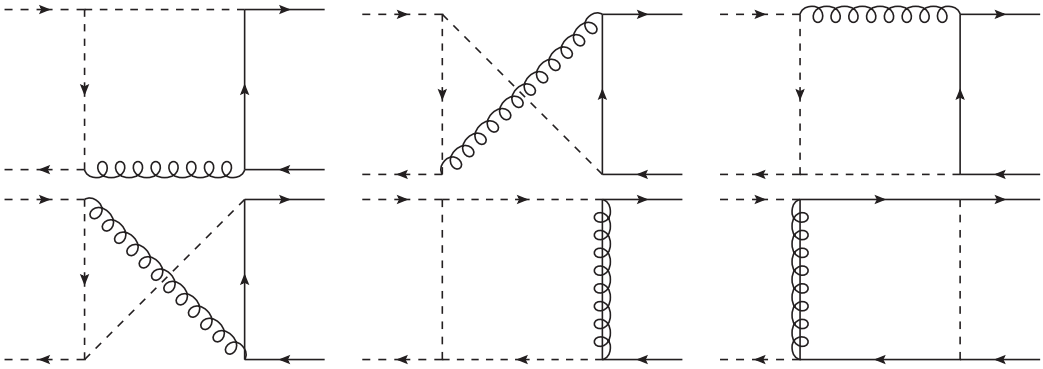

Figure 7.14.: Box-correction for $\tilde{q}\tilde{q}^* \to q\bar{q}$ including Higgs.

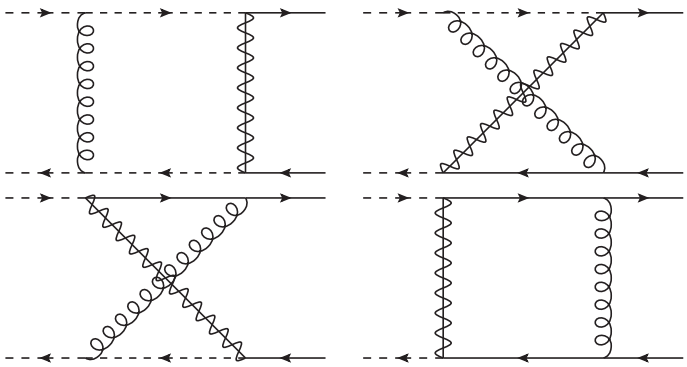

Figure 7.15.: Box-correction for $\tilde{q}\tilde{q}^* \to q\bar{q}$ including neutrinos.

8 Renormalization

In the last chapter we showed that by performing the calculation of the virtual corrections in D dimensions, the divergences of the loop integrals could be separated. However, the final result is expected to be finite. The infrared divergences cancel with the contributions of the emission of an additional gluon. For the ultraviolet divergences the renormalization has to be considered, in this case divergences are drawn into the fields and parameters of the Lagrangian.

To illustrate the basic strategy the simpler ϕ^4-theory will be used as an example in the following section. We briefly show the relevant differences of different popular renormalization schemes. Furthermore, we will introduce the `DM@NLO` renormalization scheme, which has been specially adapted for this purpose due to its unproblematic use in large ranges of the MSSM parameter space.

8.1. Renormalization Principle

The multiplicative renormalization principle will be performed on an introductory example, the ϕ^4-theory The Lagrangian of the ϕ^4-theory is given by

$$\mathcal{L} = \frac{1}{2}\partial^\mu\phi_0\partial_\mu\phi_0 - \frac{m_0^2}{2}\phi_0^2 - \frac{\lambda_0}{4!}\phi_0^4. \tag{8.1}$$

As before, the calculation will be done in D-dimensions, therefore if the dimension of the Lagrangian $\mathcal{L}$ is D the field ϕ_0 has dimension $\frac{D-2}{2}$. Those the coupling constant λ_0 would get dimension $\frac{4-D}{2}$, but the coupling constant should be dimensionless, therefore a parameter μ will be introduced which will make the coupling constant dimensionless

$$\lambda_0 \to \lambda_0\mu^{\frac{4-D}{2}}. \tag{8.2}$$

This parameter μ is the so called *renormalization scale*. It is the same parameter that was introduced in the loop integral (7.18) to retain the mass dimension. Further the multiplicative renormalization factors are introduced to all bare field Z_ϕ, couplings Z_λ

and masses Z_m in the Lagrangian, for the ϕ^4-theory they can be defined as

$$\phi_0 = \sqrt{Z_\phi}\phi \tag{8.3}$$
$$\lambda_0 = Z_\lambda \lambda \tag{8.4}$$
$$m_0^2 = Z_m m^2. \tag{8.5}$$

In the perturbative theory, this leads to

$$\phi_0 = (1 + \frac{1}{2}\delta Z_\phi)\phi \tag{8.6}$$
$$\lambda_0 = (1 + \frac{1}{2}\delta Z_\lambda)\lambda \tag{8.7}$$
$$m_0^2 = (1 + \delta Z_m)m^2. \tag{8.8}$$

The resulting Lagrangian from (8.1) yields

$$\begin{aligned}\mathcal{L} =& \frac{1}{2}\partial^\mu\phi\partial_\mu\phi + \frac{1}{2}\delta Z_\phi \partial^\mu\phi\partial_\mu\phi - \frac{m^2}{2}\phi^2 - (\delta Z_m + \delta Z_\phi)\frac{m^2}{2}\phi^2 \\ &- \frac{\lambda}{4!}\phi^4 - (\delta Z_\lambda + 2\delta Z_\phi)\frac{\lambda}{4!}\phi^4 + \mathcal{O}(\delta Z^2) \\ =& \mathcal{L}_{\text{ren}} + \mathcal{L}_{\text{count}}.\end{aligned} \tag{8.9}$$

The Lagrangian can be split in a renormalized part $\mathcal{L}_{\text{ren}}$ and a counterterm Lagrangian $\mathcal{L}_{\text{count}}$

$$\mathcal{L}_{\text{ren}} = \frac{1}{2}\partial^\mu\phi\partial_\mu\phi - \frac{m^2}{2}\phi^2 - \frac{\lambda}{4!}\phi^4 \tag{8.10}$$
$$\mathcal{L}_{\text{count}} = \frac{1}{2}\delta Z_\phi\partial^\mu\phi\partial_\mu\phi - (\delta Z_m + \delta Z_\phi)\frac{m^2}{2}\phi^2 - (\delta Z_\lambda + 2\delta Z_\phi)\frac{\lambda}{4!}\phi^4. \tag{8.11}$$

The divergences are absorbed in the counterterm part. As far as the loop calculation are of order one, higher Terms $\mathcal{O}(\delta Z^2)$ do not have to be considered. These results can now be used to define similar Feynman rules:

$= \frac{i}{p^2 - m^2 + i\varepsilon}$

$= i[(p^2 - m^2)\delta Z_\phi - m^2\delta Z_m]$

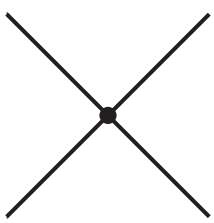
$= -i\lambda$

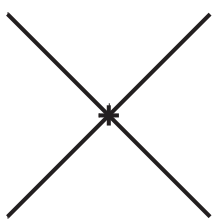
$= -i(\delta Z_\lambda + 2\delta Z_\phi).$

(8.12)

The counterterms are not uniquely defined but depend on a chosen renormalization scheme. Each renormalization scheme has its cons and pros, depending on the situation a suitable renormalization scheme is chosen.

DR and $\overline{\text{DR}}$ Renormalization Scheme

For the pure divergence subtraction the dimensional reduction (DR) scheme is used, so the counterterms only include the divergent terms and no finite ones. As a first step the next-leading-order propagator will be taken into account to derive the mass counterterm δZ_m in the ϕ^4-theory. The NLO propagator includes the pure propagator, the self energy and the counterterm,

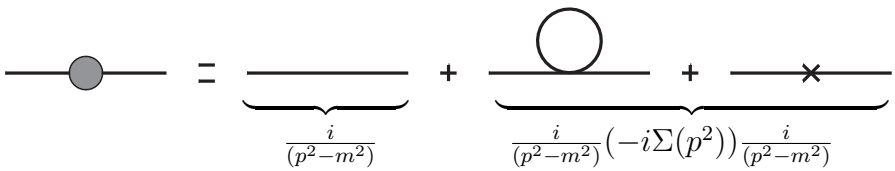

$$\frac{i}{(p^2-m^2)} + \frac{i}{(p^2-m^2)}(-i\Sigma(p^2))\frac{i}{(p^2-m^2)} = \frac{i}{(p^2-m^2)}\left(1+\frac{\Sigma(p^2)}{(p^2-m^2)}\right), \tag{8.13}$$

where $\Sigma(p^2)$ is the mass correction,

$$-i\Sigma(p^2) = -i\frac{\lambda}{16\pi^2}A_0(m^2) + i[(p^2-m^2)\delta Z_\phi - m^2\delta Z_m]. \tag{8.14}$$

The term proportional to the scalar loop function $A_0(m^2)$ comes from the self energy of the propagator, the remaining part is the previous calculated counterterm. The loop integral is independent of p, therefore one can set $\delta Z_\phi = 0$[1] without loss of generality. Using the definition of $A_0(m^2)$ in Eq. (7.24) the mass correction is expressed as

$$-i\Sigma(p^2) = -i\frac{\lambda}{16\pi^2}\left[\frac{1}{\varepsilon} - \gamma_E + \ln(4\pi) - \ln\left(\frac{m^2-i\varepsilon}{\mu^2}\right) + 1\right] - im^2\delta Z_m. \tag{8.15}$$

As it was mentioned in the beginning, the dimensional reduction counterterm is defined to cancel only the pure divergence meaning $\approx \frac{1}{\epsilon}$. This leads to the renormalization factor

$$\delta Z_m^{\text{DR}} = \frac{\lambda}{32\pi^2}\frac{1}{\varepsilon} \tag{8.16}$$

and the finite mass correction

$$\Sigma(p^2) = \frac{\lambda m^2}{32\pi^2}\left[-\gamma_E + \ln(4\pi) + 1 - \ln\left(\frac{m^2-i\varepsilon}{\mu^2}\right)\right]. \tag{8.17}$$

[1] This is a special feature of the ϕ^4-theory.

The $\overline{\text{DR}}$ scheme not only subtract the pure divergence, but includes the whole Δ_{UV}-term (7.25)

$$\delta Z_m^{\overline{\text{DR}}} = \frac{\lambda}{32\pi^2}\Delta_{\text{UV}} \tag{8.18}$$

$$\Sigma(p^2) = \frac{\lambda m^2}{32\pi^2}\left[1 - \ln\left(\frac{m^2 - i\varepsilon}{\mu^2}\right)\right]. \tag{8.19}$$

In both renormalization schemes the corrected mass depend on the renormalization scale μ.

On-Shell Renormalization Scheme

The on-shell renormalization scheme is of interest for particle, with a directly measurable mass, like the top quark. The ansatz in this scheme is to have the renormalized mass as the measured one. Therefore no mass corrections enter the renormalized mass. To ensure this, the scheme has to fulfill two renormalization conditions:

$$\Re\Sigma(p^2)|_{p^2=m^2} = 0\,, \tag{8.20}$$

$$\lim_{p^2\to m^2}\frac{1}{p^2 - m^2}\Sigma(p^2) = 1\,. \tag{8.21}$$

The first condition ensures that the renormalized mass is the physical mass of the particle. The second condition forces the residuum to the value of one. By a performed Taylor series of the mass correction around the pole mass

$$\Sigma(p^2) = \Sigma(p^2)|_{p^2=m^2} + \frac{d^2}{dp^2}\Sigma(p^2)|_{p^2=m^2}(p^2 - m^2) + \dots \tag{8.22}$$

and taking the first renormalization condition into account, we end up with

$$\frac{\Sigma(p^2)}{p^2 - m^2} = \frac{d^2}{dp^2}\Sigma(p^2)|_{p^2=m^2} = 0. \tag{8.23}$$

For our example ϕ^4-theory, the on-shell mass counterterm is given by

$$\delta Z_m^{\text{OS}} = -\frac{\lambda}{32\pi^2}\left[\Lambda_{\text{UV}} - \ln\left(\frac{m^2 - i\varepsilon}{\mu^2}\right) + 1\right]. \tag{8.24}$$

As it was given as a condition of the on-shell schemes, the mass correction is equal to zero.

$$\Sigma(p^2) = 0 \tag{8.25}$$

Thus the renormalized mass is at the same time the physical mass and receives no corrections. Therefore the mass counterterm contains additional finite terms.

8.2. Renormalization Scheme in DM@NLO

The goal of DM@NLO is to provide the calculation of the cross sections including one-loop corrections for processes that contribute to relic density. These shall be determined uniformly for all processes. For this purpose a viable renormalization scheme must be provided that can be reliably used over large regions of the MSSM parameter space. Difficulties are the definition of the bottom (s)quark and top (s)quark sectors so that they behave well over the full parameter space. While the top quark is directly measurable and does not form hadronic states, the on-shell scheme can be used, whereas the bottom quark forms hadronic states and is not directly measurable, so the $\overline{\text{DR}}$ scheme would be a preferred choice. As the squarks are included in the calculation as external particles, a treatment of the squark sectors in the on-shell renormalization scheme is recommended.

The trilinear coupling of the bottom quark A_b also requires careful handling. Using an on-shell renormalization scheme for A_b, we obtain the following renormalization constant δA_b [134]

$$\delta A_b = \frac{1}{m_b}\left[-\left(A_b - \mu \tan\beta\right)\delta m_b + \dots\right]. \tag{8.26}$$

For a parameter region where $\mu \tan\beta >> A_b$, the counterterm would receive a large shift, which would result in a large correction of A_b [134]. In addition, this would also lead to large corrections in the Higgs mass. Therefore the trilinear coupling should be treated in the $\overline{\text{DR}}$ scheme. Therefore, a hybrid on-shell DR schema is used to avoid potential problems with sensitive parameters. In the next sections the details of the renormalization scheme with respect to the renormalization of the squark, quark, gluon and gluino sector are discussed. Furthermore, the renormalization of the strong coupling constant α_s is briefly summarized. The renormalization and factorization scale is set to

$$\mu = \sqrt{m_{\tilde{t}_1} m_{\tilde{t}_2}}. \tag{8.27}$$

8.2.1. Quark Sector

The renormalization considering the quark sector was investigated in Ref. [114]. When considering the quark sector, we restrict ourselves to the third generation of quarks, therefore in the following the mixture of quarks does not have to be considered.

The parameter to be renormalized are the quark fields and masses. The wave-function renormalization is performed by introducing counterterms $\delta Z_{L/R}$ for each chirality of the third generation squarks

$$\begin{pmatrix} q_L \\ q_R \end{pmatrix} \to \begin{pmatrix} 1 + \frac{1}{2}\delta Z_L & 0 \\ 0 & 1 + \frac{1}{2}\delta Z_R \end{pmatrix} \begin{pmatrix} q_L \\ q_R \end{pmatrix}. \tag{8.28}$$

The renormalization condition (8.21) fixed the wave-function renormalization constants

$$\delta Z_L = \Re\Big[- \Pi_L(m_q^2) - m_q^2\Big(\dot{\Pi}_L(m_q^2) + \dot{\Pi}_R(m_q^2)\Big) + \frac{1}{2m_q}\Big(\Pi_{SL}(m_q^2) - \Pi_{SR}(m_q^2)\Big) - m_q\Big(\dot{\Pi}_{SL}(m_q^2) + \dot{\Pi}_{SR}(m_q^2)\Big)\Big] , \tag{8.29}$$

$$\delta Z_R = \delta Z_L(L \leftrightarrow R) , \tag{8.30}$$

where $\Pi_{L,R}(k^2)$ and $\Pi_{SL,SR}(k^2)$ represent the vector and scalar parts of the two-point Green's function as in Ref. [135] and $\dot{\Pi}(m^2) = [\frac{\partial}{\partial k^2}\Pi(k^2)]_{k^2=m^2}$.

As a next step, we introduce the squark mass counterterm. The top and bottom quarks are treated in different renormalization schemes.

As already mentioned, the top mass is renormalized on-shell. The mass of the top is set to its physical mass $m_t = 173.1\,\text{GeV}$, the counterterm for the top quark mass is defined as

$$\delta m_t^{\mathtt{OS}} = \frac{1}{2}\Re\Big[m_t\Big(\Pi_L(m_t^2) + \Pi_R(m_t^2)\Big) + \Pi_{SL}(m_t^2) + \Pi_{SR}(m_t^2)\Big] . \tag{8.31}$$

The bottom mass requires special considerations, as it cannot be measured directly in experiments and forms hadrons. In order to obtain a bottom mass in the $\overline{\mathtt{DR}}$ scheme of the MSSM, some intermediate steps have to be taken. First the bottom mass is conventionally extracted in the $\overline{\mathtt{MS}}$ [2] renormalization scheme. By using the next-to-next-to-leading or renormalization group evolution, the mass of the bottom quark is obtained at a scale Q. This mass $m_b^{\overline{\mathtt{MS}},\mathrm{SM}}(Q)$ is then converted to a mass $m_b^{\overline{\mathtt{DR}},\mathrm{SM}}(Q)$ in the $\overline{\mathtt{DR}}$ renormalization scheme. In the last step it must be considered that the threshold correction Δm_b contributes the mass through the transition from SM to MSSM. The corresponding counterterm

$$\delta m_b^{\overline{\mathtt{DR}}} = (-2)\frac{\alpha_s C_F}{4\pi} m_b^{\overline{\mathtt{DR}}}\Delta , \tag{8.32}$$

is determined with the mass in the $\overline{\mathtt{DR}}$ scheme

$$m_b^{\overline{\mathtt{DR}},\mathrm{MSSM}}(Q) = m_b^{\overline{\mathtt{DR}},\mathrm{SM}}(Q) - \Delta m_b. \tag{8.33}$$

A way the mass of the quarks can enter the calculations is through the Yukawa coupling of the Higgs bosons to the quarks. QCD and top quark induced corrections to the Yukawa coupling of Higgs boson to bottom quark are already calculated up to order $\mathcal{O}(\alpha_s^4)$ [136]. These are used to determine the effective Yukawa coupling. This effective coupling is defined by

$$[h_b^{\overline{\mathtt{MS}},\mathrm{QCD},\Phi}(Q)]^2 = [h_b^{\overline{\mathtt{MS}},\Phi}(Q)]^2\left[1 + \Delta_{\mathrm{QCD}} + \Delta_t^{\Phi}\right] , \tag{8.34}$$

[2] $\overline{\mathtt{MS}}$ is a minimal subtraction renormalization scheme in dimensional regularization of the SM. The whole divergent factor is absorbed in the counterterm.

for each Higgs boson $\Phi = h^0, H^0, A^0$, where $[h_b^{\overline{\mathtt{MS}},\Phi}(Q)]^2$ corresponds to the usual $\overline{\mathtt{MS}}$-Yukawa coupling of Higgs boson to bottom quarks. The QCD corrections Δ_{QCD} are given by

$$\begin{aligned}\Delta_{\mathrm{QCD}} = &\frac{\alpha_s(Q)}{\pi} C_F \frac{17}{4} + \frac{\alpha_s^2(Q)}{\pi^2}\Big[35.94 - 1.359 n_f\Big] \\ &+ \frac{\alpha_s^3(Q)}{\pi^3}\Big[164.14 - 25.77 n_f + 0.259 n_f^2\Big] \\ &+ \frac{\alpha_s^4(Q)}{\pi^4}\Big[39.34 - 220.9 n_f + 9.685 n_f^2 - 0.0205 n_f^3\Big],\end{aligned} \tag{8.35}$$

and the top quark induced corrections Δ_t^Φ for each Higgs boson Φ are

$$\Delta_t^h = \frac{\alpha_s^2(Q)}{\pi^2}\frac{1}{\tan\alpha\tan\beta}\Big[1.57 - \frac{2}{3}\log\frac{Q^2}{m_t^2} + \frac{1}{9}\log^2\frac{m_b^2(Q)}{Q^2}\Big], \tag{8.36}$$

$$\Delta_t^H = \frac{\alpha_s^2(Q)}{\pi^2}\frac{\tan\alpha}{\tan\beta}\Big[1.57 - \frac{2}{3}\log\frac{Q^2}{m_t^2} + \frac{1}{9}\log^2\frac{m_b^2(Q)}{Q^2}\Big], \tag{8.37}$$

$$\Delta_t^A = \frac{\alpha_s^2(Q)}{\pi^2}\frac{1}{\tan^2\beta}\Big[\frac{23}{6} - \log\frac{Q^2}{m_t^2} + \frac{1}{6}\log^2\frac{m_b^2(Q)}{Q^2}\Big], \tag{8.38}$$

enters the corrected Yukawa coupling. These correction are taken into account, excluding the one-loop part as it is provided consistently through our own calculation.

Due to large $\tan\beta$ or large A_b the Yukawa coupling to bottom quarks can receive large corrections even beyond the next-to-leading order. This large correction can affect our analysis significantly, therefore we include these corrections. The corrections are resummend in all orders in pertubation theory [132, 137], denoting the resumable part by Δ_b. With these the bottom quark Yukawa coupling is defined as

$$h_b^{\mathrm{MSSM},h}(Q) = \frac{h_b^{\overline{\mathtt{MS}},QCD,h}(Q)}{1+\Delta_b}\Big[1 - \frac{\Delta_b}{\tan\alpha\tan\beta}\Big], \tag{8.39}$$

$$h_b^{\mathrm{MSSM},H}(Q) = \frac{h_b^{\overline{\mathtt{MS}},QCD,H}(Q)}{1+\Delta_b}\Big[1 + \Delta_b\frac{\tan\alpha}{\tan\beta}\Big], \tag{8.40}$$

$$h_b^{\mathrm{MSSM},A}(Q) = \frac{h_b^{\overline{\mathtt{MS}},QCD,A}(Q)}{1+\Delta_b}\Big[1 - \frac{\Delta_b}{\tan^2\beta}\Big]. \tag{8.41}$$

As before, one-loop corrections are excluded and only the resummed remainder is considered, since the one-loop contributions are already part of our calculation.

8.2.2. Squark Sector

As in the last section, we only consider squarks of the third generation, stop and sbottom. The wave-function renormalization counterterm δZ_{ij} is defined by

$$\tilde{q}_i \to \Big(\delta_{ij} + \frac{1}{2}\delta Z_{ij}\Big)\tilde{q}_i, \tag{8.42}$$

including also off-diagonal terms in contrast to the case of the quark. The requirement of the squark loop to have a unit residue (8.21), fixed the wave-function renormalization counterterm. As a condition, we require that the mixing for on-shell squarks is absent, leading to the counterterms

$$\delta Z_{ii} = -\Re\Big[\dot{\Pi}^{\tilde{q}}_{ii}(m^2_{\tilde{q}_i})\Big] \tag{8.43}$$

$$\delta Z_{ij} = \frac{2\Re\Big[\Pi^{\tilde{q}}_{ij}(m^2_{\tilde{q}_j})\Big]}{m^2_{\tilde{q}_i} - m^2_{\tilde{q}_j}}\,, \qquad \text{for } i \neq j\,, \tag{8.44}$$

with the two-point Green's function $\Pi^{\tilde{q}}_{ij}$ for squarks.

Omitted by the mixing of squark of the third generation, the renormalization of the squark masses is complicated. The masses $m^2_{\tilde{q}_i}$ for stops and sbottoms at leading order are obtained by diagonalization of the mass matrix

$$U^{\tilde{q}} \begin{pmatrix} m^2_{LL} & m^2_{LR} \\ m^2_{RL} & m^2_{RR} \end{pmatrix} (U^{\tilde{q}})^\dagger \;=\; \begin{pmatrix} m^2_{\tilde{q}_1} & 0 \\ 0 & m^2_{\tilde{q}_2} \end{pmatrix}\,, \tag{8.45}$$

where

$$m^2_{LL} \;=\; M^2_{\tilde{Q}} + (I^{3L}_q - e_q\, s^2_W)\cos 2\beta\, m^2_Z + m^2_q\,, \tag{8.46}$$

$$m^2_{RR} \;=\; M^2_{\{\tilde{U},\,\tilde{D}\}} + e_q\, s^2_W \cos 2\beta\, m^2_Z + m^2_q\,, \tag{8.47}$$

$$m^2_{LR} \;=\; m^2_{RL} = m_q\Big(A_q - \mu\,(\tan\beta)^{-2I^{3L}_q}\Big)\,, \tag{8.48}$$

relating the input parameters in the whole squark sector, which are defined in different renormalization schemes. In the next step, we determine the dependence of the soft supersymmetry-breaking squark mass parameters $M^2_{\tilde{Q}}$ and $M^2_{\{\tilde{U},\,\tilde{D}\}}$ of the three on-shell masses $m_{\tilde{b}_1}$, $m_{\tilde{b}_2}$, $m_{\tilde{t}_1}$ and the input parameters contained in m^2_{LR} (A_q, m_q). In the sbottom sector the parameters $M^2_{\tilde{Q}}$ and $M^2_{\tilde{D}}$ are contained in the matrix elements $m^2_{\tilde{b},LL}$ and $m^2_{\tilde{b},RR}$, which are given by the on-shell masses as

$$\begin{aligned} m^2_{\tilde{b},LL} \;&=\; \tfrac{1}{2}\Big(m^2_{\tilde{b}_1} + m^2_{\tilde{b}_2}\Big) \pm \tfrac{1}{2}\sqrt{\Big(m^2_{\tilde{b}_1} - m^2_{\tilde{b}_2}\Big)^2 - 4m^4_{\tilde{b},LR}}\,, \\ m^2_{\tilde{b},RR} \;&=\; \tfrac{1}{2}\Big(m^2_{\tilde{b}_1} + m^2_{\tilde{b}_2}\Big) \mp \tfrac{1}{2}\sqrt{\Big(m^2_{\tilde{b}_1} - m^2_{\tilde{b}_2}\Big)^2 - 4m^4_{\tilde{b},LR}}\,. \end{aligned} \tag{8.49}$$

One notices that there are two possible values for the parameters $M^2_{\tilde{Q}}$ and $M^2_{\tilde{D}}$ and consequently also for the third parameter $M^2_{\tilde{U}}$ which can be found in one of the diagonal elements of the non-diagonal scalar top mass matrix and is related to the first two

parameters through

$$m^2_{\tilde{t},RR} = \frac{1}{m^2_{\tilde{t},LL} - m^2_{\tilde{t}_1}} \times \left(m^2_{\tilde{t}_1} m^2_{\tilde{t},LL} - m^4_{\tilde{t}_1} + m^4_{\tilde{t},LR}\right). \tag{8.50}$$

The parameter $M^2_{\tilde{Q}}$ is common to both elements $m^2_{\tilde{b},LL}$ and $m^2_{\tilde{t},LL}$. Given the freedom to choose from two possible solutions for the squark soft supersymmetry-breaking mass parameter, we can end up with two possibly very different mass matrices and two different sets of mixing matrices (three out of four masses of the squarks would be the same in both cases as they are used as input). In order to ensure a naturally small correction to the mixing matrices when changing between our and the $\overline{\mathtt{DR}}$ renormalization scheme, we always select the solution which preserves the hierarchy between the mass matrix elements in the scalar top quark sector $m^2_{\tilde{t},LL}$ and $m^2_{\tilde{t},RR}$ which was present in the pure $\overline{\mathtt{DR}}$ scheme.

The $\overline{\mathtt{DR}}$ counterterms of the trilinear parameters are given by

$$\begin{aligned}\delta A^{\overline{\mathtt{DR}}}_{\tilde{q}} = \frac{1}{m_q}\Big[&U^{\tilde{q}}_{11}U^{\tilde{q}}_{12}(\delta m^2_{\tilde{q}_1})^{\overline{\mathtt{DR}}} + U^{\tilde{q}}_{21}U^{\tilde{q}}_{22}(\delta m^2_{\tilde{q}_2})^{\overline{\mathtt{DR}}} \\ &+ (U^{\tilde{q}}_{21}U^{\tilde{q}}_{12} + U^{\tilde{q}}_{11}U^{\tilde{q}}_{22})(m^2_{\tilde{q}_1} - m^2_{\tilde{q}_2})\delta\theta^{\overline{\mathtt{DR}}}_{\tilde{q}} - \frac{\delta m^{\overline{\mathtt{DR}}}_q}{m_q}(U^{\tilde{q}}_{11}U^{\tilde{q}}_{12}m^2_{\tilde{q}_1} + U^{\tilde{q}}_{21}U^{\tilde{q}}_{22}m^2_{\tilde{q}_2})\Big].\end{aligned} \tag{8.51}$$

The mixing angles $\theta_{\tilde{t}}$ and $\theta_{\tilde{b}}$ enter the calculation through the vertices and therefore need to be renormalized. The corresponding counterterms read

$$\begin{aligned}(\delta m^2_{\tilde{q}_i})^{\overline{\mathtt{DR}}} =& \frac{\alpha_s C_F}{4\pi}\frac{c_\epsilon}{\epsilon}\Big[\Big((U^{\tilde{q}}_{i1})^2 - (U^{\tilde{q}}_{i2})^2\Big)^2 m^2_{\tilde{q}_i} - m^2_{\tilde{q}_i} + (U^{\tilde{q}}_{21}U^{\tilde{q}}_{11} - U^{\tilde{q}}_{22}U^{\tilde{q}}_{12})^2 m^2_{\tilde{q}_j} \\ &+ 8m_q m_{\tilde{g}} U^{\tilde{q}}_{i1}U^{\tilde{q}}i2 - 4m^2_{\tilde{g}} - 4m^2_q\Big],\end{aligned} \tag{8.52}$$

$$\begin{aligned}\delta\theta_{\tilde{q}} =& \frac{1}{\Big(U^{\tilde{q}}_{21}U^{\tilde{q}}_{12} + U^{\tilde{q}}_{11}U^{\tilde{q}}_{22}\Big)\Big(m^2_{\tilde{q}_1} - m^2_{\tilde{q}_2}\Big)}\Big(\delta m_q\Big(A_q - \mu(\tan\beta)^{-2I^{3L}_q}\Big) \\ &+ m_q\delta A_q - U^{\tilde{q}}_{11}U^{\tilde{q}}_{12}(\delta m^2_{\tilde{q}_1} - \delta m^2_{\tilde{q}_2})\Big).\end{aligned} \tag{8.53}$$

Which also includes the mass counterterm of the heavy stop

$$\begin{aligned}\delta m^2_{\tilde{t}_2} =& \frac{1}{U^{\tilde{t}}_{21}U^{\tilde{t}}_{12}}\Big[(U^{\tilde{t}}_{21}U^{\tilde{t}}_{12} + U^{\tilde{t}}_{11}U^{\tilde{t}}_{22})\Big((U^{\tilde{b}}_{11})^2\delta m^2_{\tilde{b}_1} + (U^{\tilde{b}}_{21})^2\delta m^2_{\tilde{b}_2} \\ &+ 2U^{\tilde{b}}_{11}U^{\tilde{b}}_{21}(m^2_{\tilde{b}_1} - m^2_{\tilde{b}_2})\delta\theta_{\tilde{b}} - 2m_b\delta m_b - (U^{\tilde{t}}_{11})^2\delta m^2_{\tilde{t}_1} + 2m_t\delta m_t\Big) \\ &- 2U^{\tilde{t}}_{11}U^{\tilde{t}}_{21}\Big(\delta m_t\Big(A_t - \frac{\mu}{\tan\beta}\Big) + m_t\delta A_t - U^{\tilde{t}}_{11}U^{\tilde{t}}_{12}\delta m^2_{\tilde{t}_1}\Big)\Big].\end{aligned} \tag{8.54}$$

8.2.3. Gluon Sector

As DM@NLO also includes processes with gluon in the final state and therefore as an extermal particle, it requires renormalization [116]. Again using a wave-function renormalization constant Z_g

$$A^\mu \to \sqrt{Z_g} A^\mu = \Big[1 + \frac{1}{2}\delta Z_g\Big] A^\mu \tag{8.55}$$

to rescale the gluon field. The wave-function renormalization constant is connected to the general two-point Green's function of a vector field, parameterized as

$$\Pi^{\mu\nu}(k^2) = \Big[\mathrm{g}^{\mu\nu} - \frac{k^\mu k^\nu}{k^2}\Big]\Pi^T(k^2) + \frac{k^\mu k^\nu}{k^2}\Pi^L(k^2)\,, \tag{8.56}$$

with transverse Π^T and longitudinal Π^L form factors. Considering the condition Eq. (8.21)m the renormalization constant is expressed by

$$\delta Z_g = -\Re\Big[\frac{\partial \Pi^T(k^2)}{\partial k^2}\Big|_{k^2=0}\Big]\,, \tag{8.57}$$

containing ultraviolet as well as infrared divergences. Separating these divergences, the ultraviolet part of the renormalization constant is given by

$$\delta Z_g^{\mathrm{UV}} = \frac{\alpha_s}{4\pi}\frac{1}{\epsilon}\Big[C_A - 2T_f n_q\Big]\,, \tag{8.58}$$

with n_q indicating number of all quarks. The infrared divergent part of the renormalization constant is given by

$$\delta Z_g^{\mathrm{IR}} = \frac{\alpha_s}{4\pi}\frac{1}{\epsilon}\Big[-\frac{5}{3}C_A + \frac{4}{3}T_f n_{q'}\Big] \tag{8.59}$$

where $n_{q'}$ is the number of effectively massless quarks.

8.2.4. Gluino Sector

In all our analyses we adopt a convention where not only the complete next-to-leading order corrections to the cross section should be rendered UV finite, but also all building blocks such as the n-particle irreducible Green's functions should be UV finite as well. This choice requires to introduce wave-function renormalization constants not only to the fields that correspond to the initial and final state particles but also to fields that give rise to internal propagators. In our case, the only strongly interacting particle that only appears in a propagator in our amplitude is the gluino.

In the case of the gluino, both wave function and mass have to renormalized in order for the vertex corrections and propagator corrections to be separately UV finite. To this

end, we introduce counterterms to the gluino wave function $\delta Z_{\tilde{g}}^{L,R}$ and the gluino mass $\delta m_{\tilde{g}}$ as

$$\psi_{\tilde{g}} \rightarrow \left(1 + \tfrac{1}{2}\delta Z_{\tilde{g}}^{L} P_L + \tfrac{1}{2}\delta Z_{\tilde{g}}^{R} P_R\right)\psi_{\tilde{g}}\,, \tag{8.60}$$

$$m_{\tilde{g}} \rightarrow m_{\tilde{g}} + \delta m_{\tilde{g}}\,. \tag{8.61}$$

All gluino counterterms are determined by considering the gluino two-point Green's function. The one-loop contribution to the two-point Green's function is given by the gluino self-energy diagrams shown in Fig. 7.4. This contribution can be parameterized as

$$\begin{aligned}\Pi(k) =& \not{k}\left(P_L\Pi^L(k^2) + P_R\Pi^R(k^2)\right) \\ &+ m_{\tilde{g}}\left(P_L\Pi^{SL}(k^2) + P_R\Pi^{SR}(k^2)\right),\end{aligned} \tag{8.62}$$

where $\Pi^{L,R}(k^2)$ and $\Pi^{SL,SR}(k^2)$ are form factors which receive contributions from the corresponding self-energy diagrams.

Even though the gluino is not an external particle in the processes considered in this analysis, we still require that the residue of the propagator at one-loop order is set to unity. This condition fixes the wave-function renormalization constant using the form-factors as

$$\begin{aligned}\delta Z_{\tilde{g}}^{L/R} =& -\Pi^{L/R}(m_{\tilde{g}}^2) + \tfrac{1}{2}\Big(\Pi^{SL/SR}(m_{\tilde{g}}^2) \\ &- \Pi^{SR/SL}(m_{\tilde{g}}^2)\Big) - m_{\tilde{g}}^2\Big(\dot{\Pi}^{L/R}(m_{\tilde{g}}^2) + \dot{\Pi}^{R/L}(m_{\tilde{g}}^2) \\ &+ \dot{\Pi}^{SL/SR}(m_{\tilde{g}}^2) + \dot{\Pi}^{SR/SL}(m_{\tilde{g}}^2)\Big),\end{aligned} \tag{8.63}$$

where $\dot{\Pi}^i(m_{\tilde{g}}^2) = \frac{\partial}{\partial k^2}\,\Pi^i(k^2)|_{k^2=m_{\tilde{g}}^2}$. Using the gluino wave-function counterterm renders both the propagator and vertex corrections separately UV finite. Moreover, given that the gluino is not an external particle, renormalization of its wave-function is not necessary for UV finiteness of the full next-to-leading order amplitude and so the full amplitude is independent of the gluino wave-function counterterm. This constitutes another consistency check of our analytical calculation.

The mass counterterm is determined from the on-shell condition which requires that the gluino mass $m_{\tilde{g}}$, which is an input parameter, is identical with the position of the pole of the gluino propagator. It is given as

$$\begin{aligned}\delta m_{\tilde{g}} =& \tfrac{1}{2} m_{\tilde{g}}\Re\left(\Pi^L(m_{\tilde{g}}^2) + \Pi^R(m_{\tilde{g}}^2)\right. \\ &\left.+\Pi^{SL}(m_{\tilde{g}}^2) + \Pi^{SR}(m_{\tilde{g}}^2)\right)\,.\end{aligned} \tag{8.64}$$

8.2.5. α_S Renormalization

As a last step the renormalization of the strong coupling constant α_s [116] is to perform. The counterterms will be defined in the $\overline{\mathtt{DR}}$-scheme. The value is scale dependent and has to be obtained from the conventional value extracted from experimental data at the scale $Q = m_Z$ if the mass of the Z-boson. The steps that have to be taken are the change of scale and the change to the $\overline{\mathtt{DR}}$ renormalization scheme. Furthermore effects of heavy particles and all colored sparticles have to be considered. The scale dependence of the strong coupling constant in the SM in the $\overline{\mathtt{MS}}$-scheme at $N^m LO$ is given by

$$\frac{\mathrm{d}a_s}{\mathrm{d}\log\mu_r^2} = \beta_{\mathrm{N}^m\mathrm{LO}}(a_s) = -\sum_{k=0}^{m} a_s^{k+2}\beta_k\,, \tag{8.65}$$

introducing the shorthand notation $a_s = \frac{\alpha_s^{\overline{\mathtt{MS}},SM,n_f=5}}{4\pi}$, with n_f as the number of effectively massless quark flavors. In our case we use the expansion coefficient β_m of the β function at $m = 3$, at N^{m}LO [138]

$$\begin{aligned}
\beta_0 &= 11 - \frac{2}{3}n_f \\
\beta_1 &= 102 - \frac{38}{3}n_f \\
\beta_2 &= \frac{2857}{2} - \frac{5033}{18}n_f + \frac{325}{54}n_f^2 \\
\beta_3 &= 29243.0 - 6946.3n_f + 405.089n_f^2 + \frac{1093}{729}n_f^3\,.
\end{aligned} \tag{8.66}$$

After shifting the scale using the three-loop renormalization group equations from $Q^2 = m_Z^2$ to scale of the calculation $Q^2 = Q_{\mathrm{fin}}$, we change the strong coupling constant in the $\overline{\mathtt{DR}}$-scheme [139]

$$\alpha_s^{\overline{\mathtt{DR}}} = \alpha_s^{\mathtt{MS}}\left[1 + \frac{\alpha_s^{\mathtt{MS}}}{\pi}\frac{C_A}{12} + \left(\frac{\alpha_s^{\mathtt{MS}}}{\pi}\right)^2\left(\frac{11}{72}C_A^2 - \frac{1}{8}C_F T n_f\right)\right], \tag{8.67}$$

where both coupling constants are evaluated at the same scale. Taking the effects of heavy top quark and heavy supersymmetric particles into account, the final strong coupling constant is determined by

$$\alpha_s^{\mathrm{full}} = \alpha_s^{\overline{\mathtt{DR}}}\left[1 - \frac{\alpha_s^{\overline{\mathtt{DR}}}}{\pi}\zeta_1 + \left(\frac{\alpha_s^{\overline{\mathtt{DR}}}}{\pi}\right)^2(2\zeta_1^2 - \zeta_2)\right], \tag{8.68}$$

with the first-order decoupling coefficient ζ_1 is given by

$$\zeta_1 = -\frac{1}{6}\log\frac{Q_{\mathrm{fin}^2}}{m_t^2} - \frac{1}{24}\sum_q\sum_{i=1,2}\log\frac{Q_{\mathrm{fin}^2}}{m_{\tilde{q}_i}^2} - \frac{1}{2}\log\frac{Q_{\mathrm{fin}}^2}{m_{\tilde{g}}^2}\,. \tag{8.69}$$

The second order is too long to be shown here, we refere to [140]. The counterterm of α_s in the MSSM in the $\overline{\mathtt{DR}}$-scheme is

$$\delta\alpha_s = \frac{\alpha_s}{8\pi}\Delta\left[n_q - 3C_A\right]. \tag{8.70}$$

8.3. Vertex Counterterms

Having counterterms for masses, mixing angles, the strong coupling constant and the wave function renormalization constants, the vertex counterterms can be constructed. In the following, the construction of a vertex counterterm is presented on the example of the gluon-quark-quark vertex Eq. (B.16).

Having the Lagrangian

$$\mathcal{L} = -g_s \mathrm{T}^a_{s,t} G^a_\mu \bar{q}_{i,s} \gamma^\mu q_{j,t} \,, \tag{8.71}$$

the corresponding coupling can be written as

$$(i\mathrm{T}^a_{s,t})\gamma^\mu (g_L^{gqq} PL + g_R^{gqq} PR) \,, \tag{8.72}$$

with

$$g_L^{gqq} = -g_s \delta_{ij} \,, \tag{8.73}$$
$$g_R^{gqq} = -g_s \delta_{ij} \,. \tag{8.74}$$

The vertex counterterm has the same form as the tree level

$$(i\mathrm{T}^a_{s,t})\gamma^\mu (\delta g_L^{gqq} PL + \delta g_R^{gqq} PR) \,, \tag{8.75}$$

where the constants $\delta g_{L/R}^{gqq}$ receive contributions from the renormalization of the strong coupling constant entering in form of $\Delta g_s \sim \frac{\delta \alpha_s}{\alpha_s}$. Furthermore the wave function renormalization constants of the gluon and the quarks enter the vertex counter term, leading to

$$\delta g_L^{gqq} = -g_s \Big(\Delta g_s + \frac{1}{2} (\delta Z_g + \delta Z_L(q_i)^* + \delta Z_L(q_j)) \Big) \delta_{ij} \,, \tag{8.76}$$
$$\delta g_R^{gqq} = -g_s \Big(\Delta g_s + \frac{1}{2} (\delta Z_g + \delta Z_R(q_i)^* + \delta Z_R(q_j)) \Big) \delta_{ij} \,. \tag{8.77}$$

9 Real Emission

Processes (6.1) and (6.2) can emit massless gluons, these diagrams also contribute to the calculation of the NLO corrections. To discuss the emission of another particle, we need to extend the calculation of the phase space from two particles in the final state to a three particle final state. The emission of an additional massless particle results in IR divergences, as did the virtual corrections. These IR divergences should cancel each other out with the ones of the virtual corrections. The divergences result from the integration of the gluon phase space. With phase space slicing, the integration can be divided into different regions, whereby only one region retains the divergences.

In the following we discuss the phase space of the three particle final states, as well as phase space slicing. In the end, we consider the real emission of gluons in our two processes.

9.1. The Phase Space Element for Three Particle Final States

In order to determine the three particle phase space, first a parametrization of it will be defined, see Fig. 9.1. The pulses p_a and p_b are those of the incoming particles, while k_1 k_2 and k_3 are those of the outgoing particles. Here the pulses lay in two planes, k_1, k_2 and k_3 give the plane ϵ and p_a, p_b and k_3 lie in the plane σ. ξ is the angle between k_3 and k_1. η is the angle between the two normals to the plane σ and ϵ. The phase space element of the three particle final state is of the form

$$\mathrm{d}\Gamma = \frac{\mathrm{d}^4k_1\mathrm{d}^4k_2\mathrm{d}^4k_3}{(2\pi)^5}\delta(k_1^2-m_3^2)\delta(k_2^2-m_4^2)\delta(k_3^2-m_5^2)\delta^{(4)}(p_1+p_2-k_1-k_2-k_3)\,. \quad (9.1)$$

As a first step the delta function $\delta^{(4)}(p_1+p_2-k_1-k_2-k_3)$ is used to eliminate the integration over k_2

$$\mathrm{d}\Gamma = \frac{\mathrm{d}^4k_1\mathrm{d}^4k_3}{(2\pi)^5}\delta(k_1^2-m_3^2)\delta(k_2^2-m_4^2)\delta(k_3^2-m_5^2)\Big|_{k_2=p_1+p_2-k_1-k_3}\,. \quad (9.2)$$

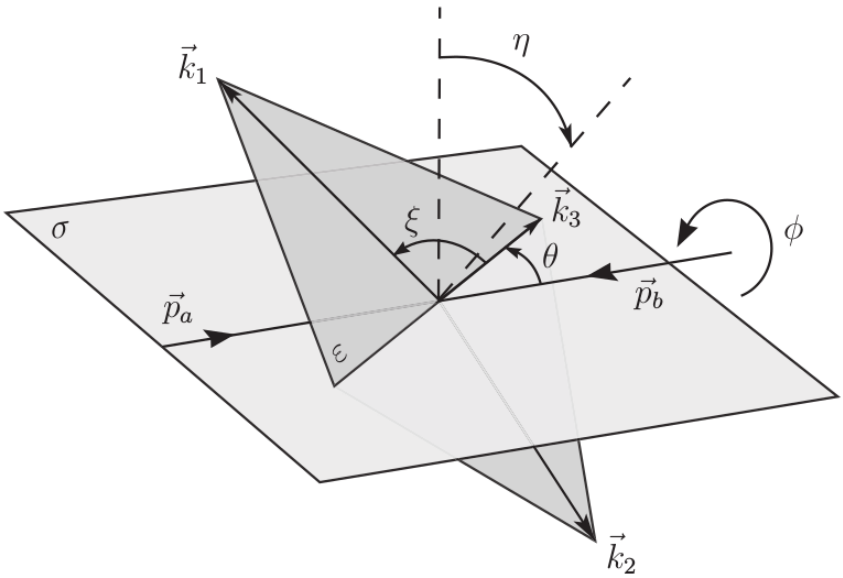

Figure 9.1.: The phase space of a $2 \to 3$ process [129].

The delta-functions $\delta(k_i^2 - m_i^2)$ can be applied by rewriting the integration over the four-momenta into

$$\mathrm{d}^4k\delta(k^2 - m^2) = |\vec{k}|^2\mathrm{d}|\vec{k}|\mathrm{d}k^0 d\Omega\delta((k^0)^2 - |\vec{k}|^2 - m^2). \tag{9.3}$$

Rewriting $\mathrm{d}|\vec{k}| \to \frac{\mathrm{d}|\vec{k}|^2}{2|\vec{k}|}$ yields

$$\mathrm{d}^4k\delta(k^2 - m^2) = \frac{|\vec{k}|}{2}\mathrm{d}|\vec{k}|^2\mathrm{d}k^0\mathrm{d}\Omega\delta((k^0)^2 - |\vec{k}|^2 - m^2). \tag{9.4}$$

By integrating $\mathrm{d}|\vec{k}|^2$ one receives $|\vec{k}| = \sqrt{k_0^2 - m^2}$, which leads to

$$\mathrm{d}^4k\delta(k^2 - m^2) = \frac{\sqrt{(k^0)^2 - m^2}}{2}\mathrm{d}k^0\mathrm{d}\Omega. \tag{9.5}$$

Therefore, the phase space element becomes

$$\mathrm{d}\Gamma = \frac{|k\vec{k}_1||\vec{k}_3|}{4}\frac{1}{(2\pi)^5}\mathrm{d}k_1^0\mathrm{d}\Omega_1\mathrm{d}k_3^0\mathrm{d}\Omega_3\delta(k_2^2 - m_2^2) \tag{9.6}$$

with

$$\mathrm{d}\Omega_1 = \mathrm{d}\cos\xi\mathrm{d}\eta \tag{9.7}$$

$$\mathrm{d}\Omega_3 = \mathrm{d}\cos\theta\mathrm{d}\phi\,. \tag{9.8}$$

Here, $\mathrm{d}\Omega_1$ is defined in respect to $\vec{k}_3$ and Ω_3 in respect to the collision plane. Rewriting the δ-function $\delta(k_2^2 - m_4^2)$

$$k_2^2 - m_4^2 = (k_2^0)^2 - |\vec{k}_2|^2 - m_4^2 \tag{9.9}$$

and using the three-momenta conservation

$$\vec{p}_a + \vec{p}_b = \vec{k}_1 + \vec{k}_2 + \vec{k}_3 = 0\,, \tag{9.10}$$

$|\vec{k}_2|$ can be eliminated

$$\begin{aligned} |\vec{k}_2| =& |\vec{k}_1|^2 + |\vec{k}_3|^2 + 2\vec{k}_1 \cdot \vec{k}_3 \\ =& |\vec{k}_1|^2 + |\vec{k}_3|^2 + 2|\vec{k}_1||\vec{k}_3|\cos\xi \end{aligned} \tag{9.11}$$

$$\begin{aligned} k_2^2 - m_4^2 =& (k_2^0)^2 - |\vec{k}_1|^2 - |\vec{k}_3|^2 - 2|\vec{k}_1||\vec{k}_3|\cos\xi - m_4^2 \\ =& (\sqrt{s} - k_1^0 - k_3^0)^2 + m_3^2 + m_5^2 - m_4^2 - 2\sqrt{(k_1^0)^2 - m_3^2}\sqrt{(k_3^0)^2 - m_5^2}\cos\xi\,. \end{aligned} \tag{9.12}$$

Furthermore, energy conservation was used to rewrite k_2^0

$$k_1^0 + k_2^0 + k_3^0 = \sqrt{s} \tag{9.13}$$

and the fact that the outgoing momenta are on-shell $k_i^2 = m_i^2$. As a next step, the integration over $\cos\xi$ has to be performed. Using

$$\int \delta(f(x))\mathrm{d}x = \frac{1}{|f'(x_0)|} \tag{9.14}$$

with

$$f'(\cos\xi) = -2\sqrt{(k_1^0)^2 - m_3^2}\sqrt{(k_3^0)^2 - m_5^2} \tag{9.15}$$

the phase space element reduces to

$$\mathrm{d}\Gamma = \frac{1}{8}\frac{1}{(2\pi)^5}\mathrm{d}k_1^0\mathrm{d}\eta\mathrm{d}k_3^0\mathrm{d}\cos\theta\mathrm{d}\phi\,. \tag{9.16}$$

Rewritten the δ-function (9.12) yields

$$\cos\xi = \frac{(\sqrt{s} - k_1^0 - k_3^0)^2 + m_3^2 + m_5^2 - m_4^2 - (k_1^0)^2 - (k_3^0)^2}{2\sqrt{(k_1^0)^2 - m_3^2}\sqrt{(k_3^0)^2 - m_5^2}}\,. \tag{9.17}$$

The integration variables that are left over are two energies k_1^0 and k_3^0 and three angles η, θ and ϕ.

Introduction of Dimensionless Variables

Instead of using masses and energies it is common to use dimensionless variables, defined as

$$x_i = \frac{2k_i^0}{\sqrt{s}} \qquad \mu_i = \frac{m_i}{\sqrt{s}}\,. \tag{9.18}$$

The energy conservation of the new particles becomes

$$2 = v_1 + x_2 + x_3\,. \tag{9.19}$$

Substitution of the integration variables $\mathrm{d}x_i = \frac{2}{\sqrt{s}}\mathrm{d}k_i^0$ gives the phase space element

$$\mathrm{d}\Gamma = \frac{s}{32}\frac{1}{(2\pi)^5}\mathrm{d}x_1\mathrm{d}\eta\mathrm{d}x_3\mathrm{d}\cos\theta\mathrm{d}\phi\,. \tag{9.20}$$

Furthermore, $\cos\xi$ can be rewritten to

$$\cos\xi = \frac{(2-x_1-x_3)^2 + 4\mu_3 + 4\mu_5 - 4\mu_4 - x_1^2 - x_3^2}{2\sqrt{x_1^2 - 4\mu_3^2}\sqrt{x_3^2 - \mu_5^2}}\,. \tag{9.21}$$

Integration Boundaries

The angles give only a relative position related to the plane ε, therefore the angles are not bounded through conservation laws, leading to the following integration boundaries

$$\eta \,\epsilon\, (0, 2\pi), \qquad \phi \,\epsilon\, (0, 2\pi), \qquad \theta \,\epsilon\, (0, \pi)\,. \tag{9.22}$$

Hence, x_1 and x_3 are bounded through the conservation laws, which are included in $\cos\xi$ Eq. (9.21)

$$|\cos\xi| \leq 1\,. \tag{9.23}$$

The limitation leads to two equations

$$\begin{aligned} f(x_1, x_3) =& (2-x_1-x_3)^2 + 4\mu_3^2 + 4\mu_5^2 - 4\mu_4^2 - x_1^1 - x_3^2 - 2\sqrt{x_1^2 - 4\mu_3^2}\sqrt{x_3^2 - 4\mu_5^2} \leq 0 \\ g(x_1, x_3) =& (2-x_1-x_3)^2 + 4\mu_3^2 + 4\mu_5^2 - 4\mu_4^2 - x_1^1 - x_3^2 + 2\sqrt{x_1^2 - 4\mu_3^2}\sqrt{x_3^2 - 4\mu_5^2} \geq 0. \end{aligned} \tag{9.24}$$

The boundaries of x_1 andx_3 are given by

$$f(x_1, x_3) = 0 \qquad \text{and} \qquad g(x_1, x_3) = 0\,. \tag{9.25}$$

To include a cutoff energy for the emitted gluon, the integration of x_1 is integrated first. The boundaries of x_1 can be calculated by solving (9.25)

$$x_{\min}^{\max} = \frac{1}{2\overline{\tau}}\left[\overline{\sigma}(\overline{\tau} + \mu_+\mu_-) \pm \sqrt{x_3^2 - 4\mu_5^2}\sqrt{(\overline{\tau} - \mu_+^2)(\overline{\tau} - \mu_-^2)}\right]\,, \tag{9.26}$$

with the definitions

$$\overline{\sigma} = 2 - x_3, \quad \overline{\tau} = 1 - x_3 + \mu_5^2, \quad \mu_\pm = \mu_3 \pm \mu_4\,. \tag{9.27}$$

Summary of Phase Space Element

The integration of the phase space element reduced to the integration over three angles η, ϕ, θ and two energies k_1^0, k_3^0

$$\mathrm{d}\Gamma = \frac{1}{8}\frac{1}{(2\pi)^5}\mathrm{d}k_1^0\mathrm{d}\eta\mathrm{d}k_3^0\mathrm{d}\cos\theta\mathrm{d}\phi\,. \tag{9.28}$$

The integration boundaries for the angles are given by

$$\eta\,\epsilon\,(0,2\pi), \qquad \phi\,\epsilon\,(0,2\pi), \qquad \theta\,\epsilon\,(0,\pi)\,. \tag{9.29}$$

The boundaries of the energies are limited by conservation laws

$$(k_3^0)^{\min} = m_5, \qquad (k_3^0)^{\max} = \frac{\sqrt{s}}{2} - \frac{(m_3+m_4)^2 - m_5}{2\sqrt{s}}\,, \tag{9.30}$$

$$(k_1^0)^{\max}_{\min} = \frac{1}{2\tau}\left[\sigma(\tau + m_+m_-) \pm |\vec{k}_3|\sqrt{(\tau - m_+^2)(\tau - m_-^2)}\right]\,, \tag{9.31}$$

with

$$\sigma = \sqrt{s} - k_3^0, \quad \tau = s - 2\sqrt{s}k_3^0 + m_5^2, \quad m_\pm = m_3 \pm m_4\,. \tag{9.32}$$

Massless Particle in final state

If one of the final state particles is massless (e.g. photon or gluon) (we choose the particle with the moment k_3 to be massless), the formulas are simplified because m_5=0 (in dimensionless case $\mu_5 = 0$). If the emission of a massless particle is treated with the phase space slicing method, Chapter 9.3, the integration limit for the energy k_3^0 is set to a suitable cut ΔE for a minimal energy of the outgoing massless particle. The angle from the massless particle to the beam axis θ and the lower limit of the particle energy k_3^0 changes the limits to

$$\theta\,\epsilon\,(\Delta\theta, \pi - \Delta\theta), \qquad (k_3^0)^{\min} = \Delta E\,. \tag{9.33}$$

9.2. Parametrization of Final State Momenta

To perform the integration of the phase space the 4-momenta have to be rewritten in the previous introduced parameters $x_1, x_3, \eta, \cos\theta, \phi$ (or in $k_1^0, k_3^0, \eta, \cos\theta, \phi$). The squared amplitudes can be expressed in terms of the masses and scalar products of the

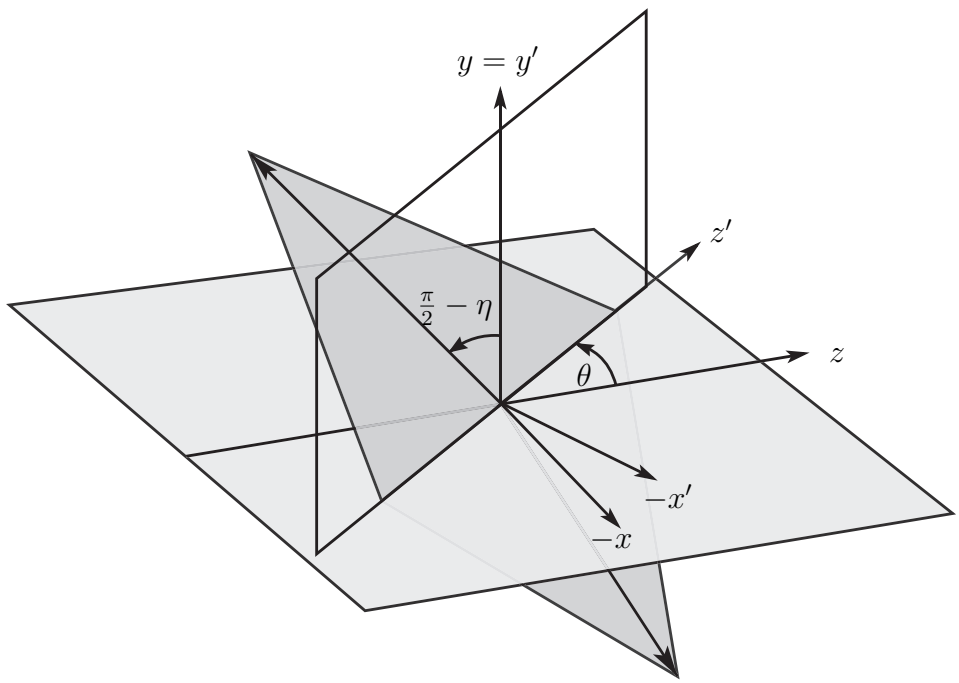

Figure 9.2.: New coordinate system for the calculation of the incoming 3-momenta of the $2 \to 3$ process [129].

4-momenta. Therefore we rewrite the scalar products. The energy conservation

$$\begin{aligned} s =& (k_1 + k_2 + k_3)^2 = k_1^2 + k_2^2 + k_3^2 + 2k_1.k_2 + 2k_1.k_3 + 2k_2.k_3 \\ =& - k_1^2 + k_2^2 + k_3^2 + 2k_1.(k_1 + k_2 + k_3) + 2k_2.k_3 \\ =& - k_1^2 + k_2^2 + k_3^2 + 2\sqrt{s}k_1^0 + 2k_2.k_3 \\ =& - m_3^2 + m_4^2 + m_5^2 + sx_1 + 2k_2.k_3 \end{aligned} \tag{9.34}$$

is leads to

$$2k_1.k_3 = s(1 - x_2) - m_1^2 + m_2^2 - m_3^2 \tag{9.35}$$
$$2k_2.k_3 = s(1 - x_1) + m_1^2 - m_2^2 - m_3^2 \tag{9.36}$$
$$2k_1.k_2 = s(1 - x_3) - m_1^2 - m_2^2 + m_3^2 \,. \tag{9.37}$$

Choosing the coordinate system as depicted in Fig. 9.2, choosing the beam axis along the z-axis. The y-axis is defined perpendicular to the plane defined by the beam axis and the 3-momentum $\vec{k}_3$, the x-axis results from $\vec{x} \times \vec{y} = \vec{z}$.

Within the definition of the coordinate system the the 4-momenta p_a, p_b and k_3 can

be written as

$$p_1^\mu = \frac{\sqrt{s}}{2}\left(1+\mu_1^2-\mu_2^2, 0, 0, \sqrt{(1-\mu_1^2-\mu_2^2)^2-4\mu_1^2\mu_2^2}\right) \tag{9.38}$$

$$p_2^\mu = \frac{\sqrt{s}}{2}\left(1-\mu_1^2+\mu_2^2, 0, 0, -\sqrt{(1-\mu_1^2-\mu_2^2)^2-4\mu_1^2\mu_2^2}\right) \tag{9.39}$$

$$k_3^\mu = \frac{\sqrt{s}}{2}\left(x_3, \sqrt{x_3^2-4\mu_3^2}\sin\theta, 0, \sqrt{x_3^2-4\mu_3^2}\cos\theta\right) . \tag{9.40}$$

One momenta can always be eliminated by rewriting it in terms of the other four momenta,leaving only the 4-momentum k_1 undefined. Using the reference frame defined by(x', y', z') as in Fig. 9.2, the angles ξ and η can be seen like the angles of the spherical coordinates leading to the components

$$(k_1)_{x'} = |\vec{k}_1| \sin\xi \sin\eta \tag{9.41}$$

$$(k_1)_{y'} = |\vec{k}_1| \sin\xi \cos\eta \tag{9.42}$$

$$(k_1)_{z'} = |\vec{k}_1| \sin\xi . \tag{9.43}$$

The transformation back to the frame (x, y, z) is performed by

$$x = x' \cos\theta + z' \sin\theta \tag{9.44}$$

$$y = y' \tag{9.45}$$

$$z = -x' \sin\theta + z' \cos\theta . \tag{9.46}$$

Resulting in

$$k_1^\mu = \frac{\sqrt{s}}{2}\left(x_1, \sqrt{x_1^2-4\mu_1^2}\vec{n}\right) \tag{9.47}$$

with the unit vector $\vec{n}$ defined as

$$n_x = (\cos\xi \sin\theta + \sin\xi \sin\eta \cos\theta) \tag{9.48}$$

$$n_y = \sin\xi \cos\eta \tag{9.49}$$

$$n_z = (\cos\xi \cos\theta - \sin\xi \sin\eta \sin\theta) . \tag{9.50}$$

The scalar products therefore can be expressed as

$$p_1 \cdot p_2 = \frac{s}{2}\left(1 - \mu_1^2 - \mu_b^2\right) \tag{9.51}$$

$$p_1 \cdot k_1 = \frac{s}{4}\Big[x_1\left(1 + \mu_1^2 - \mu_2^2\right) - \sqrt{x_1^2 - 4\mu_1^2}\sqrt{\left(1 - \mu_1^2 - \mu_2^2\right)^2 - 4\mu_1^2\mu_2^2} \tag{9.52}$$

$$\cdot(\cos\xi\cos\theta - \sin\xi\sin\eta\sin\theta)\Big] \tag{9.53}$$

$$p_1 \cdot k_3 = \frac{s}{4}\Big(\left(1 - \mu_b^2 + \mu_a^2\right)x_3 \tag{9.54}$$

$$- \sqrt{x_3^2 - 4m_3^2}\sqrt{1 - 2\left(\mu_a^2 + \mu_b^2\right) + \left(\mu_a^2 - \mu_b^2\right)^2}\cos\theta\Big) \tag{9.55}$$

$$p_1 \cdot k_2 = \frac{s}{2}\left(1 - \mu_b^2 + \mu_a^2\right) - p_1 \cdot k_1 - p_1 \cdot k_3 \tag{9.56}$$

$$p_2 \cdot k_1 = -\,p_1 \cdot k_1 + m_1^2 + k_1 \cdot k_2 + k_1 \cdot k_3 \tag{9.57}$$

$$,\, p_2 \cdot k_2 = -\,p_1 \cdot k_3 + m_3^2 + k_1 \cdot k_3 + k_2 \cdot k_3 \tag{9.58}$$

$$p_2 \cdot k_3 = -\,p_1 \cdot k_2 + m_2^2 + k_1 \cdot k_2 + k_2 \cdot k_3\,. \tag{9.59}$$

9.3. Phase Space Slicing

The IR-divergences from the virtual corrections are compensated by the emission of an additional massless particle with zero energy, in our case the gluon. Since detectors have an energy detection threshold, massless particles with almost no energy are not detectable, so that processes with and without an extra gluon, with an energy below this threshold, can be considered identical. To treat the three particle final state, the phase space is divided as seen in Fig. 9.3 with the corresponding cross section

$$\sigma^{\text{real}} = \sigma^{\text{soft}}\left(\frac{1}{\varepsilon_{\text{IR}}}, \Delta E\right) + \sigma^{\text{hard}}(\Delta E)\,, \tag{9.60}$$

with the cut-off gluon energy ΔE dividing the phase space, so that a soft cross section (σ^{soft}) can be calculated separately from the hard cross section (σ_{hard}). In our case, we do not need to distinguish between collinear and non-collinear contributions to the hard cross section, the collinear contribution is only of importance if the emitting particle is also massless. Since we consider third generation quarks in the final state, there is no need. The IR divergences only contribute to the soft cross section. Using the fact that the gluon energy is small the soft differential cross section can be factorized into the differential cross section without an additional gluon and an universal factor. The IR divergence can be extracted from this factor, discussed in Sec. 9.4. The hard cross section is determined by the integration of the summed amplitude squares depending on the scalar products of the momenta in the $2 \to 3$ phase space. The final complete cross section σ^{real} is independent of the cut-off energy ΔE.

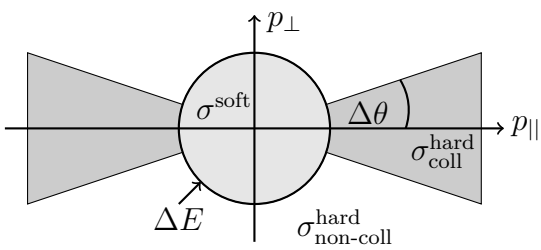

Figure 9.3.: Illustration of phase space slicing [129]. The parameter space is splitted in a region defined by an cut-off energy ΔE giving rise to the so-called soft cross section (σ^{soft}). The hard cross section (σ_{hard}) is further divided in a collinear and a non-collinear part. Whereby the collinear part is of importance if the emitting particle is also massless.

9.4. Soft Gluon Emission

The $2 \to 3$ processes contributing to the calculation of the annihilation cross section of the process (6.1) are depicted in Figs. 9.9 and 9.10, the ones of the process 6.2 are shown in Figs. 9.5 9.6 9.8 and 9.7. Emissions of a gluon from propagator in case of gluino t-channel and gluon s-channel or emission from vertex like in gluon s-channel do not lead to divergences and are therefore only considered in σ^{hard}.

In the following we show the factorization of the divergent part of a $2->3$ process in terms the $2->2$ phase space. As an example we take the emission of a gluon from an initial squark with momentum p_1, see Fig. 9.4. The Amplitude of this diagram is

$$\mathcal{M}^H_{\text{softgluon},p_1} = i\bar{u}(k_1)(g_1^L PL + g_1^R P_R)v(k_2)\frac{1}{s-m_h^2}g_2\frac{1}{(p_1-k_3)^2-m_{\tilde{q}}^2}g_s(2p_1^\alpha - k_3^\alpha)\epsilon^*_\alpha(k_3)\,, \tag{9.61}$$

for simplicity we neglect the color factors for the illustration of the factorization. The coupling g_s results from the gluon-squark-squark coupling (B.5), g_1^L, g_1^R and g_2 are the couplings of the tree level amplitude. Therefore the amplitude can be rewritten in terms of the tree level amplitude $\mathcal{M}^H_{\text{Tree}}$

$$\mathcal{M}^H_{\text{softgluon},p_1} = -\frac{g_s}{(p_1-k_3)^2-m_{\tilde{q}}^2}(2p_1^\alpha - k_3^\alpha)\epsilon^*_\alpha(k_3)\mathcal{M}^H_{\text{Tree}}\,. \tag{9.62}$$

Simplifying the denominator $(p_1-k_3)^2-m_{\tilde{q}}^2 = 2p_1k_3$, since $p_1^2 = m_{\tilde{q}}^2$ and k_3^2 considered zero. Furthermore in the numerator k_3 does not contribute to the calculation, ending up with

$$\mathcal{M}^H_{\text{softgluon},p_1} = -g_s\frac{p_1^\alpha\epsilon^*_\alpha(k_3)}{p_1.k_3}\mathcal{M}^H_{\text{Tree}}\,. \tag{9.63}$$

Considering the analog calculation of the other diagrams in Fig 9.6, we end up with

$$\mathcal{M}^H_{\text{softgluon},p_1} = -g_s\Big[\frac{p_1^\alpha\epsilon^*_\alpha(k_3)}{p_1.k_3} - \frac{p_2^\alpha\epsilon^*_\alpha(k_3)}{p_2.k_3} - \frac{k_1^\alpha\epsilon^*_\alpha(k_3)}{k_1.k_3} + \frac{k_2^\alpha\epsilon^*_\alpha(k_3)}{k_2.k_3}\Big]\mathcal{M}^H_{\text{Tree}}\,. \tag{9.64}$$

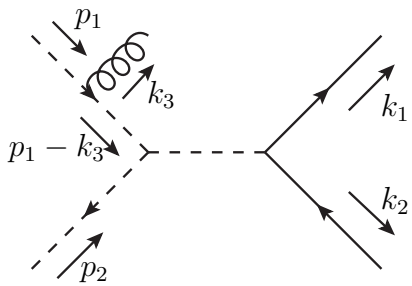

Figure 9.4.: Real emission of Higgs s-channel for $\tilde{q}\tilde{q}^* \to q\bar{q}$ with the emission of a gluon from the incoming squark with the momentum p_1. To illustrate the momenta convention within the calculation.

Going one step further and considering the squared amplitude, including the color factors

$$\begin{aligned}|\mathcal{M}^H_{\text{softgluon}}|^2 = |\mathcal{M}^H_{\text{Tree}}|^2 \times (-g_s^2)\Bigg\{ & C_F\Bigg[\frac{p_1^2}{(p_1.k_3)^2} + \frac{p_2^2}{(p_2.k_3)^2} + \frac{k_1^2}{(k_1.k_3)^2} + \frac{k_2^2}{(k_2.k_3)^2} \\ & - \frac{p_1.p_2}{(p_1.k_3)(p_2.k_3)} - \frac{k_1.k_2}{(k_1.k_3)(k_2.k_3)}\Bigg] \\ & + 0\Bigg[- \frac{p_1.k_1}{(p_1.k_3)(k_1.k_3)} - \frac{p_2.k_2}{(p_2.k_3)(k_2.k_3)} \\ & + \frac{p_1.k_2}{(p_1.k_3)(k_2.k_3)} + \frac{p_2.k_1}{(p_2.k_3)(k_1.k_3)}\Bigg]\Bigg\}. \end{aligned} \tag{9.65}$$

The average squared amplitude can be plugged in the cross section

$$\mathrm{d}\sigma = \int\limits_{|\vec{k}_3|\leq\Delta E} \frac{\mathrm{d}^3k_1}{(2\pi)^3 2E_1}\frac{\mathrm{d}^3k_2}{(2\pi)^3 2E_2}\frac{\mathrm{d}^3k_3}{(2\pi)^3 2E_3}\frac{1}{2s}(2\pi)^4\delta^{(4)}(p-k_1-k_2-k_3)\overline{|\mathcal{M}^H_{\text{softgluon}}|^2}\,, \tag{9.66}$$

with $2s$ as the flux factor and ΔE the cut-off energy of the gluon. In the soft approximation $p-k_1-k_2-k_3 = p-k_1-k_2$ is valid, simplifies the delta function to $\delta^{(3)}(p-k_1-k_2)$. In the center of mass system the cross section can be rewritten as

$$\mathrm{d}\sigma = \int\limits_{|\vec{k}_3|\leq\Delta E} \frac{\mathrm{d}k_1 k_1^2 \mathrm{d}\Omega}{(2\pi)^3 2E_1 2E_2}\frac{\mathrm{d}^3k_3}{(2\pi)^3 2E_3}\frac{1}{2s}(2\pi)\delta(E_{\text{CM}}-E_1-E_2)\overline{|\mathcal{M}^H_{\text{softgluon}}|^2}(\vec{k}_2\to\vec{k}_1)\,, \tag{9.67}$$

with $E_1 = \sqrt{k_1^2 - m_1^2}$ and $E_2 = \sqrt{k_2^2 - m_2^2}$. By introducing a new variable

$$\mathrm{d}(E_1 + E_2) = \Big(\frac{k_1}{E_1} + \frac{k_1}{E_2}\Big)\mathrm{d}k_1 \tag{9.68}$$

for the integration, the integral becomes

$$\mathrm{d}\sigma = \int \frac{\mathrm{d}(E_1+E_2)k_1^2\mathrm{d}\Omega}{16\pi^2 k_1(E_1+E_2)}\frac{1}{2s}\delta(E_{\mathrm{CM}} - E_1 - E_2) \int\limits_{|\vec{k}_3|\leq\Delta E} \frac{\mathrm{d}^3k_3}{(2\pi)^3 2E_3}\overline{|\mathcal{M}^H_{\mathrm{softgluon}}|^2}(\vec{k}_2 \to \vec{k}_1)\,. \tag{9.69}$$

Integrating out the delta function gives

$$\mathrm{d}\sigma = \int \frac{k_1\mathrm{d}\Omega}{16\pi^2 E_{\mathrm{CM}}}\frac{1}{2s} \int\limits_{|\vec{k}_3|\leq\Delta E} \frac{\mathrm{d}^3k_3}{(2\pi)^3 2E_3}\overline{|\mathcal{M}^H_{\mathrm{softgluon}}|^2}(\vec{k}_2 \to \vec{k}_1, (E_1+E_2) \to E_{\mathrm{CM}})\,, \tag{9.70}$$

with $\overline{|\mathcal{M}^H_{\mathrm{softgluon}}|^2}(\vec{k}_2 \to \vec{k}_1, (E_1+E_2) \to E_{\mathrm{CM}})$ in the kinematics of the $2 \to 2$ process. Writing Eq.(9.70) as the differential cross section for a $2 \to 2$ process

$$\left(\frac{\mathrm{d}\sigma}{\mathrm{d}\Omega}\right) = \frac{k_1}{16\pi^2 E_{\mathrm{CM}}}\frac{1}{2s}\sum_{\mathrm{spin}}\overline{|\mathcal{M}|^2}\,, \tag{9.71}$$

factorizes nicely. The soft gluon result can be written in the form

$$\left(\frac{\mathrm{d}\sigma}{\mathrm{d}\Omega}\right) = -\left(\frac{\mathrm{d}\sigma}{\mathrm{d}\Omega}\right)_{\mathrm{Tree}} \times \frac{g_s^2}{(2\pi)^3}\int\limits_{|\vec{k}_3|\leq\Delta E}\frac{\mathrm{d}^3k_3}{2E_3}T \tag{9.72}$$

where T includes the kinematic structure

$$T = C_F\Big[\frac{p_1^2}{(p_1.k_3)^2} + \frac{p_2^2}{(p_2.k_3)^2} + \frac{k_1^2}{(k_1.k_3)^2} + \frac{k_2^2}{(k_2.k_3)^2} - \frac{p_1.p_2}{(p_1.k_3)(p_2.k_3)} - \frac{k_1.k_2}{(k_1.k_3)(k_2.k_3)}\Big]\,. \tag{9.73}$$

The remaining integrals, which have to be solved, have the general form

$$I_{ab} = \int\limits_{|\vec{k}_3|\leq\Delta E}\frac{\mathrm{d}^3k_3}{2E_3}\frac{2a.b}{(a.k_3)(b.k_3)}\,. \tag{9.74}$$

This integral is investigated within several publications [128] and theses [5], therefore we will restrict ourselves to the solution of the general integral

$$I_{ab} = \frac{4\pi\alpha(a.b)}{(\alpha a)^2 - b^2}\Bigg\{\frac{1}{2}\ln\frac{4\Delta^2}{\lambda^2}\ln\frac{(\alpha a)^2}{b^2} + \Bigg[\frac{1}{4}\ln^2\Big(\frac{P^0 - |\vec{P}|}{P^0 + |\vec{P}|}\Big) + \mathrm{Li}_2\Big(1 - \frac{P^0 - |\vec{P}|}{v}\Big) + \mathrm{Li}_2\Big(1 - \frac{P^0 + |\vec{P}|}{v}\Big)\Bigg]_{P=b}^{P=a\alpha}\Bigg\}\,, \tag{9.75}$$

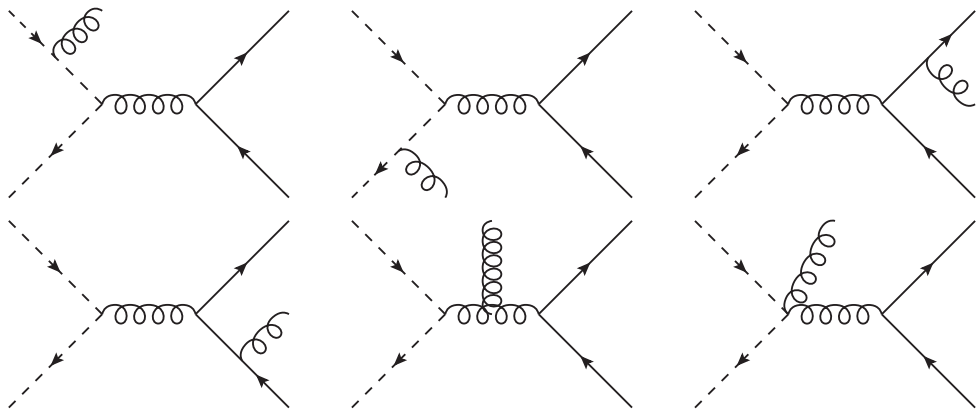

Figure 9.5.: Real emission of gluon s-channel for $\tilde{q}\tilde{q}^* \to q\bar{q}$.

where λ is the polarization of the emitted gluon and Δ the boundary. The spence function Li_2 used here is defined in Sec. A.1. The constant α is given by the defined 4-momenta p and q such that

$$\left.\begin{aligned} p &= \alpha a \\ q &= b \end{aligned}\right\} (p-q)^2 = 0\,, \tag{9.76}$$

choosing the solution which fulfills

$$\frac{\alpha a^0 - b^0}{b^0} > 0\,. \tag{9.77}$$

The parameter v is defined through an introduced short hand notation

$$l = p^0 - q^0 = \pm|\vec{p} - \vec{q}| \quad \text{and} \quad vl = q.(p-q) = \frac{1}{2}(p^2 - q^2)\,. \tag{9.78}$$

In the case that a and b are equal, the integral has the expression

$$I_{a^2} = 2\pi \left\{ \ln \frac{4\Delta^2}{\lambda^2} + \frac{a^0}{|\vec{a}|} \ln \left(\frac{a^0 - |\vec{a}|}{a^0 + |\vec{a}|} \right) \right\}. \tag{9.79}$$

With the solution of the Integral we can obtain the results for (9.72).

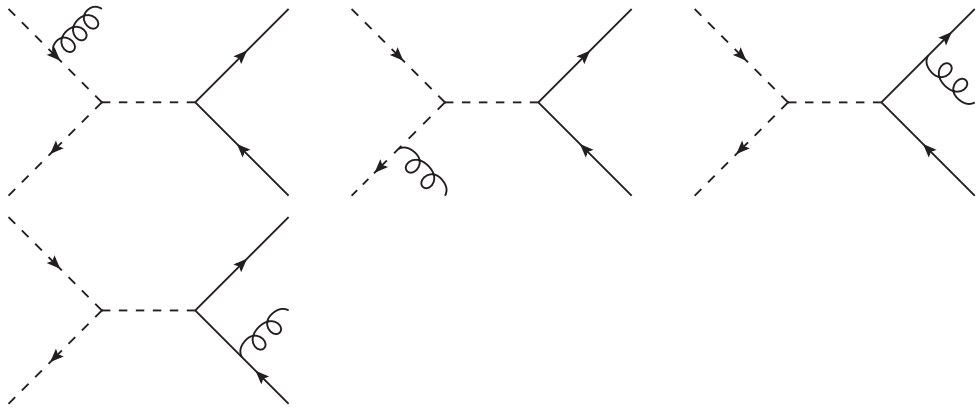

Figure 9.6.: Real emission of higgs s-channel for $\tilde{q}\tilde{q}^* \to q\bar{q}$.

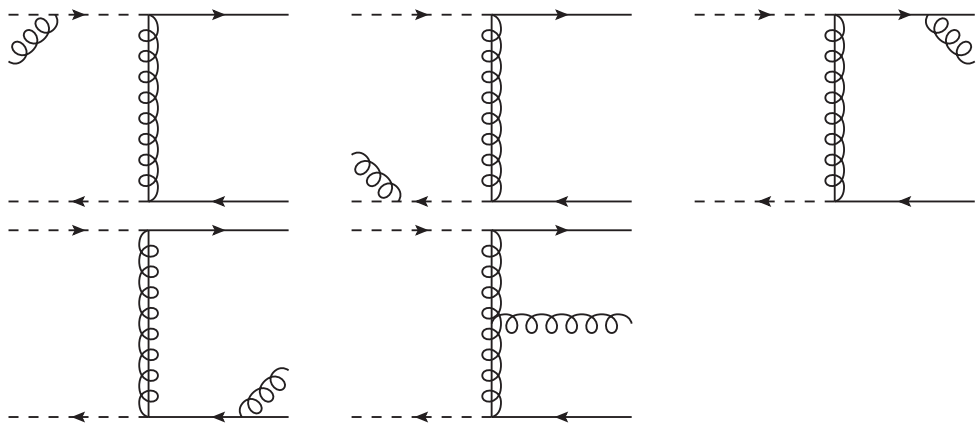

Figure 9.7.: Real emission of gluino t-channel for $\tilde{q}\tilde{q}^* \to q\bar{q}$.

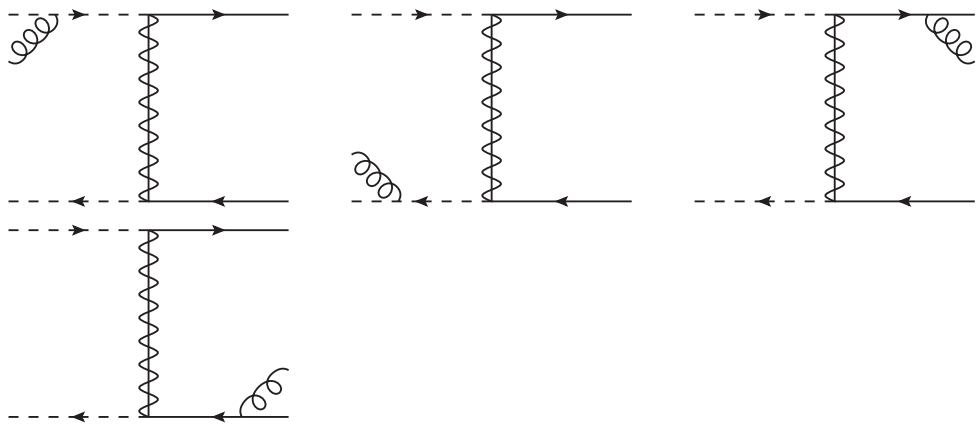

Figure 9.8.: Real emission of neutralino t-channel for $\tilde{q}\tilde{q}^* \to q\bar{q}$.

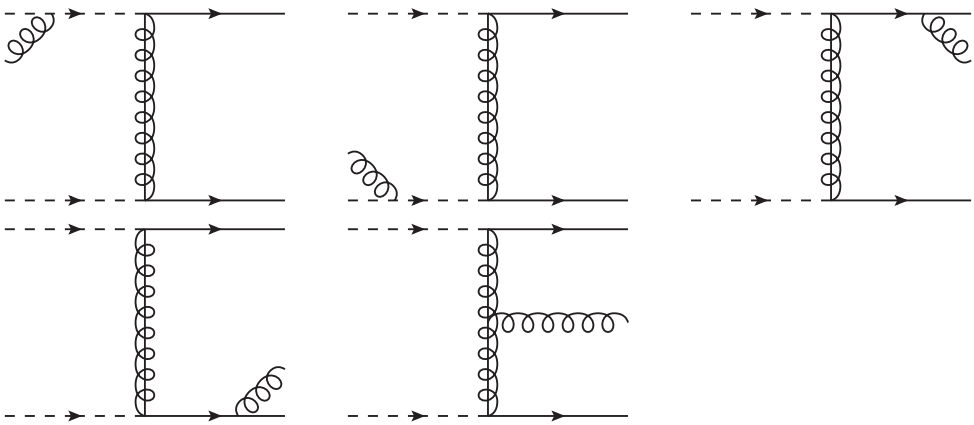

Figure 9.9.: Real emission of gluino t-channel for $\tilde{q}\tilde{q} \to qq$.

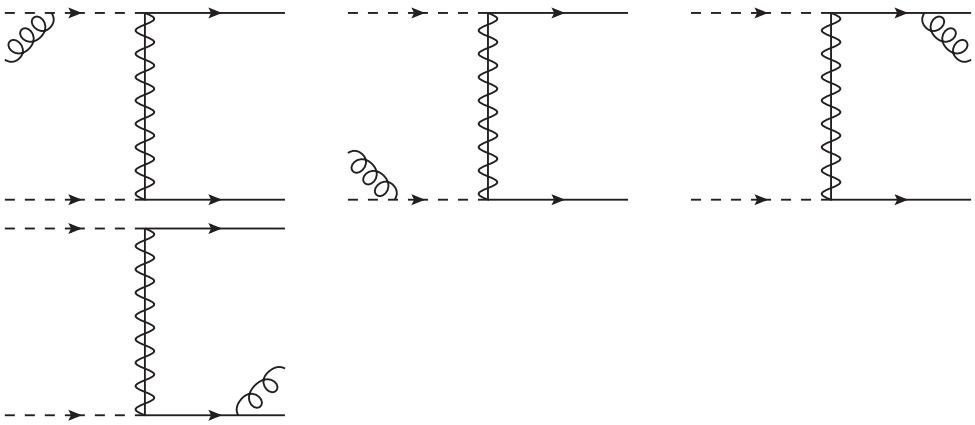

Figure 9.10.: Real emission of neutralino t-channel for $\tilde{q}\tilde{q} \to qq$.

10 Sommerfeld Enhancement

When calculating the relic density in our case, an important contribution comes from the annihilation of squarks moving with non-relativistic velocities. If annihilating, non-relativistic particles couple to much lighter force mediators which in our case are the gluons, the annihilation cross section is modified due to the well-known Sommerfeld effect [141]. The reason for this modification is that the exchange of n gluons between the initial state squarks (see Fig. 10) contains a correction proportional to $(\alpha_s/v_{\text{rel}})^n$. This correction becomes significant and can spoil the perturbative expansion when the relative velocity of the squark pair v_{rel} is comparable to the strong coupling constant α_s. In such a case these contributions have to be resummed to all orders leading to the Sommerfeld effect.

Small relative velocities occur naturally in the freeze-out regime, $E_{\text{kin}} \sim T_{\text{FO}} \sim m_{\tilde{\chi}_1^0}/25$ and therefore the Sommerfeld resummation is expected to be relevant in the case of dark matter annihilation in general and in our case in particular.

As for our processes of interest, $\tilde{q}_i\tilde{q}'_j \to qq'$ and $\tilde{q}_i(\tilde{q}'_j)^* \to q\bar{q}'$, the cross section is dominated by the s-wave component (see Figs. 6.11, 6.12). We can factorize the resummed

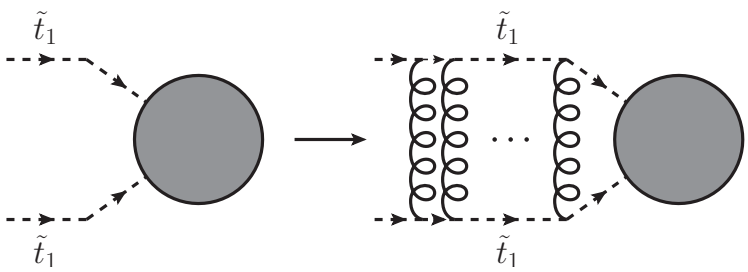

Figure 10.1.: Ladder diagram for a LO Coulomb potential. For non-relativistic velocities, the initial state particles couple to light mediators, modifying the annihilation cross section.

cross section as

$$(\sigma v)_{\text{resum}} = S_{0,[\overline{\mathbf{3}}]}\,(\sigma v)^{\text{Tree}}_{\tilde{q}\tilde{q}\to qq,[\overline{\mathbf{3}}]} + S_{0,[\mathbf{6}]}\,(\sigma v)^{\text{Tree}}_{\tilde{q}\tilde{q}\to qq,[\mathbf{6}]}\,, \tag{10.1}$$

$$(\sigma v)_{\text{resum}} = S_{0,[\mathbf{1}]}\,(\sigma v)^{\text{Tree}}_{\tilde{q}\tilde{q}^*\to q\bar{q},[\mathbf{1}]} + S_{0,[\mathbf{8}]}\,(\sigma v)^{\text{Tree}}_{\tilde{q}\tilde{q}^*\to q\bar{q},[\mathbf{8}]}\,, \tag{10.2}$$

where we have split the leading-order cross section according to its color contribution to the triplet and sextet (singlet and octet) configurations (see Sec. 6.3). $S_{0,\{[\overline{\mathbf{3}}],[\mathbf{6}],[\mathbf{1}],[\mathbf{8}]\}}$ indicate the corresponding s-wave Sommerfeld factors, whose evaluation we discuss in the following. In the non-relativistic limit, the resummation of the gluon exchange diagrams as shown in Fig. 10 amounts to solving the Schrödinger equation with the corresponding Coulomb potential. The Coulomb potential including gluon loops at next-to-next-to-leading order was evaluated in [142] and extended by fermion loops in Ref. [143]. In the $\overline{\text{MS}}$scheme, the Coulomb potential reads [144]

$$\begin{aligned} V^{[\mathbf{R}]}(r) &= C^{[\mathbf{R}]}\,\frac{\alpha_s(\mu_C^{[\mathbf{R}]})}{r} \\ &\times \left\{1 + \frac{\alpha_s(\mu_C^{[\mathbf{R}]})}{4\pi}\left[2b_0\left(\ln(\mu_C^{[\mathbf{R}]}r) + \gamma_E\right) + a_1\right]\right\}, \end{aligned} \tag{10.3}$$

with $\gamma_E = 0.5772$ being the Euler-Mascheroni constant. Furthermore, we have defined

$$b_0 = \frac{11}{3}C_A - \frac{4}{3}T_f n_f\,, \tag{10.4}$$

$$a_1 = \frac{31}{9}C_A - \frac{20}{9}T_f n_f\,, \tag{10.5}$$

where b_0 corresponds to the one-loop β-function coefficient with $C_A = 3$ and $T_F = 1/2$. We treat the top as the only massive quark, such that we set the number of massless quarks to five ($n_f = 5$). The Coulomb potential, given in Eq. (10.3), describes the interaction of any non-relativistic colored particles transforming in general $SU(3)$-representations $\mathbf{R_1}$ and $\mathbf{R_2}$. The color structure of such a scattering process can be decomposed as

$$\mathbf{R_1} \otimes \mathbf{R_2} = \mathbf{R}' \oplus \mathbf{R}''\,. \tag{10.6}$$

The color factor $C^{[\mathbf{R}]}$ is given in terms of the quadratic Casimir operators of the relevant $SU(3)$-representations as

$$\begin{aligned} C^{[\mathbf{R^i}]} &= T_1^a T_2^a = \frac{1}{2}\left[(T_1^a + T_2^a)^2 - (T_1^a)^2 - (T_2^a)^2\right] \\ &= \frac{1}{2}\left(C_2^{\mathbf{R^i}} - C_2^{\mathbf{R}_1} - C_2^{\mathbf{R}_2}\right) \qquad \text{where} \quad \mathbf{R^i} = \mathbf{R}', \mathbf{R}''\,. \end{aligned} \tag{10.7}$$

In the case considered here, the two squarks in the initial state both transform under the fundamental representation of $SU(3)$ and the color decomposition is $\mathbf{3} \otimes 3 = \overline{3} \oplus 6$.

Using the quadratic Casimir operators for the fundamental, the sextet, the singlet and the octet representations, we obtain [145]

$$C^3 = -\frac{1}{2}\left(1+\frac{1}{N_c}\right) = -2/3\,, \tag{10.8}$$

$$C^{\mathbf{6}} = \frac{1}{2}\left(1-\frac{1}{N_c}\right) = 1/3\,, \tag{10.9}$$

$$C^{\mathbf{1}} = C_F = \frac{3}{4}\,, \tag{10.10}$$

$$C^{\mathbf{8}} = -\frac{1}{2N_c}\,. \tag{10.11}$$

The Sommerfeld factors are then obtained by solving the Schrödinger equation

$$\Big[-\frac{2}{m_{\rm red}}\nabla^2 + V^{[\mathbf{R}]}(\mathbf{r}) - \Big(\sqrt{s}+i\Gamma_{\tilde{t}_1}\Big)\Big]\mathcal{G}^{[\mathbf{R}]}\Big(\mathbf{r};\sqrt{s}+i\Gamma_{\tilde{t}_1}\Big) = \delta^{(3)}(\mathbf{r}) \tag{10.12}$$

with the reduced mass $m_{\rm red} = (m_{\tilde{q}}\, m_{\tilde{q}'})/(m_{\tilde{q}}+m_{\tilde{q}'})$ of the two annihilating particles $\tilde{q}$ and $\tilde{q}'$. The solution of the Schrödinger equation with the NLO Coulomb potential defined in Eq. (10.3) is given by the Green's function $\mathcal{G}^{[\mathbf{R}]}(\mathbf{r}, E+i\Gamma_{\tilde{t}_1}) = \mathcal{G}^{[\mathbf{R}]}(\mathbf{r}, \mathbf{r}'=0, E+i\Gamma_{\tilde{t}_1})$. The Sommerfeld factor which is used to correct the cross section in Eq. (10.1) is given by a ratio of two Green's functions at the origin ($\mathbf{r}=0$) [146, 147]

$$S_{0,[\mathbf{R}]} = \frac{\Im[\mathcal{G}^{[\mathbf{R}]}(\mathbf{0}, E+i\Gamma_{\tilde{t}_1})]}{\Im[\mathcal{G}_0(\mathbf{0}, E+i\Gamma_{\tilde{t}_1})]}\,, \tag{10.13}$$

where the Green's function $\mathcal{G}_0(\mathbf{0}, E+i\Gamma_{\tilde{t}_1})$ stands for the solution of the Schrödinger equation without any Coulomb potential. The solution to Eq. (10.12) at the origin is well known [148], and we consider here all terms up to NLO,

$$G^{[\mathbf{R}]}(\mathbf{0};\sqrt{s}+i\Gamma_{\tilde{t}_1}) = \frac{i m_{\rm red}^2 v_{\rm s}}{\pi} + \frac{C^{[\mathbf{R}]}\alpha_s(\mu_C^{[\mathbf{R}]})m_{\rm red}^2}{\pi} \times \left[g_{\rm LO} + \frac{\alpha_s(\mu_C^{[\mathbf{R}]})}{4\pi} g_{\rm NLO}\right], \tag{10.14}$$

where the LO and NLO contributions are given by

$$g_{\rm LO} = L - \psi^{(0)}, \tag{10.15}$$

$$\begin{aligned} g_{\rm NLO} = \beta_0\Big[&L^2 - 2L(\psi^{(0)} - \kappa\psi^{(1)}) + \kappa\psi^{(2)} + (\psi^{(0)})^2 \\ &- 3\psi^{(1)} - 2\kappa\psi^{(0)}\psi^{(1)} + 4\ {}_4F_3(1,1,1,1;2,2,1-\kappa;1)\Big] \\ &+ a_1\Big[L - \psi^{(0)} + \kappa\psi^{(1)}\Big]\,. \end{aligned} \tag{10.16}$$

In Eqs. (10.15)-(10.16) and in the following, we use the short-hand notation

$$\kappa = \frac{iC^{[\mathbf{R}]}\alpha_s(\mu_C^{[\mathbf{R}]})}{2v}, \tag{10.17}$$

$$v_{\mathrm{s}} = \sqrt{\frac{\sqrt{s} + i\Gamma_{\tilde{t}_1} - 2m_{\mathrm{avg}}}{2m_{\mathrm{red}}}}, \tag{10.18}$$

$$L = \ln \frac{i\mu_C^{[\mathbf{R}]}}{4m_{\mathrm{red}}v_{\mathrm{s}}} \,. \tag{10.19}$$

Moreover, $\psi^{(n)} = \psi^{(n)}(1-\kappa)$ is the n-th derivative of $\psi(z) = \gamma_{\mathrm{E}} + \mathrm{d}/\mathrm{d}z \ln\Gamma(z)$ with the argument $(1-\kappa)$, ${}_4F_3(1,1,1,1;2,2,1-\kappa;1)$ a hypergeometric function, and $m_{\mathrm{avg}} = (m_{\tilde{q}} + m_{\tilde{q}'})/2$ the average mass of the two incoming particles. Note that in the case of identical initial state particles the parameter v_{s} in Eq. (10.18) is the non-relativistic velocity of one of the incoming particles, and should not be confused with $v_{\mathrm{rel}} = 2v_{\mathrm{s}}$, the relativistic, relative velocity of the two annihilating particles. In order to calculate the Sommerfeld factor in Eq. (10.13), we also need the Green's function that solves the system without any potential term in Eq. (10.12), which is given by

$$\Im[\mathcal{G}_0(\mathbf{0}, E + i\Gamma_{\tilde{t}_1})] = \frac{m_{\mathrm{red}}^2 v_{\mathrm{s}}}{\pi} \,. \tag{10.20}$$

Finally, we need to fix the scale μ_C that appears in the potential and has an impact on the evaluation of α_s in the Sommerfeld factor. We follow here the treatment presented in Ref. [145] and set

$$\mu_C^{[\mathbf{R}]} = \max\left\{4m_{\mathrm{red}}v_{\mathrm{s}}, \mu_B^{[\mathbf{R}]}\right\} \,, \tag{10.21}$$

where $4m_{\mathrm{red}}v_{\mathrm{s}}$ is motivated by the typical momentum exchange of the gluons in the ladder diagram and the scale $\mu_B^{[\mathbf{R}]}$ corresponds to twice the inverse Bohr radius r_B. It is defined via

$$\mu_B^{[\mathbf{R}]} \equiv 2/r_B = 2C^{[\mathbf{R}]}m_{\mathrm{red}}\alpha_s(\mu_B^{[\mathbf{R}]}) \,. \tag{10.22}$$

In order to obtain $\mu_B^{[\mathbf{R}]}$, we solve Eq. (10.22) iteratively.

As the box diagrams in the full NLO calculation also contain the velocity-enhanced part of the one-gluon exchange, which is at the same time already included in the Sommerfeld resummation, we have to subtract this contribution in order to avoid any double counting.

To isolate the velocity-enhanced term from the box contribution, we expand the box contribution in the relative velocity (for details see App. C.3). We then construct the subtracted cross section $(\sigma v)_{\mathrm{NLO}}^{\mathrm{sub}}$ based on the expanded matrix element of the box diagrams given in Eq. (C.20). The leading velocity-enhanced term of the subtracted cross section is

$$(\sigma v)_{\mathrm{NLO}}^{\mathrm{sub}} \sim \sum_{\mathbf{R}} \left(\frac{\alpha_s(\mu_R)\pi}{v_{\mathrm{rel}}}\right) C_{\mathrm{box}}^{[\mathbf{R}]} (\sigma v)_{\mathrm{Tree}}^{\mathbf{R}} \,. \tag{10.23}$$

Comparing Eq. (10.23) with the next-to-leading order part of the Sommerfeld resummation which arises from the imaginary part of $g_{\rm LO}$, namely $g_{\rm LO}^{\rm sub} = i\pi/2$, and reads

$$(\sigma v)_{\rm resum}^{\rm NLO} = \sum_{\mathbf{R}} \left(\frac{C^{[\mathbf{R}]} \alpha_s(\mu_C^{[\mathbf{R}]})\pi}{2 v_{\rm s}} \right) (\sigma v)_{\rm Tree}^{\mathbf{R}} \,, \tag{10.24}$$

we see, that given $C^{[\mathbf{R}]} = C_{\rm box}^{[\mathbf{R}]}$ and $v_{\rm s} = v_{\rm rel}/2$, the two expressions differ in the scale at which the strong coupling constant is being evaluated. While in the perturbative NLO calculation α_s is evaluated at the renormalization scale $\mu_R = \sqrt{m_{\tilde{q}} m_{\tilde{q}'}}$, in Sommerfeld resummation the characteristic scale μ_C is used. By choosing to use Eq. (10.23) to avoid the double counting, we make use of the fact that the natural scale used in the description of the interaction between incoming particles at small velocities is μ_C. This is consistently used to all orders in the resummed cross section $(\sigma v)_{\rm resum}$ given by Eq. (10.1).

The full next-to-leading order cross section including consistently also the Sommerfeld resummation reads

$$(\sigma v)^{\rm full} = (\sigma v)_{\rm NLO} + (\sigma v)_{\rm resum} - (\sigma v)_{\rm NLO}^{\rm sub} \,. \tag{10.25}$$

Because of the large trilinear couplings in the scenarios, it might be interesting to study the Sommerfeld enhancement coming from the exchange of Higgs bosons [149, 150, 151, 152, 153, 154]. In the regime of Sommerfeld enhancement, also bound state formation can potentially occur, giving rise to new annhilation channels and thus altering the relic density prediction. This has been previously studied for stop-antistop annihilation for both gluon [155] and Higgs exchange [156]. Such studies, however, are far beyond the scope of this work and are left for future analyses.

11 Numerical Results

11.1. The NLO Cross Section Results

In this section we present the first result of our analysis, which is the impact of SUSY-QCD next-to-leading order corrections on the annihilation cross sections of scalar top or bottom pairs. Apart from the cross section (or more precisely σv) we also show in arbitrary units the Boltzmann distribution function which is involved in the calculation of the thermal average $\langle \sigma v \rangle$ at the freeze-out temperature (grey shaded area). It should serve as a reminder that the cross section contributes to the determination of the relic density only in a limited range in the center-of-mass momentum p_{cm}.

11.1.1. Scenario I

In the first scenario introduced in Sec. 6.1, the mass splitting between the lightest neutralino and the lightest stop quark is relatively large. As a result the dark matter annihilation cross section receives important contributions not only from the stop pair annihilation into top quarks but also from the neutralino-stop co-annihilation into a top quark and a gluon and other final states. The results of SUSY-QCD corrections for these processes are shown in Fig. 11.1. As described in the previous section, the next-to-leading order cross section consists of vertex corrections, propagator corrections, box corrections, counterterm contributions and the real radiation cross section, which has to be added to render the prediction infrared finite. The corrections from each contribution are not shown in Fig. 11.1 due to the cancellations of the ultraviolet and infrared divergencies between the contributions, which make each contribution on its own ill defined. In addition to the NLO cross section, we include also the enhanced higher-order contributions stemming from the non-relativistic Coulomb correction.

In case of the annihilation of a pair of scalar top quarks, both initial particles are colored and in the limit of vanishing relative velocity of the squark pair, the Coulomb corrections dominate the full corrected cross section. The origin of these corrections is the exchange of multiple gluons between a pair of slowly moving squarks in the initial state and the details were discussed in Sec. 10. The effect of the Coulomb corrections strongly

depend on the color multiplet, in which the pair of squarks transform. Based on the color decomposition presented in Sec. 6.3, the annihilation cross section $\tilde{t}_1\,\tilde{t}_1 \;\to\; t\,t$ in Scenario I is dominated by the contribution where the squark pair forms a $SU(3)-$sextet (see Fig. 6.11). In this representation the multiple exchange of the gluons can be described by a repulsive non-relativistic QCD potential, as discussed in detail in Sec. 10. That is why the Coulomb corrections in this case cause a reduction of the cross section. As already discussed in the previous section, the next-to-leading order cross section contains the one-loop contribution included also in the Coulomb enhancement. This one-loop contribution can be traced back to all box diagrams in Fig. 7.12, where one gluon is exchanged between the incoming squarks. The contribution from this class of diagrams dominates the one-loop cross section for small velocities and is so large that it causes the cross section with one-loop corrections to be negative (see the green dashed line in Fig. 11.1). As discussed in Sec. 10, in order to prevent double counting, we remove the part of the box contribution which is already included in the Coulomb resummation. This allows us to quantify the pure one-loop correction to the annihilation cross section without any enhancement (red dash-dotted line in Fig. 11.1). We see that the one-loop correction without the enhancement is a large positive correction of about 30-40% over a large range of p_{cm}.

Comparing the result for the non-enhanced NLO cross section with the full result, which is the sum of the non-enhanced NLO cross section and the Sommerfeld corrections shows that the latter are important for all relevant values of p_{cm}. Starting at the largest value of $p_{cm} \sim 600$ GeV which is still relevant for the determination of the relic density, we observe that the Coulomb corrections already reduce the constant 30% NLO correction by a few percent. For smaller relative velocities corresponding to $p_{cm} \sim 150$ GeV, the NLO correction is fully cancelled by the Coulomb corrections, and for very slow velocities the Coulomb corrections take over and the overall correction is large and negative. For almost vanishing velocities the total cross section becomes negative due to this large negative correction. Even though a negative cross section is unphysical, the fact that the cross section vanishes should not be very surprising. The dynamics of the squark pair in the regime when Coulomb corrections are very large (meaning for vanishing velocities) correspond to a motion of the pair in a highly repulsive QCD potential. This in turn means that large repulsive forces repel one squark from the other reducing the probability of annihilation and thereby reducing the cross section. The cross section becomes negative only for $p_{cm} < 10$ GeV, which is irrelevant for the relic density determination, as for such small momenta it is multiplied by an almost vanishing Boltzmann distribution function.

In summary, we can conclude that SUSY-QCD corrections to $\tilde{t}_1\,\tilde{t}_1 \;\to\; t\,t$ are sizeable either through the one-loop corrections for large p_{cm} or the enhanced Coulomb corrections for small p_{cm}.

The co-annihilation processes important in this scenario were discussed in detail in Refs. [114, 116]. In Fig. 11.1 we also show the effect of the SUSY-QCD corrections on the co-annihilation cross sections in Scenario I. We see that the next-to-leading order

corrections in the case of co-annihilations are substantial ranging from -30% in the case of the co-annihilation into top quark and Higgs-boson final state to +50% in the case of the top gluon final state. There are a few substantial differences such as the fact that the corrections are negative in the case of co-annihilations with electroweak bosons or Higgs bosons in the final state or that there is a large difference between our leading order result and the `micrOMEGAs` result for the co-annihilations with electroweak and Higgs bosons, which can be traced to a different definition of underlying parameters in our renormalization scheme. The next-to-leading order correction with respect to the `micrOMEGAs` result is largely reduced to at most -10%. Given that our leading order prediction for the co-annihilations into top quark and a gluon coincides with `micrOMEGAs` prediction, the large next-to-leading order correction gives directly also the correction with respect to the `micrOMEGAs` result.

11.1.2. Scenario II

In the second scenario, the choice of parameters such as $\tan\beta$ and the gaugino and squark mass parameters cause the masses of the lightest neutralino, the lightest scalar top and bottom quarks to be almost degenerate. This leads to different processes contributing significantly to the total dark matter annihilation cross section. The smaller mass difference renders co-annihilations ineffective and the fact that three particles are mass degenerate leads to a larger number of annihilations. Moreover, the large value of $\tan\beta$ enhances the gaugino exchange in the case of the stop-sbottom annihilation, and this together with a different color structure makes this annihilation dominant in the case of Scenario II.

The full next-to-leading order results for three dominant processes are shown in Fig. 11.2. The processes $\tilde{t}_1\,\tilde{t}_1 \;\to\; t\,t$ and $\tilde{b}_1\,\tilde{b}_1 \;\to\; b\,b$ have very similar features to the annihilation of a pair of scalar top quarks in Scenario I. The main difference in this scenario is the process $\tilde{t}_1\,\tilde{b}_1 \;\to\; t\,b$, which has an entirely different decomposition of the leading order cross section in terms of the t- and u-channel exchanges combined with a different color decomposition, which is essential in explaining the behaviour of the NLO cross section. Similar to the already discussed case of $\tilde{t}_1\,\tilde{t}_1 \;\to\; t\,t$, the NLO correction contains a velocity enhanced term, which is already resummed in the Sommerfeld correction. In order to avoid double counting, we define again the non-enhanced NLO correction $\sigma_{\mathrm{NLO_B}}$ where we subtract the term which is already accounted for by the Sommerfeld resummation (red dash-dotted curve in Fig. 11.2). As one can see in Fig. 11.2, the non-enhanced NLO correction is substantial in all processes in Scenario II. In the case of stop pair or sbottom pair annihilations, this NLO correction is compensated by a large and negative Sommerfeld correction which is here derived from a repulsive QCD potential. The color decomposition of the $\tilde{t}_1\,\tilde{b}_1 \;\to\; t\,b$ shows (see Fig. 6.11) that in contrast to the other processes, the cross section is here dominated by the part where the initial stop and sbottom quarks transform as a $SU(3)-$triplet. In this color configur-

ation a pair of slowly moving squarks experiences an attractive strong force, which leads to a large enhancement of the annihilation cross section. Comparing the full result (solid blue line in Fig. 11.2) with the result containing just the non-enhanced NLO corrections, we see that the Sommerfeld enhancement is important over the whole region in p_{cm} that is relevant for the calculation of the relic density.

It is worth mentioning that due to the large value of $\tan\beta$ in Scenario II and to the fact that the chargino u-channel exchange gives an important contribution to the cross section $\tilde{t}_1\,\tilde{b}_1 \;\to\; t\,b$, the Yukawa corrections to the chargino exchange can give a non-negligible contribution. We have included the $\tan\beta$ dependent Yukawa corrections even beyond next-to-leading order in the full result and show their effect separately in Fig. 11.2 (yellow dashed line). Even though the Yukawa corrections are non-negligible, they are small (about 3%) compared to the remaining SUSY-QCD corrections or to the Sommerfeld enhancement.

The full correction to $\tilde{t}_1\,\tilde{b}_1 \;\to\; t\,b$ is larger than 50% over the whole relevant range of p_{cm} and can even exceed 100% (without threatening perturbativity as this correction originates from a resummation). We will show in the next section that using the fully corrected annihilation cross sections in Scenario II has a large impact on the relic density.

11.1.3. Scenario III

In the third scenario, the squark mass parameter cause the masses of the scalar top and bottom quark mass to be almost degenerate. The Higgs mass which is almost twice the third squark mass lead to an resonance, enhancing the squark-anti-squark annihilation through the s-channel Higgs boson exchange. Making the annihilation dominant for the relic density calculation.

Due to the fact that this annihilation is still under investigation, we will confine ourselves on the stop-anti-stop annihilation cross section, which is shown in Fig. 11.3.

In contrast to the cross sections discussed above, the NLO cross section (green dashed line) contains resummation contributions. In order to avoid double counting of these contributions, they are deducted from the resummation contribution. This causes both the full cross section (blue solid line) and the NLO correction to have an enhancement at low p_{cm}.

The correction from the NLO contribution are large due to the Higgs resonance which already starts in the still enhanced region of the resummation. When the Higgs resonance decrease we observe a different enhancing mechanism, which is still under investigation. This enhancement occurs from the overlapping of two annihilation processes when considering the $2 \to 3$ processes. Taking for example the s-channel gluon exchange, we can have a gluon emitted from the propagator, this diagram has the same final states as the annihilation of squark-anti-squark into gluon-pair final state, when one of the final state gluons annihilates further into a quark-pair. The squared amplitude of this diagram usually cancels the nearly divergent parts of the gluon renormalization. For smaller masses,

like the bottom quark mass, this enhancement becomes even larger. The treatment of this enhancement is part of further research.

11.2. Impact on the neutralino relic density

We finally come to the discussion of the impact of the corrections presented in the last chapters on the neutralino relic density $\Omega_{\tilde{\chi}_1^0} h^2$. To this end, we have implemented the corrections into the numerical code `DM@NLO`, which is used as an extension to `micrOMEGAs`. In practice, this means that the Boltzmann equation is still integrated using the latter, while the cross section calculation of the relevant processes (see Tab. 6.2) is performed by `DM@NLO` instead of `CalcHEP`.

In the following, we will illustrate the impact of the corrections by comparing the relic density obtained using the full `DM@NLO` NLO calculation to the values obtained using the tree-level calculation of `micrOMEGAs`/ `CalcHEP`. Since scenario III is still under investigation, the analysis here is reduced to the first two scenarios.

11.2.1. Scenario I

We start by examining the impact of NLO corrections in the vicinity of Scenario I, where we compare the relic density obtained from the `micrOMEGAs` calculation to the one obtained using our full NLO result as presented in the last chapters. The impact is illustrated in Fig. 11.4, where we show the corresponding viable regions of parameter space in the M_1-$M_{\tilde{t}_R}$ plane. As can be seen, the favoured parameter region where the calculated relic density satisfies the experimental constraint, Eq. (3.9), is shifted towards smaller mass parameters in order to compensate the increased annihilation cross section. It is important to note that this shift is larger than the width of the band which corresponds to the *Planck* 2σ-uncertainties.

The situation changes for higher masses, where the processes discussed in this work and corrected at the NLO level, are less relevant. The correction of the remaining processes relevant in this part of parameter space are left for future work.

In Fig. 11.5, we show the same results in the vicinity of Scenario I, but this time projected onto the plane of the physical neutralino and stop masses. Note that, here, the variation of the physical masses solely stems from varying the parameters M_1 and $M_{\tilde{t}_R}$, respectively, while all other soft parameters, including those that in general may influence the neutralino and stop masses, are kept fixed to the values of Table 6.1. From Fig. 11.5, we see that the cosmologically favoured region of parameter space is shifted by about 7 GeV in both the neutralino and the lighter stop mass.

These results lead to the conclusion that the corrections presented in this work are relevant when performing an extraction of either physical masses or fundamental model parameters from cosmological data. Let us note that this conclusion is the same as for

the previous analyses of other processes entering the calculation of $\Omega_{\tilde{\chi}_1^0}h^2$ [109, 110, 111, 113, 114, 116, 117].

In order to get a better understanding of the impact of the different contributions to the annihilation cross section σ_{ann}, and consequently to the relic density $\Omega_{\tilde{\chi}_1^0}h^2$, we have performed a one-dimensional scan along the region where `micrOMEGAs` predicts the correct relic density varying simultaneously the parameters M_1 and $M_{\tilde{t}_R}$. The result of this scan is shown in Fig. 11.6 as a function of both parameters while all other parameters were fixed to the values given in Tab. 6.1.

First, it can be noticed that our tree-level prediction differs from the `micrOMEGAs` result. This is a direct consequence of the corresponding difference in the annihilation cross sections, as discussed in Sec. 6.2 and shown, e.g., in Fig. 11.1. Taking into account the corrections discussed in Sec. 7, it can be seen that the total correction is split into two parts associated with the relevant classes of processes, namely $\tilde{t}_1\tilde{t}_1 \to tt$ and $\tilde{\chi}_1^0\tilde{t}_1 \to qg, qV, q\phi$. Fig. 11.1 shows that the correction to the relic density in Scenario I is dominated by the corrections to the co-annihilation processes even though at leading order these processes contribute about a factor two less than $\tilde{t}_1\tilde{t}_1 \to tt$. This is a consequence of the Sommerfeld supression of the annihilation cross section as discussed in Sec. 11.1. Moreover, we see that for lower bino/squark mass parameters $M_1/M_{\tilde{t}_R}$ the correction to the co-annihilation processes is numerically more important than for large mass parameters. This is explained by the fact that the relative importance of the co-annihilation processes is higher in this region of parameter space (see, e.g., Fig. 6.4). Moving towards higher values of M_1, the relative importance of the stop-pair annihilation increases and, consequently, the associated correction to the relic density becomes more important.

Overall, the relic density obtained using our full (i.e. NLO including resummation) caluclation is about 6% smaller than the one obtained by using `micrOMEGAs`. Again, we emphasize that this shift is more important than the uncertainty given by the *Planck* measurement, which is, at the 2σ confidence level of about 2%.

11.2.2. Scenario II

Let us now focus on Scenario II, where not only $\tilde{t}_1\tilde{t}_1 \to tt$ is relevant, but also the related processes $\tilde{b}_1\tilde{b}_1 \to bb$ and $\tilde{t}_1\tilde{b}_1 \to tb$ give sizeable contributions to the annihilation cross section σ_{ann}. Therefore they need as well to be corrected at the NLO level including the resummation, as discussed in the last chapters.

Again, we start by depicting the parameter region compatible with the measured value for the relic density (see the second row of plots in Fig. 11.4) in the vicinity of Scenario II, in this case in the M_1-$M_{\tilde{q}_L}$ plane, which are the relevant neutralino and squark mass parameters. Similar to Scenario I, as discussed above, the viable regions with respect to the relic density is shifted towards lower masses. Here, the shift is again more important than the uncertainty and is much larger than in Scenario I. It corresponds to a shift

of about 17 GeV in the bino mass parameter M_1 and about 15 GeV in the left-handed squark mass parameter $M_{\tilde{q}_L}$.

In terms of physical masses, shown in Fig. 11.5, this corresponds to a shift of about 17 GeV for the neutralino mass, and of about 15 GeV in the lighter stop mass. Once more, these findings underline the importance of the presented corrections in the light of precision cosmology. It is to be noted that for this part of the analysis only M_1 and $M_{\tilde{q}_L}$ have been varied and the results have been projected on the so obtained plane of the physical neutralino and stop masses, while all other parameters have remained fixed to the values given in Tab. 6.1.

In order to decompose our full NLO prediction for the relic density into the contributions from different processes, we show in Fig. 11.6 the NLO corrected contributions to the relic abundance from individual processes along the region where `micrOMEGAs` predicts the correct relic density varying simultaneously the parameters M_1 and $M_{\tilde{q}_L}$. We see that already using our tree-level annihilation cross section with differently defined input parameters shifts the relic density by a few percent (black dashed line). In all remaining contributions we use our tree-level annihilation cross section for all relevant processes. Starting from our tree-level, a very small correction of about 1% in the whole region comes from including NLO corrections only to the $\tilde{t}_1\tilde{t}_1 \to tt$ and $\tilde{b}_1\tilde{b}_1 \to bb$. It is important to point out that the reason for this extremely small correction is the Sommerfeld enhancement, which in this case in fact suppresses the cross section. This is due to the repulsive nature of the dominant $SU(3)-$sextet contribution. Even if the full correction to the cross section was large and negative for small p_{cm} (see Fig. 11.2), interestingly the correction to the thermal averaged cross section is still positive leading to a drop in relic density. The largest contribution comes from the annihilation cross section of $\tilde{t}_1\tilde{b}_1 \to tb$. The first reason is the large contribution of this process to the total annihilation cross section already at tree-level (see Tab. 6.2). The second reason is the large Sommerfeld enhancement emerging from the attractive potential of the dominant $SU(3)-$triplet contribution, which in this case makes the full correction to the cross section extremely large. We see that depending on the dominant contribution of the color decomposition, $SU(3)-$sextet or $SU(3)-$triplet, the Sommerfeld corrections either suppresses or enhances the cross section such that the total SUSY-QCD correction to the relic density over the whole range is about 25%. This results in the visible shift of the preferred parameter region, which is much larger than the experimental uncertainty given in Eq. (3.9).

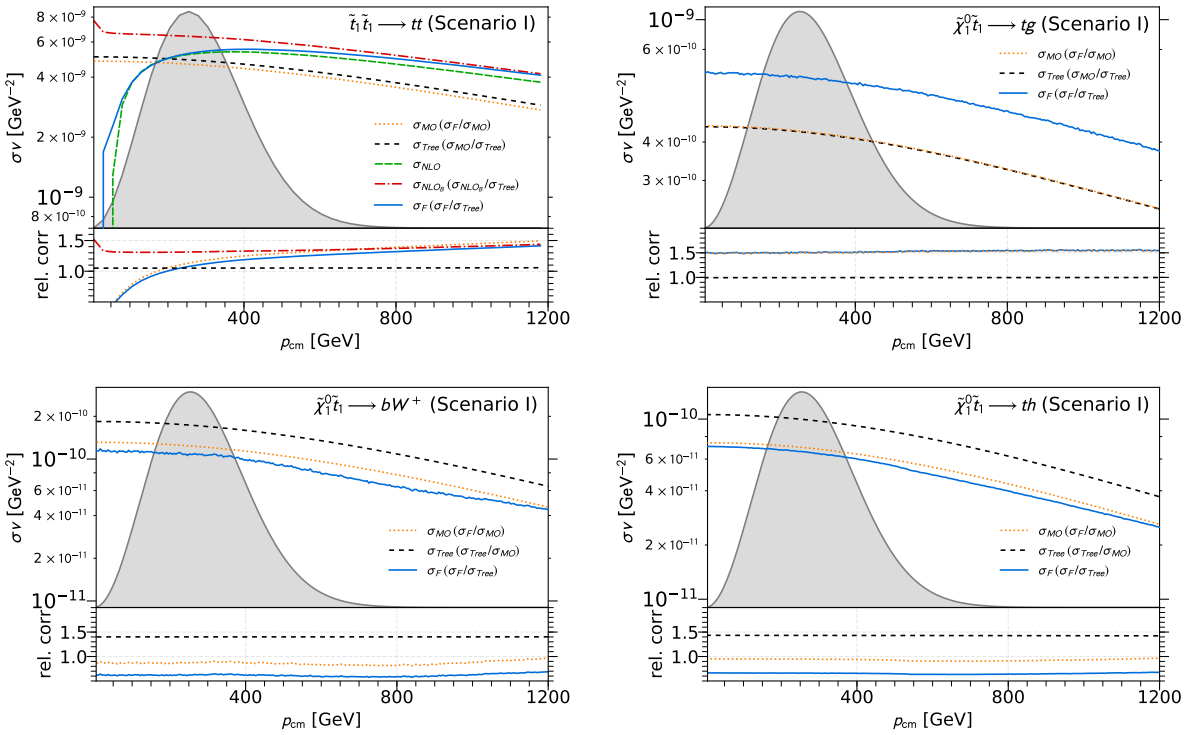

Figure 11.1.: Annihilation cross section σv for the stop annihilation into top quarks (first panel) and neutralino-stop co-annihilation (three remaining panels) for Scenario I, computed using the `micrOMEGAs` tree-level calculation (MO), our leading-order calculation (Tree), our fixed-order NLO calculation (NLO, only first panel), our fixed-order NLO calculation without the velocity enhanced part of the box contributions ($\mathrm{NLO_B}$, only first panel), and our full NLO calculation including resummation (F). The lower part shows various relative cross sections according to the second part of the legend.

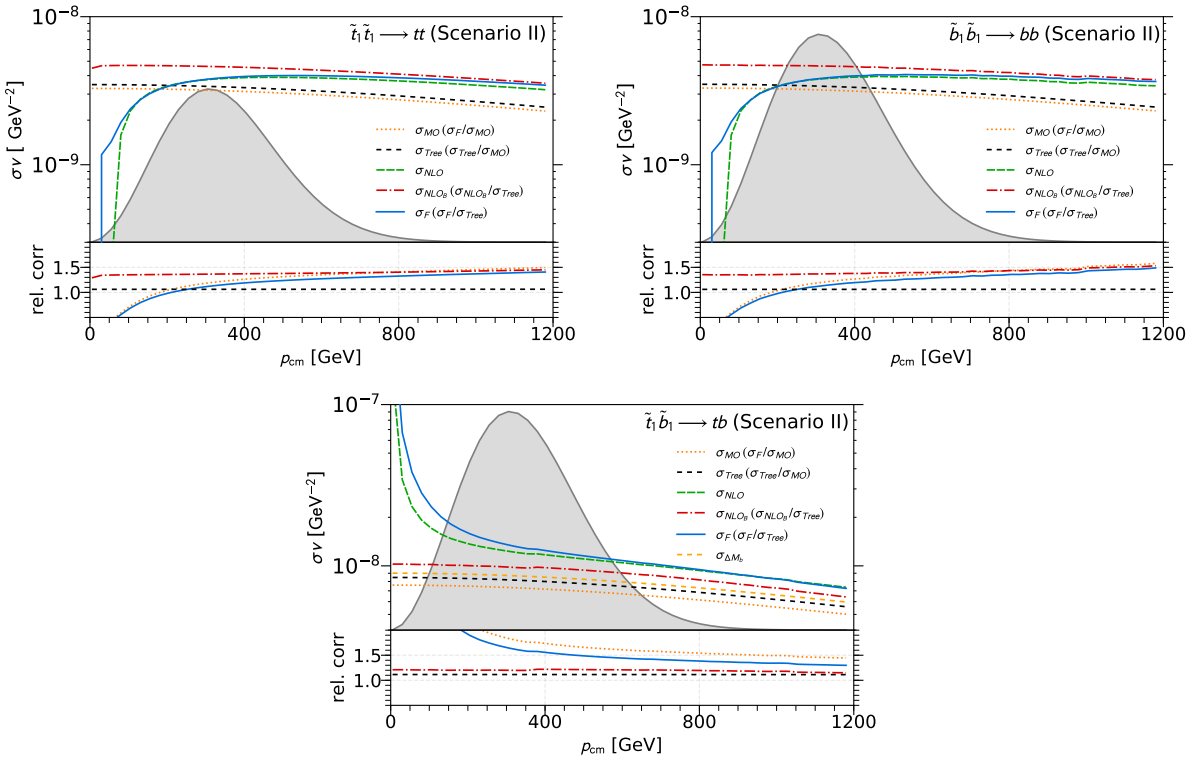

Figure 11.2.: Same as Fig. 11.1 for the three quark-annihilation processes relevant in Scenario II. In the last panel, we show in addition the cross section for chargino u-channel exchange with β-enhanced Yukawa corrections ($\sigma_{\Delta M_b}$).

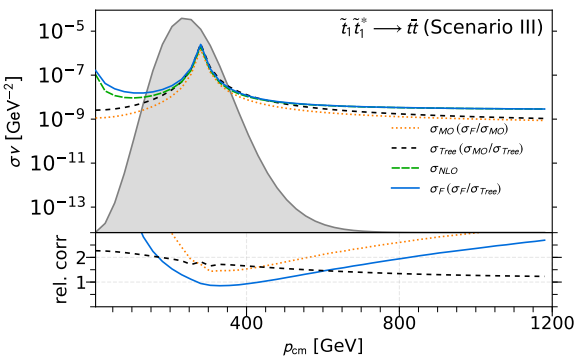

Figure 11.3.: Annihilation cross section σv for the stop-anti-stop annihilation process relevant in Scenario III.

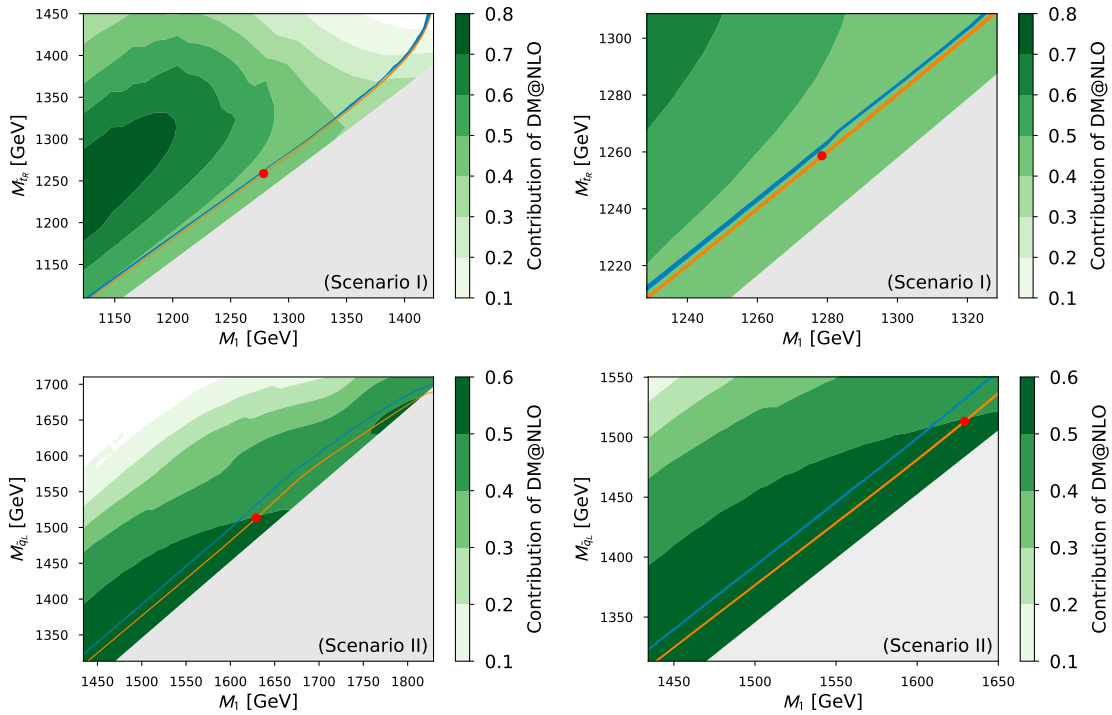

Figure 11.4.: Parameter regions compatible with the *Planck* limits given in Eq. (3.9) presented in the M_1-$M_{\tilde{t}_R}$ plane around Scenario I and in the M_1-$M_{\tilde{q}_L}$ plane around Scenario II. The orange band corresponds to the `micrOMEGAs` calculation, while the blue band stems from the full `DM@NLO` one-loop calculation. The right panel corresponds to a zoom into the left panel around Scenario I (or Scenario II), which is indicated by the red dot. Grey regions are excluded due to stop LSP.

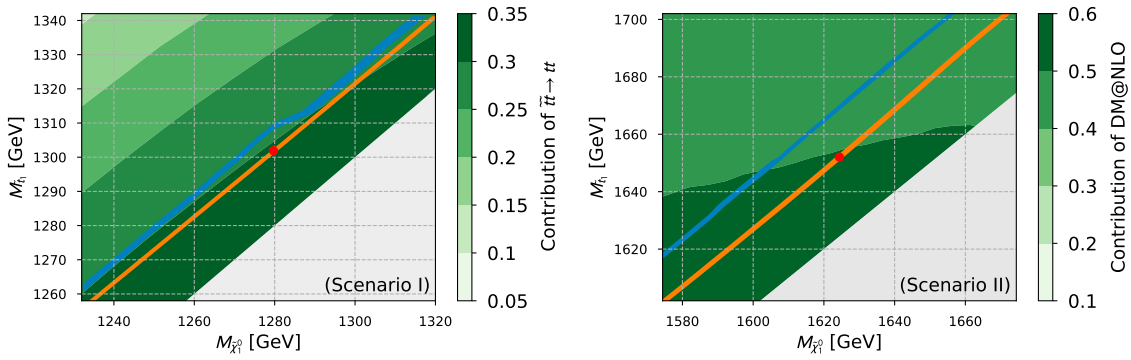

Figure 11.5.: Same as Fig. 11.4, but projected into the plane of the physical neutralino and stop masses.

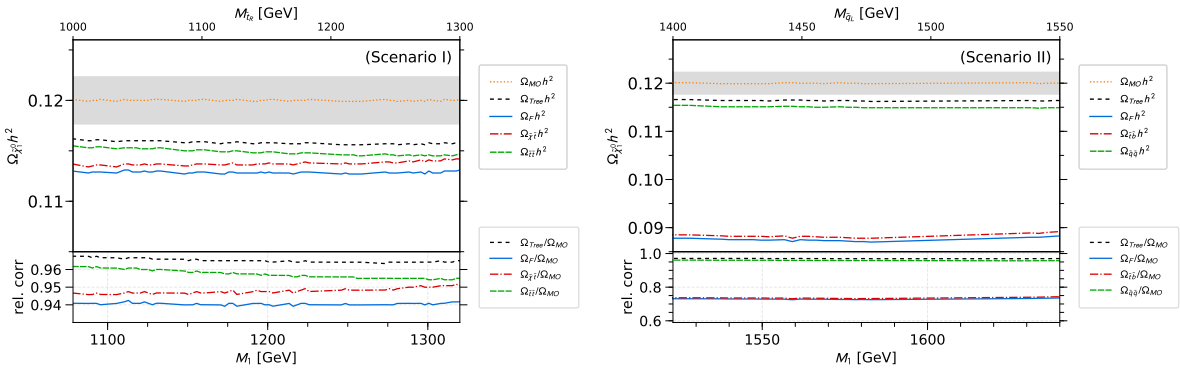

Figure 11.6.: Upper part: Neutralino relic density $\Omega_{\tilde{\chi}_1^0}h^2$ along the parameter region satisfying the experimental constraints on the relic abundance. Both, the bino mass parameter M_1 and the squark mass parameter $M_{\tilde{t}_R}$ (or $M_{\tilde{q}_L}$) around Scenario I (or Scenario II). In both plots we show the values obtained using `micrOMEGAs` ($\Omega_{\mathrm{M}O}h^2$), our tree-level calculation ($\Omega_{\mathrm{T}ree}h^2$), our full one-loop calculation including the resummation ($\Omega_{\mathrm{F}}h^2$). For Scenario I, we also show the value obtained correcting only neutralino-stop co-annihilation ($\Omega_{\tilde{\chi}_1^0\tilde{t}_1}h^2$), and the value obtained correcting only stop-pair annihilation ($\Omega_{\tilde{t}_1\tilde{t}_1}h^2$). Similar for Scenario II we show the effect of correcting only the stop and sbottom pair annihilations ($\Omega_{\tilde{q}_1\tilde{q}_1}h^2$) and the stop-sbottom annihilations ($\Omega_{\tilde{t}_1\tilde{b}_1}h^2$). Lower part: Impact of the different contributions relative to the relic density obtained by using `micrOMEGAs`.

12 Conclusion

Although the Standard Model successfully describes countless experimental observations in (astro)particle physics, some questions remain unanswered. As a part of this thesis, the MSSM was discussed as a possible extension of the Standard Model. The basic structure of the supersymmetric algebra was discussed all the way to the Lagrange density. The MSSM was summarized including its particle content. Current analyses of ATLAS and CMS were shown, which gave information about the parameter space in the MSSM for our later analysis.

With the open question on the nature of dark matter we reviewed astrophysical observations. We discussed properties and possible particle candidates for dark matter. We also briefly talked about ongoing experimental research on dark matter, including its current results. Furthermore, we discussed the determination of the relic density, which is well predicted by the Planck collaboration.

As an experimental project, the electric field configuration of the Hamamatsu R12199-02 MOD three-inch PMT was investigated using a finite element simulation. The considered setups are relevant for use of this PMT in the newly developed optical module of the future extension of the IceCube neutrino telescope. The negative impact of conductive materials in the vicinity of the photocathode or the dynode system, associated with increased noise levels, was reproduced in the study. The effectiveness of the intended noise reduction measures, i.e. connecting the PMT reflectors to the cathode potential and coating the PMT with a conductive layer at the same potential ("HA coating"), could also be demonstrated. This study resulted in an improved understanding of the mechanisms of increased PMT noise as well as its reduction.

Scenarios in the MSSM with light stops are still very appealing due to their potential to address many problems that the MSSM with heavy particles might have. The contribution of squark- and squark-anti-squark annihilation to relic density as a function of mass difference of squarks to dark matter particles was discussed, and scenarios were presented in which squark- or squark-anti-squark annihilation provide important contributions to relic density. Those scenarios pass all current experimental constraints. The scenarios and the surrounding parameter space were analyzed for contributing processes. Furthermore, the contributions of the individual channels to the respective cross sections were discussed, as well as the color separation of the respective cross sections for

identical and different particles. We focused on the SUSY-QCD corrections to squark pair annihilations into quarks and squark-anti-squark annihilation into a quark pair. We have reviewed the details of the one-loop calculation and of the Sommerfeld enhancement. We have shown that the one-loop corrections of the cross sections are sizeable even without the Sommerfeld enhancement. The Sommerfeld corrections are shown to cause two different effects depending on the nature of the strong force between the pair of incoming scalar quarks. In the case of annihilations between the same type of squarks, the enhancement turns into a reduction of the cross section as here the squarks experience a strong repulsive force. If the scalar quarks are different, however, the cross section is strongly enhanced due to the attractive strong force, like it is the case for squark-anti-squark annihilation. Finally, we have investigated the impact of the corrections of the squark annihilation on the predicted relic density of the first two scenarios. We have demonstrated in our typical scenarios that even with the Sommerfeld reduction, the corrections are larger than the experimental uncertainty. In case of an enhancement, the corrections cause a 25% shift in the preferred parameter region where the relic density satisfies the experimental constraints.

Further investigation is needed to finalize the analysis on the squark-anti-squark annihilation. Here the enhancement due to the overlapping of different processes has to investigated. This will be part of future research.

A lot of processes which contribute to the calculation of the relic density are already implemented in `DM@NLO`, starting with the annihilation of neutralinos, including also co-annihilation with squarks and furthermore squark annihilation to electro weak final states as in quark final states. In each case, the NLO SUSY-QCD corrections resulted in large corrections regarding the cross section and a significant shift of the relic density line within the parameter space. For future projects the implementation of squark-anti-squark in gluon pair final states remains, which is most likely a leading process, considering squark-anti-squark annihilation in quark-anti-quark final states. Furthermore, the consideration of stau-anti-stau is planed. During the analysis of the scenarios, Sec 6.1, it also became apparent that in many regions of the parameter space gluino annihilation and co-annihilation with squarks are important processes for the calculation of the relic density.

A Summary of Formulae

In the following formulae used in the calculation contributing to the thesis are listed below.

A.1. Euler di-logarithm

The spence function is defined as

$$\mathrm{Li}_2(z) = -\int_0^z \frac{dt}{t} \ln(1-t) = -\int_0^1 \frac{dt}{t} \ln(1-zt) \tag{A.1}$$

with the relations

$$\Im\left[\mathrm{Li}_2(z+i\epsilon)\right] = \pi \ln(z)\theta(z-1) \tag{A.2}$$

and

$$\frac{d}{dz}\mathrm{Li}_2(z) = -\frac{\ln(1-z)}{z}\,. \tag{A.3}$$

Summary of useful values

$$\mathrm{Li}_2(0) = 0 \tag{A.4}$$

$$\mathrm{Li}_2(1) = \frac{\pi^2}{6} \tag{A.5}$$

$$\mathrm{Li}_2(-1) = \frac{\pi^2}{12} \tag{A.6}$$

$$\mathrm{Li}_2(\frac{1}{2}) = \frac{\pi^2}{12} - \frac{\ln^2(2)}{2} \tag{A.7}$$

and useful identities

$$\mathrm{Li}_2(z) = -\mathrm{Li}_2(1-z) - \ln z \ln(1-z) + \frac{\pi^2}{6} \tag{A.8}$$

$$\mathrm{Li}_2(z) = -\mathrm{Li}_2\left(\frac{1}{2}\right) - \frac{1}{2}\ln^2(-z) - \frac{\pi^2}{6} \tag{A.9}$$

$$\mathrm{Li}_2(z) = \mathrm{Li}_2\left(\frac{1}{1-z}\right) + \frac{1}{2}\ln^2(1-z) - \ln(-z)\ln(1-z) - \frac{\pi^2}{6} \tag{A.10}$$

$$\mathrm{Li}_2(z) = -\mathrm{Li}_2\left(\frac{z}{z-1}\right) - \frac{1}{2}\ln^2(1-z) + \frac{\pi^2}{2} + i\pi \ln\left(\frac{z-1}{z^2}\right) \text{ if } z > 1 \tag{A.11}$$

A.2. Dirac Algebra

Here we present a short list of used formulae of the Dirac algebra [157].

A.2.1. Dirac Matrices

$$\begin{aligned} \not{p} &= \gamma^\mu p_\mu \\ \{\gamma^\mu, \gamma^\nu\} &= 2\mathrm{g}^{\mu\nu} \\ \not{k}\gamma^\nu &= -\gamma^\nu \not{k} + 2k^\nu \\ \not{a}\not{b} &= -\not{b}\not{a} + 2a\cdot b \\ \gamma_\nu\gamma^\nu &= 4 \end{aligned}$$

$$\begin{aligned} \gamma_\mu \not{a}\gamma^\mu &= -2\not{a} \\ \gamma_\mu \not{a}\not{b}\gamma^\mu &= 4a\cdot b \\ \gamma_\mu \not{a}\not{b}\not{c}\gamma^\mu &= -2\not{c}\not{a}\not{b} \\ \not{k}\gamma^\nu &= -\gamma^\nu\not{k} + 2k^\nu \\ (a-\gamma_5)\gamma^0 &= \gamma^0(1+\gamma_5) \end{aligned}$$

A.2.2. Spinors

$$\begin{aligned} \overline{u}(p) &= u^+(p)\gamma_0 \\ \sum_s \overline{u}(p)u(p) &= \mathrm{Tr}(\not{p}+m) \\ \sum_s v(p)\overline{v}(p) &= \mathrm{Tr}(\not{p}-m) \end{aligned}$$

$$\begin{aligned} \overline{u}(p)(\not{p}-m) &= 0 \\ (\not{p}-m)v(p) &= 0 \\ \not{k}\epsilon(k) &= 0 \end{aligned}$$

$$\begin{aligned} \textstyle\sum_s \epsilon^\star_\nu(k)\epsilon_\mu(k) &= (\mathrm{g}^{\mu\nu}) && \text{Fermi-gauge} \\ &= (-\mathrm{g}^{\mu\nu} - \tfrac{k_\mu k_\nu}{m^2}) && \text{unitary gauge} \end{aligned}$$

A.2.3. Traces

$$\mathrm{Tr}(\mathbb{1}) = 4 \qquad \mathrm{Tr}(\gamma_5 \not{a}\not{b}) = 0$$
$$\mathrm{Tr}(\gamma_5) = 0 \qquad \mathrm{Tr}(\gamma_5 \not{a}\not{b}\not{c}) = 0$$
$$\mathrm{Tr}(\not{a}\not{b}) = 4a \cdot b \qquad \mathrm{Tr}(\gamma_5 \not{a}\not{b}\not{c}\not{d}) = 4\mathrm{i}\epsilon_{\alpha\beta\gamma\rho}$$

$$\mathrm{Tr}(\not{a}\not{b}\not{c}\not{d}) = 4[(a \cdot b)](c \cdot d) + (a \cdot d)(b \cdot c) - (a \cdot c)(b \cdot d)]$$

A.3. Polarization

$$P_L = \frac{1}{2}(1 - \gamma_5) \tag{A.12}$$

$$P_R = \frac{1}{2}(1 + \gamma_5) \tag{A.13}$$

$$P_R P_L = 0 \tag{A.14}$$

$$P_R P_R = P_R \qquad P_L P_L = P_L \tag{A.15}$$

$$P_L + P_R = \mathbb{1} \tag{A.16}$$

$$\mathrm{Tr}(P_L) = 2 = \mathrm{Tr}(P_R) \tag{A.17}$$

A.4. Color

In the following we briefly discuss color relations and important formula2 [158, 159] relevant for the calculations.

A.4.1. SU(N)

The special unitary group SU(N) is made up of unitary $N \times N$ matrices. The basis of this group is given by $(N^2 - 1)$ linearly independent matrices, which are known as the hermitian generators T^a of the group. Taking a look on the SU(3) the hermitian generators, they can be related to the Gell-Mann matrices λ^a

$$(T^a)_{ij} = \frac{\lambda^a_{ij}}{2}. \tag{A.18}$$

The generators of the group SU(N) fulfill the commutation relations

$$[T^a, T^b] = \mathrm{i} f^{abc} T^c. \tag{A.19}$$

f^{abc} are the fully anti-symmetric structure constants of the SU(N). The commutation relation has to be fulfilled by each generator of SU(N). The fundamental representation is given by

$$(T^a_F)_{ij} = (T^a)_{ij} = \frac{\lambda^a_{ij}}{2}. \tag{A.20}$$

In the fundamental representation the generators of the group are normalized

$$\mathrm{Tr}(T^a_F T^b_F) = T_F \delta^{ab} \qquad \text{with} \qquad T_F = \frac{1}{2}. \tag{A.21}$$

T_F is known as the Dynkin index. The invariant quadratic Casimir operator is given by

$$\sum_{a,k} (T^a_F)_{ik} (T^a_F)_{kj} = C_F \delta_{ij} \qquad \text{with} \qquad C_F = \frac{N^2 - 1}{2N}. \tag{A.22}$$

The fundamental representation is a complex representation. The complex conjugated anti-fundamental representation $(T^a_{\overline{F}})_{ij}$ has the generators

$$(T_{\overline{F}^a})_{ij} = -(T^{\star a})_{ij}. \tag{A.23}$$

In the adjoint representation the generators are defined due to the structure constant

$$(T^a_A)_{bc} = -\mathrm{i} f_{abc} \tag{A.24}$$

with the normalization

$$\sum_{c,d} (T^c_A)_{ad} (T^c_A)_{db} = \sum_{c,d} f_{acd} f_{bcd} = C_A \delta_{ab} \qquad C_A = T_A = N. \tag{A.25}$$

The fully anti-symmetric structure constant is calculated by

$$f^{abc} = -2\mathrm{i}\mathrm{Tr}(T^a[T^b, T^c])\,. \tag{A.26}$$

The fully symmetric structure constant is defined by anti-commutation relations

$$\{T^a, T^b\} = \frac{1}{N}\delta_{ab} + d_{abc}T^c\,. \tag{A.27}$$

A.4.2. Useful Relations

$$\sum_a T^a_{ij}T^a_{kl} = \frac{1}{2}(\delta_{il}\delta_{kj} - \frac{1}{N}\delta_{ij}\delta_{kl}) \tag{A.28}$$

$$\sum_{a,k} T^a_{ik}T^a_{kj} = C_F\delta_{ij} \tag{A.29}$$

$$\mathrm{Tr}(T^a) = 0 \tag{A.30}$$

$$\mathrm{Tr}(T^aT^b) = \frac{1}{2}\delta^{ab} \tag{A.31}$$

$$\mathrm{Tr}(T^aT^bT^c) = \frac{1}{4}\left(d^{abc} + if^{abc}\right) \tag{A.32}$$

$$\mathrm{Tr}(T^aT^bT^aT^c) = -\frac{1}{4N_c}\delta^{bc} \tag{A.33}$$

$$\mathrm{Tr}(T^aT^bT^aT^b) = -\frac{1}{2}C_F \tag{A.34}$$

$$\mathrm{Tr}(T^aT^bT^bT^a) = C_F^2N_C \tag{A.35}$$

$$\mathrm{Tr}(T^aT^bT^bT^cT^aT^c) = -\frac{1}{2}C_F^2 \tag{A.36}$$

$$\mathrm{Tr}(T^aT^bT^cT^aT^bT^c) = \frac{1}{4N_c}C_F(N_c^2+1) \tag{A.37}$$

$$\mathrm{Tr}(T^bT^cT^aT^cT^bT^a) = \frac{1}{4N_c}C_F \tag{A.38}$$

$$\left(\mathrm{Tr}(T^aT^bT^c)\right)^2 = -\frac{1}{2}C_F \tag{A.39}$$

$$\mathrm{Tr}(T^aT^bT^c)\mathrm{Tr}(T^aT^cT^b) = \frac{1}{2}\left(C_F^2N_c - \frac{1}{2}C_F\right) \tag{A.40}$$

$$T^aT^b = \frac{1}{2}\left(\frac{1}{N}\delta^{ab} + (d^{abc} + \mathrm{i}f^{abc})T^c\right) \tag{A.41}$$

$$f^{acd}f^{bcd} = N\delta^{ab} \tag{A.42}$$

$$[T^a, [T^b, T^c]] = \{T^c, \{T^a, T^b\}\} - \{T^b, \{T^c, T^a\}\} \tag{A.43}$$

$$f^{abc}f^{dec} = \frac{2}{N}(\delta^{ad}\delta^{be} - \delta^{ae}\delta^{bd}) + (d^{aec}d^{bdc} - d^{bec}d^{adc}). \tag{A.44}$$

$$[T^a, [T^b, T^c]] = if^{bce}(if^{aed}T^d) \tag{A.45}$$

$$f^{acd}d^{bcd} = 0 \tag{A.46}$$

$$f^{ade}f^{bef}f^{cfd} = \frac{N}{2}f^{abc} \tag{A.47}$$

$$d^{abc}f^{cde}f^{efa} = -\frac{N}{2}d^{bdf} \tag{A.48}$$

$$d^{abc}d^{dbc} = \frac{N^2-4}{N}\delta^{ad} \tag{A.49}$$

$$d^{abk}d^{kcl} = \frac{1}{N}\left(\delta^{ac}\delta^{bl} + \delta^{al}\delta^{bc} - \delta^{ab}\delta^{cl} + f^{ack}f^{blk} + f^{alk}f^{bck}\right) \tag{A.50}$$

$$d^{abc}d^{cde}f^{efa} = \frac{3}{2}f^{bdf} \tag{A.51}$$

$$[T^a, T^b]_{st}[T^a, T^b]_{ts} = -N_c^2 C_F \tag{A.52}$$

$$\{T^a, T^b\}_{st}\{T^a, T^b\}_{ts} = C_F(N_c^2 - 2) \tag{A.53}$$

B Couplings

This chapter includes all used Feynman rules [6, 133, 160] for the calculation of the Feynman diagrams. The conventional style is, each sfermion $\tilde{f}$ is visualized by a dashed line with an arrow pointing in the flavor flow direction. A dashed line without an arrow corresponds to a scalar particle, not carrying squark flavor (e.g. higgs h^0).

B.1. Gluons

Triple-Gluon

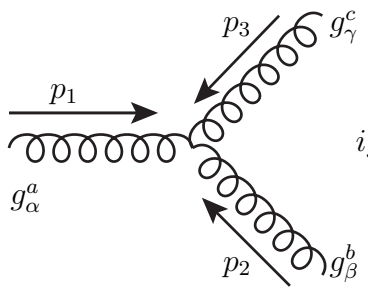

$$ig_s(i\mathrm{f}^{abc})[\mathrm{g}^{\alpha\beta}(p_1-p_2)^\gamma + \mathrm{g}^{\beta\gamma}(p_2-p_3)^\alpha + \mathrm{g}^{\gamma\alpha}(p_3-p_1)^\beta] \tag{B.1}$$

4-Gluon

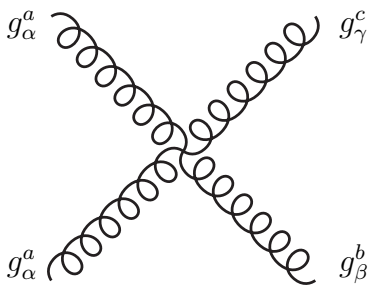

$$\begin{aligned}\mathrm{i}g_s^2[&(\mathrm{if}^{ead}\mathrm{if}^{ebc})(\mathrm{g}^{\alpha\beta}\mathrm{g}^{\delta\gamma}-\mathrm{g}^{\alpha\gamma}\mathrm{g}^{\delta\beta})\\ &+(\mathrm{if}^{eab}\mathrm{if}^{ecd})(\mathrm{g}^{\alpha\gamma}\mathrm{g}^{\delta\beta}-\mathrm{g}^{\alpha\delta}\mathrm{g}^{\beta\gamma})\\ &+(\mathrm{if}^{eac}\mathrm{if}^{edb})(\mathrm{g}^{\alpha\delta}\mathrm{g}^{\beta\gamma}-\mathrm{g}^{\alpha\beta}\mathrm{g}^{\delta\gamma})]\end{aligned} \tag{B.2}$$

Gluon-Gluino-Gluino

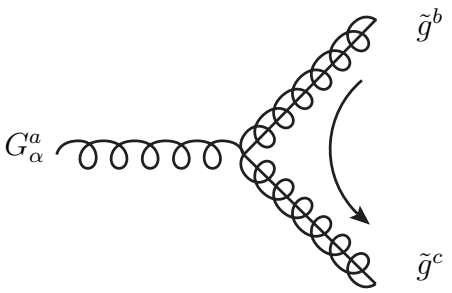

$$ig_s(if^{abc})\gamma^\alpha \tag{B.3}$$

Gluon-Quark-Quark

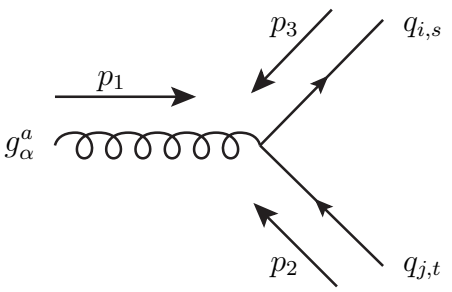

$$-ig_s\mathrm{T}^a_{st}\gamma^\alpha \tag{B.4}$$

Gluon-Squark-Squark

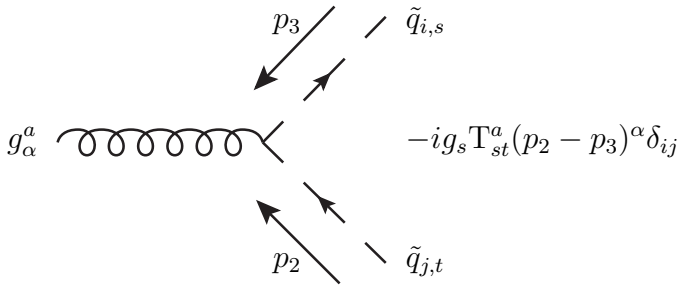

(B.5)

Gluon-Gluon-Squark-Squark

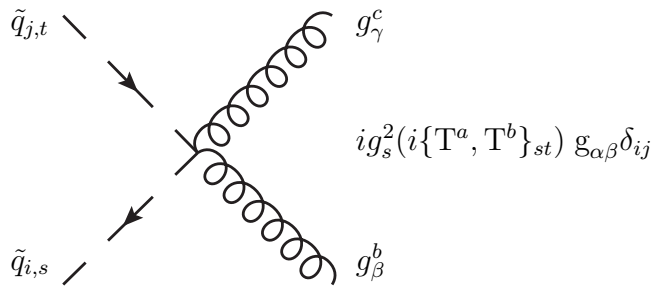

(B.6)

B.2. Gauginos

Gluino-Squark-Quark

$$R = (R_{iL}, R_{iR}) = \begin{pmatrix} \cos\theta & \sin\theta \\ -\sin\theta & \cos\theta \end{pmatrix} \tag{B.7}$$

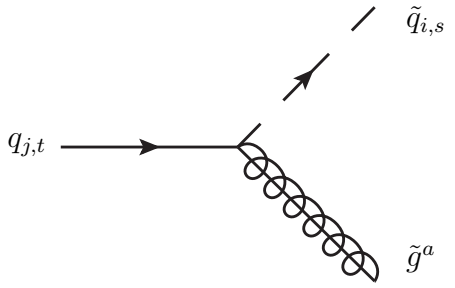

$$-\sqrt{2}ig_s \mathrm{T}^a_{st}(R_{iL}P_L - R_{iR}P_R) \tag{B.8}$$

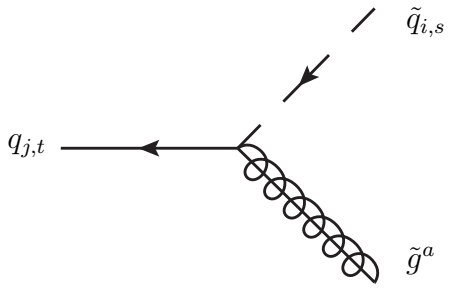

$$-\sqrt{2}ig_s \mathrm{T}^a_{ts}(R_{iL}P_L - R_{iR}P_R) \tag{B.9}$$

Neutralino-Squark-Quark

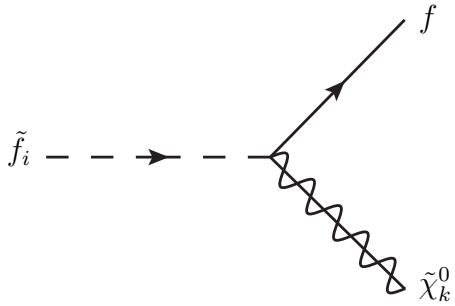

$$ig_s(a^{\tilde{f}}_{ik}P_R + b^{\tilde{f}}_{ik}P_L) \tag{B.10}$$

Chargino-Squark-Quark

$$l_{ij}^{\tilde{u}} = -gV_{j1}R_{i1}^{\tilde{u}} + h_u V_{j2}, R_{i2}^{\tilde{u}}, \qquad l_{ij}^{\tilde{d}} = -gU_{j1}R_{i1}^{\tilde{d}} + h_d U_{j2}, R_{i2}^{\tilde{d}} \tag{B.11}$$

$$k_{ij}^{\tilde{u}} = h_d U_{j1} R_{i2}^{\tilde{u}}, \qquad k_{ij}^{\tilde{d}} = h_u V_{j2} R_{i1}^{\tilde{d}} \tag{B.12}$$

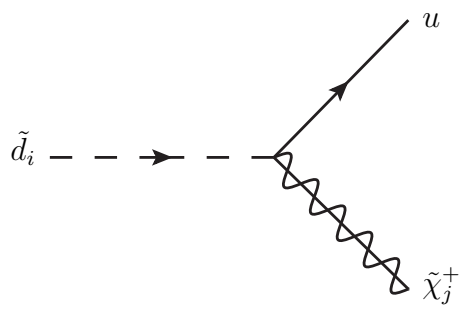

$$ig_s(l_{ij}^{\tilde{d}} P_R + k_{ij}^{\tilde{d}} P_L) \tag{B.13}$$

B.3. 4 Squarks

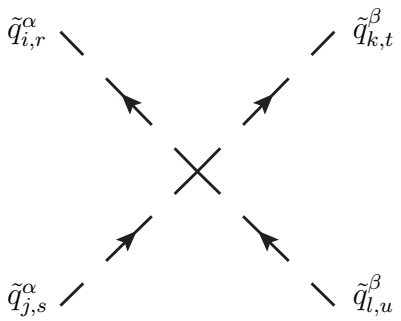

$$-ig_s^2[\mathrm{T}_{rs}^a T_{tu}^a A_{ij}^{\alpha} A_{kl}^{\beta} + \delta_{\alpha\beta} \mathrm{T}_{ru}^a T_{ts}^a A_{il}^{\alpha} A_{kj}^{\alpha}] \tag{B.14}$$

B.4. Vector Bosons

Vector Boson-Quark-Quark

The Lagrangian is given as

$$\begin{aligned}\mathcal{L} = &- ee_f A_\mu \overline{f}\gamma^\mu f - \frac{g}{c_w} Z_\mu^0 \overline{f}\gamma^\mu (C_L^f P_L + C_R^f P_R) f \\ &- \frac{g}{\sqrt{2}}(W_\mu^+ \overline{u}\gamma^\mu P_L d + W_\mu^- \overline{d}\gamma^\mu P_L u)\end{aligned} \tag{B.15}$$

with the coefficient $C_L^f = I_f^{3L} - e_f s_w^2$ and $C_R^f = -e_f s_w^2$.

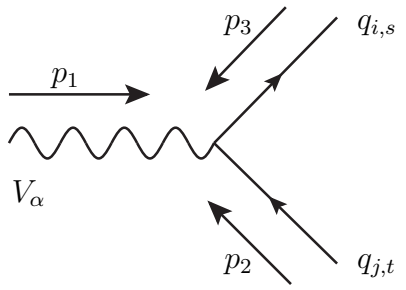

$$\begin{aligned} \gamma &: -iee_f\gamma^\mu \\ Z^0 &: -i\tfrac{g}{c_w}\gamma^\mu(C_L^f P_L + C_R^f P_R) \\ W^\pm &: -i\tfrac{g}{\sqrt{2}}\gamma^\mu P_L \end{aligned} \tag{B.16}$$

$$\begin{aligned} \gamma: &\quad -\mathrm{i}ee_f\delta_{st}\gamma^\mu \\ Z^0: &\quad -\mathrm{i}\frac{g}{c_W}Z_{ij}^{\tilde{f}}(k_1-k_2)^\mu \end{aligned} \tag{B.17}$$

$$Z_{ij}^{\tilde{f}} = C_L^f R_{i1}^{\tilde{f}} R_{j1}^{\tilde{f}} + C_R R_{i2}^{\tilde{f}} R_{j2}^{\tilde{f}} = \begin{pmatrix} (I_f^{3L}\cos^2\theta_{\tilde{f}} - s_W^2 c_f) & -\frac{1}{2}I_f^{3L}\sin 2\theta_f \\ -\frac{1}{2}I_f^{3L}\sin 2\theta_f & (I_f^{3L}\cos^2\theta_{\tilde{f}} - s_W^2 e_f) \end{pmatrix} \tag{B.18}$$

Vector Boson-Squark-Squark

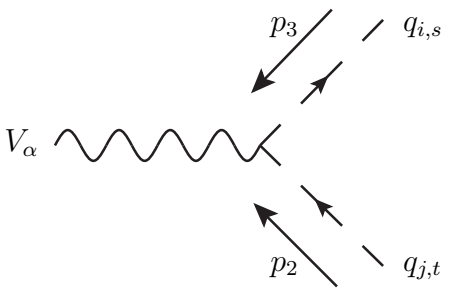

$$\begin{aligned} \gamma &: -iee_f\delta_{ij}\delta_{st}(k_1-k_2)^\mu \\ Z^0 &: -i\tfrac{g}{c_W}\delta_{st}\gamma^\mu(C_L^f P_L + C_R^f P_R) \\ W^\pm &: -i\tfrac{g}{\sqrt{2}}\gamma^\mu P_L\delta_{st} \end{aligned} \tag{B.19}$$

B.5. Higgs Boson

Higgs-Quark-Quark

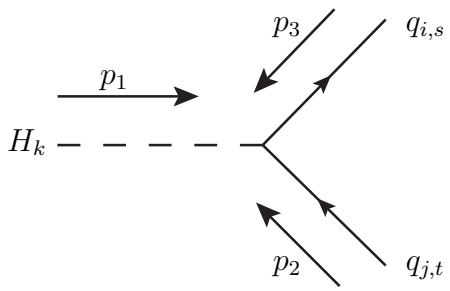

$$h^0, H^0 \;:\; is_k^f(P_R + P_L)$$
$$A^0, G^0 \;:\; is_k^f(P_R - P_L)$$
$$H_l^+ \;:\; i(y_l^t P_L + y_l^b P_R) \tag{B.20}$$

$$s_1^t = -g\frac{m_t \cos\alpha}{2m_W \sin\beta} \qquad s_1^b = -g\frac{m_b \sin\alpha}{2m_W \cos\beta}$$
$$s_2^t = -g\frac{m_t \sin\alpha}{2m_W \sin\beta} \qquad s_2^b = -g\frac{m_b \cos\alpha}{2m_W \cos\beta}$$
$$s_3^t = ig\frac{m_t \cot\alpha}{2m_W} \qquad s_3^b = ig\frac{m_b \tan\beta}{2m_W}$$
$$s_4^t = ig\frac{m_t}{2m_W} \qquad s_4^b = -ig\frac{m_b}{2m_W}$$
$$y_1^t = g\frac{m_t \cot\beta}{\sqrt{2}m_W} \qquad y_1^b = g\frac{m_b \tan\beta}{\sqrt{2}m_W}$$
$$y_2^t = g\frac{m_t}{2m_W} \qquad y_2^b = -g\frac{m_b}{2m_W}$$

Higgs-Squark-Squark

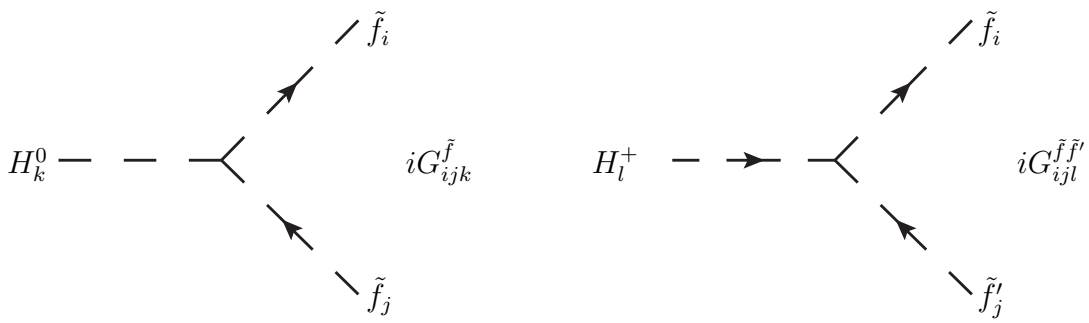

(B.21)

with $g_z = \frac{g}{c_w}$, $H_k^0 = \{h^0, H^0, A^0, G^0\}$,$H_k^+ = \{H^+, G^+, H^-, G^-\}$ and $H_k^- \equiv (H_k^+)^* = \{H^+, G^+, H^-, G^-\}$

$$G_{ijk}^{\tilde{f}} \equiv G(H_k^0 \tilde{f}_i^* \tilde{f}_j) = \left[R^{\tilde{f}} G_{LR,k}^{\tilde{f}} (R^{\tilde{f}})^T\right]_{ij} \tag{B.22}$$

$$G_{LR,1}^{\tilde{t}} = \begin{pmatrix} g_z m_z (I_t^{3L} - e_t s_w^2) s_{\alpha+\beta} - \sqrt{2} h_t m_t c_\alpha & -\frac{h_t}{\sqrt{2}}(A_t c_\alpha + \mu s_\alpha) \\ -\frac{h_t}{\sqrt{2}}(A_t c_\alpha + \mu s_\alpha) & g_z m_z e_t s_W^2 s_{\alpha+\beta} - \sqrt{2} h_t m_t c_\alpha \end{pmatrix}, \tag{B.23}$$

$$G_{LR,1}^{\tilde{b}} = \begin{pmatrix} g_z m_z (I_b^{3L} - e_b s_w^2) s_{\alpha+\beta} + \sqrt{2} h_b m_b s_\alpha & -\frac{h_b}{\sqrt{2}}(A_b s_\alpha + \mu c_\alpha) \\ -\frac{h_b}{\sqrt{2}}(A_b s_\alpha + \mu c_\alpha) & g_z m_z e_b s_W^2 s_{\alpha+\beta} + \sqrt{2} h_b m_b s_\alpha \end{pmatrix} \tag{B.24}$$

$$G_{LR,2}^{\tilde{f}} = G_{LR,1}^{\tilde{f}} \quad \text{with} \alpha \to \alpha - \frac{\pi}{2} \tag{B.25}$$

$$G_{LR,3}^{\tilde{t}} = -\sqrt{2} h_t \begin{pmatrix} 0 & -\frac{\mathrm{i}}{2}(A_t c_\beta + \mu s_\beta) \\ \frac{\mathrm{i}}{2}(A_t c_\beta + \mu s_\beta) & 0 \end{pmatrix} \tag{B.26}$$

$$G_{LR,3}^{\tilde{b}} = -\sqrt{2} h_b \begin{pmatrix} 0 & -\frac{\mathrm{i}}{2}(A_b s_\beta + \mu c_\beta) \\ \frac{\mathrm{i}}{2}(A_b s_\beta + \mu c_\beta) & 0 \end{pmatrix} \tag{B.27}$$

$$G_{LR,4}^{\tilde{f}} = G_{LR,3}^{\tilde{f}} \quad \text{with} \beta \to \beta - \frac{\pi}{2} \tag{B.28}$$

$s_x = \sin x$, $c_x = \cos x$ and $s_w \equiv \sin\theta_W$. α is used as the mixing angle of the Higgs-system, with the Yukawa couplings

$$h_t = \frac{g m_t}{\sqrt{2} m_W s_b} \quad h_b = \frac{g m_b}{\sqrt{2} m_W c_b}. \tag{B.29}$$

For charged Higgs-Bosons to two sfermions:

$$G_{ijk}^{\tilde{f}\tilde{f}'} \equiv G(H_k^\pm \tilde{f}_i^* \tilde{f}_j') = G_{jik}^{\tilde{f}'\tilde{f}} = \left[R^{\tilde{f}} G_{LR,k}^{\tilde{f}\tilde{f}'} (R^{\tilde{f}'})^T\right]_{ij} \tag{B.30}$$

$$G_{LR,1}^{\tilde{t}\tilde{b}} = \begin{pmatrix} h_b m_b \sin\beta + h_t m_t \cos\beta - \frac{g m_W}{\sqrt{2}} \sin 2\beta & h_b(A_b \sin\beta + \mu \cos\beta) \\ h_t(A_t \cos\beta + \mu \sin\beta) & h_t m_b \cos\beta + h_b m_t \sin\beta \end{pmatrix} \tag{B.31}$$

$$G_{LR,1}^{\tilde{b}\tilde{t}} = \begin{pmatrix} h_b m_b \sin\beta + h_t m_t \cos\beta - \frac{g m_W}{\sqrt{2}} \sin 2\beta & h_t(A_t \cos\beta + \mu \sin\beta) \\ h_b(A_b \sin\beta + \mu \cos\beta) & h_t m_b \cos\beta + h_b m_t \sin\beta \end{pmatrix} \tag{B.32}$$

$$G_{LR,2}^{\tilde{f}\tilde{f}'} = G_{LR,1}^{\tilde{f}\tilde{f}'} \quad \text{with} \beta \to \beta - \frac{\pi}{2} \tag{B.33}$$

C Tensor Reduction

C.1. Loop Integrals

In the following the occurring loop integrals within the NLO calculation are listed, following the introduced notation for the tensor reduction in Sec. 7.

$$A_0(m^2) = \frac{(2\pi\mu)^{(4-D)}}{\mathrm{i}\pi^2} \int\limits_q d^D q \frac{1}{q^2 - m^2 + \mathrm{i}\epsilon} \tag{C.1}$$

$$A_2(m^2) = \frac{(2\pi\mu)^{(4-D)}}{\mathrm{i}\pi^2 D} \int\limits_q d^D q \frac{q^\mu q^\nu}{q^2 - m^2 + \mathrm{i}\epsilon} \tag{C.2}$$

$$B_0(p_1^2, m_0^2, m_1^2) = \frac{(2\pi\mu)^{(4-D)}}{\mathrm{i}\pi^2} \int\limits_q d^D q \frac{1}{(q^2 - m_0^2 + \mathrm{i}\epsilon)[(q+p_1)^2 - m_1^2 + \mathrm{i}\epsilon]} \tag{C.3}$$

$$p_1^\nu B_1(p_1^2, m_0^2, m_1^2) = \frac{(2\pi\mu)^{(4-D)}}{\mathrm{i}\pi^2} \int\limits_q d^D q \frac{q^\nu}{(q^2 - m_0^2 + \mathrm{i}\epsilon)[(q+p_1)^2 - m_1^2 + \mathrm{i}\epsilon]} \tag{C.4}$$

$$\begin{aligned} &C_0(p_1^2, m_0^2, m_1^2, m_2^2) = \\ &\frac{(2\pi\mu)^{(4-D)}}{\mathrm{i}\pi^2} \int\limits_q d^D q \frac{1}{(q^2 - m_0^2 + \mathrm{i}\epsilon)[(q+p_1)^2 - m_1^2 + \mathrm{i}\epsilon][(q+p_2)^2 - m_2^2 + \mathrm{i}\epsilon]} \end{aligned} \tag{C.5}$$

$$\begin{aligned} &p_1^\nu C_1(p_1^2, m_0^2, m_1^2, m_2^2) + p_2^\nu C_2(p_1^2, m_0^2, m_1^2, m_2^2) = \\ &\frac{(2\pi\mu)^{(4-D)}}{\mathrm{i}\pi^2} \int\limits_q d^D q \frac{q^\nu}{(q^2 - m_0^2 + \mathrm{i}\epsilon)[(q+p_1)^2 - m_1^2 + \mathrm{i}\epsilon][(q+p_2)^2 - m_2^2 + \mathrm{i}\epsilon]} \end{aligned} \tag{C.6}$$

$$
\begin{aligned}
&C^{\mu\nu} = \\
&\frac{(2\pi\mu)^{(4-D)}}{\mathrm{i}\pi^2} \int\limits_q d^D q \frac{q^\mu q^\nu}{(q^2 - m_0^2 + \mathrm{i}\epsilon)[(q+p_1)^2 - m_1^2 + \mathrm{i}\epsilon][(q+p_2)^2 - m_2^2 + \mathrm{i}\epsilon]} \\
&= g^{\mu\nu} C_{00} + p_1^\mu p_1^\nu C_{11} + (p_1^\mu p_2^\nu + p_2^\mu p_1^\nu) C_{12} + p_2^\mu p_2^\nu C_{22}
\end{aligned}
\tag{C.7}
$$

If the masses are equal, there are the following relations between the integrals:

$$B_1(p^2, m^2, m^2) = -\frac{1}{2} B_0(p^2, m^2, m^2) \tag{C.8}$$

$$B_{00}(p^2, m^2, m^2) = \frac{1}{6}(A_0(m^2) + 2m^2 B_0 + p^2 B_1 + 2m^2 - \frac{p^2}{3}) \tag{C.9}$$

$$B_{11}(p^2, m^2, m^2) = \frac{1}{6p^2}(2A_0(m^2) - 2m^2 B_0 - 4p^2 B_1 - 2m^2 + \frac{p^2}{3}) \tag{C.10}$$

C.2. Divergencies in Loop Integrals

The Tabs. C.1 and C.2 show the ultraviolet divergent and infrared divergent loop integrals with the corresponding divergencies.

Integral	UV div
$A_0(m^2)$	$m^2\Delta$
$A_2(m^2)$	$\frac{m^4}{4}\Delta$
$B_0(p^2, m_0^2, m_1^2)$	Δ
$B_1(p^2, m_0^2, m_1^2)$	$-\frac{1}{2}\Delta$
$B_{00}(p^2, m_0^2, m_1^2)$	$-\left(\frac{p^2}{12} - \frac{1}{4}(m_0^2 + m_1^2)\right)\Delta$
B_{11}	$\frac{1}{3}\Delta$
$\dot{B}_{00}$	$-\frac{1}{12}\Delta$
C_{00}	$\frac{1}{4}\Delta$

Table C.1.: Ultraviolet divergent loop integrals.

Integral	IR div
$\dot{B}_0(m^2,\lambda^2,m^2) = \dot{B}_0(m^2,m^2,\lambda^2)$	$-\frac{1}{2m^2}\ln\lambda^2$
$\dot{B}_1(m^2,m^2,\lambda^2)$	$\frac{1}{2m^2}\lambda^2$
$\dot{B}_1(m^2,\lambda^2,m^2)$	0
$\dot{B}_{11}(m^2,m^2,\lambda^2)$	$-\frac{1}{2m^2}\ln\lambda^2$
$C_0(m_1^2,s,m_2^2,\lambda^2,m_1^2,m_2^2)$	$-\frac{\ln\beta_0}{\kappa}\ln\lambda^2$

Table C.2.: Infrared divergent loop integrals.

C.3. Small Velocity Expansion of the Box Contribution

In order to subtract the velocity enhanced part of the NLO contribution that is already included in the Sommerfeld resummation, we expand the corresponding contribution of the box diagrams in the relativistic relative velocity [161]

$$v_{\text{rel}} = \frac{\sqrt{\lambda(s,m_1^2,m_2^2)}}{s-m_1^2-m_2^2}\,, \tag{C.11}$$

with $\lambda(a,b,c) = a^2+b^2+c^2-2ab-2ac-2bc$.

All box diagrams that contain the velocity enhanced contribution feature an exchange of a massless gluon between the incoming pair of scalar quarks. A generic diagram showing the masses of internal and external particles is shown in Fig. C.1. The matrix element contains tensor coefficients

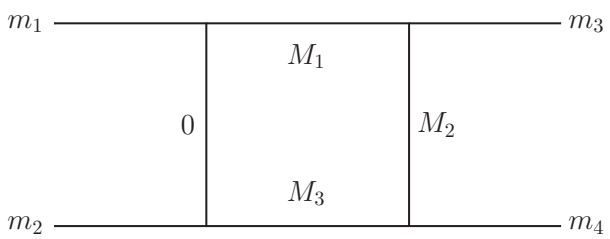

Figure C.1.: Box diagram corresponding to the gluon exchange.

$$\begin{aligned} D_i\Big(p_{10}^2,p_{21}^2,p_{32}^2,p_{30}^2,p_{20}^2,p_{31}^2,M_0^2,M_1^2,M_2^2,M_3^2\Big) &= \\ D_i\Big(m_1^2,m_3^2,m_4^2,m_2^2,t_i,s,0,m_1^2,M_2^2,m_2^2\Big)\,, \end{aligned} \tag{C.12}$$

where t_i are the Mandelstam variables t or u depending on the box diagram. The velocity enhanced terms in the box contribution are contained in the scalar 4-point integrals $D_0\Big(m_1^2, m_3^2, m_4^2, m_2^2, t_i, s, 0, m_1^2, M_2^2, m_2^2\Big)$ [162]. The full enhanced box matrix element consisting of box diagrams, where different gauginos with mass m_χ are exchanged, can be written using the corresponding color decomposed tree-level matrix element (see Eq. (6.12)) as

$$\begin{aligned} M_{\text{box}} = \sum_{t_i} \sum_{\chi} M_{\text{box}}^{\chi,t_i} = \\ &\Big(C_{\text{box}}^{[\bar{\mathbf{3}}]} M_{\bar{\mathbf{3}}}^{\text{Tree},\chi,t_i} C_{stij}^{\{\bar{\mathbf{3}},\bar{\mathbf{3}}\}} + C_{\text{box}}^{[\mathbf{6}]} M_{\mathbf{6}}^{\text{Tree},\chi,t_i} C_{stij}^{\{\mathbf{6},\mathbf{6}\}}\Big) \times \\ &2\frac{\alpha_s}{4\pi}(s - m_1^2 - m_2^2)(t_i - m_\chi^2)\, D_0\,, \end{aligned} \tag{C.13}$$

where the tensor integral has the arguments as in Eq. (C.12) with $M_2 = m_\chi$ and the color factors $C_{\text{box}}^{[\mathbf{R}]}$ are given as

$$C_{\text{box}}^{[\bar{\mathbf{3}}]} = -\frac{N_c + 1}{2N_c}\,, \qquad C_{\text{box}}^{[\mathbf{6}]} = \frac{N_c - 1}{2N_c}\,. \tag{C.14}$$

The scalar integral for the specific arguments from Eq. (C.12) can be written as

$$\begin{aligned} D_0 = \frac{x_{13}}{m_1 m_2 (t_i - m_\chi^2)(1 - x_{13}^2)} \times \\ &\Bigg\{ 2\ln(x_{13}) \left[-\frac{c_\epsilon}{\epsilon} - \ln\left(\frac{\mu m_\chi}{m_\chi^2 - t_i}\right) + \ln(1 - x_{13}^2) \right] \\ &+ \ln^2(x_{12}) + \ln^2(x_{23}) + \text{Li}_2(x_{13}^2) \\ &+ \sum_{k,l=\pm 1} \mathcal{L}i_2(x_{13}, x_{12}^k, x_{23}^l) - \frac{\pi^2}{6} \Bigg\}\,, \end{aligned} \tag{C.15}$$

where c_ϵ is defined in Eq. 7.35. The generalized polylogarithm in Eq. (C.15) is defined as [162]

$$\mathcal{L}i_2(x_1, \ldots, x_n) = \text{Li}_2\left(1 - \prod_{i=1}^n x_i\right) + \left[\ln\left(\prod_{i=1}^n x_i\right) - \sum_{i=1}^n \ln(x_i)\right]$$

$$\left[\ln\left(1 - \prod_{i=1}^n x_i\right) - \theta\left(\left|\prod_{i=1}^n x_i\right| - 1\right) \times \right. \tag{C.16}$$

$$\left. \left(\ln\left(-\prod_{i=1}^n x_i\right) - \frac{1}{2}\ln\left(\prod_{i=1}^n x_i\right) - \frac{1}{2}\sum_{i=1}^n \ln(x_i)\right)\right]\,. \tag{C.17}$$

The variables x_{ij} are defined using the loop masses M_i and M_j as well as the invariant combinations of 4-momenta p_{ij}^2, as given in Eq. (C.12), as

$$x_{ij} = \frac{\sqrt{1 - \frac{4M_iM_j}{p_{ij}^2 - (M_i - M_j)^2}} - 1}{\sqrt{1 - \frac{4M_iM_j}{p_{ij}^2 - (M_i - M_j)^2}} + 1}\,. \tag{C.18}$$

In our case the only velocity dependent x_{ij} is x_{13} which for $M_1 = m_1$, $M_2 = m_\chi$ and $M_3 = m_2$ gives

$$\begin{aligned} x_{13} &= -\frac{2(s - m_1^2 - m_2^2) - 2\sqrt{\lambda(s, m_1^2, m_2^2)}}{4m_1 m_2} \\ &= -\frac{(1 - v_{\text{rel}})}{\sqrt{1 - v_{\text{rel}}^2}}\,, \end{aligned} \tag{C.19}$$

having used the relative velocity as defined in Eq. (C.11). Given the color factors $C_{\text{box}}^{[\mathbf{R}]}$ are independent of the exchanged gaugino, we can simplify the enhanced matrix element as

$$\begin{aligned} 2\Re\Big(M_{\text{box}} M_{\text{Tree}}^\dagger\Big) &= \sum_{t_i,t_j}\sum_{\chi,\chi'} 2\Re\Big(M_{\text{box}}^{\chi,t_i}\Big(M_{\text{Tree}}^{\chi',t_j}\Big)^\dagger\Big) \\ = \sum_{t_i,t_j}\sum_{\chi,\chi'} \Bigg(C_{\text{box}}^{[\overline{\mathbf{3}}]}\Big(M_{\text{Tree},\overline{\mathbf{3}}}^{\chi,t_i}\Big(M_{\text{Tree},\overline{\mathbf{3}}}^{\chi',t_j}\Big)^\dagger\Big) \\ + C_{\text{box}}^{[\mathbf{6}]}\Big(M_{\text{Tree},\mathbf{6}}^{\chi,t_i}\Big(M_{\text{Tree},\mathbf{6}}^{\chi',t_j}\Big)^\dagger\Big)\Bigg) 2\Re(F_{\text{box}}^{\chi,t_i})\,, \end{aligned} \tag{C.20}$$

where $F_{\text{box}}^{\chi,t_i}$ is given by

$$\begin{aligned} F_{\text{box}}^{\chi,t_i} \;=\; & \frac{\alpha_s}{\pi}\frac{(s - m_1^2 - m_2^2)}{2m_1 m_2}\frac{x_{13}}{(1 - x_{13}^2)} \times \\ & \Bigg\{2\ln(x_{13})\left[-\frac{c_\epsilon}{\epsilon} - \ln\left(\frac{\mu m_\chi}{m_\chi^2 - t_i}\right) + \ln(1 - x_{13}^2)\right] \\ & + \ln^2(x_{12}) + \ln^2(x_{23}) + \text{Li}_2(x_{13}^2) \\ & + \sum_{k,l=\pm 1}\mathcal{L}i_2(x_{13}, x_{12}^k, x_{23}^l) - \frac{\pi^2}{6}\Bigg\}\,. \end{aligned} \tag{C.21}$$

We first expand the expression in the relative velocity v_{rel} retaining just the leading term. The pre-factor can be expressed in terms of the relative velocity using

$$\frac{(s - m_1^2 - m_2^2)}{2m_1 m_2}\frac{x_{13}}{(1 - x_{13}^2)} = -\frac{1}{2v_{\text{rel}}}\,. \tag{C.22}$$

Taking the real part of the $F_{\text{box}}^{\chi,t_i}$ factor results in

$$\begin{aligned} 2\Re(F_{\text{box}}^{\chi,t_i}) = -\frac{\alpha_s}{\pi}\frac{1}{v_{\text{rel}}}\,\Re\Bigg\{ & \ln^2(x_{12}) + \ln^2(x_{23}) + \text{Li}_2(1) \\ & + \sum_{k,l=\pm 1}\mathcal{L}i_2(-1, x_{12}^k, x_{23}^l) - \frac{\pi^2}{6}\Bigg\}\,. \end{aligned} \tag{C.23}$$

This expression seems to be implicitly dependent on the mass of the gaugino m_χ through the variables x_{12} and x_{23}. However, this dependence vanishes after a more careful analysis, making the factor $2\Re(F_{\text{box}}^{\chi,t_i})$ generic for all underlying hard processes.

We will show the universality explicitly for a simple case where $m_1 = m_2$ (i.e. $x_{12} = x_{23}$) and where all x_{ij} are purely real. In such a case $\mathcal{L}i_2(-1, x_{12}^k, x_{23}^l)$ reduces to a simple polylogarithm $\text{Li}_2\left(1 + x_{12}^{k+l}\right)$. The factor then reduces to

$$2\Re(F_{\text{box}}^{\chi,t_i}) = -\frac{\alpha_s}{\pi}\frac{1}{v_{\text{rel}}}\,\Re\Big\{2\ln^2(x_{12}) + 2\,\text{Li}_2(2) + \text{Li}_2\Big(1 + x_{12}^2\Big) + \text{Li}_2\Big(1 + x_{12}^{-2}\Big)\Big\}\,, \tag{C.24}$$

which can be simplified using [163]

$$\text{Li}_2(z) = -\text{Li}_2\left(\frac{z}{z-1}\right) - \frac{1}{2}\ln^2(1-z) \quad z < 1\,. \tag{C.25}$$

The use of this identity eliminates all dependence on x_{12} and the factor greatly simplifies to

$$2\Re(F_{\text{box}}^{\chi,t_i}) = -\frac{\alpha_s}{\pi}\frac{1}{v_{\text{rel}}}\pi^2\,. \tag{C.26}$$

Even though we have derived this particularly simple result in a special case, the same can be obtained in the most general case as well. With such a universal factor the one-loop contribution to the squared matrix element from the enhanced box contribution is just

$$2\Re\Big(M_{\text{box}}M_{\text{Tree}}^\dagger\Big) = \left(-\frac{\alpha_s}{v_{\text{rel}}}\pi\right)\Big(C_{\text{box}}^{[\overline{\mathbf{3}}]}\,|M_{\overline{\mathbf{3}}}^{\text{Tree}}|^2 + C_{\text{box}}^{[\mathbf{6}]}\,|M_{\mathbf{6}}^{\text{Tree}}|^2\Big)\,. \tag{C.27}$$

This expression is compatible with the next-to-leading part of the Sommerfeld enhancement after we realize that in the non-relativistic case the relative velocity can be easily related to the velocity used in the Sommerfeld enhancement for identical incoming particles (see Eq. (10.18)) as $v_{\text{rel}} = 2v_{\text{s}}$.

Bibliography

[1] ATLAS collaboration. 'Summary of the ATLAS experiment's sensitivity to supersymmetry after LHC Run 1 - interpreted in the phenomenological MSSM'. In: *JHEP* 10 (2015), p. 134. DOI: 10.1007/JHEP10(2015)134. arXiv: 1508.06608 [hep-ex].

[2] Vardan Khachatryan et al. 'Phenomenological MSSM interpretation of CMS searches in pp collisions at sqrt(s) = 7 and 8 TeV'. In: *JHEP* 10 (2016), p. 129. DOI: 10.1007/JHEP10(2016)129. arXiv: 1606.03577 [hep-ex].

[3] Stephen P. Martin. 'A Supersymmetry primer'. In: (1997). [Adv. Ser. Direct. High Energy Phys.18,1(1998)], pp. 1–98. DOI: 10.1142/9789812839657_0001, 10.1142/9789814307505_0001. arXiv: hep-ph/9709356 [hep-ph].

[4] Howard E. Haber and Laurel Stephenson Haskins. 'Supersymmetric Theory and Models'. In: *Proceedings, Theoretical Advanced Study Institute in Elementary Particle Physics : Anticipating the Next Discoveries in Particle Physics (TASI 2016): Boulder, CO, USA, June 6-July 1, 2016*. WSP. WSP, 2018, pp. 355–499. DOI: 10.1142/9789813233348_0006. arXiv: 1712.05926 [hep-ph].

[5] Julia Harz. 'Supersymmetric QCD Corrections and Phenomenological Studies in Relation to Coannihilation of Dark Matter'. PhD thesis. Universität Hamburg, 2013.

[6] Karol Kovařík. 'Precise predictions for sfermion pair production at a linear collider'. PhD thesis. Comenius University, Bratislava, 2005.

[7] Georges Aad et al. 'Observation of a new particle in the search for the Standard Model Higgs boson with the ATLAS detector at the LHC'. In: *Phys. Lett.* B716 (2012), pp. 1–29. DOI: 10.1016/j.physletb.2012.08.020. arXiv: 1207.7214 [hep-ex].

[8] Serguei Chatrchyan et al. 'Observation of a new boson at a mass of 125 GeV with the CMS experiment at the LHC'. In: *Phys. Lett.* B716 (2012), pp. 30–61. DOI: 10.1016/j.physletb.2012.08.021. arXiv: 1207.7235 [hep-ex].

[9] Georges Aad et al. 'Combined Measurement of the Higgs Boson Mass in *pp* Collisions at $\sqrt{s} = 7$ and 8 TeV with the ATLAS and CMS Experiments'. In: *Phys. Rev. Lett.* 114 (2015), p. 191803. DOI: 10.1103/PhysRevLett.114.191803. arXiv: 1503.07589 [hep-ex].

[10] Eldad Gildener and Steven Weinberg. 'Symmetry breaking and scalar bosons'. In: *Phys. Rev. D* 13 (12 June 1976), pp. 3333–3341. DOI: 10.1103/PhysRevD.13.3333. URL: https://link.aps.org/doi/10.1103/PhysRevD.13.3333.

[11] Eldad Gildener. 'Gauge-symmetry hierarchies'. In: *Phys. Rev. D* 14 (6 Sept. 1976), pp. 1667–1672. DOI: 10.1103/PhysRevD.14.1667. URL: https://link.aps.org/doi/10.1103/PhysRevD.14.1667.

[12] David Bailin and Alex Love. 'String unification, grand unification and string loop threshold corrections'. In: *Physics Letters B* 292.3 (1992), pp. 315 –320. ISSN: 0370-2693. DOI: https://doi.org/10.1016/0370-2693(92)91181-8. URL: http://www.sciencedirect.com/science/article/pii/0370269392911818.

[13] Lucia Hošeková. 'One-loop Calculations of the Decay of a Neutral Higgs Boson into Two Photons in the MSSM'. MA thesis. Comenius University, Bratislava, 2007.

[14] K. Kovařík. 'Physik jenseits des Standardmodells'. Exerciese sheets.

[15] Sidney Coleman and Jeffrey Mandula. 'All Possible Symmetries of the S Matrix'. In: *Phys. Rev.* 159 (5 July 1967), pp. 1251–1256. DOI: 10.1103/PhysRev.159.1251. URL: https://link.aps.org/doi/10.1103/PhysRev.159.1251.

[16] R. Haag, J. T. Łopuszański and M. Sohnius. 'All possible generators of supersymmetries of the S-matrix'. In: *Nuclear Physics B* 88 (Mar. 1975), pp. 257–274. DOI: 10.1016/0550-3213(75)90279-5.

[17] J. Wess and B. Zumino. 'Supergauge Transformations in Four-Dimensions'. In: *Nucl. Phys.* B70 (1974), pp. 39–50. DOI: 10.1016/0550-3213(74)90355-1.

[18] J. Wess and B. Zumino. 'Supergauge Invariant Extension of Quantum Electrodynamics'. In: *Nucl. Phys.* B78 (1974), p. 1. DOI: 10.1016/0550-3213(74)90112-6.

[19] Manuel Drees. 'An Introduction to supersymmetry'. In: *Current topics in physics. Proceedings, Inauguration Conference of the Asia-Pacific Center for Theoretical Physics (APCTP), Seoul, Korea, June 4-10, 1996. Vol. 1, 2.* 1996. arXiv: hep-ph/9611409 [hep-ph].

[20] Manuel Drees, Rohini Godbole and Probir Roy. *Theory and phenomenology of Sparticles: an account of four-dimensional N=1 supersymmetry in high-energy physics.* Singapore: World Scientific, 2004. URL: https://cds.cern.ch/record/873465.

[21] A. Djouadi et al. 'The Minimal supersymmetric standard model: Group summary report'. In: *GDR (Groupement De Recherche) - Supersymetrie Montpellier, France, April 15-17, 1998.* 1998. arXiv: hep-ph/9901246 [hep-ph].

[22] ATLAS collaboration. 'Search for squarks and gluinos with the ATLAS detector in final states with jets and missing transverse momentum using $\sqrt{s} = 8$ TeV proton–proton collision data'. In: *JHEP* 09 (2014), p. 176. DOI: 10.1007/JHEP09(2014)176. arXiv: 1405.7875 [hep-ex].

[23] N. Aghanim et al. 'Planck 2018 results. VI. Cosmological parameters'. In: (2018). arXiv: 1807.06209 [astro-ph.CO].

[24] Michael Klasen, Martin Pohl and Günter Sigl. 'Indirect and direct search for dark matter'. In: *Prog. Part. Nucl. Phys.* 85 (2015), pp. 1–32. DOI: 10.1016/j.ppnp.2015.07.001. arXiv: 1507.03800 [hep-ph].

[25] Martin Bauer and Tilman Plehn. 'Yet Another Introduction to Dark Matter'. In: (2017). arXiv: 1705.01987 [hep-ph].

[26] Einasto Jaan. 'Dark Matter'. In: *arXiv:0901.0632v2 [astro-ph.CO]* (2010).

[27] Mariangela Lisanti. 'Lectures on Dark Matter Physics'. In: *Proceedings, Theoretical Advanced Study Institute in Elementary Particle Physics: New Frontiers in Fields and Strings (TASI 2015): Boulder, CO, USA, June 1-26, 2015*. 2017, pp. 399–446. DOI: 10.1142/9789813149441_0007. arXiv: 1603.03797 [hep-ph].

[28] Moritz Meinecke. 'SUSY-QCD Corrections to the (Co)Annihilation of Neutralino Dark Matter within the MSSM'. PhD thesis. Westfälische Wilhelms-Universität Münster, 2015.

[29] Patrick Steppeler. 'Radiative corrections for the direct detection of neutralino dark matter and its relic density'. PhD thesis. Westfälische Wilhelms-Universität Münster, 2016.

[30] Sonja Esch. 'Dark Matter, Neutrinomasses and Lepton Flavor Violation in Radiative See-Saw Models'. PhD thesis. Westfälische Wilhelms-Universität Münster, 2018.

[31] J. C. Kapteyn. 'First Attempt at a Theory of the Arrangement and Motion of the Sidereal System'. In: *apj* 55 (May 1922), p. 302. DOI: 10.1086/142670.

[32] J. H. Jeans. 'The Motions of Stars in a Kapteyn Universe'. In: *mnras* 82 (Jan. 1922), pp. 122–132. DOI: 10.1093/mnras/82.3.122.

[33] J. H. Oort. 'Some peculiarities in the motion of stars of high velocity'. In: *bain* 1 (Sept. 1922), p. 133.

[34] F. Zwicky. 'Die Rotverschiebung von extragalaktischen Nebeln'. In: *Helvetica Physica Acta6, 110-127* (1933).

[35] P. Binétruy. 'Cosmology and Gravitation: the grand scheme for High-Energy Physics'. In: *Proceedings, 2012 European School of High-Energy Physics (ESHEP 2012): La Pommeraye, Anjou, France, June 06-19, 2012*. 2014, pp. 217–291. DOI: 10.5170/CERN-2014-008.217. arXiv: 1504.07050 [gr-qc].

[36] Douglas Clowe et al. 'A direct empirical proof of the existence of dark matter'. In: *Astrophys. J.* 648 (2006), pp. L109–L113. DOI: 10.1086/508162. arXiv: astro-ph/0608407 [astro-ph].

[37] D.J. Fixsen. 'The Temperature of the Cosmic Microwave Background'. In: *Astrophys.J.* 707 (2009), pp. 916–920. DOI: 10.1088/0004-637X/707/2/916. eprint: 0911.1955.

[38] C. Bennett G. F. Smoot et al. 'Structure in the COBE differential microwave radiometer first year maps'. In: *Astrophys.J.* 396 (1992).

[39] D. J. Fixsen et al. 'The Cosmic Microwave Background spectrum from the full COBE FIRAS data set'. In: *Astrophys. J.* 473 (1996), p. 576. DOI: 10.1086/178173. arXiv: astro-ph/9605054 [astro-ph].

[40] A. Kogut et al. 'Three-Year Wilkinson Microwave Anisotropy Probe (WMAP) Observations: Foreground Polarization'. In: *Astrophys. J.* 665 (2007), pp. 355–362. DOI: 10.1086/519754. arXiv: 0704.3991 [astro-ph].

[41] URL: www.esa.int/spaceinimages/Images/2013/03/Planck_CMB.

[42] Igor R. Klebanov and Arkady A. Tseytlin. 'Intersecting M-branes as four-dimensional black holes'. In: *Nucl. Phys.* B475 (1996). [,309(1996)], pp. 179–192. DOI: 10.1016/0550-3213(96)00338-0. arXiv: hep-th/9604166 [hep-th].

[43] Gianfranco Bertone, Dan Hooper and Joseph Silk. 'Particle dark matter: Evidence, candidates and constraints'. In: *Phys. Rept.* 405 (2005), pp. 279–390. DOI: 10.1016/j.physrep.2004.08.031. arXiv: hep-ph/0404175 [hep-ph].

[44] Julio F. Navarro, Carlos S. Frenk and Simon D. M. White. 'The Structure of cold dark matter halos'. In: *Astrophys. J.* 462 (1996), pp. 563–575. DOI: 10.1086/177173. arXiv: astro-ph/9508025 [astro-ph].

[45] Volker Springel et al. 'Simulating the joint evolution of quasars, galaxies and their large-scale distribution'. In: *Nature* 435 (2005), pp. 629–636. DOI: 10.1038/nature03597. arXiv: astro-ph/0504097 [astro-ph].

[46] A. A. Klypin, S. Trujillo-Gomez and J. Primack. 'Dark Matter Halos in the Standard Cosmological Model: Results from the Bolshoi Simulation'. In: *apj* 740, 102 (Oct. 2011), p. 102. DOI: 10.1088/0004-637X/740/2/102. arXiv: 1002.3660.

[47] Anatoly A. Klypin et al. 'Where are the missing Galactic satellites?' In: *Astrophys. J.* 522 (1999), pp. 82–92. DOI: 10.1086/307643. arXiv: astro-ph/9901240 [astro-ph].

[48] W. L. Freedman et al. 'Final results from the Hubble Space Telescope key project to measure the Hubble constant'. In: *Astrophys. J.* 553 (2001), pp. 47–72. DOI: 10.1086/320638. arXiv: astro-ph/0012376 [astro-ph].

[49] Priyamvada Natarajan et al. 'Constraints on the collisional nature of the dark matter from gravitational lensing in the cluster a2218'. In: *Astrophys. J.* 580 (2002), pp. L17–L20. DOI: 10.1086/345547. arXiv: astro-ph/0207045 [astro-ph].

[50] Xue-lei Chen, Steen Hannestad and Robert J. Scherrer. 'Cosmic microwave background and large scale structure limits on the interaction between dark matter and baryons'. In: *Phys. Rev.* D65 (2002), p. 123515. DOI: 10.1103/PhysRevD.65.123515. arXiv: astro-ph/0202496 [astro-ph].

[51] Joel R. Primack. 'Whatever happened to hot dark matter?' In: *SLAC Beam Line* 31N3 (2001), pp. 50–57. arXiv: astro-ph/0112336 [astro-ph].

[52] Matteo Viel et al. 'How cold is cold dark matter? Small scales constraints from the flux power spectrum of the high-redshift Lyman-alpha forest'. In: *Phys. Rev. Lett.* 100 (2008), p. 041304. DOI: 10.1103/PhysRevLett.100.041304. arXiv: 0709.0131 [astro-ph].

[53] Keith A. Olive, Gary Steigman and Terry P. Walker. 'Primordial nucleosynthesis: Theory and observations'. In: *Phys. Rept.* 333 (2000), pp. 389–407. DOI: 10.1016/S0370-1573(00)00031-4. arXiv: astro-ph/9905320 [astro-ph].

[54] Richard H. Cyburt et al. 'New BBN limits on physics beyond the standard model from ^4He'. In: *Astropart. Phys.* 23 (2005), pp. 313–323. DOI: 10.1016/j.astropartphys.2005.01.005. arXiv: astro-ph/0408033 [astro-ph].

[55] Richard H. Cyburt et al. 'Updated nucleosynthesis constraints on unstable relic particles'. In: *Phys. Rev.* D67 (2003), p. 103521. DOI: 10.1103/PhysRevD.67.103521. arXiv: astro-ph/0211258 [astro-ph].

[56] Georg G. Raffelt. 'Particle physics from stars'. In: *Ann. Rev. Nucl. Part. Sci.* 49 (1999), pp. 163–216. DOI: 10.1146/annurev.nucl.49.1.163. arXiv: hep-ph/9903472 [hep-ph].

[57] M. Milgrom. 'A modification of the Newtonian dynamics as a possible alternative to the hidden mass hypothesis'. In: *apj* 270 (July 1983), pp. 365–370. DOI: 10.1086/161130.

[58] Bernard J. Carr. 'Recent developments in the search for baryonic dark matter'. In: *Phase transitions in the early universe: Theory and observations. Proceedings, NATO ASI, International School of Astrophysics 'Daniel Chalonge', 8th Course dedicated to Andrei D. Sakharov, Erice, Italy, December 6-17, 2000.* 2001, pp. 267–283. arXiv: astro-ph/0102389 [astro-ph].

[59] A. Boyarsky et al. 'Sterile Neutrino Dark Matter'. In: *Prog. Part. Nucl. Phys.* 104 (2019), pp. 1–45. DOI: 10.1016/j.ppnp.2018.07.004. arXiv: 1807.07938 [hep-ph].

[60] Morad Aaboud et al. 'Search for dark matter and other new phenomena in events with an energetic jet and large missing transverse momentum using the ATLAS detector'. In: *JHEP* 01 (2018), p. 126. DOI: 10.1007/JHEP01(2018)126. arXiv: 1711.03301 [hep-ex].

[61] Mihailo Backović et al. 'Direct Detection of Dark Matter with MadDM v.2.0'. In: *Phys. Dark Univ.* 9-10 (2015), pp. 37–50. DOI: 10.1016/j.dark.2015.09.001. arXiv: 1505.04190 [hep-ph].

[62] Morad Aaboud et al. 'Search for new phenomena in final states with an energetic jet and large missing transverse momentum in pp collisions at $\sqrt{s} = 13$ TeV using the ATLAS detector'. In: *Phys. Rev.* D94.3 (2016), p. 032005. DOI: 10.1103/PhysRevD.94.032005. arXiv: 1604.07773 [hep-ex].

[63] A. M. Sirunyan et al. 'Search for new physics in final states with an energetic jet or a hadronically decaying W or Z boson and transverse momentum imbalance at $\sqrt{s} = 13$ TeV'. In: *Phys. Rev.* D97.9 (2018), p. 092005. DOI: 10.1103/PhysRevD.97.092005. arXiv: 1712.02345 [hep-ex].

[64] R. Agnese et al. 'New Results from the Search for Low-Mass Weakly Interacting Massive Particles with the CDMS Low Ionization Threshold Experiment'. In: *Phys. Rev. Lett.* 116.7 (2016), p. 071301. DOI: 10.1103/PhysRevLett.116.071301. arXiv: 1509.02448 [astro-ph.CO].

[65] D. S. Akerib et al. 'Limits on Spin-Dependent WIMP-Nucleon Cross Section Obtained from the Complete LUX Exposure'. In: *Phys. Rev. Lett.* 118 (25 June 2017), p. 251302. DOI: 10.1103/PhysRevLett.118.251302. eprint: 1608.07648. URL: https://link.aps.org/doi/10.1103/PhysRevLett.118.251302.

[66] E. Aprile et al. 'First Dark Matter Search Results from the XENON1T Experiment'. In: *Phys. Rev. Lett.* 119.18 (2017), p. 181301. DOI: 10.1103/PhysRevLett.119.181301. arXiv: 1705.06655 [astro-ph.CO].

[67] Xiangyi Cui et al. 'Dark Matter Results From 54-Ton-Day Exposure of PandaX-II Experiment'. In: *Phys. Rev. Lett.* 119.18 (2017), p. 181302. DOI: 10.1103/PhysRevLett.119.181302. arXiv: 1708.06917 [astro-ph.CO].

[68] G. Angloher et al. 'Results on light dark matter particles with a low-threshold CRESST-II detector'. In: *Eur. Phys. J.* C76.1 (2016), p. 25. DOI: 10.1140/epjc/s10052-016-3877-3. arXiv: 1509.01515 [astro-ph.CO].

[69] E. Behnke et al. 'Final Results of the PICASSO Dark Matter Search Experiment'. In: *Astropart. Phys.* 90 (2017), pp. 85–92. DOI: 10.1016/j.astropartphys.2017.02.005. arXiv: 1611.01499 [hep-ex].

[70] C. Amole et al. 'Dark Matter Search Results from the PICO−60 C_3F_8 Bubble Chamber'. In: *Phys. Rev. Lett.* 118 (25 June 2017), p. 251301. DOI: 10.1103/PhysRevLett.118.251301. URL: https://link.aps.org/doi/10.1103/PhysRevLett.118.251301.

[71] M. G. Aartsen et al. 'Improved limits on dark matter annihilation in the Sun with the 79-string IceCube detector and implications for supersymmetry'. In: *JCAP* 1604.04 (2016), p. 022. DOI: 10.1088/1475-7516/2016/04/022. arXiv: 1601.00653 [hep-ph].

[72] K. Choi et al. 'Search for neutrinos from annihilation of captured low-mass dark matter particles in the Sun by Super-Kamiokande'. In: *Phys. Rev. Lett.* 114.14 (2015), p. 141301. DOI: 10.1103/PhysRevLett.114.141301. arXiv: 1503.04858 [hep-ex].

[73] M. Ackermann et al. 'Searching for Dark Matter Annihilation from Milky Way Dwarf Spheroidal Galaxies with Six Years of Fermi Large Area Telescope Data'. In: *Phys. Rev. Lett.* 115.23 (2015), p. 231301. DOI: 10.1103/PhysRevLett.115.231301. arXiv: 1503.02641 [astro-ph.HE].

[74] Katherine Garrett and Gintaras Duda. 'Dark Matter: A Primer'. In: *Adv. Astron.* 2011 (2011), p. 968283. DOI: 10.1155/2011/968283. arXiv: 1006.2483 [hep-ph].

[75] URL: www.mpi-hd.mpg.de/hfm/HESS/.

[76] URL: https://veritas.sao.arizona.edu/veritas-science.

[77] URL: https://fermi.gsfc.nasa.gov/science/eteu/dm/.

[78] O. Adriani et al. 'Ten years of PAMELA in space'. In: *Riv. Nuovo Cim.* 40.10 (2017), p. 1. DOI: 10.1393/ncr/i2017-10140-x. arXiv: 1801.10310 [astro-ph.HE].

[79] Farinaldo S. Queiroz and Clarissa Siqueira. 'Search for Semi-Annihilating Dark Matter with Fermi-LAT, H.E.S.S., Planck, and the Cherenkov Telescope Array'. In: (2019). arXiv: 1901.10494 [hep-ph].

[80] M. G. Aartsen et al. 'Search for neutrinos from decaying dark matter with IceCube'. In: *Eur. Phys. J.* C78.10 (2018), p. 831. DOI: 10.1140/epjc/s10052-018-6273-3. arXiv: 1804.03848 [astro-ph.HE].

[81] C. Amole et al. 'Dark Matter Search Results from the PICO-2L C_3F_8 Bubble Chamber'. In: *Phys. Rev. Lett.* 114.23 (2015), p. 231302. DOI: 10.1103/PhysRevLett.114.231302. arXiv: 1503.00008 [astro-ph.CO].

[82] C. Amole et al. 'Dark matter search results from the PICO-60 CF_3I bubble chamber'. In: *Phys. Rev.* D93.5 (2016), p. 052014. DOI: 10.1103/PhysRevD.93.052014. arXiv: 1510.07754 [hep-ex].

[83] A. Albert et al. 'Dark Matter Limits From Dwarf Spheroidal Galaxies with The HAWC Gamma-Ray Observatory'. In: *Astrophys. J.* 853.2 (2018), p. 154. DOI: 10.3847/1538-4357/aaa6d8. arXiv: 1706.01277 [astro-ph.HE].

[84] A. U. Abeysekara et al. 'A Search for Dark Matter in the Galactic Halo with HAWC'. In: *JCAP* 1802.02 (2018), p. 049. DOI: 10.1088/1475-7516/2018/02/049. arXiv: 1710.10288 [astro-ph.HE].

[85] M. Ackermann et al. 'Constraints on the Galactic Halo Dark Matter from Fermi-LAT Diffuse Measurements'. In: *ApJ* 761, 91 (Dec. 2012), p. 91. DOI: 10.1088/0004-637X/761/2/91. arXiv: 1205.6474 [astro-ph.CO].

[86] E. Aprile et al. 'The XENON1T Dark Matter Experiment'. In: *Eur. Phys. J.* C77.12 (2017), p. 881. DOI: 10.1140/epjc/s10052-017-5326-3. arXiv: 1708.07051 [astro-ph.IM].

[87] E. Aprile et al. 'Constraining the spin-dependent WIMP-nucleon cross sections with XENON1T'. In: (2019). arXiv: 1902.03234 [astro-ph.CO].

[88] E. Aprile et al. 'Limits on Spin-Dependent WIMP-Nucleon Cross Sections from 225 Live Days of XENON100 Data'. In: *Phys. Rev. Lett.* 111 (2 July 2013), p. 021301. DOI: 10.1103/PhysRevLett.111.021301. URL: https://link.aps.org/doi/10.1103/PhysRevLett.111.021301.

[89] Jingkai Xia et al. 'Constraining WIMP-Nucleon Effective Interactions from PandaX-II Experiment'. In: (2018). arXiv: 1807.01936 [hep-ex].

[90] Paolo Gondolo and Graciela Gelmini. 'Cosmic abundances of stable particles: Improved analysis'. In: *Nucl. Phys.* B360 (1991), pp. 145–179. DOI: 10.1016/0550-3213(91)90438-4.

[91] M. Cannoni. 'Relativistic $< \sigma v_{\rm rel} >$ in the calculation of relics abundances: a closer look'. In: *Phys. Rev.* D89.10 (2014), p. 103533. DOI: 10.1103/PhysRevD.89.103533. arXiv: 1311.4494 [astro-ph.CO].

[92] Dan Hooper. 'Particle Dark Matter'. In: *Proceedings of Theoretical Advanced Study Institute in Elementary Particle Physics on The dawn of the LHC era (TASI 2008): Boulder, USA, June 2-27, 2008.* 2010, pp. 709–764. DOI: 10.1142/9789812838360_0014. arXiv: 0901.4090 [hep-ph]. URL: http://lss.fnal.gov/cgi-bin/find_paper.pl?conf-09-025.

[93] Edward W. Kolb and Michael S. Turner. 'The Early Universe'. In: *Front. Phys.* 69 (1990), pp. 1–547.

[94] I.A. Stegun M. Abramowitz. *Handbook of Mathematical Functions.* 378. Dover Publications Inc., 1972.

[95] URL: https://icecube.wisc.edu/.

[96] Silvia Bravo. *IceCube Upgrade for precision neutrino physics and astrophysics kicks off.* 2018. URL: https://icecube.wisc.edu/news/view605.

[97] M. A. Unland Elorrieta et al. 'Characterisation of the Hamamatsu R12199-01 HA MOD photomultiplier tube for low temperature applications'. In: *JINST* 14.03 (2019), P03015. DOI: 10.1088/1748-0221/14/03/P03015. arXiv: 1902.01714 [physics.ins-det].

[98] Lew Classen. 'The mDOM - a multi-PMT digital optical module for the IceCube-Gen2 neutrino telescope'. PhD thesis. Friedrich-Alexander-Universität Erlangen-Nürnberg, 2017.

[99] Martin Antonio Unland Elorrieta. 'Studies on dark rates induced byradioactive decays of the multi-PMTdigital optical module for future IceCube extensions'. MA thesis. Westfälische Wilhelms-Universität Münster, 2017.

[100] A.G.Wright. *The Photomultiplier Handbook*. Oxford University Press, 2017.

[101] S. Adrián-Martínez. 'A method to stabilise the performance of negatively fed KM3NeT photomultipliers'. In: *JINST* 11.12 (2016), P12014. DOI: 10.1088/1748-0221/11/12/P12014.

[102] Autodesk Inventor 2018, Autodesk, Inc. URL: www.autodesk.eu/products/inventor/.

[103] COMSOL Multiphysics v. 5.2, COMSOL AB. URL: www.comsol.com.

[104] H. Löhner et al. 'The multi-PMT optical module for KM3NeT'. In: *Nuclear Instruments and Methods in Physics Research Section A: Accelerators, Spectrometers, Detectors and Associated Equipment* 718 (2013). Proceedings of the 12th Pisa Meeting on Advanced Detectors, pp. 513 –515. ISSN: 0168-9002. DOI: https://doi.org/10.1016/j.nima.2012.11.049. URL: http://www.sciencedirect.com/science/article/pii/S0168900212013861.

[105] Eckart Lorenz and Manel Martinez. 'The Magic telescope'. In: *Astronomy & Geophysics* 46.6 (Dec. 2005), pp. 6.21–6.25. ISSN: 1366-8781. DOI: 10.1111/j.1468-4004.2005.46621.x. eprint: http://oup.prod.sis.lan/astrogeo/article-pdf/46/6/6.21/522663/46-6-6.21.pdf. URL: https://doi.org/10.1111/j.1468-4004.2005.46621.x.

[106] R. Cornils et al. 'The optical system of the HESS imaging atmospheric Cherenkov telescopes, Part 2: Mirror alignment and point spread function'. In: *Astropart. Phys.* 20 (2003), pp. 129–143. DOI: 10.1016/S0927-6505(03)00172-5. arXiv: astro-ph/0308247 [astro-ph].

[107] G. Belanger et al. 'MicrOMEGAs: A Program for calculating the relic density in the MSSM'. In: *Comput. Phys. Commun.* 149 (2002), pp. 103–120. DOI: 10.1016/S0010-4655(02)00596-9. arXiv: hep-ph/0112278 [hep-ph].

[108] P. Gondolo et al. 'DarkSUSY: Computing supersymmetric dark matter properties numerically'. In: *JCAP* 0407 (2004), p. 008. DOI: 10.1088/1475-7516/2004/07/008. arXiv: astro-ph/0406204 [astro-ph].

[109] Björn Herrmann and Michael Klasen. 'SUSY-QCD Corrections to Dark Matter Annihilation in the Higgs Funnel'. In: *Phys. Rev.* D76 (2007), p. 117704. DOI: 10.1103/PhysRevD.76.117704. arXiv: 0709.0043 [hep-ph].

[110] Björn Herrmann, Michael Klasen and Karol Kovařík. 'Neutralino Annihilation into Massive Quarks with SUSY-QCD Corrections'. In: *Phys. Rev.* D79 (2009), p. 061701. DOI: 10.1103/PhysRevD.79.061701. arXiv: 0901.0481 [hep-ph].

[111] Björn Herrmann, Michael Klasen and Karol KovaříSk. 'SUSY-QCD effects on neutralino dark matter annihilation beyond scalar or gaugino mass unification'. In: *Phys. Rev.* D80 (2009), p. 085025. DOI: 10.1103/PhysRevD.80.085025. arXiv: 0907.0030 [hep-ph].

[112] Björn Herrmann. 'Radiative corrections to neutralino annihilation: Recent developments'. In: *PoS* IDM2010 (2011), p. 123. DOI: 10.22323/1.110.0123. arXiv: 1011.6550 [hep-ph].

[113] B. Herrmann et al. 'One-loop corrections to gaugino (co)annihilation into quarks in the MSSM'. In: *Phys. Rev.* D89.11 (2014), p. 114012. DOI: 10.1103/PhysRevD.89.114012. arXiv: 1404.2931 [hep-ph].

[114] J. Harz et al. 'Neutralino-stop coannihilation into electroweak gauge and Higgs bosons at one loop'. In: *Phys. Rev.* D87.5 (2013), p. 054031. DOI: 10.1103/PhysRevD.87.054031. arXiv: 1212.5241 [hep-ph].

[115] Julia Harz et al. 'Impact of SUSY-QCD corrections on neutralino-stop co-annihilation and the neutralino relic density'. In: *PoS* Corfu2012 (2013), p. 075. DOI: 10.22323/1.177.0075. arXiv: 1302.3525 [hep-ph].

[116] J. Harz et al. 'One-loop corrections to neutralino-stop coannihilation revisited'. In: *Phys. Rev.* D91.3 (2015), p. 034028. DOI: 10.1103/PhysRevD.91.034028. arXiv: 1409.2898 [hep-ph].

[117] J. Harz et al. 'SUSY-QCD corrections to stop annihilation into electroweak final states including Coulomb enhancement effects'. In: *Phys. Rev.* D91.3 (2015), p. 034012. DOI: 10.1103/PhysRevD.91.034012. arXiv: 1410.8063 [hep-ph].

[118] J. Harz et al. 'Theoretical uncertainty of the supersymmetric dark matter relic density from scheme and scale variations'. In: *Phys. Rev.* D93.11 (2016), p. 114023. DOI: 10.1103/PhysRevD.93.114023. arXiv: 1602.08103 [hep-ph].

[119] S. Schmiemann et al. 'Squark-pair annihilation into quarks at next-to-leading order'. In: (2019). arXiv: 1903.10998 [hep-ph].

[120] Michael Klasen, Karol Kovařík and Patrick Steppeler. 'SUSY-QCD corrections for direct detection of neutralino dark matter and correlations with relic density'. In: *Phys. Rev.* D94.9 (2016), p. 095002. DOI: 10.1103/PhysRevD.94.095002. arXiv: 1607.06396 [hep-ph].

[121] Michael Klasen, Karol Kovařík and Saskia Schmiemann. 'Direct detection of neutralino dark matter with DM@NLO'. In: *PoS* EPS-HEP2017 (2017), p. 068. DOI: 10.22323/1.314.0068. arXiv: 1709.02681 [hep-ph].

[122] B. C. Allanach et al. 'SUSY Les Houches Accord 2'. In: *Comput. Phys. Commun.* 180 (2009), pp. 8–25. DOI: 10.1016/j.cpc.2008.08.004. arXiv: 0801.0045 [hep-ph].

[123] Werner Porod. 'SPheno, a program for calculating supersymmetric spectra, SUSY particle decays and SUSY particle production at e+ e- colliders'. In: *Comput. Phys. Commun.* 153 (2003), pp. 275–315. DOI: 10.1016/S0010-4655(03)00222-4. arXiv: hep-ph/0301101 [hep-ph].

[124] W. Porod and F. Staub. 'SPheno 3.1: Extensions including flavour, CP-phases and models beyond the MSSM'. In: *Comput. Phys. Commun.* 183 (2012), pp. 2458–2469. DOI: 10.1016/j.cpc.2012.05.021. arXiv: 1104.1573 [hep-ph].

[125] G. Belanger et al. 'MicrOMEGAs 2.0: A Program to calculate the relic density of dark matter in a generic model'. In: *Comput. Phys. Commun.* 176 (2007), pp. 367–382. DOI: 10.1016/j.cpc.2006.11.008. arXiv: hep-ph/0607059 [hep-ph].

[126] M. Beneke, P. Falgari and C. Schwinn. 'Soft radiation in heavy-particle pair production: All-order colour structure and two-loop anomalous dimension'. In: *Nucl. Phys.* B828 (2010), pp. 69–101. DOI: 10.1016/j.nuclphysb.2009.11.004. arXiv: 0907.1443 [hep-ph].

[127] G. Passarino and M. J. G. Veltman. 'One Loop Corrections for e+ e- Annihilation Into mu+ mu- in the Weinberg Model'. In: *Nucl. Phys.* B160 (1979), pp. 151–207. DOI: 10.1016/0550-3213(79)90234-7.

[128] Gerard 't Hooft and M. J. G. Veltman. 'Scalar One Loop Integrals'. In: *Nucl. Phys.* B153 (1979), pp. 365–401. DOI: 10.1016/0550-3213(79)90605-9.

[129] Karol Kovařík. 'Hitchhiker's guide to Renormalization'.

[130] N. Baro, F. Boudjema and A. Semenov. 'Full one-loop corrections to the relic density in the MSSM: A Few examples'. In: *Phys. Lett.* B660 (2008), pp. 550–560. DOI: 10.1016/j.physletb.2008.01.031. arXiv: 0710.1821 [hep-ph].

[131] N. Baro et al. 'Relic density at one-loop with gauge boson pair production'. In: *Phys. Rev.* D81 (2010), p. 015005. DOI: 10.1103/PhysRevD.81.015005. arXiv: 0910.3293 [hep-ph].

[132] Marcela Carena et al. 'Effective Lagrangian for the $\bar{t}bH^+$ interaction in the MSSM and charged Higgs phenomenology'. In: *Nucl. Phys.* B577 (2000), pp. 88–120. DOI: 10.1016/S0550-3213(00)00146-2. arXiv: hep-ph/9912516 [hep-ph].

[133] Dipl. Ing. Helmut Eberl. 'Strahlungskorrekturen im minimalen supersymmetrischen Standardmodell'. PhD thesis. Technische Universität Wien, 1998.

[134] S. Heinemeyer, H. Rzehak and C. Schappacher. 'Proposals for Bottom Quark/Squark Renormalization in the Complex MSSM'. In: *Phys. Rev.* D82 (2010), p. 075010. DOI: 10.1103/PhysRevD.82.075010. arXiv: 1007.0689 [hep-ph].

[135] K. Kovařík et al. 'Full O(alpha) corrections to e+ e- —> f (i) anti-f (j)'. In: *Phys. Rev.* D72 (2005), p. 053010. DOI: 10.1103/PhysRevD.72.053010. arXiv: hep-ph/0506021 [hep-ph].

[136] K. G. Chetyrkin and A. Kwiatkowski. 'Second order QCD corrections to scalar and pseudoscalar Higgs decays into massive bottom quarks'. In: *Nucl. Phys.* B461 (1996), pp. 3–18. DOI: 10.1016/0550-3213(95)00616-8. arXiv: hep-ph/9505358 [hep-ph].

[137] Jaume Guasch, Petra Hafliger and Michael Spira. 'MSSM Higgs decays to bottom quark pairs revisited'. In: *Phys. Rev.* D68 (2003), p. 115001. DOI: 10.1103/PhysRevD.68.115001. arXiv: hep-ph/0305101 [hep-ph].

[138] J. A. M. Vermaseren, S. A. Larin and T. van Ritbergen. 'The four loop quark mass anomalous dimension and the invariant quark mass'. In: *Phys. Lett.* B405 (1997), pp. 327–333. DOI: 10.1016/S0370-2693(97)00660-6. arXiv: hep-ph/9703284 [hep-ph].

[139] R. Harlander, L. Mihaila and M. Steinhauser. 'Two-loop matching coefficients for the strong coupling in the MSSM'. In: *Phys. Rev.* D72 (2005), p. 095009. DOI: 10.1103/PhysRevD.72.095009. arXiv: hep-ph/0509048 [hep-ph].

[140] A. Bauer, L. Mihaila and J. Salomon. 'Matching coefficients for $\alpha(s)$ and $m(b)$ to $\mathcal{O}(\alpha^2(s))$ in the MSSM'. In: *JHEP* 02 (2009), p. 037. DOI: 10.1088/1126-6708/2009/02/037. arXiv: 0810.5101 [hep-ph].

[141] A. Sommerfeld. 'Über die Beugung und Bremsung der Elektronen'. In: *Annalen der Physik* 403 (1931), pp. 257–330. DOI: 10.1002/andp.19314030302.

[142] W. Fischler. 'Quark-antiquark potential in QCD'. In: *Nuclear Physics B* 129.1 (1977), pp. 157 –174. ISSN: 0550-3213. DOI: https://doi.org/10.1016/0550-3213(77)90026-8. URL: http://www.sciencedirect.com/science/article/pii/0550321377900268.

[143] A. Billoire. 'How heavy must quarks BE in order to build coulombic qoverlineq bound states?' In: *Physics Letters B* 92 (May 1980), pp. 343–347. DOI: 10.1016/0370-2693(80)90279-8.

[144] M. R. Kauth, A. Kress and J. H. Kühn. 'Gluino-squark production at the LHC: the threshold'. In: *Journal of High Energy Physics* 12, 104 (Dec. 2011), p. 104. DOI: 10.1007/JHEP12(2011)104. arXiv: 1108.0542 [hep-ph].

[145] Martin Beneke, Pietro Falgari and Christian Schwinn. 'Threshold resummation for pair production of coloured heavy (s)particles at hadron colliders'. In: *Nucl. Phys.* B842 (2011), pp. 414–474. DOI: 10.1016/j.nuclphysb.2010.09.009. arXiv: 1007.5414 [hep-ph].

[146] S. Cassel. 'Sommerfeld factor for arbitrary partial wave processes'. In: *J. Phys.* G37 (2010), p. 105009. DOI: 10.1088/0954-3899/37/10/105009. arXiv: 0903.5307 [hep-ph].

[147] Kaoru Hagiwara, Yukinari Sumino and Hiroshi Yokoya. 'Bound-state Effects on Top Quark Production at Hadron Colliders'. In: *Phys. Lett.* B666 (2008), pp. 71–76. DOI: 10.1016/j.physletb.2008.07.006. arXiv: 0804.1014 [hep-ph].

[148] Y. Kiyo et al. 'Top-quark pair production near threshold at LHC'. In: *Eur. Phys. J.* C60 (2009), pp. 375–386. DOI: 10.1140/epjc/s10052-009-0892-7. arXiv: 0812.0919 [hep-ph].

[149] M. Drees, J. M. Kim and K. I. Nagao. 'Potentially Large One-loop Corrections to WIMP Annihilation'. In: *Phys. Rev.* D81 (2010), p. 105004. DOI: 10.1103/PhysRevD.81.105004. arXiv: 0911.3795 [hep-ph].

[150] Andrzej Hryczuk, Roberto Iengo and Piero Ullio. 'Relic densities including Sommerfeld enhancements in the MSSM'. In: *JHEP* 03 (2011), p. 069. DOI: 10.1007/JHEP03(2011)069. arXiv: 1010.2172 [hep-ph].

[151] M. Beneke, Charlotte Hellmann and P. Ruiz-Femenia. 'Heavy neutralino relic abundance with Sommerfeld enhancements - a study of pMSSM scenarios'. In: *JHEP* 03 (2015), p. 162. DOI: 10.1007/JHEP03(2015)162. arXiv: 1411.6930 [hep-ph].

[152] M. Beneke, C. Hellmann and P. Ruiz-Femenia. 'Non-relativistic pair annihilation of nearly mass degenerate neutralinos and charginos III. Computation of the Sommerfeld enhancements'. In: *JHEP* 05 (2015), p. 115. DOI: 10.1007/JHEP05(2015)115. arXiv: 1411.6924 [hep-ph].

[153] Julia Harz and Kalliopi Petraki. 'Higgs Enhancement for the Dark Matter Relic Density'. In: *Phys. Rev.* D97.7 (2018), p. 075041. DOI: 10.1103/PhysRevD.97.075041. arXiv: 1711.03552 [hep-ph].

[154] S. Biondini. 'Bound-state effects for dark matter with Higgs-like mediators'. In: *JHEP* 06 (2018), p. 104. DOI: 10.1007/JHEP06(2018)104. arXiv: 1805.00353 [hep-ph].

[155] Julia Harz and Kalliopi Petraki. 'Radiative bound-state formation in unbroken perturbative non-Abelian theories and implications for dark matter'. In: *JHEP* 07 (2018), p. 096. DOI: 10.1007/JHEP07(2018)096. arXiv: 1805.01200 [hep-ph].

[156] Julia Harz and Kalliopi Petraki. 'Higgs-mediated bound states in dark-matter models'. In: *JHEP* 04 (2019), p. 130. DOI: 10.1007/JHEP04(2019)130. arXiv: 1901.10030 [hep-ph].

[157] A.J.G. Hey I.J.R. Aitchison. *Gauge theories in particle physics.* Vol. 1 and 2. Taylor & Francis.

[158] A. J. Macfarlane, A. Sudbery and P. H. Weisz. 'On Gell-Mann's λ-matrices,d-andf-tensors, octets, and parametrizations ofS U (3)'. In: *Communications in Mathematical Physics* 11.1 (Mar. 1968), pp. 77–90. ISSN: 1432-0916. DOI: 10.1007/BF01654302. URL: https://doi.org/10.1007/BF01654302.

[159] Vera Derya. *Color factors in QCD*. Oct. 2008. URL: https://lpsc.in2p3.fr/schien/Rapports/derya.pdf.

[160] Masaaki Kuroda. 'Complete Lagrangian of MSSM'. In: (1999). arXiv: hep-ph/9902340 [hep-ph].

[161] Mirco Cannoni. 'Lorentz invariant relative velocity and relativistic binary collisions'. In: *Int. J. Mod. Phys.* A32.02n03 (2017), p. 1730002. DOI: 10.1142/S0217751X17300022. arXiv: 1605.00569 [hep-ph].

[162] A. Denner and S. Dittmaier. 'Scalar one-loop 4-point integrals'. In: *Nucl. Phys.* B844 (2011), pp. 199–242. DOI: 10.1016/j.nuclphysb.2010.11.002. arXiv: 1005.2076 [hep-ph].

[163] L. Lewin. *Polylogarithms and Associated Functions*. New York: North-Holland, 1981.

[164] J. D. Hunter. 'Matplotlib: A 2D graphics environment'. In: *Computing In Science & Engineering* 9.3 (2007), pp. 90–95. DOI: 10.1109/MCSE.2007.55.

[165] D. Binosi and L. Theußl. 'JaxoDraw: A graphical user interface for drawing Feynman diagrams'. In: *Computer Physics Communications* 161.1 (2004), pp. 76 –86. ISSN: 0010-4655. DOI: https://doi.org/10.1016/j.cpc.2004.05.001. URL: http://www.sciencedirect.com/science/article/pii/S0010465504002115.

Lebenslauf

Name:	Saskia Schmiemann
Geburtsort und -datum:	Deutschland Lübbecke | 05 Juni 1991

Berufserfahrung

seit 03.2016	Wissenschaftliche Mitarbeiterin Westfälische Wilhelms Universität Münster
10.2013 - 02.2016	Studentische Hilfsstelle - Übungsgruppenleiterin

Studium und Schule

seit 03.2016	Doktorarbeit: *SUSY-QCD corrections to dark matter annihilation* Erster Betreuer: Prof. Dr. Michael Klasen Zweiter Betreuer: Prof. Dr. A. Kappes
01.2016	M.Sc. in Physik an der WWU Münster Masterarbeit: *Electroweak neutralino annihilation processes in DM@NLO* Betreuer: Prof. Dr. Michael Klasen, Dr. K. Kovařík
04.2014 - 02.2016	Masterstudium WWU Münster
02.2014	B.Sc. in Physik an der WWU Münster Bachelorarbeit: *Coulomb corrections to squark-pair production at the LHC* Betreuerin: Jun. Prof. Dr. Anna Kulesza
09.2010 - 03.2014	Bachelorstudiengang WWU Münster
2010	Abitur Goethe Gymnasium Ibbenbüren

Acknowledgements

At this point I would like to thank all those who made this work possible for me and who accompanied me on my way here. First of all I would like to thank Prof. Dr. Michael Klasen, who gave me the opportunity to work on this topic. Thank you very much for the interesting work and everything I learned during this time.

Furthermore, I would like to thank my second supervisor Prof. Dr. Alexander Kappes, who has considered really interesting topics for my experimental side project and has supported me in the realization. Many thanks for the great time.

Very special thanks go to Priv.-Doz. Dr. Karol Kovařík, who accompanied me on the whole way of this work, from whom I really learned a lot. Thank you very much for all the explanations, discussions, advices and the open listening.

I would like to thank my long-time office colleague Dr. Sonja Esch for the great time in our office, the discussions, the help and the laughter.

I would also like to thank our collaboration colleagues from `DM@NLO`, Dr. Björn Hermann for the discussions, the comparative calculations and the nice stays at LATPh and Julia Hartz for the discussions also late in the evening via Skype.

I would like to thank Dr. Lew Classen for his support in the experimental side project and Martin Unland Elorrieta for the work he put into our publication.

Special thanks to Daniel Schwartländer and Christoph Kabelitz, who have accompanied me since the beginning of my studies.

I would also like to thank all the other colleagues who accompanied me on my way, Marthijn Sunder, Sybrand Zeinstra, Johannes Branahl, Dr. Jens Salomon, Dr. Jury Fiaschi, Kevin Eckert, Laura Moreno and all the others.

Furthermore, I would like to thank the RTG 2149 *Strong and Weak Interactions - from Hadrons to Dark Matter*, where as an associated member I received a lot of support in the form of summer schools, workshops, retreats and much more. I would also like to thank all members of the RTG for the great time we had.

Now I would also like to thank people who did not work with me but accompanied me during this time. First of all I would like to thank my fiancé Steffen Diekschulte, who especially helped me to create the model of the PMT with Autodesk Inventor. But above all because he has supported me over the years, believed in me and encouraged me. I would also like to thank my family who has always believed in me, supported me all my life and made the path I have taken possible. Thank you very much, I am really grateful for everything.

The figures presented in this paper have been generated using `MatPlotLib` [164]. Feynman diagrams within this work were produced using JaxoDraw [165].